THE UNIVERSITY OF
WARWICK

University of Warwick institutional repository: http://go.warwick.ac.uk/wrap

A Thesis Submitted for the Degree of PhD at the University of Warwick

http://go.warwick.ac.uk/wrap/66300

This thesis is made available online and is protected by original copyright.

Please scroll down to view the document itself.

Please refer to the repository record for this item for information to help you to cite it. Our policy information is available from the repository home page.

Control of the Nanostructure and Microtribology of Magnetron Sputtered Surfaces

by

Yvonne B. Gerbig

A thesis submitted in partial fulfilment of the requirements for the degree of Doctor of Philosophy in Engineering

University of Warwick, School of Engineering

March 2006

Table of Contents

List of Illustrations ---- v

List of Tables ---- xvi

Acknowledgement ---- xix

Dedication ---- xxi

Declaration ---- xxii

Abstract ---- xxiii

List of Abbreviations and Acronyms ---- xxiv

List of Symbols ---- xxvi

Chapter 1: Introduction ---- 1

1.1 Research Approach of the Thesis ---- 7

1.2 Layout of the Thesis ---- 9

Chapter 2: Principles of Sputter Deposition and Thin Film Growth ---- 10

2.1 Sputter Deposition of Thin Films ---- 10

2.1.1 Processing of Plasma ---- 11

2.1.2 Interaction of Plasma with Target ---- 12

2.1.3 Sputtering Techniques ---- 13

2.2 Thin Film Growth ---- 16

2.2.1 Nucleation and Early Stage Growth ---- 16

2.2.2 Evolution of Film Morphology ---- 18

2.2.3 Development of Crystallographic Texture ---- 27

2.3 Chromium Nitride Thin Film ---- 29

Chapter 3: Principles of Microtribology ---- 32

3.1 Friction in Nano and Microscale Contacts ---- 32

3.1.1 Adhesive Interaction Contribution to the Friction Force ---- 34

3.1.2 Contribution of Asperity Wear to the Friction Force ---------- 37
3.1.3 Stick-Slip Contribution to the Friction Force ---------- 37
3.1.4 Contact Angles on Surfaces ---------- 38
3.1.5 Friction in Lubricated Contacts ---------- 39
3.2 Wear in Micro and Nanoscale Contacts ---------- 41
3.2.1 Adhesive Wear ---------- 42
3.2.2 Abrasion ---------- 43
3.2.3 Tribochemical Wear ---------- 43
3.2.4 Surface Fatigue Wear ---------- 44
Chapter 4: Preparation and Characterisation of Nanostructured Surfaces ---------- 46
4.1 Surface Preparation ---------- 46
4.1.1 Nanostructuring of Surfaces ---------- 46
4.1.2 Modification of Surface Chemistry ---------- 53
4.2 Analysis of Properties of Nanostructured Thin Films ---------- 56
4.2.1 Characterisation of Film Morphology ---------- 57
4.2.2 Determination of Topographical Parameters ---------- 59
4.2.3 Analysis of Surface Chemistry ---------- 61
4.2.4 Measurement of Mechanical Properties ---------- 61
4.2.5 Determination of Wettability of Nanostructures ---------- 64
4.3 Characterisation of Microtribological Performance of Nanostructured Thin Films ---------- 66
4.3.1 Microtribometer ---------- 66
4.3.2 Experiments on Friction and Wear in Unlubricated Contacts (EG 1) ---------- 72
4.3.3 Comparison of Nanostructured Surfaces in Lubricated Contacts (EG 2) ---------- 76
4.3.4 Experiments on Friction of Hydrophobic and Hydrophilic Surfaces (EG 3) ---------- 76
4.3.5 Investigated Surfaces ---------- 78
4.3.6 Specification of Counter Bodies and Lubricants Used in the Tests ---------- 80
Chapter 5 Nanostructuring of Surfaces ---------- 82
5.1 Classification and Description of Topography Types ---------- 83
5.1.1 Topography Type P (Pyramid) ---------- 83
5.1.2 Topography Type G (Grain) ---------- 87
5.1.3 Topography Type CR (Crater) ---------- 88
5.1.4 Topography Type C (Cone) ---------- 89
5.1.5 Topography Type R (Ribbon) ---------- 90
5.1.6 Topography Type H (Hillock) ---------- 90

5.2 Growth Conditions for Topography Types ---- **91**
5.2.1 Topography Type P ---- 92
5.2.2 Topography Type G ---- 94
5.2.3 Topography Type CR ---- 94
5.2.4 Topography Type C ---- 95
5.2.5 Topography Type R ---- 95
5.2.6 Topography Type H ---- 95
5.3 Size Modification of Topographical Features ---- **96**
5.3.1 Topography Type P ---- 97
5.3.2 Topography Type G ---- 99
5.3.3 Topography Type CR ---- 101
5.3.4 Topography Type C ---- 102
5.3.5 Topography Type R ---- 103
5.3.6 Topography Type H ---- 105
5.4 Discussion of the Morphological Evolution ---- **106**
5.4.1 Topography Type P ---- 106
5.4.2 Topography Type G ---- 108
5.4.3 Topography Type CR ---- 109
5.4.4 Topography Type C ---- 110
5.4.5 Topography Types R and H ---- 110
5.5 Mechanical Properties of Topography Types ---- **111**
5.6 Reproducibility of Thin Film Properties ---- **113**
Chapter 6: Microtribology of Selected Nanostructures ---- **116**
6.1 Friction and Wear of Nanostructured Surfaces in Unlubricated Contacts (EG 1) ---- **117**
6.1.1 Properties of Nanostructures Investigated in EG 1 ---- 117
6.1.2 Frictional Behaviour of Nanostructured Surfaces under Nearly Wear-free Conditions 120
6.1.3 Load-Carrying Capacity (LCC) of Nanostructured Surfaces ---- 130
6.1.4 Long Term Stability (LTS) of Nanostructured Surfaces ---- 147
6.2 Comparison of Nanostructured Surfaces in Lubricated Contacts (EG 2) ---- **152**
6.2.1 Surfaces Investigated in EG 2 ---- 152
6.2.2 Microfrictional Behaviour of Nanostructured Surfaces in Lubricated Contacts ---- 152
6.2.3 Comparison of the Microfrictional Behaviour of Lubricated, Crater-like Structured Surfaces at Low Loads ---- 154

6.2.4 Comparison of the Microfrictional Behaviour of Lubricated, Crater-like Structured Surfaces at Higher Loads ---- 158

6.3 Effect of Nanoscale Topography and Chemical Composition of Surfaces on Their Microfrictional Behaviour (EG 3) ---- 163

6.3.1 Surfaces Tested in EG 3 ---- 163

6.3.2 Influence of Nanostructure on Wettability ---- 163

6.3.3 Influence of Structure on Frictional Behaviour ---- 166

6.3.4 Comparison between Friction on Hydrophilic and Hydrophobic Surfaces ---- 169

6.3.5 Correlation between Surface Wettability and Frictional Behaviour ---- 172

6.3.6 Influence of Sliding Velocity on Friction of Different Surface Structures ---- 173

Chapter 7: Summary, Conclusions and Outlook ---- 178

7.1 Nanostructuring of Thin Films (In-Process Structuring) ---- 178

7.1.1 Applicability of In-Process Structuring ---- 179

7.1.2 Validity of Topography-Zone Model for Other Coating Materials ---- 180

7.2 Microtribological Behaviour of In-Process Structured Surfaces ---- 180

7.3 Future Work ---- 183

7.3.1 Extension of Topography-Zone-Model ---- 183

7.3.2 Further Microtribological Studies on In-Process Structured Surfaces ---- 183

References ---- 185

Appendix ---- 211

A.1 Definition of Topographical Parameters ---- 211

A.2 Calculation of Contact Pressure in Tribological Tests ---- 216

A.3 Examples of Analysis Data Obtained for Nanostructures ---- 219

A.4 Publications and Presentations Arising from this Work ---- 252

List of Illustrations

Chapter 1

Figure 1.1: Examples of nanostructured surfaces used in different application fields to enhance surface functionality.

Figure 1.2: Parameter range for tribotesting, adapted from Dvorak, Woodland & Unertl (1998).

Chapter 2

Figure 2.1: Energy regimes of knock-on events: (a) single-knock on (low energy), (b) linear cascade (high energy), (c) non-linear cascade (very high energy), after (Ohring 2002).

Figure 2.2: Simplified cross section (a) of a rectangular planar magnetron taken through the plane B-B' in the sketch (b), taken from Penfold (1995). Item 1 is the nonmagnetic metal case which houses the magnet assembly, item 2 is an insulator to insulate the magnet assembly from the case; item 3 is the magnetisable rear yoke of the magnetic assembly, item 4 are the permanent magnets and item 5 the magnetisable pole pieces for the magnets.

Figure 2.3: Schematic representation of plasma confinement observed in conventional magnetrons and unbalanced magnetrons of type 1 and type 2, after Kelly & Arnell (2000).

Figure 2.4: Basic modes of thin film growth: (a) Island (or Volmer-Weber) growth, (b) Layer (or Frank-Van der Merwe) growth, (c) Stranski-Krastanov growth, adapted from Ohring (2002).

Figure 2.5: Schematic illustration of the parameters influencing film growth in PVD processes, after Kadlec, Musil &Vyskočil (1992).

Figure 2.6: SZM for evaporated film as proposed by Movchan & Demchishin (1969).

Figure 2.7: SZM for sputtered film as proposed by Thornton (1977). The schematic representation shows the superposition of physical processes that establishes structural zones.

Figure 2.8: SZM for sputtered films as proposed by Messier, Giri & Roy (1984).

Figure 2.9: Deposition rate and deposited phases of chromium nitride thin films as a function of the nitrogen partial pressure during reactive sputtering of chromium with a sputter power of 8 kW, total pressure of 8 mTorr, and a bias voltage of -125 V, adapted from Glocker & Shah (1995).

Chapter 3

Figure 3.1: Effect of surface roughness on the contact angle: (a) Wenzel regime (b) Cassie-Baxter regime, adapted from (NTC 2005).

Figure 3.2: Figure 3.2: Stribeck curve showing the variation of the friction force as function of the sliding speed, bulk viscosity of the lubricating fluid and the load applied in the three lubrication regimes: 1-boundary, 2-mixed, 3-full-film. The film thickness, believed to correspond to each of the lubrication regimes, is also shown. Adapted from Israelachvili (1995).

Figure 3.3: Post of a sidewall friction device when running in dry air (a) and in air at 40 % relative humidity (b), taken from Romig, Dugger & McWorther (2003).

Figure 3.4: Physical interactions between abrasive particles and the surfaces of materials, adapted from Zum Gahr (1988).

Chapter 4

Figure 4.1: (a) Configuration of the deposition system used to deposit chromium nitride thin films. The components are abbreviated as follows: Backing valve (BV), Cathode in arc evaporation mode (C-ARC), Cathode gas valve (CGV), Cathode in UBM mode (C-UBM), Heater (H), High vacuum valve (HVV), Mass flow controller (MFC), Penning gauge (PG), Pirani gauge (PiG), Roots pump (RP), Roughing valve (RV), Rotary vane pump (RVP), Substrate holder (SH), Substrate turntable (ST), Substrate planetary rotation table (T), Turbomolecular pump (TP), Viscovac gauge (VG) and

Venting valve (VV), (b) Schematic of the cathode-magnetron arrangement consisting of permanent magnet (PM) and electromagnets (EM).

Figure 4.2: XPS analysis of the 10 nm thick silicon oxide layer deposited on top of a nanostructured Cr-N film. (a) Survey spectrum, (b) Si 2p spectrum: Even after fitting only one peak due to SiO_2 is evident. (KLL = transition level of atom).

Figure 4.3: XPS analysis of the 10 nm thick HFP layer deposited on top of a nanostructured Cr-N film. (a) Survey spectrum, (b) C 1s spectrum: Peak deconvolution shows the presence of 1: $-CF_3$; 2: $-CF_2$; 3: -CF; 4: $C-CF_x$; 5: C=C, C-O; 6: C-C, C-H bonding. (KLL = transition level of atom).

Figure 4.4: Measurement of (a) advancing contact angle θ_A and (b) receding contact angle θ_R with the sessile drop method.

Figure 4.5: Image of the microtribometer. The main components are marked: (1) the *x-y* micropositioning stages powered by stepper motors (2) reciprocating unit, (3) sample, (4) counter body, (5) bending element (force transducer), (6) fibre-optic sensors to detect normal and lateral deflections of the force transducer. The inset shows a force transducer - glass spring - mounted on a steel support.

Figure 4.6: Schematic drawing of (a) fibre-optic sensor with send and receive channels; (b) intensity-Distance curve with the two different measurement region, adapted from Mollenhauer et al. (2003).

Figure 4.7: Sketch of the spring-sensor arrangement to measure the tangential (lateral) and normal deflection of the double leaf spring (a) Top view: Fibre-optical sensor S1 and mirror M1 for tangential force detection. The normal force detection is not shown (b) Side view: Fibre-optical sensor S2 and mirror M2 for the normal force detection. The tangential force detection is not shown. Adapted from Bregliozzi (2006).

Figure 4.8: Signal of the reciprocating drive (a), and tangential (friction) force signal detected in ideal case (b) and under real conditions (c). At the boundary of range I to II, counter body and sample stick. The static force $F_{F,s}$ is defined where the first slip to lower value occurs. The dynamic friction force F_F is obtained from range II and IV. Adapted from Scherge & Gorb (2001).

Chapter 5

Figure 5.1: Morphological appearance of subtype P-r: (a) SEM micrograph of the topographical features (top view), (b) SEM micrograph of the cleaved cross-section of the film, (c) TEM-bright field (BF) micrograph of column tops, (d) Diffraction pattern (DP) taken by TEM.

Figure 5.2: Morphological appearance of subtype P-f: (a) SEM micrograph of the topographical features (top view), (b) SEM micrograph of the cleaved cross-section of the film, (c) BF micrograph (TEM) of column tops, (d) DP (TEM).

Figure 5.3: Morphological appearance of subtype P-s: (a) SEM micrograph of the topographical features (top view), (b) SEM micrograph of the cleaved cross-section of the film, (c) BF micrograph (TEM) of column tops, (d) DP (TEM).

Figure 5.4: Morphological appearance of subtype P-m: (a) SEM micrograph of the topographical features (top view), (b) SEM micrograph of the cleaved cross-section of the film, (c) BF micrograph (TEM) of column tops, (d) DP (TEM).

Figure 5.5: SEM micrographs of the morphological appearance of subtype P-h: (a) Top view of P-h(I), (b) Cleaved cross-section of P-h(I), (c) Top view of P-h(II), (d) Cleaved cross-section of P-h(II).

Figure 5.6: Morphological appearance of type G: (a) SEM micrograph of the topographical features (top view), (b) SEM micrograph of the cleaved cross-section of the film, (c) TEM (BF) micrograph of cross-section, (d) DP (TEM).

Figure 5.7: Morphological appearance of type CR: (a) SEM micrograph of the topographical features (top view), (b) SEM micrograph of the cleaved cross-section of the film, (c) TEM (BF) micrograph of cross-section, (d) DP (TEM).

Figure 5.8: Morphological appearance of type C: (a) SEM micrograph of the topographical features (top view), (b) SEM micrograph of the cleaved cross-section of the film, (c) TEM (BF) micrograph of cross-section, (d) DP (TEM).

Figure 5.9: Morphological appearance of type R: (a) SEM micrograph of the topographical features (top view), (b) SEM micrograph of the cleaved cross-section of the film, (c) TEM (BF) micrograph of cross-section, (d) DP (TEM).

Figure 5.10: Morphological appearance of type H: (a) SEM micrograph of the topographical features (top view), (b) SEM micrograph of the cleaved cross-section of the film, (c) TEM (BF) micrograph of cross-section, (d) DP (TEM).

Figure 5.11: Topography-zone model for Cr-N thin films (deposited by UBM sputtering) indicating the occurrence of the different topography types as function of Ar/N_2 ratio, homologous temperature T/T_m, bias voltage U_b and deposition rate a_d (1… P-m, 2…P-s).

Figure 5.12: Definition of the topographical dimension L_x of the surface features of (a) type P (general), (b) subtype P-h (spike), (c) type G, (d) type C, (e) type R and (f) type H. The determination of the feature height H_x is shown for the topography types P, G and C in (g) and for the types R and H in (h).

Figure 5.13: Lateral dimension L_p as function of: (a) deposition rate a_d at homologous temperature T/T_m = 0.20 and Ar/N_2 ratios of 0.7 (◆), 1.0 (■),1.3 (●) and 1.5 (△) for subtypes P-r, P-m, P-s, P-f; (b) homologous T/T_m at a Ar/N_2 ratios of 0.7 (◆) and 1.5 (△) for subtype P-r. The bias voltage was set at U_b = -50 V in all experiments.

Figure 5.14: Correlation between lateral dimension L_p and height H_p of the surface features of topography type P.

Figure 5.15: Evolution of the topographical features of type P-h as function of Ar/N_2 ratio. (a) Lateral dimension $L_{p\text{-}h}$ of matrix grains of P-h(I) (△) and P-h(II) (▲) and spikes of P-h(I) (◇) and P-h(II) (◆), (b) Spike density for P-h(I) (◇) and P-h(II) (◆), The homologous temperature and the bias voltage were fixed at T/T_m = 0.23 or U_b = -75 V, respectively.

Figure 5.16: Correlation between lateral dimension L_g and height H_g of the surface feature for topography type G.

Figure 5.17: Evolution of the morphological features of type G as function of: (a) homologous temperature T/T_m (Ar/N_2 = 1.3, U_b = – 75 V, a_d = 0.85 - 0.9 µm/h), (b) Ar/N_2 ratio (T/T_m = 0.1, U_b = -125 V, a_d = 0.3 µm/h), (c) bias voltage U_b (T/T_m = 0.23, Ar/N_2 = 1.3, a_d = 0.75 - 0.8 µm/h), (d) deposition rate a_d at bias voltages of U_b of -75 V (T/T_m = 0.23, Ar/N_2 = 1.3).

Figure 5.18: Evolution of the selected surface parameters of topography type CR as (a) to (c): function of deposition rate a_d for T/T_m = 0.17 (◆) and 0.3 (■) at U_b = -250 V and a_d = 0.6 µm/h; (d) to (f): function of the bias voltage U_b for deposition rates a_d = 0.2 - 0.25 µm/h (○) and a_d = 0.5 - 0.6 µm/h (▲) at T/T_m = 0.30. The gas flow ratio was fixed at Ar/N_2 = 1.3.

Figure 5.19: Lateral dimension L_c of topography type C as function of bias voltage U_b at T/T_m = 0.23, a_d = 0.75 - 0.85 µm/h and Ar/N_2 = 1.3.

Figure 5.20: Correlation between lateral dimension L_c and height H_c of the surface feature for topography type C.

Figure 5.21: Correlation between lateral dimension L_r and height H_r of the surface feature for topography type R.

Figure 5.22: Lateral dimension L_r of topography type R as function of (a) homologous temperature T/T_m (Ar/N_2 = 1.3, U_b = -450 V, a_d = 0.9 - 1.0 µm/h); (b) Ar /N_2 ratio (T/T_m = 0.3, U_b = -250 V, a_d = 1.9 - 2.1 µm/h); (c) bias voltage U_b (T/T_m = 0.3, Ar/N_2 = 1.3, a_d = 1.1 – 1.2 µm/h); (d) deposition rate a_d (T/T_m = 0.3, Ar/N_2 = 1.3, U_b = -250 V).

Figure 5.23: Lateral dimension L_h of topography type H as function of (a) homologous temperature T/T_m (Ar/N_2 = 1.3, U_b = -75 V, a_d = 1.6 - 1.8 µm/h); (b) Ar/N_2 ratio (T/T_m = 0.3, U_b = -450 V, a_d = 1.9 - 2.1 µm/h); (c) bias voltage U_b (T/T_m = 0.3, Ar/N_2 = 1.3, a_d = 2.8 - 3.0 µm/h); (d) deposition rate a_d (T/T_m = 0.3, Ar/N_2 = 1.3, U_b = -75 V).

Figure 5.24: Correlation between lateral dimension L_h and height H_h of the surface feature for topography type H.

Figure 5.25: Growth rate of matrix grains and spikes of topography subtype P-h. The homologous temperature and the bias voltage were fixed at T/T_m = 0.23 or U_b = -75 V, respectively.

Chapter 6

Figure 6.1: Friction force F_F measured as function of the normal force F_N force on the reference (□) and Cr-N thin films with

(a) pyramid-like topography: ■ P1, ◆ P2, ▲ P3, ● P4

(b) cone-like topography: ■ C1, ◆ C2, ▲ C3

(c) crater-like topography: ■ CR1, ◆ CR2, ▲ CR3, ● CR4, ✖ CR5, − CR6.

Figure 6.2: μ as function of the summit density S_{sd} for the reference (●) and Cr-N thin films with pyramid-like structured (◆), cone-like structured (▲) and crater-like (■) structured surfaces.

Figure 6.3: Schematic drawing of the main types of F_F/F_N-n_{cycles} curves observed in the LCC tests on nanostructured Cr-N thin films.

Figure 6.4: The fitting coefficient a_2 determined for various normal loads F_N on the pyramid-like structured surface P1 (■), P2 (◆), P3 (▲) and P4 (●). The vertical bars indicate the difference between the maximum and minimum value determined in three tests.

Figure 6.5: Influence of the normal load F_N applied in the LCC tests on the coefficients a_1 and a_0 for the reference surface. The values of a_0 and a_1 were determined only for tests without occurrence of stiction.

Figure 6.6: F_F/F_N-n_{cycles} curves of the structure P1 determined for normal loads of 10 mN (■), 25 mN (◆), 50 mN (▲) and 100 mN (●).

Figure 6.7: Influence of the normal load F_N on (a) coefficient a_1 and (b) coefficient a_0 for pyramid-like structured surfaces: P1 (■, □), P2 (◆, ◇), P3 (▲, △), P4 (●, ○). The values of a_0 and a_1 were determined only for tests without occurrence of stiction.

Figure 6.8: Influence of the normal load F_N on (a) coefficient a_1 and (b) coefficient a_0 for cone-like structured surfaces: C1 (■, □), C2 (◆, ◇), C3 (▲, △). The values of a_0 and a_1 were determined only for tests without occurrence of stiction.

Figure 6.9: Influence of the normal load F_N on (a) coefficient a_1 and (b) coefficient a_0 for crater-like structured surfaces: CR1 (■, □), CR2 (◆, ◇), CR3 (▲, △), CR4 (●, ○), CR5 (✖) and CR6 (−). The values of a_0 and a_1 were determined only for tests without occurrence of stiction.

Figure 6.10: Functional correlation of lateral dimension L_p of the pyramidal features with (a) coefficient a_1 and (b) coefficient a_0 for normal loads of 10 mN (■, □), 25 mN (◆, ◇), 50 mN (▲, △) and 100 mN (●, ○).

Figure 6.11: Functional correlation between the lateral dimension L_c of the conical features and (a) coefficient a_1 and (b) coefficient a_0 for a normal load of 10 mN (■, □), 25 mN (◆, ◇), 50 mN (▲, △) and 100 mN (●, ○).

Figure 6.12: Functional correlation between the skewness S_{sk} of the crater-like structured surfaces and coefficient a_1 in the roughness range of (a) 9 nm ≤ S_q ≤ 12 nm (CR1 to CR3) and (b) 20 nm ≤ S_q ≤ 22 nm (CR4 to CR6) for a normal load of 10 mN (■, □), 25 mN (◆, ◇), 50 mN (▲, △), 100 mN (●, ○), 150 mN (✖) and 200 mN (−).

Figure 6.13: Functional correlation between the skewness S_{sk} of the crater-like structured surfaces and coefficient a_0 in the roughness range of (a) 9 nm ≤ S_q ≥ 12 nm (CR1 to CR3) and (b) 20 nm ≤ S_q ≥ 25 nm (CR4 to CR6) for a normal load of 10 mN (■, □), 25 mN (◆, ◇), 50 mN (▲, △), 100 mN (●, ○), 150 mN (✖) and 200 mN (−).

Figure 6.14: SEM images of the topography of the reference surface before (a) testing and (b) after the tribotest at 50 mN normal load.

Figure 6.15: SEM images showing the alteration of surface topography of sample P1 in tribologically stressed zone on surface P1 after testing at a normal load of 10 mN. Figure (b) is a micrograph at higher magnification from the region indicated (white-framed box) in (a).

Figure 6.16: SEM images of the tribologically stressed zone of the pyramid-like structured surface P1 after testing at different normal loads of (a) 10 mN and (b) 100 mN. The bracket marked with S represents the width of the wear track exhibiting a smoothened surface topography.

Figure 6.17: SEM images of the topography of structure C3 before testing (a), after testing at a normal load of 10 mN (b) and 250 mN (c).

Figure 6.18: Schematic profile of surfaces with (a) positive skewness, (b) highly negative skewness and (c) moderate negative skewness.

Figure 6.19: SEM images of the topography of crater-like structured surface CR5 (a) before testing (a) and after testing at a normal load of (b) 10 mN and (c) 100 mN (c). The figure shows also an element spectrum obtained by EDS of agglomerates of wear particles.

Figure 6.20: Abbot-Firestone curve of crater-like structured surfaces with positive and moderate negative skewness in two roughness ranges (AFM scan area: 20 x 20 μm^2).

Figure 6.21: Dependence of F_F/F_N on the logarithm of cycle number n_{cycles} at normal loads of 10, 50 and 150 mN for the reference surface, marked as ✖ in (a), and Cr-N films with
(a) pyramid-like structured surfaces: ■ P1, ◆ P2, ▲ P3, ● P4
(b) cone-like structured surfaces: ■ C1, ◆ C2, ▲ C3
(c) crater-like structured surfaces: ■ CR1, ◆ CR3, ▲ CR4, ● CR6.

Figure 6.22: Friction force F_F evolution as function of cycle number. The example shows a friction curve recorded on structure CR6 (lubricated with MO40, speed 25 µm/s, normal load 3 mN, cycle period 13 s).

Figure 6.23: Friction force F_F measured as function of the normal force F_N on the reference sample lubricated with MO4 in a test at a sliding speed of 300 µm/s.

Figure 6.24: Coefficient of friction μ determined for various nanostructured surfaces in tests with without (solid columns) or with application of PAO oil (striped columns). The μ values were obtained from the slopes over the normal load range 1 mN to 15 mN at a sliding velocity of 25 µm/s. The vertical bars indicate the difference between the maximum and minimum μ value determined in three tests.

Figure 6.25: Coefficient of friction μ determined on the reference and crater-likes structured surfaces (CR1 to CR6) lubricated with oil (a) PAO, (b) MO4, (c) MO40, (d) MO96 and (e) MO200 and tested

at sliding velocities of 25 µm/s (◆), 300 µm/s (◈) and 500 µm/s (◇).The vertical bars indicate the difference between the maximum and minimum μ value determined in three tests.

Figure 6.26: Coefficient of friction μ measured on the reference and different crater-like structured surfaces (CR1 to CR6) in test with sliding speeds of (a) 25, (b) 300 and (c) 500 µm/s and lubricated with various oils. (Data are redrawn from Figure 6.25).

Figure 6.27: Friction coefficient μ as function of the sliding velocity determined for the reference surface and the crater-like structured sample CR4 in unlubricated tests.

Figure 6.28: Evolution of a_1 and a_0 as function of the normal load applied for the reference and the crater-like structured surfaces CR1 to CR6 in non-lubricated and lubricated contacts (oil PAO). The values of a_1 are marked as full squares in non-lubricated conditions and as empty squares in lubricated tests. The values of a_0 are marked as full triangles in non-lubricated conditions and as empty triangles in lubricated tests. The occurrence of stiction in the non-lubricated tests is indicated by *.

Figure 6.29: Mean values of coefficients a_1 and a_0 plotted versus the skewness S_{sk} of crater-like structured surfaces in two S_q roughness ranges.

Figure 6.30: Coefficient a_1 plotted versus the core fluid retention index S_{ci} for normal load of 25 mN (◆) and 50 mN (▲). For better a illustration, a_1-S_{ci} data were presented only for selected normal loads.

Figure 6.31: Friction force F_F as function of the relative humidity RH measured for a normal load of 0.2 mN on hydrophilic surfaces with

(a) pyramid-like topography: ▲ P1, ▲ P2, ▲ P3, △ P4

(b) cone-like topography: ● C1, ● C2, ○ C3

(c) crater-like topography: ◆ CR1, ◆ CR2, ◇ CR3

and compared to a smooth reference surface (■). The vertical bars represent the variation between the minimum and maximum value in these tests.

Figure 6.32: Friction force F_F as function of the relative humidity RH measured for a 0.2 mN normal force on hydrophobic surfaces with

(a) pyramid-like topography: ▲ P1, ▲ P2, ▲ P3, △ P4

(b) cone-like topography: ● C1, ● C2, ○ C3

(c) crater-like topography: ◆ CR1, ◆ C2, ◇ CR3

and compared to a smooth reference surface (■). The vertical bars represent the variation between the minimum and maximum value in these tests.

Figure 6.33: Friction force F_F as function of sliding speed v for hydrophilic surfaces with

(a) pyramid-like topography: ▲ P1, ▲ P2, △ P3, △ P4

(b) cone-like topography: ● C1, ● C2, ○ C3

(c) crater-like topography: ◆ CR1, ◆ C2, ◇ CR3

The velocity is plotted in logarithmic scale. The lines mark the least square linear-line fits to the data points. The vertical bars represent the variation between the minimum and maximum value in these tests.

List of Tables

Chapter 2

Table 2.1: Common thin film compounds reactively sputtered and the reactive gas employed in the deposition process, after (Ohring 2002; Bunshah & Deshpandey 1990).

Table 2.2: Selected chemical, physical and mechanical properties of CrN and Cr_2N.

Chapter 4

Table 4.1: Values of the process parameters applied to deposit Cr-N thin films.

Table 4.2: Techniques applied in the thesis to analyse the functionality and related properties of surfaces.

Table 4.3: Topographical parameters selected for their relevance to the experimental group (EG) and determined by post-processing of AFM images of the nanostructures.

Table 4.4: Test conditions applied in the tribological tests of experimental group (EG) 1 and 2 to estimate the load carrying capacity (LCC), long-term stability (LTS) and frictional behaviour of nanostructured surfaces in non-lubricated or lubricated contact, respectively.

Table 4.5: Test conditions applied in the tribological experiments in EG 3.

Table 4.6: Investigated nanostructured surfaces in the different test series of the EGs.

Table 4.7: Selected properties of the counter body used in the microtribological tests.

Table 4.8: Selected properties of the lubricants used in the microtribological tests.

Chapter 5

Table 5.1: Crystallographic texture coefficient for the CrN(111), (200) and (220) crystal planes (parallel to the substrate surface) for films of different subtypes of topography type P and topography type G. The table shows the texture coefficients of the samples presented in the SEM and TEM images.

Table 5.2: Hardness, Young's modulus and residual stress of different morphology types.

Table 5.3: Average value and standard deviation of topographical parameters and mechanical properties determined for the films 1, 2, 3, which were deposited in three separate experiments conducted for each individual set (A, B or C) of deposition conditions.

Chapter 6

Table 6.1: Structural and mechanical properties of the nanostructured surface investigated in EG 1 and EG2.

Table 6.2: Topographical parameters of the investigated surfaces: Lateral dimension L_x and height H_x of the surface features, root mean square roughness S_q, skewness S_{sk}, kurtosis S_{ku}, summit curvature S_{sc}, summit density S_{sd}, rms slope σ', surface bearing index S_{bi}, core fluid retention index S_{ci}, valley fluid retention index S_{vi} and fractal dimension D.

Table 6.3: Mean values of root mean square roughness (S_q) and asperity density S_{sd}, advancing (θ_A) and receding (θ_R) contact angles determined on the smooth reference (Ref), the pyramid-like (P1 to P4), cone-like (C1 to C3) and crater-like (CR1 to CR3) structures coated with 10 nm thick SiO_2 or HFP layers. Since the topographical parameters are similar for the SiO_2 and HFP coated surfaces, the average value calculated from measurements from hydrophilic and hydrophobic sample are given.

Table 6.4: Values of F_1, F_0 and fitting confidence R^2 determined by linear-line fitting of F_F vs. ln(v) plots for the hydrophilic samples with pyramid-like (P1 to P3), cone-like (C1 to C3) and crater-like (CR1 to CR3) structures.

Table 6.5: Friction force as function of the sliding velocity, measured for 0.2 mN normal force, on pyramid-like (P1 to P4), cone-like (C1 to C3) and crater-like (CR1 to CR3) structured, hydrophobic samples.

Chapter 7

Table 7.1: Effect of process parameters homologous temperature T/T_m, Ar/N_2 ratio, bias voltage U_b and deposition rate a_d on the evolution of lateral dimension L on different topography types of chromium nitride thin films.

Acknowledgement

First of all, I would like to thank my supervisor Professor Derek G. Chetwynd for giving me the chance to be a PhD student in his group. I am very grateful for the many valuable and stimulating scientific discussions, his strong support during the work conducted for this thesis and his guidance through the British university system.

I would like to express my deepest gratitude to Imad Ahmed for counselling my research activity in his limited spare time, the inspiring talks beyond scientific topics and the encouragement through the good and bad times in the last years.

The support by Henry Haefke, who has regretfully left us much too early, will never be forgotten. I have learnt a lot from him, especially about scientific research and also project management.

All these years I could not have lasted without the company of my colleagues in the former "Micro and NanoscaleMaterials" Section at CSEM. They have been a source of inspiration as well as entertainment. My special thanks go to Giuseppe Bregliozzi and Alan Savan, for their support even after their departure from CSEM.

I thank the members of the Section "Nanoscale Technology" at CSEM who have offered me their assistance.

The following people deserve my sincere thanks for their expertise and assistance in performing and interpreting of experiments and analysis: András Kovács (MFA, Budapest)

for instructions in preparation of TEM samples of spiky matters, Corinne Nouveau (ENSAM, Cluny) for teaching how to perform and interpret XRD and stress measurements, Imad Ahmed for performing the XPS analysis, Vladislav Spassov (CSEM Neuchâtel), who conducted the TEM analysis and deposited the silicon oxide layers and Yanki Keles (CSEM Alpnach) for depositing fluorocarbon layers.

This research was funded by the Centre Suisse d'Electronique et de Microtechnique SA, Neuchâtel and partially by the Swiss Federal Office for Education and Science within the frame of the European project MICLUB (Contract No. G5RD-2001-00570). I thank them for their financial support.

Furthermore, I would like to thank Xianping Liu (University of Warwick) and Richard Sayles (Imperial College London) for examining my thesis.

Last, but not least, I would like to express my heartfelt gratitude to my parents for their constant love, patience and reassurance during all my life and especially in the last years.

To My Parents

Declaration

I declare that this thesis is my own work except for the following help with specific equipment and techniques

- TEM analysis of the chromium nitride (Cr-N) thin films and preparation of the TEM samples of a part of the thin films investigated by TEM, done by V. Spassov (CSEM SA, Neuchâtel)
- deposition of the silicon oxide (SiO_2) layers, done by V. Spassov (CSEM SA, Neuchâtel)
- deposition of hexaflouropropene (HFP) layers, done by K. Yankes (CSEM SA, Alpnach)
- XRD measurements on Cr-N thin films, done by C. Nouveau (ENSAM Cluny)
- XPS analysis of SiO_2 and HFP layers, done by S.I.-U. Ahmed (Technische Universität Ilmenau)

Information derived from the published or unpublished work of others has been acknowledged in the text and a list of references is given.

This thesis has not been submitted in any form for another degree or diploma at any university or other institution of tertiary education.

.....Y. Pelz.....
Signature

28.03.2006
Date

Abstract

The technological importance of hard thin films is well established. There is growing recognition that nanometre-scale surface structures can be controlled to the benefit of function. In-process structuring brings these ideas together. This study explores how the morphology, especially the surface topography, and microtribological behaviour of Cr-N films can be controlled during unbalanced magnetron (UBM) sputtering.

Experiments varying the sputter power, bias voltage, temperature, total pressure and Ar/N_2 ratio during UBM sputtering generated different compositions, crystallite orientations and microstructures, and six associated topography types: pyramidal (type P), grain-like (G), crater-like (CR), ribbon-like (R), conical (C) and hillock-like (H). A new empirical zone model consistently relates these topography types to process parameters. The feature dimensions are also controlled by the deposition parameters. The films have closely reproducible topographical and mechanical properties.

The microtribological behaviour for three topography types (P, C and CR) is studied under different conditions relevant to unlubricated contacts, lubricated contacts, and humid environments. Nanostructured surfaces show significantly lower friction than smooth ones, with actual reductions depending on the topography type. Friction strongly correlates with summit density (S_{sd}). Low friction ($S_{sd} \sim 3$ #/μm^2) was measured on all type CR surfaces, but only by increasing the lateral dimensions of types P and C.

Unlubricated friction is attributed principally to solid-solid adhesion, influenced by the density and curvature of summits. Wear is influenced by the density, shape and size of the surface features and by the mechanical properties of the film. Boundary lubrication reduced friction, with slight dependence on lubricant. Alongside the summits parameters, friction correlates with core fluid retention index. Applying hydrophobic and hydrophilic treatments shows that appropriate nanostructuring reduces the dependence of friction on humidity and sliding velocity, principally by controlling the summit density.

In-process structuring is clearly very useful for creating nanostructures in order to enhance the microtribological behaviour of surfaces. Further investigations are recommended into friction optimization by nanostructuring.

List of Abbreviations and Acronyms

AFM	Atomic force microscopy
BF	Bright field
BV	Backing valve
C	Cone
C-ARC	Cathode in arc evaporation mode
CGV	Cathode gas valve
CR	Crater
Cr-N	Chromium nitride
CSEM	Centre Suisse d'Electronique et de Microtechnique
C-UBM	Cathode in UBM mode
DC	Direct current
DP	Electron diffraction pattern
EDS	Energy dispersive X-ray spectroscopy
EG	Experimental group
EM	Electromagnet
fcc	face centred cubic
G	Grain
H	Hillock
hcp	hexagonal closed packed
HE	Heater
HFP	Hexafluoropropene
HVV	High vacuum valve
JCPDS	Joint committee for Powder Diffraction Studies
LCC	Load carrying capacity
LTS	Long term stability
M	Mirror

MEMS	Microelectromechanical system
MFC	Mass flow controller
MR	Measurement region
P	Pyramid
PiG	Pirani gauge
PM	Permanent magnet
PVD	Physical vapour deposition
R	Ribbon
RF	Radio frequency
RMS	Root mean square
RP	Roots pump
RV	Roughing valve
RVP	Rotary vane pump
S	Sensor
SAM	Self-assembled monolayer
SEM	Scanning force microscopy
SH	Substrate holder
ST	Substrate turntable
SZM	Structure zone model
T	Substrate planetary rotation table
TiN	Titanium nitride
TEM	Transmission electron microscopy
TP	Turbomolecular pump
UBM	Unbalanced magnetron
VG	Viscovac gauge
VV	Venting valve
XRD	X-ray diffraction
XPS	X-ray photoelectron spectroscopy

List of Symbols

a	Crystal lattice parameter (nm)
$a_{0,1,2,3}$	Coefficients in polynominal equation for fitting F_F/F_N vs. n_{cycles} data
$a_{0,mean}$	Average of a_0 value obtained at different loads (-)
$a_{1,mean}$	Average of a_1 value obtained at different loads (-)
a_d	Deposition rate (m/s in equ. 4.1, otherwise µm/h)
$a_{d,t}$	Transition deposition rate (µm/h)
a_n	Radius of the nominal contact area (m)
A	Effective current-collecting area (m^2)
$A(h_n)$	Bearing area at normalised surface height h_n (m^2)
A_c	Cross-sectional area of a capillary bridge (m^2)
A_{max}	Projected area at maximum load in indentation tests (m^2)
A_n	Nominal contact area (m^2)
A_r	Real contact area (m^2)
c	Crystal lattice parameter (nm)
C	Power in equations (6.2) and (6.3)
C_F	Variable representative for contact configuration (-)
C_P	Scaling constant (-)
C_S	Factor considering surface-specific characteristics (-)
d	Distance from column top to a certain column width w_c (m)
d_{hkl}	Crystallite size of strongest reflection hkl in XRD spectrum (m)
D	Fractal dimension (-)
e	Elementary charge $e = 1.6\ 10^{-19}$ C
$e_{max}(t)$	Maximum spacing (m) between contacting surfaces to which capillary bridge can be built in given time t
E	Young's modulus (Pa)
$E_{1,2}$	Young's modulus of surface 1 or 2 (Pa)

E^*	Composite Young's modulus of two contacting surfaces (Pa)
E_a	Activation energy for tribochemical reactions (J)
E_d	Dissipated energy (J)
E_{dth}	Threshold energy required for generating wear particles (J)
E_f	Young's modulus of film (Pa)
E_i	Ion energy (eV)
E_{ind}	Young's modulus of indenter (Pa)
E_r	Reduced Young's modulus (Pa) taken from load-indentation depth curve
E_s	Young's modulus of substrate (Pa)
$E_{\sigma Y}$	Mechanical energy (J)
f_1	Fraction of fluid in contact with material (-)
f_2	Fraction of the fluid in contact with air (-)
f_{top}	Maximum frequency of sine wave voltage signal (Hz)
$f(x_i, y_i)$	Function of the reference datum
F	Force (N)
F_0	Force at consistently-used, arbitrary reference speed (N)
F_1	Slope in F_F vs. v data plot (m/(sN))
F_{adh}	Adhesion force (N)
F_C	Capillary force (N)
$F_{C,max}$	Maximum capillary force (N)
F_E	Effective normal load (N)
F_F	Friction force (N)
$F_{F,s}$	Static friction force (N)
F_L	Lateral force (N)
F_N	Normal load (N)
$F_{stick\text{-}slip}$	Force attributed to stick-slip between contacting surfaces (N)
F_{wear}	Force attributed to wear of contacting surfaces (N)
h	Thickness of liquid film (m)
h_n	Normalised surface height (-)
$h_{n0.05}$	Normalised surface height at 5 % bearing area (-)
$h_{n0.8}$	Normalised surface height at 80 % bearing area (-)

h_{nmin}	Minimum normalised surface height (-)
H	Hardness (N/m²)
H_x	Feature height of topography type X (μm), X = P, G, C, R or H
i_i	Ion current density (A/m²)
I_{hkl}	Measured intensity of reflection hkl (-) in XRD spectrum
$I_{hkl,\,ref}$	Reference standard intensity of the reflection hkl of a reference given in JCPDS
I_i	Ion current (A)
J_a	Atom flux (atoms/m²)
J_i	Ion flux (ions/m²)
k	Spring constant (N/m)
k_L	Lateral spring constant (N/m)
k_N	Normal spring constant (N/m)
K	Shape factor (-)
K_Y	Yield coefficient (-)
l_x	Length of sampling area in x direction (m)
l_y	Length of sampling area in y direction (m)
L_s	Sampling length (m)
L_x	Lateral feature dimension of topography type X (μm) , X = P, G, C, R or H
m_u	Mass unit $m_u = 1.66\ 10^{-27}$ kg
M	Molecular weight (-)
M_{Cr}	Relative mass of chromium atom (-)
M_N	Relative mass of nitrogen atom (-)
M_r	Average relative mass of a film-forming atom (-)
n_{cycles}	Number of cycles in reciprocating tribotests (-)
$N(t)$	Number of contacting and near-containing asperities (-) where capillarity builds up as function of residence time t
N_s	Number of summits (-)
p	Pressure (Pa)
p_s	Saturation pressure of a gas at ambient temperature (Pa)
P	Target (sputter) power (W)
P_{max}	Maximum load in indentation tests (N)

$P(\omega)$	Power spectral density (m^2)
r	Roughness factor or Wenzel ratio (-)
r_a	Substrate curvature after deposition (m)
r_b	Substrate curvature before deposition (m)
R	Radius of counter body (m)
R^2	Fitting confidence (-)
R_{asp}	Average curvature of the asperity (m)
R_q	Standard deviation of the surface heights (m)
s	Linear displacement (m) in reciprocating sliding tests
S_{bi}	Surface bearing index (-)
S_{ci}	Core fluid retention index (-)
S_{ku}	Kurtosis (-)
S_q	RMS roughness (nm)
S_{sc}	Summit curvature (nm)
S_{sd}	Summit density (#/μm^2)
S_{sk}	Skewness (-)
S_{tp}	Surface bearing area ratio (-)
S_{vi}	Valley fluid retention index (-)
t	Time (s)
t_a	Condensation time for one liquid monolayer (s)
t_d	Deposition time (h)
t_f	Film thickness (m)
t_s	Thickness of substrate (m)
T	Substrate temperature (°C)
T_{hkl}	Texture coefficient (-)
T_m	Melting temperature of deposit (°C)
U_b	Bias voltage (V)
$U_{b,t}$	Transition bias voltage (V)
U_i	Ion potential (V)
U_{pl}	Plasma potential (V)
U_{top}	Maximum voltage of sine wave voltage signal (V)

v	Relative sliding velocity (m/s)
v_a	Critical velocity corresponding to t_a (m/s)
V	Wear volume (m^3)
$V_v(h_{n0.05})$	Void volume at a normalised height at 5 % surface area (m^3)
$V_v(h_{n0.8})$	Void volume at a normalised height at 80 % surface area (m^3)
w_c	Column width (µm)
w_{ci}	Initial column width (µm)
$w_{c,max}$	Maximum column width (µm)
w_p	Width of pyramidal features (µm)
x_b	Beam deflection (m)
$x_{b,L}$	Lateral beam deflection (m)
$x_{b,N}$	Normal beam deflection (m)
x_{Cr}	Number of chromium atoms forming a Cr-N film (-)
x_N	Number of nitrogen atoms forming a Cr-N film (-)
$z(x_i, y_i)$	Function of the original surface with $x_i = i\Delta x$ and $y_j = j\Delta y$, whereby $i = 1, 2, \ldots, M$ and $j = 1, 2, \ldots, N$
α	Fraction of dry contact (-)
α_v	Angle of incident vapour particles (°)
β_c	Angle of declination between column axis and substrate normal (°)
β_{hkl}	Half normal width of reflection hkl in XRD spectrum (m)
γ_l	Interfacial energy at liquid/gas boundary (J/m^2)
γ_s	Interfacial energy at the surface/gas boundary (J/m^2)
γ_{sl}	Interfacial energy at the solid/liquid boundary (J/m^2)
δ	Plastic indentation depth (µm)
η_{asp}	Area density of asperities (#/μm^2)
η_l	Dynamic viscosity of a liquid (Ns/m^2)
$\eta(x, y)$	Function of a residual surface
θ	Contact angle of a solid surface with a liquid (°)
$\theta_{1,2}$	Contact angle of a solid surface 1 or 2 with a liquid (°)
θ'	Contact angle at rough surfaces (°)
θ_A	Advancing contact angle (°)

θ_{hkl}	Position of the hkl reflection in XRD spectrum (°)
θ_R	Receding contact angle (°)
λ	Dominant wavelength in power spectral density (m)
λ_c	Typical width of the distribution of distance between the surfaces (m)
λ_{mfp}	Mean-free path length (m)
λ_r	Radiation wavelength (m)
μ	Friction coefficient (-)
μ_{adh}	Friction coefficient resulting from adhesion (-)
ν	Poisson's ratio (-)
$\nu_{1,2}$	Poisson's ratio of a surface 1 or 2 (-)
ν_{ind}	Poisson's ratio of indenter (-)
ν_s	Poisson's ratio of substrate (-)
ρ	Density (m^3/kg)
ρ_m	Molecular density of a liquid ($molecules/m^3$)
σ	RMS height (m)
σ'	RMS slope (-)
σ_{asp}	Standard deviation of the asperity heights (m)
σ_r	Residual stress (Pa)
τ_a	Average shear strength of dry contact (N/m^2)
τ_l	Average shear strength of the liquid film (N/m^2)
τ_s	Distance between two adjacent points of data sampling (m)
ϕ_{adh}	Adhesion factor (m^2/N)
ϕ_c	Capillarity factor (m^2/N)
ψ	Plasticity index (-)
ω	Frequency (1/m)
ω_h	High frequency cut off (1/m)
ω_l	Low frequency cut off (1/m)
#	Number, used in unit #/μm^2

Chapter 1

Introduction

In recent years, the importance of understanding and controlling the topography of surfaces for their functionality has been recognized and has been intensively investigated. One of the most popular phenomena in this context is the self-cleaning behaviour of surfaces or lotus effect, which was described first by Barthlott & Neinhuis (1997). It has been demonstrated that super-hydrophobic surfaces require not only low-surface energy, but also a certain topography, e.g. Uelzen & Müller (2003); Inoue et al. (2000); Favia et al. (2003). Recently, there has been a medical research focus on how cell growth or bacterial adhesion is influenced by the surface topography of implants and surgical instruments (Dalby et al. 2003; Scheideler et al. 2003; Whitehead, Colligon & Verran 2005). Other examples where the surface topography can have a major effect on functionality are found in fields of optics (Walzer et al. 2004; Walze et al. 2005), thermal insulation (Bi, Xu & Gong 2000; Wellman, Deakin & Nicholls 2005), corrosion-protection (Li & Li 2006) and tribology (Ortmann et al. 2003; Zhou et al. 2003). Figure 1.1 shows examples where nanostructuring of surfaces is applied in order to improve their functional performance.

Especially in tribology, the geometric state of the mating surfaces is one of the crucial parameters. When pressed against each other, junctions between the surfaces are formed only in a small number of contacts. The conditions in those contacts (e.g. pressure distribution, size and stiffness) depend substantially on the topography of the contacting

surfaces (Schargott & Popov 2006). The processes occurring in these contacts (e.g. deformation, tribochemical reactions) primarily control the evolution of friction and wear in the system.

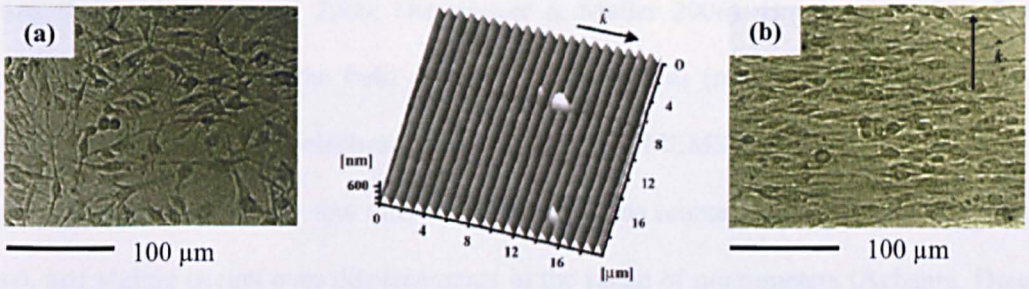

Holographic surface relief grating (depth ~ 250 nm and period ~ 1 µm) for controlled cell orientation: The cells grow with random orientation in the flat region (a), but towards the groove direction on a structured surface (b), taken from Baac. et al. (2004).

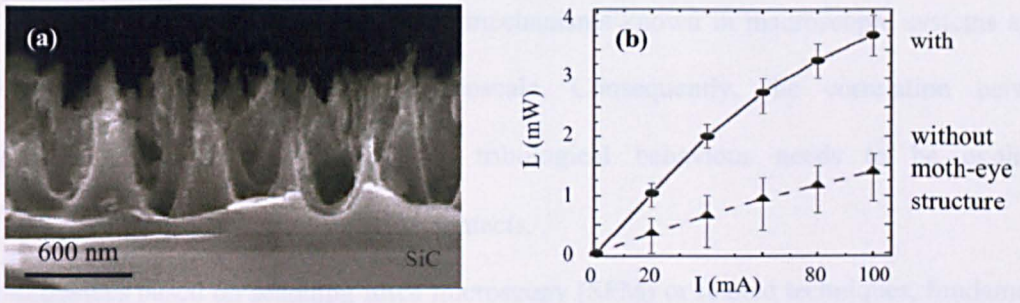

Improvement in light extraction efficiency in light-emitting diode using moth-eye structure: (a) cross-sectional image of moth-eye structure, (b) Light output L - current I characteristics of diode, taken from Iwaya et al. (2006)

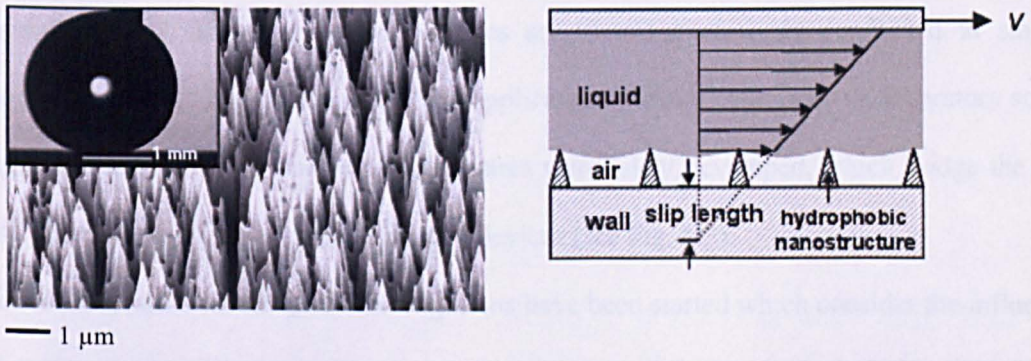

Drag reduction in microfluidic channels: Moving liquid sits on closely-spaced hydrophobic posts by surface tension, taken from Kim & Choi (2006)

Figure 1.1: Examples of nanostructured surfaces used in different application fields to enhance surface functionality.

The dependence of tribological behaviour on the surface topography has been widely investigated in macroscale contacts for a large range of operation conditions and applications (Lakshmipathy & Sagar 1992; Hu & Dean 2000; Xiao et al. 2003; Wiklund, Wihlborg & Rosén 2004; Nyman et al. 2006; Ostermeyer & Müller 2006). However, more and more applications emerge from the field of miniaturised devices (microsystems) such as micro-motors, mini-robots, microelectromechanical systems (MEMS) or bio-implants, where the normal forces are as low as few micro or milli-Newtons (contact pressures of a few MPa or less), and sliding occurs over displacements in the range of micrometers (Achanta, Drees & Celis 2005). Under such conditions, friction and wear are more influenced by the surface properties than macroscopic systems are. Therefore, different behaviour and mechanisms or, at least, different relative importance of mechanisms known in macroscopic systems apply when moving to the micro or nanoscale. Consequently, the correlation between topographical characteristics and the tribological behaviour needs to be explicitly investigated for micro and nanoscaled contacts.

With devices based on scanning force microscopy (SFM) or related techniques, fundamental mechanisms of friction and wear can be investigated on the atomic or nano level (Binggeli et al. 1993; Gnecco et al. 2003; Bhushan 2005; Bennewitz 2005). Nevertheless, the nanotribological studies with such devices are almost exclusively conducted in single-asperity mode. In order to simulate more-application relevant conditions on laboratory scale, experimental set-ups such as microtribometers were lately developed, which bridge the gap between macroscopic and nanoscopic test devices (see Fig. 1.2).

Just recently, microtribological investigations have been started which consider the influence of surface topography in multi-asperity contacts (e.g. Scherge & Gorb 2001; Hild 2005; Bregliozzi 2006). Many of these studies focus on correlations between friction and the mean-square roughness of a single type of surface topography that was generated either by chemical etching or mechanical polishing. Systematic studies about the influence of shape and size of nanoscaled surface features on friction, and also on wear in microcontacts are

still missing. This information, however, is important as there is a special interest in analysing the dependence of the microtribological behaviour on the topography for systems operated in presence of a fluid lubricant or in humid environment (Hild 2005; Bregliozzi 2006).

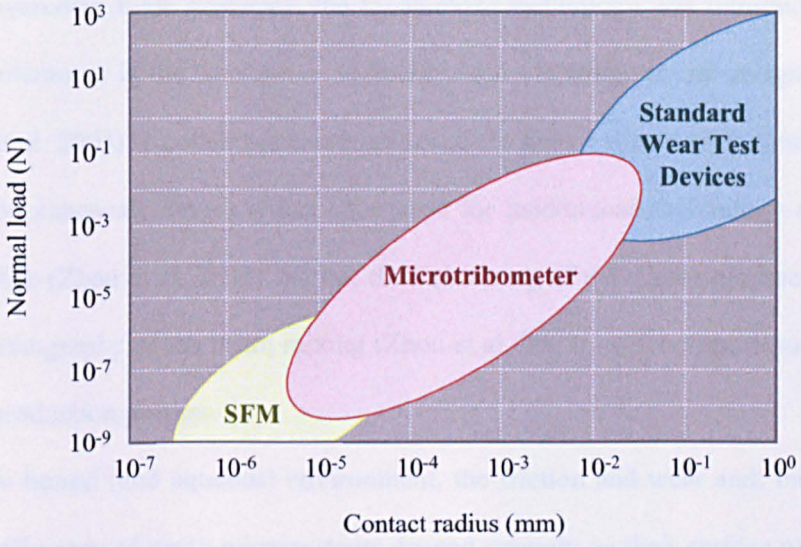

Figure 1.2: Parameter range for tribotesting, adapted from Dvorak, Woodland & Unertl (1998).

In a lubricated system, friction varies according to the amount of lubricant present in the contact zone between two surfaces sliding against each other. Under conditions of minimum (or starved) lubrication the lubricant film may no longer be continuous. In this case, lubrication of the contact depends, to a large extent, on retention of the lubricant in cavities present on the surface. Size, geometry and distribution of these cavities are crucial factors that determine the capability of the surface to entrap microscopic quantities of lubricant and to dispense and transport it to the actual contact points within the contact zone. Optimum system performance requires a thorough knowledge of the relationship existing between lubricant properties (e.g. viscosity), operating conditions (e.g. contact load, sliding velocity) and surface properties (e.g. topography). The surface topography needs to be adapted accordingly on the basis of this knowledge (Lo & Horng 1999; Zhou et al. 2003; Gerbig et al. 2005). In recent years, this relationship has been intensively investigated mainly for regular micro-pore arrangements produced by lasertexturing, for example, of the disk in

head/disk systems (Ranjan et al. 1991; Khurshudov et al. 1997; Tang et al. 2000). Lasertexturing can not be implemented without great difficulties in the production process. Additionally, the bumps formed by molten materials around the pores might interfere with the flying head if the bump height is not smaller than the flying height of the head. To overcome these problems, the load/unload technology was introduced, which requires tight tolerances in the mechanical assembly, and adaptation in the design of the disk drive (Zhou et al. 2003). Another approach proposed the use of sliders with controlled surface roughness (in nanoscale range) without the need for load/unload technology or zone texturing on the disk (Zhou et al. 2003). So far, the structuring of the sliders has been realised only either by lithography or ion beam mixing (Zhou et al. 2003), which impose supplementary steps in the production process.

In humid (and aqueous) environment, the friction and wear and, thus, the functionality and efficiency of many microsystems depend strongly on their surface wettability (Komvopoulos 1996; Mastrangelo 1997; Maboudian 1998). For example, poor wettability with water (or hydrophobicity) results in a decrease of pull-off forces in head/disk systems (Ando & Ino 1998; Usui, Umehara & Kato 2000) or a reduction of flow resistance in microfluidics (Kim & Choi 2006). It is known that the wettability of surfaces is affected by their chemical composition and topography (Wenzel 1936; Cassie & Baxter 1944; Onda et al. 1996). Yet, the combined influence of both factors on the wettability and also on the microscale friction has not been studied systematically for nanoscaled topographies.

Simultaneously, with the progress in micro and nanoengineering, various techniques for structuring or patterning of surface in the micro and nanoscale range were developed, such as plasma etching (Collaud Coen et al. 2003), electrochemical micromachining (Landolt, Chauvy & Zinger 2003), micromaching using ion, electron or laser beams (Bolse et al. 2005; Daniel, Mücklich & Liu 2003; Booth 2004), lithography (Munnik et al. 2003; Seekamp et al. 2002) or replication techniques (Schift et al. 2000; Lu & Chen 2004).

Unfortunately, some of these techniques are to expensive and/or time consuming to be presently applied in mass-market production. Others are applicable only to flat surfaces. In this context, a new approach which is later referred to as in-process structuring might become interesting. By in-process structuring, a thin film is deposited with a topography controlled by an appropriate adjustment of the parameters in the deposition process. In-process structuring is based on conventional physical vapour deposition (PVD) or chemical vapour deposition (CVD) technologies. These technologies have been used for a long time on industrial scale and their suitability for coating 3-D surfaces has often been demonstrated (Novák et al. 1999; Ohring 2002). In many microsystems, components are coated anyway to realise a specific functionality such as low friction, wear resistance, erosion resistance or anti-fouling properties (Rajan et al. 1998; Ledermann et al. 2000; Zhou et al. 2000, 2003; Haneien et al. 2001; Radhakrishnan et al. 2002; Bouaidat et al. 2004). In these cases, in-process structuring might provide a path for better exploitation (optimization) of the coating functionality without adding further steps to the production process of a microsystem. Nevertheless, the application of in-process structuring requires knowledge of the correlations between topography of the thin film and parameters of the deposition process and, further, the ability to modify the geometric dimensions of the topographical features in a controlled manner.

Over the last decades different models have been presented to describe coating morphology (topography and microstructure) as a function of process parameters (Movchan & Demchishin 1969; Thornton 1977; Messier, Giri & Roy 1984; Musil et al. 1990; Kelly & Arnell 1998; Barna & Adamik 1998). However, these models were mainly focused on the evolution of the microstructure and less on the surface topography of thin films. To our knowledge, systematic investigations of the correlations between topography and deposition parameters with special focus on the modification of the topographical features as function of the process parameters have not been carried out for thin films.

1.1 Research Approach of the Thesis

The goal of this work is to evaluate the potential of in-process structuring to improve the microtribological behaviour of thin films. That requires the development of the technique of in-process structuring to a stage where the surface topography can be reproducibly modified in a controlled way. For this purpose, the following approach was chosen:

- Determination of topography types obtainable by varying the deposition parameters
- Identification of key deposition parameters influencing the topographical evolution
- Specification of growth conditions for each type of topography
- Investigation of the relation between key deposition parameters and the dimensions of the topographical features
- Evaluation of the reproducibility of the nanostructuring results.

The development was carried out for chromium nitride (Cr-N) thin films deposited by unbalanced magnetron (UBM) sputtering process. Chromium nitride films are known for their remarkable functional properties including high hardness and mechanical strength (Yao & Su 1997; Hurkmans et al. 1999; He et al. 2000; Tu, Dhu & Tsai 2000; Almer et al. 2000; Hoy, Sloof & Janssen 2004), high wear resistance (Su et al. 1997; Gåhlin et al. 1995; Berg et al. 1996; Tricoteaux et al. 2003), chemical inertness and corrosion resistance (Bertrand, Mahdjoub & Meunier 2000; Navinšek & Panjan 1993; Ürgen & Fuat Çakir 1997), and high temperature stability (Djouadi et al. 2002; Milosev et al. 1996; Esaka et al. 1997). As a result, they are technologically important for applications such as wear-resistant coatings for tools in metal cutting and metal forming (Vetter et al. 1996; Navinšek, Panjan & Milošev 1997; Broszeit, Friedrich & Berg 1999; Panjan et al. 2001; Lousa et al. 2001) as well as protective coatings in plastic injection machines (Cunha et al. 2000) and wood cutting machines (Labidi et al. 2005). Cr-N films have also been shown to provide improved system adherence when applied as an interfacial layer between diamond films and steel (Fayer, Glozman & Hoffman 1995; Glozman & Hoffman 1997). Moreover, Cr-N offer potential for uses such as optical coatings, especially for selective solar absorbers (Sikkens et al. 1983;

Graf et al. 1997). In microtechnology they are used as diffusion barrier coatings (Huber & Hofmann 1994; Benien et al. 1991), in phase-shift masks for photolithography (Carcia et al. 1997) and in etch-resistant hardmasks for X-ray absorber patterning (Tsuboi et al. 1997). Quite recently, Cr-N films have been used for nanostructuring a polymer surface (Gerbig, Phani & Haefke 2005).

After the reproducibility of the in-process structuring was confirmed, the influence of the in-process structuring on the microtribological behaviour of surfaces was evaluated. Hereby, the microtribological behaviour of differently nanostructured surfaces was investigated in lubricated contacts and in humid environment. For an efficient, functional performance of nanostructured topographies, it is essential that the geometrical appearance of the surface features remains widely unchanged during loading. Therefore, the mechanical stability of the surface features, which corresponds to their wear resistance, was analysed in separate tests. Finally, the microtribological functionality of in-process structured surfaces was studied in three main groups of experiments. The tests for experimental group (EG) 1 were carried out to gain information about the friction behaviour and wear resistance of the nanostructures with respect to the load applied and the duration of loading in wear mapping tests, whereby it was of particular interest to specify when and which kind of wear was observed for the different types and dimensions of nanostructures. Furthermore, parts of the tests in EG 1 are regarded as reference tests for experiments carried out under lubricated conditions in EG 2.

The main goal of the tribological tests performed in EG 2 was the determination of the lubrication-efficiency of differently nanostructured surfaces compared to each other and in comparison to smooth surfaces. The efficiency of a structure in supporting the system lubrication was evaluated with respect to the decrease in friction in comparison to results on unlubricated surface with the same topography (tests of EG 1).

In EG 3, the influence of nanoscale topographical features on wettability (with water) and microtribological behaviour was studied. The purpose of the investigation is to gain knowledge about the influence of the structure shape as well as the dimension of

topographical features on the functionality of hydrophilic and hydrophobic surfaces. In order to modify the surface chemistry, a thin layer of a hydrophilic or hydrophobic material was deposited on the nanostructured surfaces.

1.2 Layout of the Thesis

This thesis deals with two main topics emerging from different fields of materials research and engineering: nanostructuring of thin films by physical vapour deposition (in-process structuring) and the microtribology of nanostructured surfaces. Accordingly, the first chapter is an introduction to the subject of nanostructuring of surfaces in order to modify their functional performance, especially for microtribological applications. In this context, the relevance and potential of the new method of in-process structuring is explained. Following this, Chapter 2 explains the principle of physical vapour deposition with special emphasis on the correlation between deposition parameters and the morphological evolution of thin films. The theoretical background of microtribology, the other main topic of this thesis, is covered in Chapter 3. This chapter describes in a general way various mechanisms for generating friction and gives an overview about the different types of wear occurring in microcontacts. Chapter 4 presents the techniques that were applied in this thesis for preparing nanostructured surfaces and also provides experimental details about the characterisation of the application-relevant properties as well as the functional behaviour of nanostructured surfaces. In Chapter 5, the results of the deposition experiments are summarized and the potential of in-process structuring for nanostructuring of surfaces is analysed. Chapter 6 discusses the microtribology of the differently nanostructured surfaces created in this thesis. Finally, Chapter 7 draws conclusions about the work presented and indicates directions of future research.

Chapter 2

Principles of Sputter Deposition and Thin Film Growth

In order to create nanostructured surfaces, an approach (in-process structuring) based on the technique of physical vapour deposition (PVD) was chosen to manipulate the topography of chromium nitride (Cr-N) films. Chapter 2 introduces the technology of physical vapour deposition with special emphasise on sputter deposition techniques. The basic principles in growth of PVD deposited thin films are described, and the main factors influencing the morphological evolution of the films are summarized here. Furthermore, the chapter informs about properties of the investigated Cr-N thin films.

2.1 Sputter Deposition of Thin Films

Sputter deposition (sputtering) is a form of physical vapour deposition together with evaporation and ion plating. In all types of PVD, elements or compounds condense onto a substrate from a vapour phase. In the case of evaporation, the vapour is produced from material localised in a heated source (Graper 1995), whereas the vapour forming material particles in sputter deposition are expelled from a solid surface (target) by bombardment with high-energy particles (Shah 1995). Ion plating is a hybrid process consisting of both, sputtering and evaporation. In this case, the substrate surface and/or the surface of the evaporated film are subjected to a flux of high-energy particles in order to modify the interfacial region between film and substrate and/or the film properties (Mattox 1998).

Sputtering is a widely-used technique in research and industry due to its various characteristics, such as the capability of depositing refractory and insulating film materials, high uniformity of film thickness and prevention of droplet* deposition, a common phenomenon occurring in evaporation processes. In sputter deposition, the following issues have to be considered for forming high quality films:

- Generation of plasma in the deposition chamber (see section 2.1.1)
- Creation of vapour by bombardment of target material with plasma ions (see section 2.1.2)
- Formation and growth of a film by deposition of vapour particles on the substrate (see section 2.2)

2.1.1 Processing of Plasma

In order to create and sustain a plasma, three basic groups of techniques are commonly used in thin film deposition. All of them rely on the ionization of background gas by accelerated electrons. In the first group, the electrons are generated by applying a high voltage to a set of metal electrodes within the vacuum chamber. This sort of plasma excitation (diode discharge) is employed for example in DC (direct current) diodes, RF (radio frequency) diodes and magnetrons. The techniques of the second group apply electric fields through an insulator to break down the plasma and cause ionisation. Examples for these techniques include microwave and electron cyclone resonance plasma devices. A third means of driving plasma is by injection of large currents of electrons that are emitted from a filament or another electron source, e.g. the Kaufman-like ion source.

Since the plasma was created by diode discharge for depositing the films discussed here, this technique is described more in detail in the following pages.

In diode discharge, at first the pressure in the deposition chamber is reduced to the base pressure. Afterwards the chamber is backfilled with a background (or sputter) gas, usually argon. Later a negative voltage is applied to the cathode (target). The electrons are emitted as sec-

* Droplets are solidified macroparticles of molten target material.

ondary electrons from the cathode and accelerated towards the anode (substrate and/or chamber walls), thereby gaining energy. If they gain sufficient energy on their way, they can cause ionisation or excitation of the gas atoms due to inelastic collisions (Rossnagel 1991):

Ionisation: $e^- + Ar \rightarrow Ar^+ + 2e^-$

Excitation into an electronically excited state: $e^- + Ar \rightarrow Ar^* + e^-$

Energised gas atoms can also transfer their energy to other atoms resulting in excitation (Penning excitation) or even ionisation (Penning ionisation). The lifetime of the excited species is relatively short, hundreds of ps up to tens of ns (Curtis 1984), and is followed by radiative decay and emission of a photon. Due to this typical photon emission, plasmas are also known as glow discharges.

2.1.2 Interaction of Plasma with Target

In certain energy ranges, the ion bombardment of the target surface leads to the ejection of target atoms due to collisions involving a momentum exchange from incoming ions to the target. The ejection of target particles (sputtering) requires a sequence of collisions to change the momentum vector direction towards the target surface. In low energy knock-on processes (single knock-on), a target atom located on the surface receives only a glancing blow and may transfer its energy to a neighbouring surface atom that is then possibly ejected from the surface (Fig. 2.1a). At higher energies, atoms undergo several collisions inside the target before sputtering is initiated (Fig. 2.1b). Instead of initiating a collision cascade, a primary knock-on atom can itself get reflected. In case when the impacting particle has a very high energy, nearly all target atoms can be set in motion (Fig 2.1c), which leads to a non-linear collision cascade and, thus, nonlinear sputtering of atoms (Webb, Kerford & Way 1999).

The ratio of sputtered atoms to number of incident particles (sputter yield) depends on the characteristics of the target material, the mass ratio of incident particle to target atom and the energy of the incident particle.

In addition to the described interactions, further processes that may also occur at the target surface are emission of secondary electrons, reflection of gas ions and their neutralization, burying of gas ions in the target with/without simultaneous ejection of target atoms and emission of X-rays and/or photons (Shah 1995).

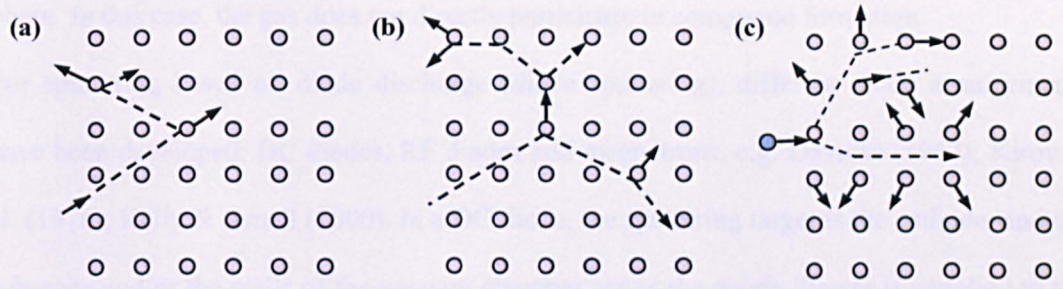

Figure 2.1: Energy regimes of knock-on events: (a) single-knock on (low energy), (b) linear cascade (high energy), (c) non-linear cascade (very high energy), after (Ohring 2002).

2.1.3 Sputtering Techniques

Sputter processes can be conducted in a reactive or non-reactive mode to deposit compound materials. In reactive mode, thin films of compounds are deposited by sputtering from a metallic target in presence of a reactive gas generally mixed with inert working gas, usually argon. Examples of common thin film compounds deposited with reactive sputtering and the reactive gases employed in these processes are briefly listed in Table 2.1.

Table 2.1: Common thin film compounds reactively sputtered and the reactive gas employed in the deposition process, after (Ohring 2002; Bunshah & Deshpandey 1990).

Compounds	Reactive gas	Examples
Carbides	Methane, Acetylene, Propane	TiC, WC, SiC, VC, ZrC
Nitrides	Nitrogen, Ammonia	CrN, AlN, Si_3N_4, CN_x, ZrN, TiN, HfN
Oxides	Oxygen	Al_2O_3, TiO_2, SiO_2, ZrO_2, In_2O_3
Sulphides	Hydrogen sulphide	MoS_2, CuS, ZnS, TiS_2

Besides maintaining the target sputtering, the plasma fulfils a second function by increasing the reactivity of the working gas. The reactive mode requires careful process control to avoid

compound formation on the surface of the metallic target (target poisoning). Target poisoning leads to changes in the chemical composition of the deposited film and reduced deposition rates, because the sputter yield of a compound is usually lower than that of the metal. In non-reactive mode, sputtering of the compound target is carried out in an inert gas atmosphere. In this case, the gas does not directly participate in compound formation.

For sputtering based on diode discharge (diode sputtering), different diode arrangements have been developed: DC diodes, RF diodes and magnetrons, e.g. Davidse (1967); Kirov et al. (1976); Kelly & Arnell (2000). In a DC diode, the sputtering target is the cathode, and the substrate and/or the walls of the vacuum chamber act as the anode. Power is supplied to the target by a DC source. For RF diodes, the power supply is a high voltage RF source. As for the DC diode, substrate and/or chamber walls form the anode and the sputtering target is the cathode. By switching from a negative to the positive half cycle during operation, positive charge accumulation is equalized. This enables sputtering from an insulating target.

The magnetron is a magnetically-assisted discharge (Penning 1936). In order to create a strong magnetic field, permanent and/or electromagnets magnets are added to a DC diode or RF diode arrangement. This magnetic field is oriented parallel to the target surface, whereby the electric field extends perpendicular to it. According to the Lorentz force law, the interaction of magnetic and electric fields bend the trajectories of the emitted electrons into convoluted spiral-like patterns across the target surface and trap the electrons near the target surface. In this manner, a well-confined plasma can be maintained in the near-surface regions, which gives rise to an increase in ionisation probability and in plasma density. Consequently, the sputtering rate on the target is increased and, hence, the deposition rate. Furthermore, sputtering from the substrate and chamber walls as well as the substrate heating, both undesired effects, are diminished during the deposition and the requirements regarding the working gas pressure are reduced.

The magnetron configuration can vary from gun type (Penfold 1995) to cylindrical post, hollow cathode, rectangular planar, belt or conical type (Westwood 1988). Figure 2.2 shows a sketch of a rectangular, planar magnetron.

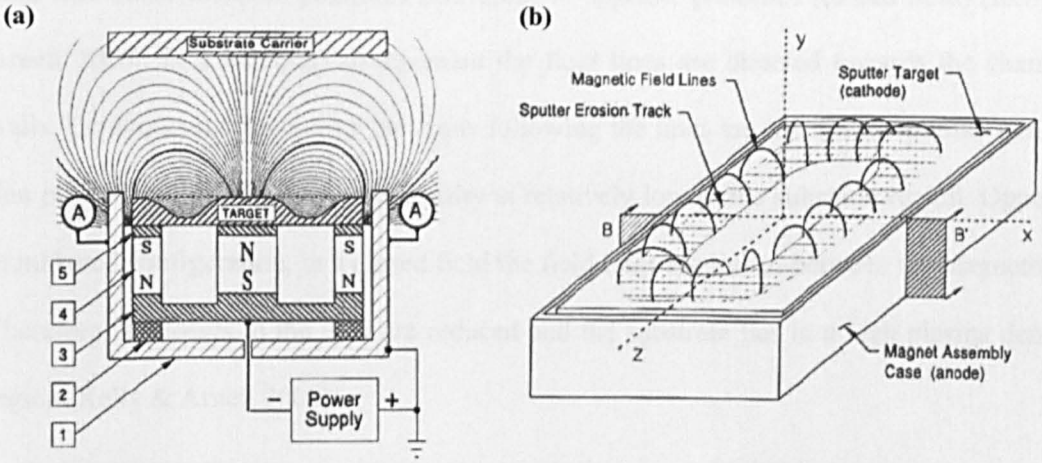

Figure 2.2: Simplified cross section (a) of a rectangular planar magnetron taken through the plane B-B' in the sketch (b), taken from Penfold (1995). Item 1 is the nonmagnetic metal case which houses the magnet assembly, item 2 is an insulator to insulate the magnet assembly from the case; item 3 is the magnetisable rear yoke of the magnetic assembly, item 4 are the permanent magnets and item 5 the magnetisable pole pieces for the magnets.

The strength of the magnetic poles of a magnetron device can be balanced or unbalanced. An unbalanced magnetron is a magnetron where the centre pole is either strengthened (type 1) or weakened (type 2) relative to the outer pole (Window & Savvides 1986). When using an unbalanced magnetron, the magnetic field lines leave the central region of the target and intersect the substrate region. The electrons are less fully trapped near the target and, as a result, the plasma is extended towards the substrate (Fig. 2.3). As a result, the flux of the plasma ions in the substrate region is significantly increased, which leads to an enhanced ion bombardment of the film. A principal application of this type of device is the deposition of nitride films by reactive sputtering (Sproul et al. 1990). Without the increased ion flux pro-

vided by the unbalanced target, the substrate temperature would need to be raised significantly to form nitride phases.

In a multiple magnetron system, the magnetic arrays in adjacent magnetrons can be configured with either identical polarities (mirrored) or opposite polarities (closed field) (Kelly & Arnell 2000). In a mirrored arrangement the field lines are directed towards the chamber walls. Consequently, secondary electrons following the lines are lost for the plasma generation process and, thus, the plasma density is relatively low in the substrate region. Opposite to mirrored configuration, in a closed field the field lines are linked between the magnetrons. Therefore, the losses to the wall are reduced and the substrate lies in a high plasma density region (Kelly & Arnell 2000).

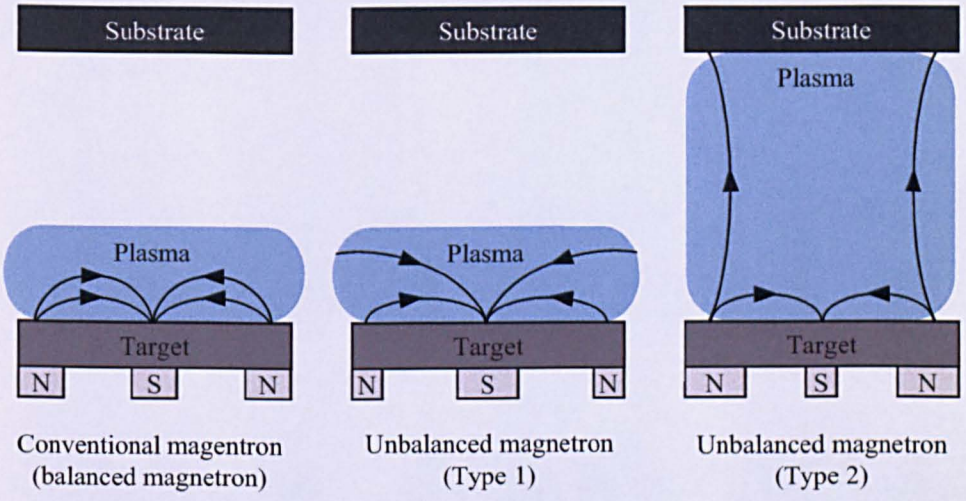

Figure 2.3: Schematic representation of plasma confinement observed in conventional magnetrons and unbalanced magnetrons of type 1 and type 2, after Kelly & Arnell (2000).

2.2 Thin Film Growth

2.2.1 Nucleation and Early Stage Growth

When a substrate is exposed to vapour particles, the particles adsorb on the surface either by van der Waal forces (physisorption) or by ionic or covalent bonding (chemisorption). The adsorbed atoms (adatoms) then start to diffuse on the substrate surface. Hereby, the diffusivity depends on the interaction between adatom and substrate as well as the temperature. Oc-

casionally, re-evaporation of single adatoms may occur. By random diffusion, one atom joins another atom and forms a stable doublet with lower diffusivity. With time, more vapour flux arrives on the surface, and the size and density of stable clusters (islands) increases till they coalesce to form a continuous film. The early growth stage of a thin film can proceed according to one of the following models:

(1) Island (Volmer-Weber) mode

The smallest stable clusters grow in three dimensions to form islands (Fig. 2.4a), since the deposited atoms are more strongly bound to each other than to substrate.

(2) Layer (Frank-Van der Merwe) mode

The smallest stable clusters extend in two dimensions and form planar sheets (Fig. 2.4b). In this case, the deposited atoms are more strongly bound to the substrate than to each other.

(3) Stranski-Krastanov mode

This mode is a combination of the preceding ones. After growing of one or more monolayers, layer growth becomes unfavourable and is replaced by island formation (Fig. 2.4c).

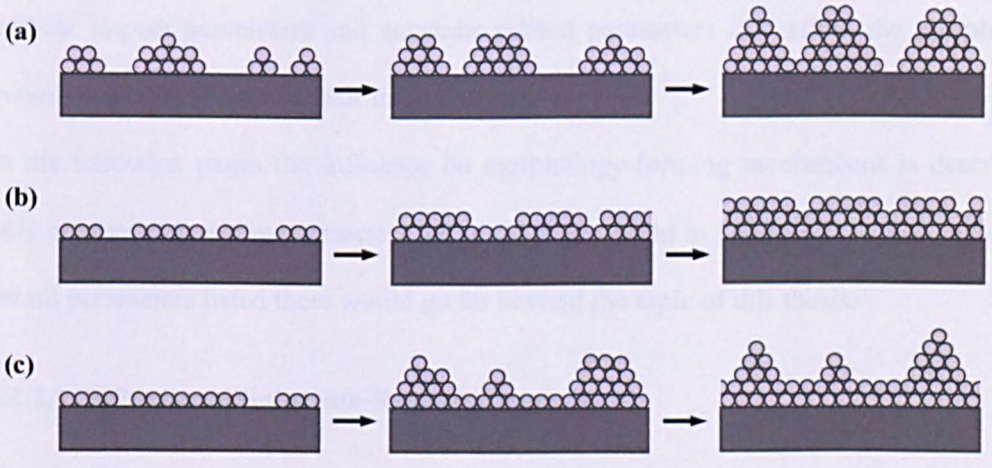

Figure 2.4: Basic modes of thin film growth: (a) Island (or Volmer-Weber) growth, (b) Layer (or Frank-Van der Merwe) growth, (c) Stranski-Krastanov growth, adapted from Ohring (2002).

During film growth, further atoms condense on the film surface, become bonded adatoms, diffuse over the surface until they desorb or are trapped at low-energy lattice sites, and finally reach an equilibrium position in the film lattice by bulk diffusion. The growth of the film is controlled by processes of shadowing, surface diffusion, bulk diffusion and desorption. The last three processes are dependent on material specific diffusion and sublimation activation energies. Shadowing arises from geometric constraint imposed by the roughness of the growing film and the line-of-sight impingement of the incident vapour particles. The dominance of one or more of these processes as a function of the temperature becomes evident by changes in the film morphology.

2.2.2 Evolution of Film Morphology

In thin film deposition, the term morphology refers to the entirety of the film structure, including the topography (e.g. shape and size of surface features, roughness) and the microstructure (e.g. grain size, grain boundary structure, porosity).

The formation of a thin film, hence its morphology, depends on various, mutually linked parameters of the deposition process. The diagram shown in Figure 2.5 gives an overview of the different groups of parameters, such as source parameters, plasma transport parameters, particle impact parameters and substrate-related parameters that affect the morphological evolution of thin films and their interrelations.

In the following pages the influence on morphology-forming mechanisms is described for only selected deposition parameters out of those presented in Figure 2.5. A thorough analysis for all parameters listed there would go far beyond the topic of this thesis.

2.2.2.1 Influence of Substrate-Related Parameters

Temperature

The substrate temperature controls the topography, microstructure and composition of thin films by affecting the diffusion processes (thus, the adatom mobility) as well as the rate of any chemical reactions occurring on the substrate (Bunshah & Deshpandey 1990). Generally,

an increase in substrate temperature leads to the formation of less porous microstructures (Movchan & Demchishin 1969; Müller 1985).

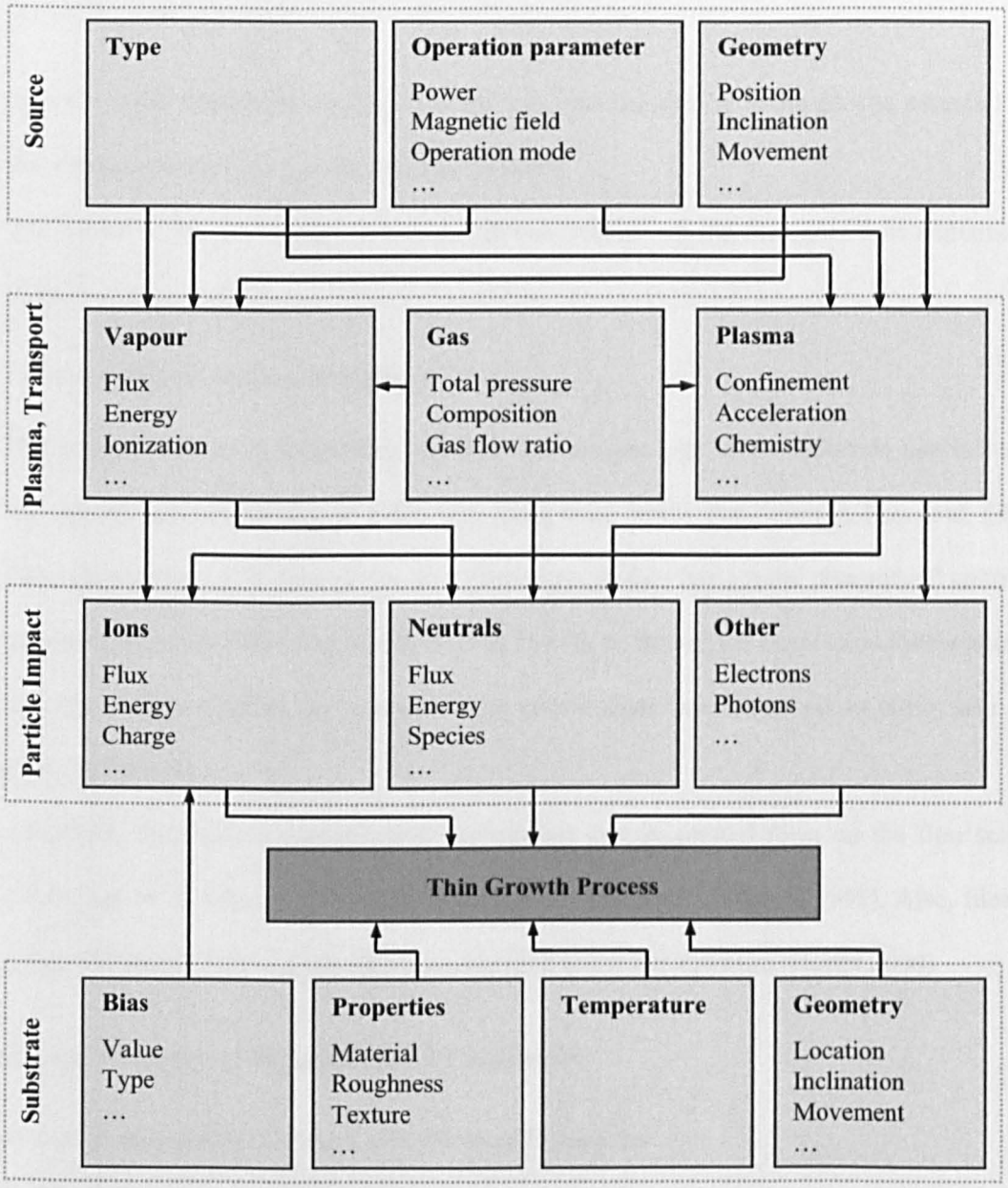

Figure 2.5: Schematic illustration of the parameters influencing film growth in PVD processes, after Kadlec, Musil &Vyskočil (1992).

Bias Voltage

The potential difference between substrate bias voltage and plasma potential influences the energy of plasma ions and of neutral particles (Kadlec et al. 1990). The functional relation

between bias voltage U_b and ion energy E_i is expressed in the following equation (Kadlec et al. 1990)

$$E_i = e \cdot U_i = e(U_{pl} - U_b) \tag{2.1}$$

where e is the elementary charge, U_i is the ion potential and U_{pl} is the plasma potential near the substrate with respect to the vacuum chamber.

The effect of the ion energy and, thus, the bias voltage on the film growth is explained in detail in section 2.2.2.3.

Substrate Cleanliness and Roughness

The composition, crystallographic structure and morphology of the substrate can influence the growth and morphology of a thin film (Jung et al. 2002). For example, Han et al. (2000) have shown that a CrN film grown on a chromium surface has a more pronounced columnar microstructure than when deposited on steel. However, deposition tends to be independent of the substrate material in the presence of an intermediate layer between an ultra-clean substrate and the film.

Generally, the substrate roughness is reproduced in exaggerated form on the film surface (Thornton 1977; Tang, Alexander & Bruizma 1990; Bales & Zangwill 1991). Also, films on rough substrates tend to grow with a pronounced columnar structure (Hones 2000).

2.2.2.2 Influence of Plasma-Related Parameters

Chamber Background Pressure and Purity of Precursors

Background pressure and purity of the gases employed in the process govern the concentration of soluble impurity in the deposited film. Impurities can affect the formation of the microstructure of thin films by pinning grain boundaries or binding of vacancies (Machelin 1995). Furthermore, the background pressure controls the deposition mode - being epitaxial*

* An epitaxial film is a single-crystal film, which is coherently oriented on a single-crystal substrate.

or not. At background pressures above 0.1 mPa, the chemically absorbed layers of impurity atoms saturate the underlying dangling bonds and stop further primary bonding to the substrate surface (Machelin 1995). The absence of dangling bonds may prevent the surface from providing a template for epitaxy.

High impurity contents can limit the grain growth in the coalescence stage due to enhanced impurity segregation at grain boundaries. Additionally, a layer of impurity particles may completely cover the whole crystal surface of a grain (surface covering layer) and block further growth of the grain (Barna & Adamik 1998).

Total Pressure

The total pressure indirectly affects film growth via its influence on energy, angular distribution and flux of ions as well as the energy and flux of energetic neutrals in the vapour. An increase of the total pressure leads to a decrease of the particle energy, and to an increase of the fraction of particles scattered to larger angles of incidence (Machelin 1995).

Partial Pressures of Sputter and Reactive Gas

The partial pressure of a gas influences the mean-free path of the particles. The mean-free path length λ_{mfp} defines the average distance travelled by a particle before collision with another particle occurs and is related to the partial pressure p by

$$\lambda_{mfp} \propto \frac{1}{p} \tag{2.2}$$

Hence, changes in the partial pressure alter the probability of collisional reactions between atoms (molecules) during their transit from target to substrate. Thereby, the formation of precursor molecules is affected and, thus, the film growth.

Due to influence of the mean free path, the sputter gas pressure also manipulates the direction and the kinetic energy of the particles to a certain extent. By increasing the sputter gas pressure, the collisional scattering by inert gas atoms is increased and the oblique component of the deposition flux is enhanced (Thornton 1977). Due to this randomisation of the particle

flux, finer-grained films are produced as a result of periodic renucleation at different crystallite sites (Avelar-Batista et al. 2004). Nevertheless, the collisions cause also an energy transfer from the vapour atoms to the sputter gas atoms (thermalization). At high sputter gas pressures, this energy transfer can be so high to due (repeated) collisions that the fraction of atoms arriving at the substrate surface is significantly lowered and the mobility of the arriving atoms may be significantly reduced in the adatom stage (Mahan 2000).

The partial pressure ratio of reactive gas to sputter gas controls the concentration of metal species in the vapour phase and, thus, the chemical composition, phase formation and microstructure of thin films, e.g. Machelin (1995) and Han et al. (2003).

2.2.2.3 Influence of Parameters Related to Particle Impact

Incident Particle Energy

The energy flux carried to the substrate by neutralized and reflected ions is affected by a variety of parameters (see Fig. 2.5), and can range from few hundred meV to a few hundred eV (Machelin 1995). Dependent on the particle energy, different phenomena can be induced by the simultaneous bombardment of the growing film with energetic particles:

(1) Resputtering of surface atoms

Resputtering occurs when energetic particles cause atoms of the film to sputter. Generally, less tightly bond atoms or atoms with high sputter yields are preferentially sputtered from the film surface. Also, regions of high curvature are particular vulnerable to resputtering. The atoms resputtered from such regions usually land nearby and promote a planarization of the surface during film growth. With increasing particle energy the resputtering of atoms from the growing film becomes increasingly important (Sundgren et al. 1983; Greene et al. 1987).

(2) Insertion of particles in growing film

High-energy particles may implant themselves in the film by forcibly displacing atoms from equilibrium sites. For example, an enhanced entrapment of argon has been

observed at high ion energies (Sundgren et al. 1983).

(3) Densification (Amorphization)

Densification or even amorphization of the microstructure of thin films is mostly attributed to penning effects (Hoffman & Thornton 1977): When particles with high kinetic energy impinge on the surface of the growing film, the momentum of the impact might be sufficient to cause local damage of the crystal lattices. These lattice defects act as preferential nucleation sites for the condensing atoms. With increasing particle energy, the number of defects and, thus, the number of nucleation sites increases. Hence, the size of the grains decreases and a dense microstructure forms. Further mechanisms involved in the densification of thin films might be the incorporation of ions, recoil implantation or resputtering of loosely bonded material.

However, Monte Carlo and molecular dynamics simulations* predict the existence of an optimum ion energy for microstructure densification (Müller 1986, 1987a). If the impinging ions have energy below this optimum value, the number of recoil events induced by their impact is small and the films are less dense. On the other hand, if the ions impact with energies larger than the optimum value, an increasing fraction of the ions is lost deeper in the lattice and leave vacancies, which cannot be filled by impinging vapour particles. This effect might lead to the reappearance of a dense columnar microstructure with voided grain boundaries at higher ion energies, as observed by Wang & Oki (1990).

Incident Particle Flux

The ratio of ion flux to atom flux arriving on the surface determines the deposition rate of a thin film (Kadlec et al. 1990). The effect of the deposition rate on film microstructure is temperature-dependent. At low substrate temperatures, the density of nucleation sites in-

* Monte Carlo simulations superimpose the statistics of atomic displacement on a geometric array of surface sites (equilibrium structures), whereas molecular dynamics simulations place a greater emphasis on the motion and physical behaviour of the involved atoms (Ohring 2002).

creases with the deposition rate, therefore crystalline films with small-sized grains or even amorphous films can be grown. At high substrate temperatures, this effect is less pronounced due to enhanced effect of the thermally activated processes of grain coalescence and grain boundary migration.

Generally, impurity concentration in the growing film and, thus, impurity-induced effect on the film structure (see section 2.2.2.2) are minimized at high deposition rates (Machelin 1995).

Angle of Incidence of Particles

A randomized vapour flux can overcome shadowing effects, which may promote the growth of fine grained films.

By varying the incidence angle of the vapour flux, it was experimentally found that the growing columnar grains are tilted towards the vapour flux when all vapour atoms arrive from the same direction. The functional correlation between the incident vapour angle α_v and the angle β_c between the column axis and the substrate normal is expressed by the tangent rule (Ohring 2002)

$$\tan \alpha_v = 2 \tan \beta_c \tag{2.3}$$

2.2.2.4 Structure Zone Models

The influence of deposition parameters on the morphology of thin films is described by structure zone models (SZMs). These SZMs mainly focus on the evolution of the microstructure.

The first SZM, developed by Movchan & Demchishin (1969), shows the effect of homologous temperature T/T_m (ratio of substrate temperature T to melting temperature T_m of deposit) on the microstructure of evaporated films. In the model they distinguish three temperature zones (zone 1, 2 and 3) in which the deposited film exhibit a characteristic microstructure (Fig. 2.6). Films grown in zone 1 ($T \leq 0.3\ T_m$) consist of dome-top shaped, tapered grains surrounded by voided grain boundaries. The films in zone 2 ($0.3 < T \leq 0.45\text{-}0.5\ T_m$) have a

columnar structure with well-defined distinct, dense, intercrystalline boundaries, while equiaxed* grains are typical for films in zone 3 ($T > 0.45\text{-}0.5\ T_m$).

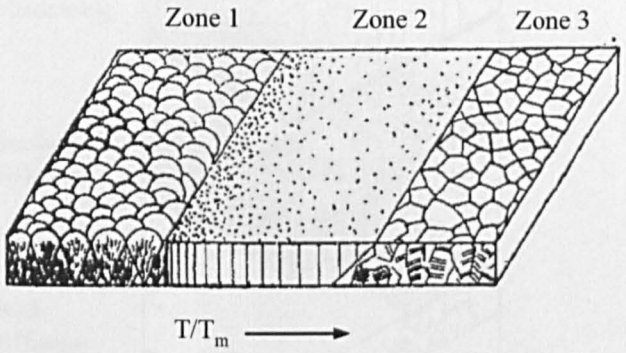

Figure 2.6: SZM for evaporated film as proposed by Movchan & Demchishin (1969).

In the following years, several, revised SZMs were proposed for evaporated films by different groups, e.g. Sanders (1971); Grovenor, Hentzell & Smith (1984); Machelin (1995). Apart form these ones; Adamik & Barna (1999) proposed an SZM that presents temperature dependent microstructures at various levels on impurity (oxygen) concentration for reactive evaporation of Al_2O_3 thin films. According to this model, the columnar growth at low temperatures is increasingly disturbed when increasing the impurity concentration due to grain boundary segregation and the formation of surface covering layers on the grain surface (see section 2.2.2.2).

SZMs of evaporated films are only partly valid for sputtered thin films, because (1) sputtered atoms have considerably higher kinetic energy than evaporated atoms, (2) the sputtered atoms may simultaneously approach the substrate in several directions, (3) an ambient gas is always present and (4) the substrate may be subjected to plasma bombardment. Thornton (1977) introduced the first SZM for sputtered films, which also considers the influence of the sputter gas pressure on the evolution of thin films (Fig. 2.7).

* Equiaxed grains are of approximately the same size in all three dimensions.

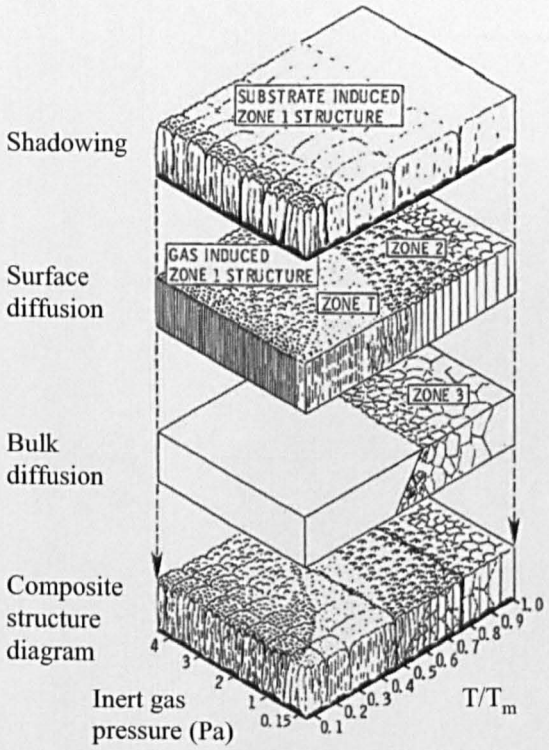

Figure 2.7: SZM for sputtered film as proposed by Thornton (1977). The schematic representation shows the superposition of physical processes that establishes structural zones.

Thornton defined four structure zones (zone 1, T, 2 and 3). Fibrous grains with voided boundaries are the result of shadowing effects, which overcome the limited adatom diffusion in zone 1 (T/T_m < 0.1 at 0.15 Pa to < 0.5 at 4 Pa). Faceted, columnar grains with dense boundaries are related to surface diffusion-controlled growth in zone 2 (T/T_m ~ 0.4-0.7). The thermally activated mechanisms of lattice and grain-boundary diffusion cause the growth of large, flat, equiaxed grains in zone 3 (T/T_m ~ 0.6-1). The films of zone T have a smooth, fine-domed surface, and consist of a dense array of poorly defined fibrous grains. Zone T may be viewed as a transition region between the zones 1 and 2.

Besides thermally induced mechanisms, bombardment with energetic particles can also influence the microstructure of a growing film. Based on this fact, Messier proposed a revised SZM for sputtered films that relates microstructural evolution as a function of the temperature and bias potential (Messier, Giri & Roy 1984). In this model, zone T is widened at the

expense of zone 1, because ion bombardment promotes adatom mobility and surface-diffusion processes (Fig. 2.8).

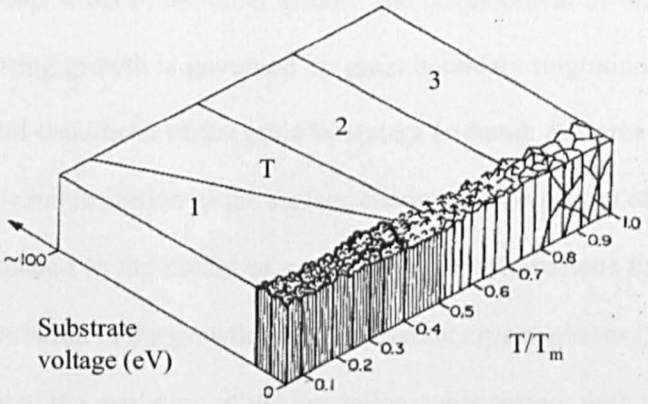

Figure 2.8: SZM for sputtered films as proposed by Messier, Giri & Roy (1984).

In a SZM developed for closed-field unbalanced magnetron sputtering, microstructures of the type of zone 1 and T do not occur (Kelly & Arnell 1998), since densification effects suppress the formation of these structures due to enhanced ion bombardment. This model indicated that lower temperatures are required for equivalent structural development in unbalanced magnetron sputtering compared to traditional sputtering.

2.2.3 Development of Crystallographic Texture

The morphological appearance of a thin film is very often connected to the crystallographic orientation of the crystal phases present in the film. In polycrystalline films, each grain has a specific crystallographic orientation with respect to a fixed reference direction. When the orientation of the grains is not random, the film is said to have a preferred crystallographic orientation or crystallographic texture (often called 'texture' although this use is avoided in most of this thesis because of possible confusion with topographical usage).

The development of a crystallographic texture is usually addressed to either competitive or restructuring growth of the grains. The phenomenon of competitive growth was at first described by Van der Drift (1967) in the evolutionary selection model. There he claims that the crystallographic texture results from variations in growth rates between different crystal

faces of the grains. Grains oriented with their faster growing directions perpendicular to the surface are preserved while slower growing grains are terminated as they intersect the columns walls of the taller grains. The development of the crystallographic texture by restructuring growth is governed by grain boundary migration, which is controlled by temperature and conditions of the grain boundary (Adamik & Barna 1996). This mechanism is driven by the minimization of the surface energy and the energy of the substrate-film interface.

Related to the model of competitive growth, various theories were proposed to explain the variation in the growth rates of different crystal phases (Schell et al. 2002). One theory correlated the evolution of the crystallographic texture with the ion-channelling direction in crystals (Dobrev 1982; Van Wyk & Smith 1980). Grains with most open lattice direction parallel to the incoming ion flux suffer the least damage and can serve as seeds for further growth of the film along the same direction. According to theory of minimising the surface energy (Hultman et al. 1991; Knuyt et al. 1995), the preferred orientation of thin films is related to preferential growth of crystallographic planes with lowest surface energy. Beside that, the anisotropy of surface bonding energy and surface diffusivity of adatoms may have a significant effect on the crystallographic texture formation, as reported by different groups (Gall et al. 2003; Greene et al. 1995; Hultman et al. 1995; Chun, Petrov & Greene 1999).

Pelleg et al. (1991) suggested that the minimization of the elastic deformation energy might be the driving force in creating crystallographic textures. In this case, the preferred orientation is determined by a competition between crystal phases with low strain energy and phases with low surface energy.

If the growing film is exposed to ion bombardment, the formation of the crystallographic texture can be ascribed to preferential resputtering. In this regime the crystalline planes with the lowest sputtering yield have the highest chance of surviving during growth (Bradley, Harper & Smith 1986). The preferential resputtering of grains with high sputter yield leads to height advantages for grains with low-sputter yields. The height advantage of grains with

low-sputter yield causes an occlusion of grains with high-sputter yield via shadowing mechanisms (Ying, Smith & Srolovitz 1996).

The crystallographic texture development in thin films can be affected by the composition, and morphology of the substrate (Ohring 2002), e.g. initiation of epitaxial growth. Also, temperature and deposition rate influence the evolution of an crystallographic texture (Adamik & Barna 1996; Ying, Smith & Srolovitz 1996). According to the capillarity theory of nucleation (Ohring 2002), low temperatures and high deposition rates form polycrystalline or amorphous films, while epitaxial films grow at high temperatures and at low deposition rates.

In case of ion bombardment of the growing film, energy and direction of the ion flux play an important role in the formation of crystallographic textures, since they may cause tilting of the microstructure towards ion flux direction, enhanced adatom mobility due to higher effective deposition temperature (Ohring 2002), resputtering of unfavourably oriented crystallites (Bradley, Harper & Smith 1986; Ying, Smith & Srolovitz 1996) and ion channelling effects (Dobrev 1982; Van Wyk & Smith 1980).

2.3 Chromium Nitride Thin Films

Chromium nitride crystals can grow in two primary phases: the face centred cubic (fcc) CrN phase and the hexagonal close packed (hcp) Cr_2N phase (Gautier & Machet 1997; Rebholz et al. 1999; Hurkmans et al. 1999; Hones, Sanjines & Lévy 1997; Bertrand, Mahdjoub & Meunier 2000). Selected chemical, physical and mechanical properties of these two phases are shown in Table 2.2.

By controlling the process parameters, pure Cr, Cr_2N or CrN films or mixtures of Cr-Cr_2N or Cr_2N-CrN can be obtained (Kuruppu et al. 1998). The deposition of pure CrN films requires only surpassing of a certain threshold pressure, as seen in Figure 2.9 and was also found in other studies, for example (Berg et al. 1996; Bertrand, Savall & Meunier 1997; Gautier & Machet 1997; Bull & Rickerby 1990). The threshold value depends on the temperature,

deposition rate, bias voltage, argon pressure, and target-substrate distance (Aouadi et al. 2002). CrN films possess usually a columnar microstructure. A model proposed by Chekour et al. (2005) describes the evolution of columnar CrN films by combining the two growth models proposed by Rickerby, Jones & Bellamy (1989) and Hones (2000). According to Chekour et al. (2005), at first cylindrical columns grow in three dimensions and form a dense structure (Rickerby model). After reaching a certain thickness, a porous columnar structure evolves due to shadowing effects induced by different growth rates of the columns (Hones model).

Table 2.2: Selected chemical, physical and mechanical properties of CrN and Cr_2N.

Property		CrN	Cr_2N
Atomic mass (g mol^{-1})		66[1]	118[1]
Crystal structure		fcc[1]	hcp[1]
Lattice parameter	*a* (nm)	0.415[1]	0.481[1]
	c (nm)	-	0.448[1]
Nominal density (g cm^{-3})		6.178[2]	6.564[2]
Melting temperature (°C)		1050 - 1500[1]	1500 - 1590[1]
Linear thermal expansion (10^{-6} K^{-1})		2.3[1]	9.4[1]
Enthalpy (kJ mol^{-1})		118.1 - 124.8[1]	25.2 - 30.8[1]
Young's modulus (10^5 N mm^{-2})		2.65 - 4.0[1]	2.7 - 3.14[1]
Poisson's ratio		0.2[1]	0.2[1]
Hardness (GPa)		12 - 28[3]	22 – 29[4,5]

[1] Friedrich (1998), [2] Hoy, Sloof & Janssen (2004), [3] Martinez et al. (2004), [4] Aouadi et al. (2001), [5] Hones, Sanjines & Lévy (1997)

Different to CrN films, pure Cr_2N films be only grown within a small pressure range (see Fig. 2.9 and Berg et al. (1996); Gautier & Machet (1997); Bull & Rickerby (1990)). At low nitrogen pressures, the proportion of nitrogen atoms is smaller than the proportion of chromium atoms available to undergo a compound forming reaction. Hence, the probability that atoms bond in Cr_2N compounds is higher than for CrN compounds. At higher bias voltages,

requirements regarding the nitrogen pressure are less critical. Under ion bombardment the lighter nitrogen atoms (M_N = 14.007 u) are preferentially resputterd from the surface compared to the heavier chromium atoms (M_{Cr} = 51.996 u) (Gautier & Machet 1997; Sugiyama et al. 1994; He et al. 2000), which supports the growth of dense Cr_2N films (Hones 2000).

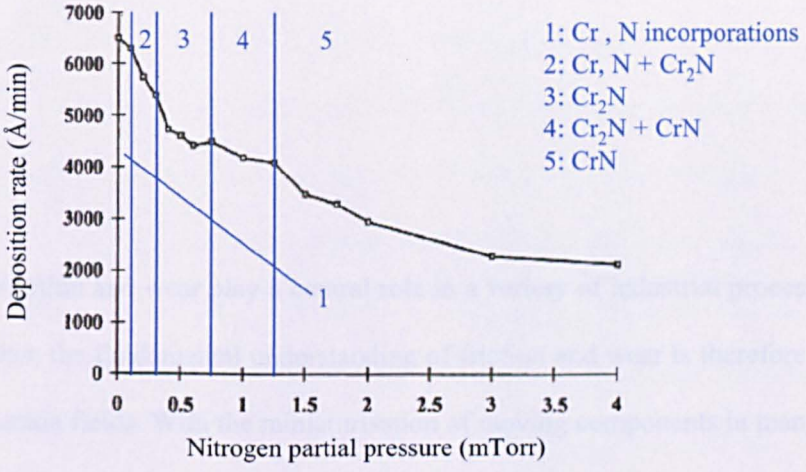

Figure 2.9: Deposition rate and deposited phases of chromium nitride thin films as a function of the nitrogen partial pressure during reactive sputtering of chromium with a sputter power of 8 kW, total pressure of 8 mTorr, and a bias voltage of -125 V, adapted from Glocker & Shah (1995).

Only few data are available about the topography of chromium nitride films since most research performed over the last decades has been almost exclusively focused on the modification of the microstructure. However, it was found that stochiometric CrN films with a (111) crystallographic texture parallel to the substrate surface exhibit triangular, faceted surface features (Bull & Rickerby 1990; Inoue, Okada & Koterazawa 2002; Zhao et al. 2005), whereas the features of substochiometric CrN films of the same crystallographic texture are rounded and of circular or elliptical shape (Bertrand, Savall & Meunier 1997; Sanjinés, Hones & Lévy 1998; Zhao et al. 2005). For CrN films with a (200) crystallographic texture, quadratic platelets oriented parallel to the substrate were observed (Bull & Rickerby 1990). Surface features of Cr_2N thin films that were cauliflower-like or needle-like, were reported by only a few groups (Bertrand, Savall & Meunier 1997; Sanjines, Hones & Lévy 1998; Zhao et al. 2005; Wang & Oki 1990).

Chapter 3

Principles of Microtribology

Friction and wear play a central role in a variety of industrial processes and systems. Due to this, the fundamental understanding of friction and wear is therefore crucial for many application fields. With the miniaturisation of moving components in many technological devices, such as surgical instruments and medical implants, robots, read/write heads, MEMS, it also is of primary importance to study friction at the micro and nanoscale. This chapter presents an overview of friction theory and wear mechanisms. Identification of and values for the models and parameters most relevant to the present work will be provided in context in later chapters, while this one remains general in its presentation.

3.1 Friction in Nano and Microscale Contacts

The relative motion of two objects at close proximity (in contact) induces non-conservative forces, which counteract the motion and, thus, give rise to the loss of mechanical energy by converting it into internal energy or heat. This phenomenon is called friction. If an object moves along a horizontal surface with an initial velocity, the friction resisting the motion is referred to as kinetic friction. To an object that is initially at rest, a minimum force must be applied to overcome the static friction and to initiate the motion. In contrast to kinetic friction, static friction is not associated with energy loss or sample heating due to the resistance to the motion.

The first friction laws were proposed by Amontons (1699) for unlubricated contacts. He found that the friction is independent of the area of surfaces but directly proportional to the normal load. Amontons explained the generation of friction by interlocking of irregularities on the mating surfaces, such that the relative motion lifts the load from one position of interlocking to another. Later, Coulomb (1785) stated that the friction force is given by a material parameter, the coefficient of friction, multiplied by the normal load. The Coulomb's law is explained on the atomic level by the Frenkel-Kontrova-Tomlinson model (Tomlinson 1929), which correlates friction to the energy dissipated when the molecules are forced into each other's atomic fields and then separated. A situation in real contacts is more complex than presented by this model. In order to cover special or to combine various friction phenomena (e.g. stiction, viscous friction), several models describing the friction in static state (e.g. Stribeck and Karnopp model) or dynamic state (e.g. Dahl, Bliman-Sorine and LuGre model) were developed for macroscopic systems over the last decades (Olsson et al. 1997).

In micro and nanotribology, friction, lubrication and wear are investigated on the length scale of micrometers to nanometeres and the force scale of millinewtons to nanonewtons. As a result, friction and wear are more influenced by the surface properties than is the case in macroscopic systems. Therefore, different behaviour and mechanisms or, at least, different relative importance of mechanism in macroscopic systems apply when moving to the micro or nanoscale.

In micro and nanoscale contacts, the friction force F_F is often expressed by (Tambe & Bhushan 2005)

$$F_F = F_{adh} + F_{wear} + F_{stick-slip} \tag{3.1}$$

where F_{adh} is the force due to adhesive interaction at the contacting surfaces, F_{wear} is the force due to wear at the interface of contacting surfaces, $F_{stick\text{-}slip}$ is the force due to stick-slip between contacting surfaces.

3.1.1 Adhesive Interaction Contribution to the Friction Force

At the dimension of nano and microstructures, adhesion can be traced back to interfacial forces:

- Solid-solid and shear adhesion: arises from the formation of adhesive bonds between two contacting surfaces, which slide against each other in the latter case.
- Capillary force: arises from the negative Laplace pressure inside the curved menisci formed between asperities of mating surfaces in the presence of a liquid (perhaps from an adsorbed film) in the contact zone.
- Electrostatic force: may arise due to an externally applied voltage across the interface, differences in material work functions of the surfaces, and electrostatic charging (Komvopoulos 1996). These forces usually vanish after a proper grounding of samples and instrumentation.
- Molecular forces: arise from dipole-dipole interactions with polar molecules (van der Waals forces). With nonpolar molecules, they are caused by the interactions of fluctuating dipoles in the individual atoms. To induce strong attraction, the spacing between the surfaces must be reduced to a distance lower than 10 nm (Bregliozzi 2006). This rarely occurs because technical surfaces are usually not atomically smooth.

With the presence of a thin liquid film at the contact interface, the adhesive friction force F_{adh} for two contacting surfaces is defined in the classical theory of adhesion as (Bowden & Tabor 2001)

$$F_{adh} = A_r\left(\alpha \cdot \tau_a + (1-\alpha)\tau_l\right) = A_r\left(\alpha \cdot \tau_a + (1-\alpha)\cdot\frac{\eta_l \cdot v}{h}\right) \tag{3.2}$$

where A_r is the real area of contact, α is the fraction of dry contact ($0 \le \alpha \le 1$), τ_a is the average shear strength of the dry contact, τ_l is the average shear strength of the liquid film, η_l is the viscosity of the liquid, v is the relative sliding velocity, and h is the thickness of the liquid.

Due to the presence of a liquid in the interface, capillary bridges form around the contacting and near-contacting asperities. For nano and microscale contacts, the capillary force becomes comparable to the normal load and, thus, the effective load, F_E, in the systems is

$$F_E = F_N + F_C \tag{3.3}$$

where F_N is the normal load and F_C is the capillary force.

The capillary force F_C at the sliding interface is given by the expression (Riedo, Lévy & Brune 2002)

$$F_C = 2 \cdot \pi \cdot R \cdot \gamma_l \cdot (\cos\theta_1 + \cos\theta_2) \cdot N(t) \tag{3.4}$$

where R is the radius of the counter body, γ_l is the surface tension of the liquid film, θ_1 and θ_2 are the contact angles of the contacting surfaces (see section 3.1.4), $N(t)$ is the number of contacting and near-contacting asperities where capillarity builds up and is a function of the rest time (or residence time) t of the counter body at the counter body-sample interface. Hereby, the equation assumes that each asperity of the samples or counter body surface has the same contact angles θ_1 or θ_2, respectively. Based on the statistical height distribution, the total number of contacting and near-contacting asperities contributing to the capillary force depends on the typical width of the distribution of distance between the surfaces, λ_c, (Bouquet et al. 1998; Riedo, Lévy & Brune 2002). The mathematical expression for $N(t)$ is

$$N(t) = \frac{e_{max}(t)}{\lambda_C} = \frac{1}{\lambda_C} \cdot \frac{1}{A_C \cdot \rho_m \cdot ln\left(\frac{p_S}{p}\right)} \cdot ln\left(\frac{t}{t_a}\right) = \frac{1}{A_C \cdot \rho_m \cdot ln\left(\frac{p_S}{p}\right)} \cdot ln\left(\frac{v_a}{v}\right) \tag{3.5}$$

where $e_{max}(t)$ is the maximum spacing to which a capillary bridge can built in a given time t, A_c is the cross-sectional area for the capillary bridge, ρ_m is the molecular density of the liquid, p_s/p is the ratio of ambient pressure to the saturation pressure at corresponding ambient temperature (equal to the relative humidity), t_a is the condensation time for one liquid monolayer, v_a is the critical velocity corresponding to the condensation time of one liquid monolayer and v is the sliding velocity.

The contribution from the capillary force to the adhesive force acts not only over the area of contacting asperities, but also the area surrounding the asperity contacts (Ando 2000). Therefore, the real contact area A_r sustains the effective load F_E and is expressed by

$$A_r = \phi_{adh} \cdot F_E \tag{3.6}$$

whith $\phi_{adh} = \frac{3.2}{E^*} \cdot \sqrt{\frac{R_{asp}}{\sigma_{asp}}}$ (for elastic contacts), $\phi_{adh} = \frac{1}{H}$ (for plastic contacts) according to Tambe & Bhushan (2005). In these equations R_{asp} is the average curvature of the asperities, σ_{asp} is the standard deviation of the asperity heights, H is the hardness and E^* is the composite Young's modulus of the two contacting surfaces, which can be calculated by

$$\frac{1}{E^*} = \left(\frac{1-\nu_1^2}{E_1} + \frac{1-\nu_2^2}{E_2} \right) \tag{3.7}$$

with Young's moduli E_1 and E_2 and Poisson's ratio ν_1 and ν_2 of the two contacting surfaces.

When inserting equations (3.3) to (3.6) into equation (3.2) the adhesive force can be calculated by

$$F_{adh} = \phi_{adh} \cdot \left(F_N - \phi_c \cdot R \cdot ln\left(\frac{\nu_a}{\nu} \right) \right) \cdot \left(\alpha \cdot \tau_a + (1-\alpha) \cdot \frac{\eta_1 \cdot \nu}{h} \right) \tag{3.8}$$

with $\phi_c = \frac{2\pi \cdot \gamma_1 (\cos\theta_1 + \cos\theta_2)}{\lambda_c \cdot A_c \cdot \rho_m \cdot ln\left(\frac{p_s}{p} \right)}$

For water films on a surface, if the contribution of viscous shearing of the water film to adhesive force can be neglected, then equation (3.8) reduces to

$$F_{adh} \sim \mu_{adh} \cdot \left(F_N - \phi_m \cdot R \cdot ln\left(\frac{\nu_a}{\nu} \right) \right) \text{ where } \mu_{adh} = \phi_{adh} \cdot \alpha \cdot \tau_\alpha \tag{3.9}$$

3.1.2 Contribution of Asperity Wear to the Friction Force

During relative motion, interactions between asperities of the two contacting surfaces may generate wear damage, e.g. fracturing, plastic deformation or tribochemical reactions. The wear of materials can be considered as result from an energy dissipation due to friction between contacting surfaces (Fouvry & Kapsa 2001; Huq & Celis 2002) and consumes the major amount of the dissipated energy during sliding (Achanta, Drees & Celis 2005). According to an energetic approach by Fouvry and Kapsa (2001), the wear-related contribution to the friction, F_{wear}, can be determined by

$$F_{wear} = \frac{\sum E_d}{s} \tag{3.10}$$

where s is the linear displacement and ΣE_d is the accumulated dissipated energy expressed by

$$\sum E_d = \frac{V \cdot \rho \cdot C_F \cdot (E\sigma_Y + E_a)}{M} + E_{dth} \tag{3.11}$$

where V is the wear volume, ρ is the density, C_F is a variable representative for contact configuration, $E\sigma_Y$ is the mechanical energy, E_a activation energy for oxidation (tribochemical reactions), M is the molar weight and E_{dth} threshold energy required before generating wear particles.

3.1.3 Stick-Slip Contribution to the Friction Force

The stick-slip phenomenon corresponds to the build up of the friction force to the static friction followed by slip at the interface once the static friction is overcome. A necessary condition for its appearance is that the static friction is higher than the dynamic friction (Diss & Brendlé 1997).

The occurrence of stick-slip can be attributed to:

- thickness-related alterations of the viscosity of the liquid present in the contact (Israelachvili, Chen & Yoshizawa 1994; Schoen, Hess & Diestler 1995; Opitz et al. 2002)

- interaction of the counterbody asperity and surface potential of the sample (atomic stick slip) (Hölscher, Schwarz & Wiesendanger 1996; Schwarz et al. 1997)
- mechanical interlocking (Rabinowicz 1995; Scherge & Gorb 2001).

3.1.4 Contact Angles on Surfaces

As mentioned in section 3.1.1, the estimation of the capillary force requires the knowledge of the contact angle of the liquid on the surfaces investigated. If a drop of a liquid is applied to a horizontal solid surface in a gas atmosphere, the drop can either spread over the surface or assume the shape of a spherical segment. Young (1805) found that the equilibrium of the force at the boundary drop-gas-solid surface can be described using the surface energies of the different phase boundaries:

$$\gamma_S = \gamma_{Sl} + \gamma_l \cdot \cos\theta \tag{3.12}$$

where γ_s is the interfacial energy at the solid surface/gas boundary (surface energy of solid surface), γ_l is the interfacial energy at the liquid/gas boundary (surface energy of the liquid), γ_{sl} is the interfacial energy at the solid/liquid boundary and θ is the contact angle. The contact angle is the angle between the baseline of the drop and the tangent at the drop boundary. The works of Wenzel (1936) and Cassie and Baxter (1944) established that besides the surface energy, the roughness of a surface determines its wettability as well. Wenzel proposed a model describing the contact angle θ' at rough surfaces as follows

$$\cos\theta' = r \cdot \cos\theta \tag{3.13}$$

where r is a roughness factor (or Wenzel ratio) which is defined as the ratio of the actual area of a rough surface to the geometric projected area, and θ is the thermodynamic contact angle on a smooth surface of the material (Young's contact angle). Since r is always larger than unity, an increase of the surface roughness enhances both the hydrophilicity of hydrophilic surfaces and the hydrophobicity of hydrophobic ones.

Cassie and Baxter proposed a model that describes the contact angle θ' at a surface composed of solid and air. Assuming that the water contact angle for air is 180°, the contact angle θ' is given by

$$\cos\theta' = f_1 \cdot \cos\theta - f_2 \tag{3.14}$$

where f_1 is the fraction of fluid in contact with material, and f_2 is the fraction of the fluid in contact with air. The concepts of Wenzel, and Cassie and Baxter are depicted in Figure 3.1.

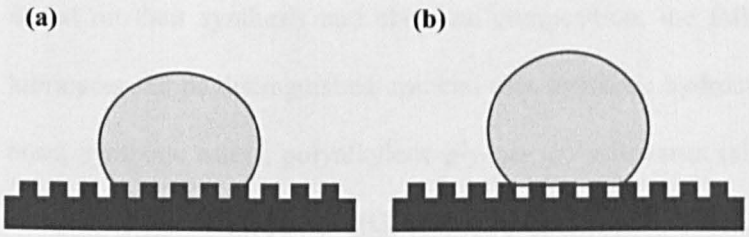

Figure 3.1: Effect of surface roughness on the contact angle: (a) Wenzel regime (b) Cassie-Baxter regime, adapted from (NTC 2005).

3.1.5 Friction in Lubricated Contacts

One of the main problems in tribology, and aims of lubrication, is to reduce or even exclude direct solid-solid contact, which could cause large adhesion, welding, and formation of large wear debris, corresponding to drastic wear rates. To overcome these difficulties, lubricants are applied in tribological systems. In industry and research, different types of lubricants can be employed, such as:

- boundary lubricants, like Langmuir-Blodgett films or self-assembled monolayers (SAM), e.g. fatty acids, silanes, thiols, phospholipids, polymeric films (Maboudian, Ashurst & Carraro 2000; Hsu 2004; Zhang & Lan 2005),
- solid film lubrication, e.g. carbon-based films, transition metal dichalcogenides, soft metal films, lubricious oxides, certain polymers (Busch 2001; Donnet & Erdemir 2004; Erdemir 2005),
- oils or greases, e.g. mineral oils, synthetic oils (Dresel 2001; Mang 2001).

Liquid lubricants find use in a wide range of applications, such as in combustion engines, gears, hydraulics, compressors, turbines, in metal working and metal forming (e.g. Mang & Dresel 2001; Lansdown 2004). Also in microsystems, speciality oils are used, especially in magnetic head-disk interfaces (Zhou et al. 2003; Wang, Miyake & Matsunuma 2005) or micromotors (Sundararajan 2001; Zhang, Meng & Li 2005). There has been a recent suggestion to employ fluid lubricants in air bag triggering mechanisms in automobiles and micromirror devices used in digital light processing equipment (Tao & Bhushan 2005).

Based on their synthesis and chemical composition, the following main groups of liquid lubricants can be distinguished: mineral oils, synthetic hydrocarbons, halogenated hydrocarbons, synthetic esters, polyalkylene glycols, polysiloxanes (silicone oils), polyphenylethers and perflourinated polyethers (Gschwender et al. 2001; Dresel 2001).

Depended on the thickness of the lubricant, various lubrication (friction) regimes can be established in a system, whereby the lubricant thickness is influenced by the test confinements (geometric design and configuration of the contact partners, their surface roughness, the viscosity of the lubricant, the sliding velocity and the loading). The Stribeck curve illustrates the trend generally observed in friction as function of a parameter combination considering sliding velocity, bulk viscosity of the lubricant and the normal load applied (Fig. 3.2). Furthermore, it shows the occurrence of the different lubrication (friction) regimes:

- Boundary lubrication: The contacting surfaces are covered with a molecular layer of the lubricant. The load applied is completely carried by contacting asperities, and the shearing takes mainly place in the lubricant layer.
- Mixed lubrication: The loading of the systems is partly carried by the contacting asperities and the lubricant film.
- Full-film lubrication: Here, two lubrication types are distinguished (hydrodynamic and elastohydrodynamic lubrication). In hydrodynamic lubrication, the surfaces are completely separated by a thick lubricant film. The deformation of the surfaces is negligible. The friction is determined by the internal friction of the lubricant that means its viscosity.

Usually, hydrodynamic lubrication occurs in contacts of high geometric conformity, whereas elastohydrodynamic lubrication is mainly found in contacts of low geometric conformity. Elastohydrodynamic lubrication results from the elastic deformation of the contact surfaces and an increase of lubricant viscosity with raising pressure.

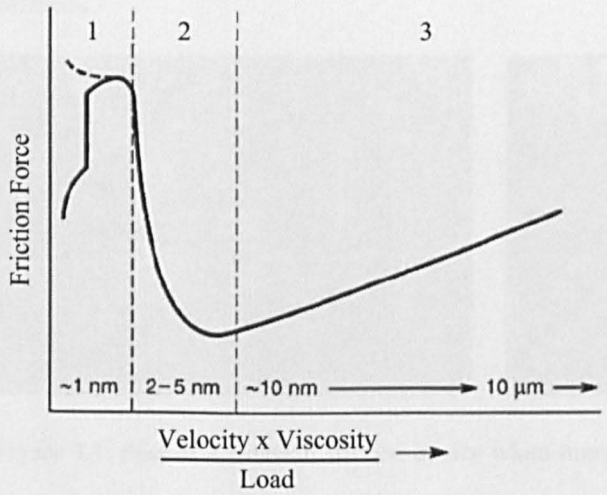

Figure 3.2: Figure 3.2: Stribeck curve showing the variation of the friction force as function of the sliding speed, bulk viscosity of the lubricating fluid and the load applied in the three lubrication regimes: 1-boundary, 2-mixed, 3-full-film. The film thickness, believed to correspond to each of the lubrication regimes, is also shown. Adapted from Israelachvili (1995).

3.2 Wear in Micro and Nanoscale Contacts

Wear may be defined as the removal of material from solid surfaces as result of mechanical and/or chemical actions and is generally accelerated by frictional heating. Beside a few marginal processes, four main types of wear are distinguished accordingly to the basic principle generating the material removal. These are (Rabinowicz 1995; Czichos & Habig 1992): (1) adhesive wear, (2) abrasive wear, (3) tribochemical wear and (4) surface fatigue wear.

Though this classification of wear types are originally developed for macroscopic systems, it is also applicable for micro/nanoscale contacts. So, adhesive and abrasive wear are often the main types of wear occurring in miniaturized systems, such as nanotractors, micromotors or rotating pivots (Beerschwinger et al. 1995; Williamson 2001; Merlijin van Spengen 2003; Zhang, Meng & Li 2005; Flater et al. 2006). Also, the occurrence of fatigue wear as well as

corrosive wear has been reported (Merlijin van Spengen 2003; Romig, Dugger & McWorther 2003; Allamed et al. 2003). For example, Figure 3.3 shows the wear on the post of a microengine from sliding experiments in dry and humid air. The water vapour was found to accelerate the formation of wear debris due to tribochemical reactions of an silicon surfaces.

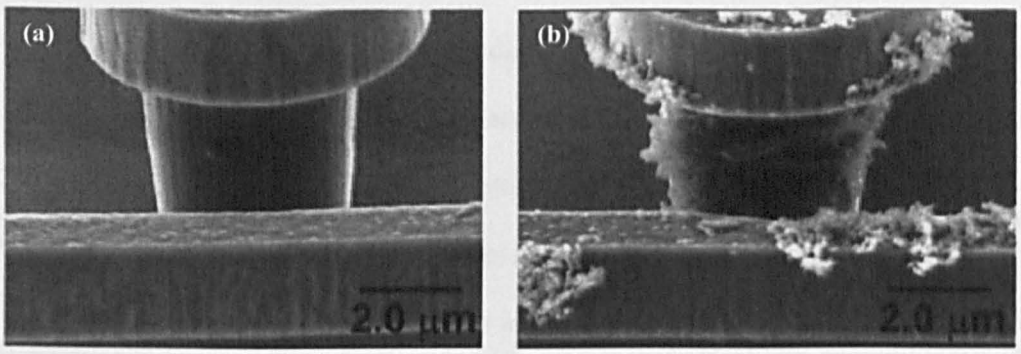

Figure 3.3: Post of a sidewall friction device when running in dry air (a) and in air at 40 % relative humidity (b), taken from Romig, Dugger & McWorther (2003).

Nevertheless, the mechanisms of wear and the correlation of wear to system parameters can vary between macro scale and micro/nanoscale contacts, since other forces and, thus, effects are relevant for the different systems.

In the following sections, the main types of wear are explained.

3.2.1 Adhesive Wear

Adhesive wear arises from interactions (adhesive forces) between atoms and molecules at the interface of the contacting solid materials. Adhesive wear is generated by a sequence of separated processes which can be described according to Mølgaard (1976) as follows. When two bodies in contact slide over each other, the contacting asperities are deformed due to locally high normal and tangential stresses. Thereby, protective covering layers on the surfaces, e.g. oxides, are destroyed, and adhesive bonds (junctions) at the interface are created according to the chemical nature of the contacting materials. The junctions are continuously made and broken while the two solids slide over each other. Usually, the junctions do not break along the original interface but within one of the materials. Fragments are pulled off

one surface and adhere to the other one. Processes like tribochemical reactions or strain hardening might modify the transferred fragments. These fragments come off the surface and are transferred back to the original surface or form loose wear particles.

3.2.2 Abrasion

Abrasion (abrasive wear) occurs when a rough hard surfaces or hard particles embedded in a soft surface slide on a softer surface and damage the interface by plastic deformation or fracture. The interaction between abrasively acting particles or asperities and the wearing surface of material can be divided into microploughing, microcutting, microcracking and microfatigue (Zum Gahr 1988). These processes are shown schematically in Figure 3.4.

In microploughing, the material is highly plastically deformed underneath the abrasive particle and pushed outward at the rim of the groove. Typical for microcutting is the generation of a microchip in front of the hard, abrasive particle. In microcracking, the generation and propagation of cracks cause a local break-off of material along the wear track when stressing the material above a critical limit. Microfatigue causes the removal of material by local fatigue due to repeated microploughing of the surface.

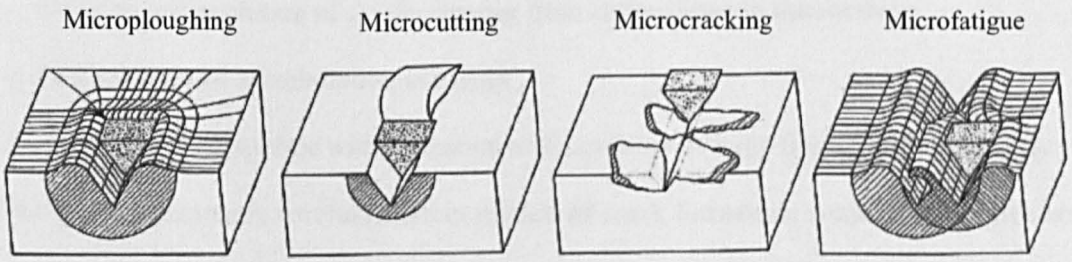

Figure 3.4: Physical interactions between abrasive particles and the surfaces of materials, adapted from Zum Gahr (1988).

3.2.3 Tribochemical Wear

Tribochemical wear is initiated by chemical reactions of the sample and counter body with the environment during tribological loading. The tribological loading can accelerate the chemical reactions due to the following mechanisms (Heidemeyer 1981):

- Removal of reaction inhibiting covering layers
- Acceleration of the transport of substances participating in the chemical reactions
- Increase in the area of reactive surface
- Increase of temperature due to friction heat
- Generation of surface atoms with free valences due to distortions in the lattices as result of plastic deformations

As result of tribochemical reactions, the properties of the surface layers of the contacting solids may be modified and, thereby, the wear resistance of the tribological system can be positively or negatively affected.

3.2.4 Surface Fatigue Wear

Surface fatigue wear can arise in a cyclic loaded contact zone of a tribosystem (e.g. by repeated sliding or rolling over the track), whereby the onset and severity of surface fatigue is determined by the loading amplitude and the cycle number. Usually, the temporal evolution of surface fatigue proceeds according to the following steps (Czichos & Habig 1992):

- Accumulation of distortions and failures in the atom lattice
- Creation and evolution of cracks ranging from atomic level to microcracks
- Propagation and accumulation of cracks
- Break up of the surface with formation and expulsion of large fragments leaving pits.

The literature contains several different models of crack formation; some of them have been confirmed in experimental investigations, e.g. Fujita (1958); Bilby, Cottrell & Swinden (1963); Vladimirov (1976); Rosenfield (1981); Pandey & Chand (2003). Those models can differ in loading and energy criteria for generation and propagation of cracks, or the contribution of an individual type of lattice failure to crack forming mechanisms. However, many of those models presume the formation of cracks to be the result of locally plastic microdeformations caused by the congestion of dislocations, e.g. at grain boundary and highly deformation-resistant particles. Under cyclic loading, persistent slip bands are created, where

strong, plastic deformations occur. The crack formation is initiated at these extrusions and intrusions as a result of the local stress at dislocation structures (Wuttke 1986).

Chapter 4

Preparation and Characterisation of Nanostructured Surfaces

This chapter describes the deposition process and parameters used to create nanostructured chromium nitride (Cr-N) thin films and to modify their surface chemistry for tribological studies. Furthermore, it summarizes the experimental details applied to characterise the morphological appearance, mechanical properties and tribological behaviour of the nanostructured films.

4.1 Surface Preparation

4.1.1 Nanostructuring of Surfaces

In this thesis, the nanostructuring of surfaces is to be obtained by in-process structuring. In-process structuring means the creation of a nanostructured surface by deposition of a film with a defined surface topography in a process that requires no additional pre- or post-treatment of the substrate (e.g. seeding, photolithographic etching) to modify the topography of the film. In this work, an unbalanced magnetron sputtering process was applied to investigate the in-process structuring of Cr-N thin films.

4.1.1.1 Deposition System

A schematic drawing of the deposition system HTC 1000-4 ABS^{TM} (Hauzer Techno Coatings) used for the deposition of the chromium nitride thin films is shown in Figure 4.1a.

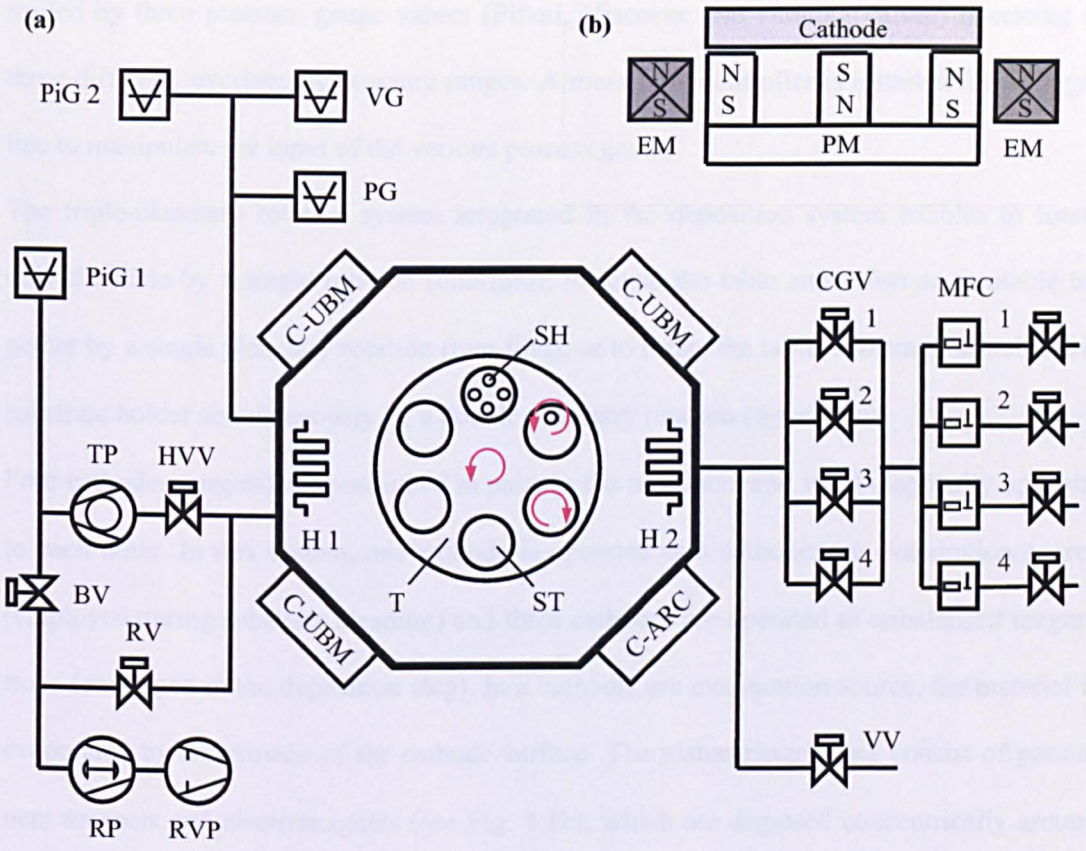

Figure 4.1: (a) Configuration of the deposition system used to deposit chromium nitride thin films. The components are abbreviated as follows: Backing valve (BV), Cathode in arc evaporation mode (C-ARC), Cathode gas valve (CGV), Cathode in UBM mode (C-UBM), Heater (H), High vacuum valve (HVV), Mass flow controller (MFC), Penning gauge (PG), Pirani gauge (PiG), Roots pump (RP), Roughing valve (RV), Rotary vane pump (RVP), Substrate holder (SH), Substrate turntable (ST), Substrate planetary rotation table (T), Turbomolecular pump (TP), Viscovac gauge (VG) and Venting valve (VV), (b) Schematic of the cathode-magnetron arrangement consisting of permanent magnet (PM) and electromagnets (EM).

The cylindrical deposition chamber is 1 m in diameter and 1 m high. Double walls permit the uniform cooling and heating of the system, using a temperature controlled, closed-loop water unit.

To adjust the pressure in the chamber, the system is equipped with a turbomolecular pump (nominal pumping speed: 2.2 m^3/s) and a roots pump (nominal pumping speed: 1000 m^3/h) in series with a rotary vane pump (nominal pumping speed: 250 m^3/h). The pressure is con-

trolled by three pressure gauge valves (Pirani, Viscovac and Penning valves) operating in three different, overlapping pressure ranges. A mass flow controller is installed for each gas line to manipulate the input of the various process gases.

The triple-planetary rotation system integrated in the deposition system enables to rotate only the table by a single rotation (one-fold), to rotate the table and substrate turntable together by a single planetary rotation (two-fold), or to rotate the table, substrate turntable and substrate holder simultaneously by a double planetary rotation (three-fold).

Four cathodes (targets) are positioned in pairs in the two doors and stand diagonally opposite to each other. In this system, one cathode is operated as a cathodic arc evaporation source (employed during substrate cleaning) and three cathodes are operated as unbalanced magnetrons (employed in the deposition step). In a cathodic arc evaporation source, the material is evaporated by arc erosion of the cathode surface. The planar magnetrons consist of permanent magnets and electromagnets (see Fig. 4.1b), which are disposed concentrically around the cathode (Münz 1991). Changes in the coil current of the electromagnets modify the unbalancing effect of the magnetron and, thus, the ionization degree of the vapour phase (Münz et al. 1991).

The magnetrons are driven by 5 kW Advanced Energy MDX DC power supplies. An additional MDX supply is used as the substrate bias supply. The current drawn from the substrate was recorded from the substrate bias supply.

The substrate temperature is monitored by thermocouples attached to the substrate holders and, thus, exposed to the same conditions as the substrates throughout the deposition process. The power to the two resistive-element heaters in the chamber is adjusted according to the readings of the thermocouples.

4.1.1.2 Deposition Process

The Cr-N thin films were deposited on polished silicon (Si) wafers (thickness 350 to 450 μm) all with a (100) crystallographic orientation in a reactive unbalanced magnetron (UBM)

sputtering system, as described above. The deposition process was conducted in the following sequence of process steps:

(1) Evacuation of deposition chamber

The chamber was evacuated to a base pressure of 0.005 Pa.

(2) Heating of deposition chamber

The chamber was heated to a temperature 50 °C below the temperature to be used in the later deposition step, since in the substrate cleaning step the temperature might rise due to intense ion bombardment.

(3) Cleaning of arc evaporation target

To remove contamination of the target surface, e.g. oxides, the Arc target was operated for 15 min with closed shutters; that is without depositing a film on the substrate. The cleaning was conducted at a current of 100 A, a bias voltage of -600 V and an argon flow of 200 sccm.

(4) Cleaning of UBM targets

As for the Arc target, the three UBM targets were also cleaned by operating them with closed shutters for 15 min at a sputter power of 6 kW. The coil current of the electromagnets was set to 4 A, bias voltage to -600 V and an argon flow to 300 sccm.

(5) Cleaning of substrate surfaces

The silicon substrates were cleaned by metal ion etching. In metal ion etching, metal atoms are generated by evaporation or sputtered from a metal target and accelerated towards the substrate due to a potential difference existing between substrate and target. The bombardment of the impinging ions causes the resputtering of contaminants from the substrate surface. In the experiments of this thesis, the substrates were etched for 15 min by chromium ions, which were generated by operating a chromium target (99.9 % Cr, Polema Ltd.) installed on the arc evaporation source. During the etching step, the current of the arc source was set to 100 A, the substrate voltage to -1000 V and the argon gas flow was adjusted to 20 sccm.

(6) Adjustment of substrate temperature

The substrate was heated to the desired temperature.

(7) Deposition of Cr-N thin film

For depositing the Cr-N films, three UBM targets (99.9 % Cr, Polema Ltd.) were operated simultaneously in a mixed argon/nitrogen atmosphere. A defined argon/nitrogen ratio was obtained by adjusting the gas flows of argon (purity: 99.5 %) and nitrogen (purity: 99.5 %) resulting in the total pressure in the deposition chamber. The magnetron drives of the UBM cathodes were operated in power regulation mode, whereas the bias supply was operated in voltage regulation mode. The coil current of the electromagnets remained unchanged at 4 A in all experiments, which means that also the ionization degree of the vapour phase was not separately modified. All depositions were carried out in two-fold rotation with a table rotation speed of 4 rpm. The deposition time was adjusted to deposit films with a thickness of about 2 μm.

(8) Venting of deposition chamber

The chamber was vented and the samples removed after the temperature in the chamber was cooled down to 50 °C.

During the deposition process, the process parameters were continuously controlled and accordingly adjusted to set values.

4.1.1.3 Experimentally Controlled Parameters in Deposition Process

With respect to the time available for the deposition experiments in this thesis, not all of the process parameters affecting the morphological evolution of thin films could be considered here. Therefore, it was decided to select six of the main process parameters in order to study their influence on the film morphology. These parameters were substrate temperature, bias voltage, Ar/N_2 flow ratio, total pressure and the cathode power. The values applied for the selected parameters in the various deposition experiments are summarized in Table 4.1.

Table 4.1: Values of the process parameters applied to deposit Cr-N thin films.

Process parameter	Applied values
Substrate temperature (T)	150, 250, 350, 450 °C
Bias voltage (U_b)	-50*, -75, -125*, - 150, -200*, -250, -350, -300*, -450, -600* V
Argon flow/nitrogen flow ratio (Ar/N_2)	0.7, 1.1, 1.3, 1.5
Total pressure (p)	0.4, 1 Pa
Sputter power of the 3 UBM cathodes (P)	2, 4, 6, 8, 10 kW

*applied only in selected experiments

The ion-to-atom flux ratio is another important parameter to consider in thin film growth (Hultman et al. 1991; Ino et al. 1997; Inoue, Okada & Koterazawa 2002). Though the ion-to-atom flux ratio was not varied in a controlled way in this study, it might differ in the experiments conducted because of its interrelation to other process parameters. Therefore, the ratio of ion flux J_i to atom flux J_a was estimated for all deposition experiments according to the following equation (Kadlec et al. 1990)

$$\frac{J_i}{J_a} = \frac{M_r \cdot m_u \cdot i_i}{\rho \cdot e \cdot a_d} \tag{4.1}$$

where M_r is the average relative mass of a film-forming atom, m_u is the mass unit, i_i is the ion current density, ρ is the film density, e is the elementary charge and a_d is the deposition rate. The average relative mass M_r can be determined by

$$M_r = x_{Cr} \cdot M_{Cr} + x_N \cdot M_N \tag{4.2}$$

where x_{Cr} and x_N is the number of chromium or nitrogen atoms forming the Cr-N film, and M_{Cr} and M_N is the relative mass of a chromium or nitrogen atom, respectively. The atomic percentages of chromium and nitrogen atoms in the deposited films were determined by energy dispersive spectroscopy (EDS). The ion current density i_i is given by the formula

$$i_i = \frac{I_i}{A} \tag{4.3}$$

where I_i is the ion current and A is the effective current-collecting area (in the thesis: the area of substrate with substrate holder and the table). At higher bias voltages ($-U_b > 50$ V), as it is the case in most of the experiments conducted in this work, it can be assumed that the ion current is equal to the substrate current (Kadlec et al. 1990).

As for all thin films, the density of chromium nitride thin films depends on the microstructure, which is influenced by the parameters applied in the deposition process (Logothetidis et al. 2004; Hoy, Sloof & Janssen 2004; Xu, Umehara & Kojima 2002; Cunha et al. 1999; He et al. 2000). For example, a density between 3.6 to $4.7 \cdot 10^3$ kg/m^3 was reported for CrN films with (111) crystallographic textures, whereas CrN thins with more pronounced (200), (311) and (220) crystallographic orientations parallel to the substrates can possess densities from 4.2 up to $5.1 \cdot 10^3$ kg/m^3 (Cunha et al. 1999). For CrN_x films ($x = 0.1$ to 1.0) with fibrous microstructures, density values close to the nominal density of CrN or Cr_2N were reported (Hoy, Sloof & Janssen 2004). With respect to their morphological appearance, the density was assumed to be $4.2 \cdot 10^3$ kg/m^3 for chromium nitride films with topography type* P, $5 \cdot 10^3$ kg/m^3 for topography types G and CR, and $6 \cdot 10^3$ kg/m^3 for topography types C, H and R in the calculation of the J_i/J_a ratio.

Since the deposition rate a_d is affected by a wide range of parameters such as (e.g. sputter rate, bias voltage and, Ar/N_2 ratio), it varied in the different deposition experiments of this study. Thus, the average deposition rate was determined from the film thickness t_f measured on cleaved chromium-nitride coated silicon wafers by scanning electron microscopy (SEM) and the deposition time t_d by

$$a_d = \frac{t_f}{t_d} \tag{4.4}$$

* The topography types P, G, CR, C, H and R are described in detail in section 5.1.

This method for determining a_d assumes that the deposition rate is constant over the film thickness. Since the microstructural evolution during the film growth is relatively homogenous for the investigated films this assumption seems to be valid.

It was found, that all depositions were carried at relatively low ion-to-atom flux ratios of $J_i/J_a < 2$. Since ion-to-atom flux ratio estimated for the experiments in this study varied over a relatively small range, the influence of this flux ratio might be regarded as being less important for the morphological evolution of the films investigated in this thesis.

4.1.2 Modification of Surface Chemistry

To alter the surface chemistry from hydrophilic to hydrophobic, the nanostructured Cr-N films were covered with a silicon oxide or hexafluoropropene layer, respectively. The preparation of these layers and relevant properties are described in the following text.

4.1.2.1 Deposition and Properties of the Silicon Oxide Layer

The silicon oxide (SiO_2) layers were deposited by RF sputtering in custom-built PVD unit used for some years at CSEM (Centre Suisse d'Electronique et de Microtechnique SA, Neuchâtel). This consists of a stainless steel reactor chamber (volume ~ 0.04 m^3) with three cathodes (targets) installed above the table (bottom electrode) on which the samples are placed. The target-sample distance is about 6 cm. The cathodes are connected with a 13.56 MHz RF power supply, whereby an impedance-matching network optimises the power transfer to the cathodes. The pumping system of this PVD unit consists of a turbomolecular pump in series with a rotary vane pump.

Prior to deposition, the deposition chamber was evacuated to a base pressure of 0.005 Pa and then backfilled with argon to obtain a total pressure of 0.4 Pa. The samples were coated with a 10 nm thick silicon oxide layer by operating the silicon oxide target for 10 min at 150 W sputter power. No bias was applied at the substrate table during the deposition.

The silicon oxide layer exhibit a hardness of a 10.3 ± 0.3 GPa (details of the measurements are given in section 4.2.4.1).

The chemical composition of the silicon oxide surface was analysed by X-ray photoelectron spectroscopy (XPS, details of the measurement are given in section 4.2.3). Figure 4.2a shows a typical survey spectrum of a silicon oxide coated nanostructured Cr-N surface obtained by XPS. Except for a small trace-like carbon peak, the spectrum only contains Si and O emissions expected for silicon oxide. No Cr or N peaks from the underlying Cr-N film could be detected indicating that the deposition was pin-hole free over the sample surface (1 x 1 cm^2). The carbon emission is present due to ambient contamination, which is unavoidable if the surface is exposed to air after deposition.

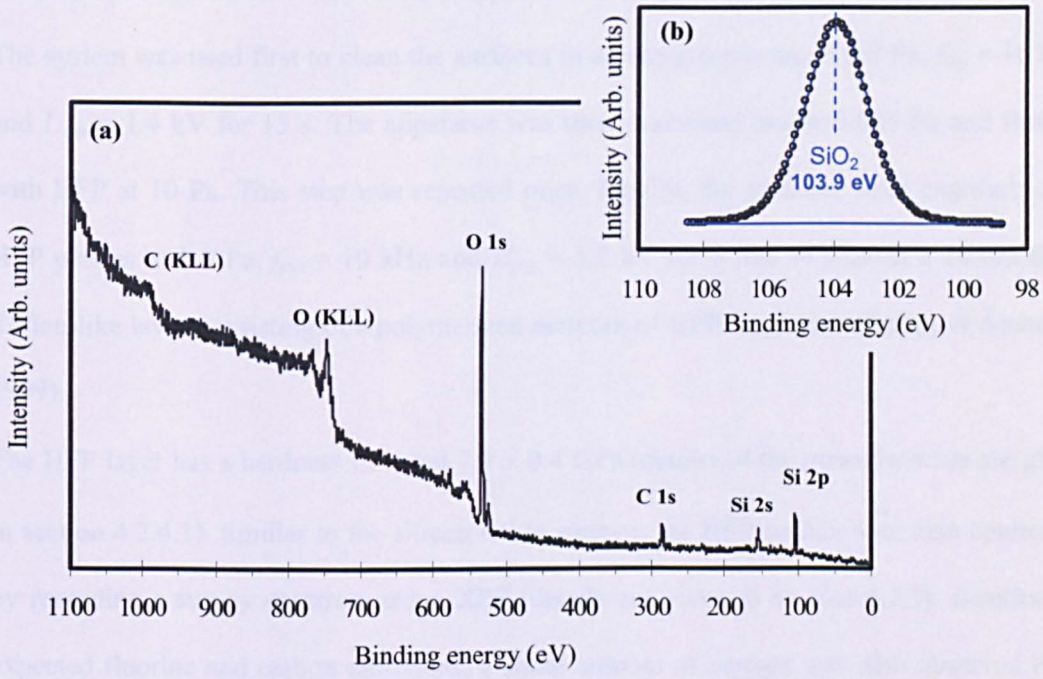

Figure 4.2: XPS analysis of the 10 nm thick silicon oxide layer deposited on top of a nanostructured Cr-N film. (a) Survey spectrum, (b) Si 2p spectrum: Even after fitting only one peak due to SiO_2 is evident. (KLL = transition level of atom).

The Si peak was further examined by recording a high-resolution Si 2p spectrum. This peak was fitted using a Gaussian-Lorentzian function to control the oxidation state of the silicon. As can been seen in Figure 4.2b, the emission shows the Si 2p peak to be that assigned to SiO_2.

4.1.2.2 Deposition and Properties of the Hexafluoropropene Layer

The hexafluoropropene (HFP) layers were deposited by a chemical vapour deposition process in another custom-built deposition unit (named Firebug). It consists of a ~ 800 cm^3 glass reactor chamber with a solid aluminium top electrode and a grounded-mesh bottom electrode on which the samples are placed. The distance between the top and the bottom electrode is 8 cm. The power supply for the top electrode was designed to output clean sine wave voltage signals in the range of f_{top} = 4-16 kHz with amplitudes up to U_{top} = 2 kV. The system uses a turbomolecular drag pump and an oil-free membrane prebacking pump. The Firebug unit is described in more details elsewhere (Knapp, Gluckenberger & Stemmer 1998).

The system was used first to clean the surfaces in an oxygen plasma at 0.4 Pa, f_{top} = 10 kHz and U_{top} = 1.4 kV for 15 s. The apparatus was then evacuated below 0.005 Pa and flushed with HFP at 10 Pa. This step was repeated once. Finally, the surfaces were exposed to an HFP plasma at 0.3 Pa, f_{top} = 10 kHz and U_{top} = 1.2 kV for 5 min to deposit a 10 nm thick Teflon-like layer consisting of a polymerized network of HFP fragments (Knapp & Stemmer 1999).

The HFP layer has a hardness of about 7.9 ± 0.4 GPa (details of the measurements are given in section 4.2.4.1). Similar to the silicon oxide surface, the HFP surface was also controlled by recording a survey spectrum using XPS (details are given in section 4.2.3). Besides the expected fluorine and carbon emissions, a small amount of oxygen was also observed (Fig. 4.3a). As in the previous case, no signal was detected from the underlying nanostructured chromium nitride film. The F/C ratio was determined to be 1.07. High-resolution spectrum of the C 1s region of the HFP layer and subsequent fitting using the same Gaussian-Lorentzian function indicates that, besides the -C-CF_x, -CF, -CF_2 and -CF_3 bonds, C-C, C-H bonds and C-O, C=C bonds are also present (Fig. 4.3b). It is not possible to determine whether these peaks were added at the time of deposition or afterwards during sample storage.

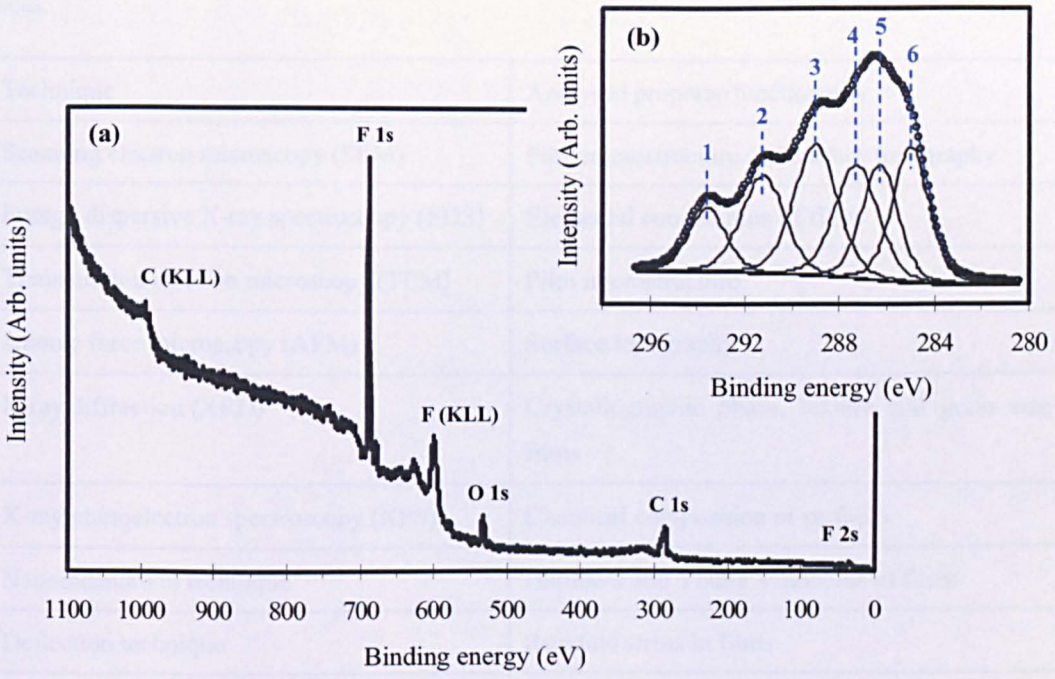

Figure 4.3: XPS analysis of the 10 nm thick HFP layer deposited on top of a nanostructured Cr-N film. (a) Survey spectrum, (b) C 1s spectrum: Peak deconvolution shows the presence of 1: $-CF_3$; 2: $-CF_2$; 3: -CF; 4: $C-CF_x$; 5: C=C, C-O; 6: C-C, C-H bonding. (KLL = transition level of atom).

4.2 Analysis of Properties of Nanostructured Thin Films

Several complementary characterisation methods have been applied in order to analyse the tribological functionality and some other functionality-relevant properties of the nanostructured surfaces. Table 4.2 summarizes the analytical techniques and information gained when used in this thesis. Most of these techniques are well-established, widely used and documented in standard reference texts, e.g. Brundle, Evans, Jr. & Wilson (1992); Sibilia (1996); Brandon & Kaplan (1999); Ohring (2002), and, therefore, not explicitly described in this work. Just for some techniques, a brief overview is included to set context for later interpretation of the test results.

Table 4.2: Techniques applied in the thesis to analyse the functionality and related properties of surfaces.

Technique	Analysed property/functionality
Scanning electron microscopy (SEM)	Film microstructure and surface topography
Energy dispersive X-ray spectroscopy (EDS)	Elemental composition of films
Transmission electron microscopy (TEM)	Film microstructure
Atomic force microscopy (AFM)	Surface topography
X-ray diffraction (XRD)	Crystallographic phase, texture and grain size of films
X-ray photoelectron spectroscopy (XPS)	Chemical composition of surfaces
Nanoindentation technique	Hardness and Young's modulus of films
Deflection technique	Residual stress in films
Contact angle measurement	Wettability of nanostructures
Microtribological tests	Friction and wear behaviour of films

4.2.1 Characterisation of Film Morphology

To evaluate the film morphology, all deposited films were examined by scanning electron microscopy (PHILIPS FEG 30 XL) and selected samples by transmission electron microscopy (PHILIPS XM-200 LaB6 source). Cross-sectional specimens for the TEM investigations were prepared as follows: two 10 x 5 mm^2 specimens were glued face to face using an epoxy resin of low viscosity, and then cut perpendicular to the coating-substrate interface into slices with an approximate thickness of 2 mm. After grinding and polishing down to 20 μm, each thin specimen was attached to a Ti holder for the final thinning by argon ion milling (BAL TEC RES 100). The rough milling was carried out in oscillation mode using a voltage of 4 kV at a current of 2.5 mA and incidence angle of 20° angle. For the fine milling, the voltage was reduced to 3 kV and the incidence angle was adjusted to values between 3° and 5°.

X-ray diffraction analysis of the deposited Cr-N thin films was carried out in the Bragg-Brentano configuration (SIEMENS D500 diffractometer/Co-Kα radiation with a wavelength

of λ_r = 1.7902 Å). A diffractometre in Bragg-Brentano geometry enables us to analyse preferentially and randomly oriented polycrystalline films. Receiving slits, specimen and focal point of the X-ray beam are located on a circle. The diffracted X-rays are focused on the receiving slits (parafocussing), which leads to an improvement of the sensitivity. The slits collimate incident X-rays, which impinge on specimen at an angle θ_{hkl}. After passing through receiving slits, diffracted X-rays are detected. The specimen rotates at one-half of the angular velocity of the detector. Since the incident and diffracted X-rays have the same angle to the surface, information only about (hkl) planes parallel to the surface can be gained.

Regarding the applied deposition conditions, it is assumed that a detected peak broadening in the XRD spectra of some coatings is probably caused by changes in grain size as well as by strain effects, so that the grain size d_{hkl} was determined from a Hall-Williamson plot in which the plot of ($\beta_{hkl}\cos\theta_{hkl}/\lambda_r$) vs. (2 $\sin\theta_{hkl}/\lambda_r$) is a straight line with an intercept of $1/d_{hkl}$ (Chalker 1991). The Hall-Williamson plot is only applicable for the grain size determination when at least three different coating-related reflections occur in the XRD spectra. In the other cases, the crystallite size d_{hkl} of the strongest reflection hkl was determined according to the Scherrer equation (Warren 1990)

$$d_{hkl} = \frac{K \cdot \lambda_r}{\beta_{hkl} \cdot \cos\theta_{hkl}} \tag{4.5}$$

where λ_r the radiation wavelength, β_{hkl} the half normal width of the reflection *hkl*, θ_{hkl} is the position of the hkl reflection and K is the shape factor of the average crystallite, which is commonly equal to unity according to Chalker (1991).

The occurrence of a preferred crystallographic orientation was estimated by calculating the texture coefficient T_{hkl} for a detected reflection hkl (Rickerby, Jones & Bellamy 1989)

$$T_{hkl} = \frac{\dfrac{I_{hkl}}{I_{hkl,ref}}}{\dfrac{1}{n}\sum_{0}^{n}\dfrac{I_{hkl}}{I_{hkl,ref}}} \tag{4.6}$$

where n is the number of reflections, I_{hkl} is the measured intensity of the reflection hkl, $I_{hkl,ref}$ is the reference standard intensity of the reflection hkl of a reference (given in JCPDS[1] cards). For films with randomly oriented grains, the texture coefficient is equal to unity.

4.2.2 Determination of Topographical Parameters

4.2.2.1 Evaluation of Topographical Evolution of Nanostructures

The lateral dimension and the height[2] of the topographical features of the topography types[3] P, G, C, R and H were measured by SEM. The topographical parameters of at least 50 features were determined for each topography type to provide a statistical guarantee for the measurement results. Since the features of topography type CR cannot be precisely described by simple, geometrical shapes, the topography of these film was characterised by atomic force microscopy (Nanoscope® Dimension™ 3100 series, Digital Instruments) in tapping mode using a conical silicon high resonance frequency probe tip (force constant: 5.5 N/m, tip curvature: 10 nm, resonant frequency: 150 ± 5 kHz). The surface topographies of ten scan areas (scan size: 10 μm x 10 μm) were measured at randomly located regions on each sample surface. The surface topography was quantitatively analysed by determining various parameters: Root mean square (RMS) roughness (S_q), skewness (S_{sk}), kurtosis (S_{ku}) and dominant wavelength λ in power spectral density. The definitions of these parameters are given in the Appendix A.1 and in references (Dong, Sullivan & Sullivan 1994a, 1994b; Thomas 1999; Mainsah, Stout & Thomas 2001). Since some of the above mentioned surface parameters depend on the sampling interval of the measuring device (Sayles & Thomas 1978), the fractal dimension D was also determined for the tested surfaces (see Appendix A.1). In this thesis, auto-levelling using a least squares plane was applied before calculating the surface pa-

[1] Joint Committee for Powder Diffraction Studies

[2] The lateral dimension and the height of the surface features is shown in Figure 5.12 for the different topography types.

[3] The topography types P, G, CR, C, H and R are described in detail in section 5.1.

rameters from AFM scans (by using the software Nanoscope III version 5.12r3 by Digital Instruments). In all scans there were 512 sampling points in both x and y directions (nominal sampling interval about 20 nm).

4.2.2.2 Characterisation of Surfaces Tested in Microtribological Studies

In order to correlate the functional performance of nanostructures with their topography, commonly used topographical parameters were calculated from the AFM images taken from the different nanostructures. Since different aspects of tribological performance were investigated in the thesis, the evaluation of topographical data needs to be adapted to the specific application. The topographical parameters which were selected with respect to their relevance to the specific experimental group (see Chapter 1) and the data processing facilities available are listed in Table 4.3.

Table 4.3: Topographical parameters selected for their relevance to the experimental group (EG) and determined by post-processing of AFM images of the nanostructures.

EG	Selected topographical parameters
1: Friction and wear in unlubricated contacts	RMS roughness S_q, skewness S_{sk}, kurtosis S_{ku}, RMS slope σ', summit density S_{sd}, summit curvature S_{sc}, fractal dimension D
2: Friction and wear in lubricated contacts	RMS roughness S_q, skewness S_{sk}, kurtosis S_{ku}, RMS slope σ', summit density S_{sd}, summit curvature S_{sc}, fractal dimension D, surface bearing index S_{bi}, core fluid retention index S_{ci}, valley fluid retention index S_{vi}
3: Friction of hydrophilic and hydrophobic surfaces	RMS roughness S_q, summit density S_{sd}

The AFM measurements were performed under the same conditions and with the same equipment as described in section 4.2.2.1.

In the tests in EG 3, the capillary force was expected to give a strong contribution to the friction in the system. Capillary bridges can form only between contacting or near-contacting asperities of the surfaces of sample and counterbody. That means that just the highest asperities of the surfaces have to be considered in the surface analysis in these tests. Therefore, the

reference line to count the summits was positioned 5 nm below the highest point in the scanned area. Thereby, as summit is a peak higher than its four nearest neighbours.
Additionally, the lateral dimension and the height of the surface features of surfaces with pyramid-like or cone-like structure were considered.

4.2.3 Analysis of Surface Chemistry

The XPS spectra were measured using non-monochromated Mg-Ka X-rays at 1253.6 eV with a full width at half maximum of 0.7 eV and a hemispherical electron energy analyser (Leybold-Heraeus EA10/100) operating in the constant pass energy mode.
Two types of measurements were performed. First a survey spectrum was measured and then a high-resolution spectrum was recorded; each in the constant analyser transmission mode at a pass energy of 50 eV. This high pass energy was chosen to minimize X-ray induced damage, which is typically observed on surfaces such as the HFP layers after long X-ray exposure times.

4.2.4 Measurement of Mechanical Properties

4.2.4.1 Hardness and Young's Modulus

The hardness and Young's modulus of the different nanostructured Cr-N films as well as the hardness of HFP and silicon oxide layers were determined by a depth-sensing nanoindentation technique (Nano-Hardness Tester, CSM Instruments) using a Berkovich indenter. In depth-sensing indentation instruments, the penetration depth of an indenter beneath the specimen surface is continuously monitored with respect to the normal load applied (Fischer-Cripps 2002). Due to equipment limitations such as machine resolution, signal-to-noise ratio, tip rounding effects, it is very difficult to obtain meaningful experimental results for indentation depths less than 10 nm (Chen, Liu & Wang 2005). Therefore, the SiO_2 and HFP films had to be deposited with a higher thickness than they possess when applied for covering the nanostructures. The SiO_2 and HFP layers were deposited on nearly atomically flat Si(100)

wafers with a thickness of 500 nm. It is assumed that thickness-related changes in morphology and chemical composition of the films can be neglected.

In order to obtain reliable results in nanoindentation tests, it is recommended that indents should have pentration depths that are significantly deeper than the surface roughness but do not exceed a critical penetration depth dependent on the film-substrate combination (Fischer-Cripps 2002; Chen, Liu & Wang 2005; Xu & Rowcliffe 2004). The maximum load for the indentations of the different films was chosen under consideration of these recommendations, which means that the indentation tests were performed at a maximum load P_{max} of ranging from 10 mN to 20 mN for the Cr-N films, 10 mN for the SiO_2 layers and 5 mN for the HFP layers. The loading and unloading rate was set to be to 20 mN/s (Cr-N films), 10 mN/s (SiO_2 layer) and 5 mN/s (HFP layer).

The hardness and Young's modulus were determined from the load-penetration curves according to the Oliver-Pharr approach (Oliver & Pharr 1992). After extracting the experimental parameters (projected area A_{max} at maximum load P_{max}, and reduced elastic modulus E_r) from the load-displacement curve, the hardness H and Young's modulus E of the tested material can then be calculated from the following mathematical expressions:

$$H = \frac{P_{max}}{A_{max}} \tag{4.7}$$

$$E = \frac{E_{ind} \cdot E_r \cdot \left(1 - \nu^2\right)}{E_{ind} + \left(\nu_{ind}^2 - 1\right) \cdot E_r} \tag{4.8}$$

where ν_{ind} is the Poisson's ration of the indenter, ν is the Poisson's ration of the material and E_{ind} the Young's modulus of the indenter.

In order to determine the elastic modulus of the chromium nitride films according to equation (4.8), the Young's modulus and Poisson's ratio of the diamond indenter and the Poisson's ratio of chromium nitride thin films were considered to be E_{ind} = 1000 GPa, ν_{ind} = 0.07

(Fischer-Cripps 2002) and $\nu = 0.2$ (see Tab. 2.2), respectively. At least 10 measurements were carried for each tested film.

4.2.4.2 Residual Stress

The residual stress σ_r of the thin films was calculated according to the Stoney's equation (Stoney 1909)

$$\sigma_r = \frac{E_s}{1-\nu_s} \cdot \frac{t_s^2}{6 \cdot t_f} \cdot \frac{1}{(r_a - r_b)} \tag{4.9}$$

where E_s and ν_s are respectively the Young's modulus and Poisson's ratio of the substrate, t_s is the thickness of the substrate, t_f is the film thickness, r_a is the curvature of the substrate after the deposition and r_b is the curvature of the substrate before the deposition.

This method can be only applied if the thin film approximation is valid (Larsson, Hedenquist & Hogmark 1996), which is the case in this study: The ratio of substrate thickness (350 to 450 μm) to film thickness (~ 2 μm) was > 100 and the lateral sample dimensions (15 x 15 mm^2) were significantly larger than the total sample thickness.

The curvature of the samples was measured in two perpendicular directions by a profilometer (DEKTAK 300, Veeco) using a diamond tip with a curvature radius of 12.5 μm and an applied load of 0.25 mN. For each thin film, at least five measurements were performed. The calculation of the residual stress requires also the knowledge of the substrate curvature before the thin film is deposited onto it. Experimental reasons prevented determination of the curvature for each silicon substrate before it was coated. To have at least an estimate of the substrate curvature in an uncoated state, samples from five different silicon wafers were analysed. The average value of the wafer curvature determined in these measurements was considered later as curvature r_b in the stress calculation. The Young's modulus and Poisson's ratio of the Si(100) substrate were inserted with $E_s = 169$ GPa (Klett et al. 1999) or $\nu_s = 0.3$ (Klett et al. 1999) in Stoney's equation, respectively.

4.2.5 Determination of Wettability of Nanostructures

The wettability with water of the different nanostructures was analysed by dynamic contact angle measurements using the sessile drop method. In the sessile drop method, a drop of a liquid is placed on the solid surface being evaluated (Berg 1993). The angle between the baseline of the drop and the tangent at the drop boundary, which corresponds to the contact angle between the liquid and the surface, is determined. The basis for the determination of contact angles is the image of the drop on the surface. The drop shape is adapted to fit a mathematical model, which is then used to calculate the contact angle.

Dynamic contact angle experiments describe the processes at the liquid/solid boundary of a drop of liquid placed on a solid surface when increasing or decreasing the drop volume, i.e. during wetting and dewetting processes. In dynamic measurements, sedimentation effects, changes due to different vapour pressures of the various components or dissolution effects are eliminated (Lugscheider & Bobzin 2003).

When measuring the advancing contact angle, a drop with certain diameter is formed on the solid surface and then slowly increased in volume (Fig. 4.4a). During determining the receding angle, the contact angle is measured as the size of the drop is being reduced (Fig. 4.4b), i.e. as the surface is being de-wetted.

By using the difference between the advancing and the receding contact angle (contact angle hysteresis) it is possible to make statements about roughness of the solid or the chemical inhomogenities. Moreover, recently it was pointed out that the hydrophobicity or lyophobicity of surfaces is described adequately only by considering the contact angle hysteresis (Chen et al. 1999; Quéré 2002).

The wettability of the different surfaces with water were analysed by a contact angle measuring device (DSA10 video contact angle measuring device, Krüss). A liquid drop of a diameter of approximately 2 mm was applied to the surface of the sample with a very fine hollow needle. By leaving the hollow needle in the drop, the drop volume was enlarged by the low-

est possible feeding rate (10 µl/min). During enlarging of the drop volume, the image of the drop was recorded every 0.2 s, and the contact angle was calculated from the drop image by using an elliptical segment function included in the software of the test device used. The enlargement was stopped when the drop size was close to 6 mm, since then the influence of gravity on the drop size is not longer negligible (Lugscheider & Bobzin 2003). When reaching the maximum drop size, the volume was reduced by the lowest possible sucking rate (10 µl/min). The image of the continuously size-reduced drop was recorded every 0.2 s, and the contact angle was calculated from that image by using an elliptical segment function.

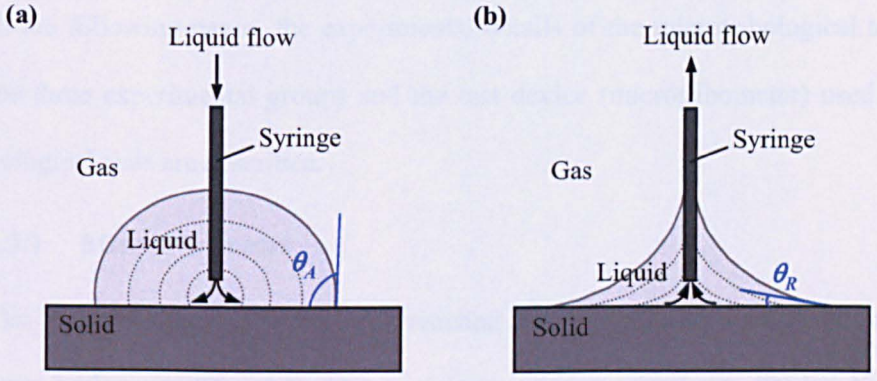

Figure 4.4: Measurement of (a) advancing contact angle θ_A and (b) receding contact angle θ_R with the sessile drop method.

For each structure, five drops were investigated to statistically guarantee the results of the measurements. Approximately 50 contact angles were determined for each drop.

For the humidity studies (EG 3), the wettability of the titanium carbide counter bodies needed also to be determined for interpreting the test results. With the available equipment the contact angle could not be measured on the actual counter bodies due to their geometry (2 mm balls). Therefore, the wettability measurements were carried out on TiC coated discs instead of balls. Discs and balls were coated during the same deposition process and polished according to the same procedure.

4.3 Characterisation of Microtribological Performance of Nanostructured Thin Films

The influence of nanostructuring on the microtribological performance of surfaces was investigated in three different experimental groups (EG) with focus on:

(1) Friction and wear of nanostructures in unlubricated contacts (section 6.1)

(2) Topography-related influence on lubrication of nanostructured surfaces (section 6.2)

(3) Effect of nanoscale topography and chemical composition of surfaces on their microtribological behaviour (section 6.3)

In the following pages, the experimental details of the microtribological tests conducted in the three experimental groups and the test device (microtribometer) used for the microtribological tests are described.

4.3.1 Microtribometer

The microtribometer (BASALT®-Precision Tester, TETRA) used in this thesis consists of three basic units (Fig. 4.5): (A) precision motion mechanisms, (B) bending element (force transducer) and (C) fibre-optic length detection system.

4.3.1.1 Precision Motion Mechanisms

There are various drives incorporated within the microtribometer for positioning the sample and the counterbody, providing reciprocating motion and for normal force adjustment.

The positioning units serve to position the sample in the *x-y* direction or the counterbody mounted on the bending element in *z* direction, respectively. These motions are achieved using stepper motors with a resolution of ± 2.5 µm. The motion range from the initial position is 10 cm in *x-y* direction and 5 cm in *z* direction.

The reciprocating motion of the sample is realised by using linear bearing which is connected onto the free end of a piezoelectric element. The other (fixed) end of this element is connected to wires for activation. When applying a voltage, the piezoelectric element flexes back and forth in the *x* direction and either pushes or pulls the linear bearing. In this way a

reciprocating motion in the range of ± 0.5 mm is provided. The sample is mounted using suitable adhesive on top of a sample holder that is fixed in the linear bearing assembly.

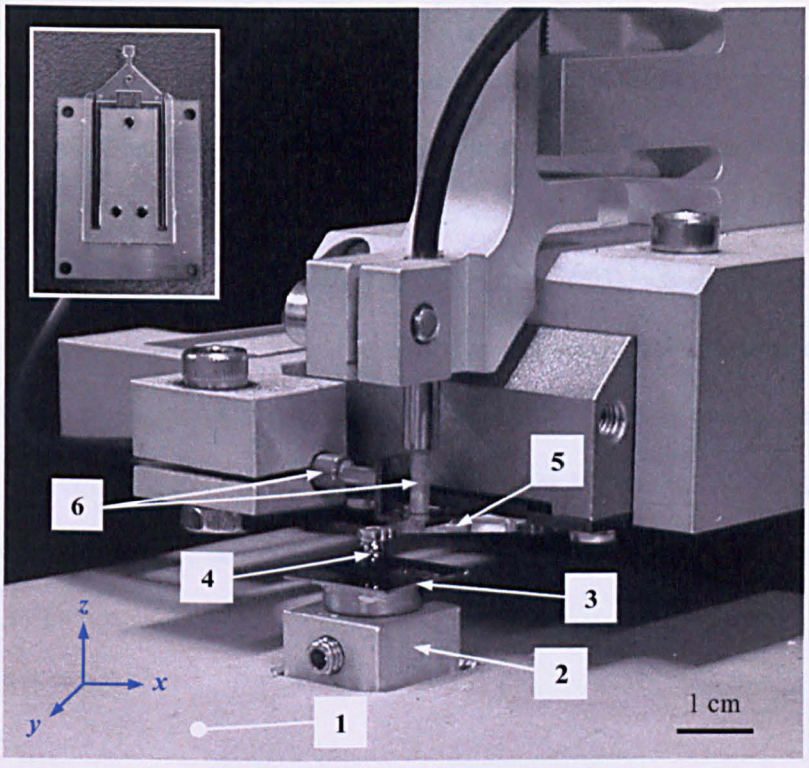

Figure 4.5: Image of the microtribometer. The main components are marked: (1) the *x*-*y* micropositioning stages powered by stepper motors (2) reciprocating unit, (3) sample, (4) counter body, (5) bending element (force transducer), (6) fibre-optic sensors to detect normal and lateral deflections of the force transducer. The inset shows a force transducer - glass spring - mounted on a steel support.

The normal force is adjusted by a controlled deflection of the bending element which is housed within the normal force adjustment unit. The normal force adjustment unit consists of a piezoelectric element connected to a flexure stage and is placed on the *z* positioning unit. By using the *z* positioning unit, the normal force is coarsely adjusted. The fine adjustment is obtained with the piezoelectric element. The normal force adjustment unit itself can provide a motion in the range of 80 µm in *z* direction with a resolution of 1 µm.

4.3.1.2 Bending Element

The bending element used in the microtribometer is a double leaf spring. The length of the beam is typically about 1 cm. In order to obtain the required spring constant of the double

leaf spring, the width, length and thickness of the beams are accordingly adjusted under consideration of the spring material. The normal spring constant is always higher than the lateral spring constant, which makes the double leaf spring particularly suited for tribological experiments. The material of the double leaf spring is usually either stainless steel or photostructured glass. The stainless steel springs are mostly used when measurements of high friction forces (above 30 mN) or tests with high normal forces (10 mN to 1 N) are required. Photostructured glass springs (Mrotzek et al. 2003), which provide a higher sensitivity than the steel springs, are mainly used for microtribological measurements in the force range of 100 nN to 30 mN. The lateral force constants of the springs can range from 5 N/m to 100 N/m and the normal force constants from 10 N/m to 200 N/m, respectively. The spring constants of the bending element need to be known to transform the measured length values to force values from

$$F = -k \cdot x_b \tag{4.10}$$

where F is the force, k is the spring constant and x_b the beam deflection.

In this case, k is either the normal (k_N) or the lateral (k_L) spring constant depending on whether the normal (x_{bN}) or the lateral deflection (x_{bL}) is applied to the equation in order to calculate the normal (F_N) or the lateral force (F_L).

The spring constant is calibrated by placing known precision weights on the end of the spring and determining its deflection. The spring constant is then obtained from the slope of the linear fit to the weight-deflection data. Since the bending element assembly can be rotated by 90°, normal as well as lateral spring constants can be easily ascertained in this manner. This method was found to provide the most reproducible results.

4.3.1.3 Fibre-Optic Detection System

Fibre-optic sensors are incorporated in the microtribometer in order to (1) monitor the reciprocating motion, (2) adjust the z-motion of the normal force drives, (3) measure the normal deflection and (4) the lateral deflection of the bending element.

The advantage of fibre-optic length detection sensors is that these sensors have a high resolution with long-term stability, yet are small, simply constructed, relatively inexpensive and easy to handle (Grattan & Sun 2000). The optical measurement inherently implies electrical isolation and the sensors are robust enough to operate in aggressive media. A further advantage is the relatively low costs of such sensors compared with other comparable length detection system, e.g. interferometers, (Scherge et al. 2000).

Fibre-optic sensors consist of send and receive channels (Fig. 4.6a). The number and arrangement of the channels in an optical fibre can vary and depend upon the required measurements range of the sensor. Incident light from a red or infrared source travels through the send channel and strikes a reflector mounted on a reciprocating unit or a drive. In the microtribometer used in this thesis, aluminium coated silicon squares were used as mirrors. The light is reflected and a fraction of it enters the receive channel. As the distance between the reflector and the ends of the optical fibre changes, the intensity of light detected by the receive channels varies. This intensity variation is transformed to provide a length value.

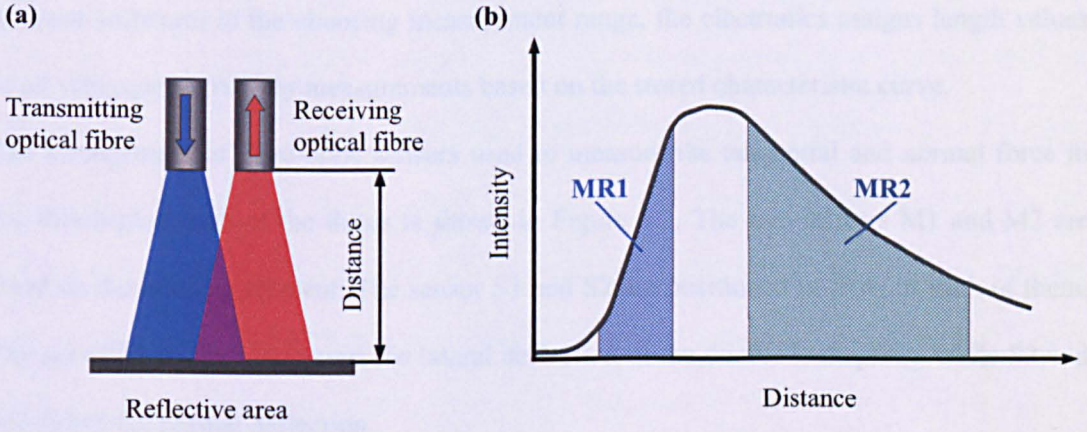

Figure 4.6: Schematic drawing of (a) fibre-optic sensor with send and receive channels; (b) intensity-Distance curve with the two different measurement region, adapted from Mollenhauer et al. (2003).

The intensity versus distance plot has a characteristic shape (Fig. 4.6b). When the reflector and fibre-optic sensor are first moved apart from an almost touching position, a reflected intensity is first recorded at a certain distance. From this point on the rise in the intensity with distance is very sharp. At a certain distance the reflected intensity reaches a maximum.

A further increase of the distance between reflector and end of fibre-optic sensor distance beyond this point results in a gradual decrease in the reflected intensity until it falls below the detection limits of the electronics. Within the intensity-distance curve, two distinct measurements regions MR1 and MR2 can be found where the intensity variation with distance is almost linear. These regions are exploited for length detection. In region MR1 the slope of the distance-intensity curve is stepper than in MR2, which means that the sensitivity in this regime is higher than in MR2. On the other hand the distance range, within a linear relationship to the intensity variation is found, is for MR1 smaller than for MR2. So generally the fibre-optic system is operated in MR1 regime when high sensitivity measurements over short deflection distances ($\leq$ 100 μm) are required. While the system is used in MR2 regime when long distance deflections have to be realised and a reduced sensitivity is tolerable.

After production of each sensor, its characteristic distance-intensity curve is determined by the manufacturer and is stored within the associated sensor electronics. Upon measuring and fixing the position of the intensity maxima (a simple process incorporated within the measurement software) in the choosing measurement range, the electronics assigns length values to all subsequent intensity measurements based on the stored characteristic curve.

The arrangement of fibre-optic sensors used to measure the tangential and normal force in the tribological tests of the thesis is shown in Figure 4.7. The two mirrors M1 and M2 are fixed on the bending element. The sensor S1 and S2 are positioned in front of each of them. The set of S1 and M1 measures the lateral deflection of the double leaf spring, while S2 and M2 detect the normal deflection.

The fibre-optic sensors installed in the microtribometer are commercial types (FOS-SLK 1417-IR, TETRA). The measurement regions are MR1 = 10 to 100 μm and MR2 = 300 to 2000 μm, whereby the resolution is given to be 1/5000 of the upper bound of the measurement region.

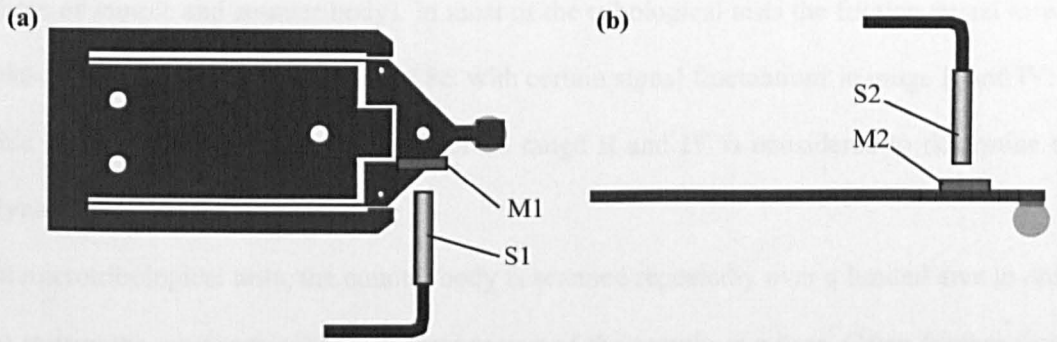

Figure 4.7: Sketch of the spring-sensor arrangement to measure the tangential (lateral) and normal deflection of the double leaf spring (a) Top view: Fibre-optical sensor S1 and mirror M1 for tangential force detection. The normal force detection is not shown (b) Side view: Fibre-optical sensor S2 and mirror M2 for the normal force detection. The tangential force detection is not shown. Adapted from Bregliozzi (2006).

4.3.1.4 Data Evaluation

The signal of the reciprocating drive and the friction force signal detected by the tangential detection system in microtribological tests are depicted in Figure 4.8. The drive is excited by a sawtooth signal (Fig. 4.8a), with the forward and backward direction of the motion. At the beginning of the forward motion (range I), counter body and sample stick together until the back driving force ($F = -k \cdot \Delta x_b$) generated by the spring equals the friction force F_F. Up to this point the relative velocity is zero. After exceeding the static friction force $F_{F,s}$ the counter body starts to slide (range II). When the direction of the horizontal drive is reversed, counter body and sample stick again until the spring force equals the friction force (range III), where it again begins to slide (range IV). The distance between the two plateaus in ranges II and IV represents twice the value of the dynamic friction force F_F. The distance between two peak values in range I and III is equal to twice the value of the static friction force $F_{F,s}$. With a similar method, the force in the vertical direction can be determined by measuring the deflection of the spring in z direction.

The tangential force signal shown in Figure 4.8b represents the theoretical friction curve, which might be recorded under ideal test conditions (e.g. no background noise, smooth sur-

faces of sample and counter body). In most of the tribological tests the friction signal resembles more the curve seen in Figure 4.8c, with certain signal fluctuations in range II and IV. In this case the average value of the signal in range II and IV is considered to determine the dynamic friction force.

In microtribological tests, the counter body is scanned repeatedly over a limited area in order to restrict the measurement to a distinct region of the sample at a time. Often friction force-normal force curves are generated in microtribological tests (Scherge & Gorb 2001; Hild 2005; Bregliozzi 2006). By fitting of these data according to an appropriate contact or friction model, the coefficient of friction can be determined from such curves.

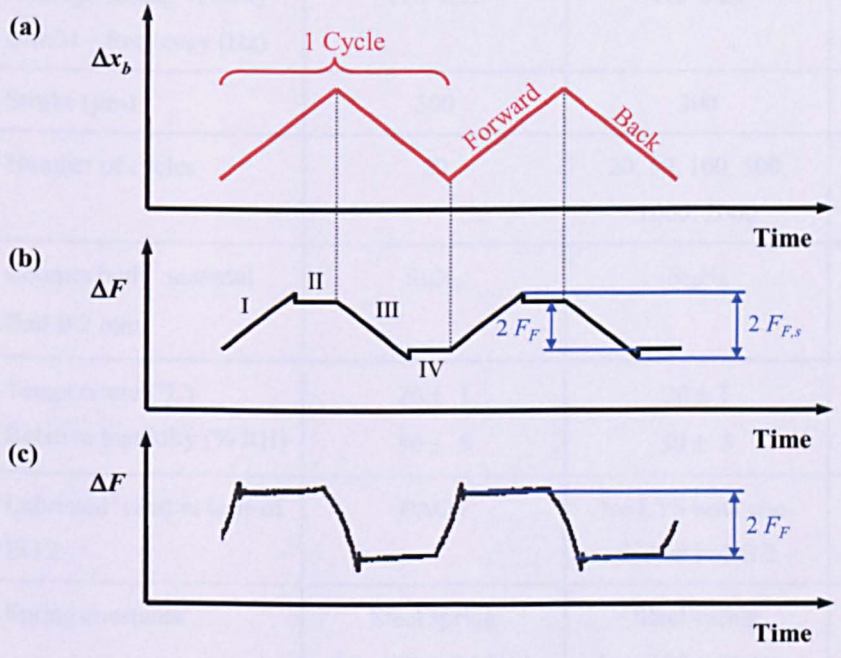

Figure 4.8: Signal of the reciprocating drive (a), and tangential (friction) force signal detected in ideal case (b) and under real conditions (c). At the boundary of range I to II, counter body and sample stick. The static force $F_{F,s}$ is defined where the first slip to lower value occurs. The dynamic friction force F_F is obtained from range II and IV. Adapted from Scherge & Gorb (2001).

4.3.2 Experiments on Friction and Wear in Unlubricated Contacts (EG 1)

In order to obtain information about the friction behaviour and wear resistance of the nanostructures with respect to the normal load applied and the duration of loading, experiments in three different test regimes were conducted (Tab. 4.4).

Table 4.4: Test conditions applied in the tribological tests of experimental group (EG) 1 and 2 to estimate the load carrying capacity (LCC), long-term stability (LTS) and frictional behaviour of nanostructured surfaces in non-lubricated or lubricated contact, respectively.

Parameter	LCC tests	LTS tests	Friction tests
Normal load (mN)	10, 25, 50, 100, 150, 200, 250	10, 50, 150	1, 3, 6, 9, 12, 15
Maximum contact pressure (MPa)[1]	for F_N = 10 mN: 253 to 403 for F_N = 250 mN: 741 to 1178	for F_N = 10 mN: 253 to 403 for F_N = 150 mN: 625 to 994	for F_N = 1 mN: 123 to 207 for F_N = 15 mN: 304 to 511
Average sliding velocity (µm/s) – frequency (Hz)	125-0.21	125-0.21	25-0.03, 300- 0.38, 500-0.63
Stroke (µm)	300	300	400
Number of cycles	20	20, 50, 100, 500, 1000, 2000	20
Counter body[2] material Ball ø 2 mm	Si_3N_4	Si_3N_4	TiC
Temperature (°C) Relative humidity (% RH)	20 ± 1 50 ± 5	20 ± 1 50 ± 5	20 ± 1 50 ± 5
Lubricant[2] used in tests of EG 2	PAO4	No LTS tests conducted in EG 2	MO4, MO40, MO96, MO200, PAO4
Spring constants[3]	Steel spring k_N = 608 ± 26 N/m k_L = 993 ± 28 N/m	Steel spring k_N = 608 ± 26 N/m k_L = 993 ± 28 N/m	Glass spring 1 k_N = 133 ± 1 N/m k_L = 33 ± 1 N/m
Number of test runs	2	2	3

[1] The calculation of the contact pressure and the values obtained for each nanostructure tested are described in Appendix A.2.

[2] Specifications of counter bodies and lubricants are given in Table 4.7 and 4.8, respectively.

[3] The spring constant was determined as described in section 4.3.1.2. The average value and the standard deviation were determined from 5 measurements.

4.3.2.1 Load-Carrying Capacity (LCC) Tests

In tests to estimate the load carrying capacity, friction and wear were analysed as function of the normal load applied on the different surfaces. To estimate the onset of detectable wear, the normal loads applied in the tests was stepwise increased from low (10 mN) to high (250 mN) values. Preliminary tests with a titanium carbide (TiC) coated steel ball as counter body had shown that material transfer from ball to sample occur without wearing-off the nanostructure even at relatively high normal loads, especially in case of crater topographies. In the literature, wear studies on hard thin films were reported, where balls made of silicon nitride (Si_3N_4) were employed without observing damage on the counter body (Achanta, Drees & Celis 2005). Therefore, Si_3N_4 ball were used in the LCC and also on long-term stability tests performed in this thesis.

The LCC tests were performed in the following way: Before testing, ball and sample were cleaned in an ultrasonic bath first in acetone, then in isopropanol and finally in ethanol, for 10 minutes each. Next, ball and sample were inserted in the microtribometer and the ball was brought in contact with the sample. Then the desired normal load was applied, and the sliding motion of the ball was initiated on the sample surface over a defined distance (stroke) and with fixed velocity for a certain number of cycles. Most of the oscillating stroke is at nominally constant speed after brief periods of acceleration, i.e. the speed profile approaches a triangular waveform. During the test, the friction force signal was continuously recorded. After the test, sample and ball were removed. The type and pattern of the wear in the contact zone was qualitatively analysed by SEM. The following test with the next higher load was performed with a new sample and ball. This approach should avoid any alterations of the counter body surface (e.g. due to wear), which might occur during the tests at high loads and, affect the measurements in the following tests. Though a new sample and new ball were used for each test, the order of the tests actually does not matter in this test series. However, some of the later described test regimes retain the ball and so should be performed from the lowest load upwards. The same procedure is adopted routinely in all test series.

4.3.2.2 Long-Term Stability (LTS) Tests

In order to analyse the long-term stability of selected nanostructures, the amount and type of wear occurring was qualitatively determined as a function of the number of cycles (test duration) for a low, medium and high normal load. The loads were chosen based on the results of the LCC tests.

The cleaning of the samples, the tribological tests and the evaluation of wear were performed according the same procedure as applied for the LCC tests.

4.3.2.3 Friction Tests

In order to measure the friction without being significantly affected by wear-related changes in surface topography or chemistry, friction force measurements were conducted as function of the applied normal load under nearly-wear free conditions. Therefore, the normal loads chosen for these tests were well below the load where the onset of observable wear (plastic deformation of asperities and shearing of deformed material) was found to occur for the different structures in the wear mapping tests.

All microtribological tests conducted in this regime follow the same procedure: The test-run was started by bringing the counter body in contact with the surface and applying the desired normal load, starting with the lowest normal load. The reciprocating motion was then initiated and maintained for 20 cycles during which time the friction force was continuously recorded. After completion, the reciprocating motion was stopped, the counter body withdrawn from the sample surface and moved to a new y-position located at 200 µm from the previous one. The test was then repeated with a higher normal load until the maximum normal load was reached. Prior to performing each test series, ball and sample were cleaned in an ultrasonic bath first in acetone, then in isopropanol and finally in ethanol, for 10 minutes each.

4.3.3 Comparison of Nanostructured Surfaces in Lubricated Contacts (EG 2)

Here, the goal of the experiments was to investigate how far nanostructuring can influence the lubrication effects, namely the reduction of friction and the minimization of wear, in the system. In order to study the lubrication efficiency of nanostructures, the results obtained when applying a lubricant needed to be compared to results determined in tests under unlubricated conditions (EG1). For this purpose, lubricated tests were conducted under conditions similar to those in EG 1 (Tab. 4.4). Hereby, the LCC tests serve mainly to estimate changes in friction and wear due to nanostructuring of lubricated contacts. In the friction tests, the correlation existing between friction force and nanostructure was analysed at various sliding velocities and for oils with different viscosities in these experiments. The friction dependence on the lubricant viscosity was studied for mineral oils. Since synthetic oils are more widely used in microsystems than mineral oils are, polyalphaolefin, an synthetic oil, was also applied in the friction tests, and chosen as lubricant in the LCC tests of EG 2.

Since the results obtained for lubricated and nonlubricated conditions are to be compared, the microtribological tests in EG 2 were conducted according to the same procedure as applied in the corresponding tests of EG 1. The only difference from the tests in EG 1 is that before a test of EG 2 was started, 2 µl of the selected oil was applied on the surface of the sample (1 x 1 cm^2) with a precision pipette and excess oil was removed from the sample surface by using a rubber blade. This method ensured that the only oil remaining on the sample was stored in surface cavities (minimum lubrication). Furthermore, it should be noted that the load-test series in the friction tests of EG 2 were performed without intermediate cleaning or renewed oil application on the sample surface.

4.3.4 Experiments on Friction of Hydrophobic and Hydrophilic Surfaces (EG 3)

As previously mentioned, the interest of research was focussed on how the size and type of nanoscaled surface features may affect the friction dependence on relative humidity and sliding velocity for hydrophilic and hydrophobic surfaces. To create surfaces with nearly identical topography but completely different surface chemistry and, thus, wetting behaviour, the

structured Cr-N thin films were covered by an additional layer. To alter the surface chemistry to be either hydrophilic or hydrophobic, a 10 nm thick SiO_2 or HFP layer were deposited on the Cr-N thin films (see section 4.1.2). Though Cr-N thin films are partly hydrophilic, they were still covered with silicon oxide to ensure that the chemical composition of all hydrophilic surfaces was the same. Otherwise, the slight compositional differences between the various Cr-N films, which were presumably negligible under the more severe conditions in EG 1 and EG 2, may influence the results at the relatively low loads applied here.

Table 4.5 shows the experimental conditions applied to investigate the influence of relative humidity (humidity tests) and sliding speed (velocity tests) on the microfrictional behaviour of the differently structured hydrophilic and hydrophobic surfaces.

For all hydrophilic and hydrophobic surfaces, the same test procedure was applied in the microtribological test conducted: Prior to each experiment, the balls were cleaned in an ultrasonic bath first in acetone, then in isopropanol and finally in ethanol, for 10 min each. Since the investigated surfaces were stored in sealed boxes immediately after being coated, the samples were just swiped with a lint-free tissue soaked in ethanol before performing the experiments. After inserting the sample, the relative humidity in the test chamber was adjusted to a defined value by using different salt solutions to obtain 30, 50, 70 or 90 % RH or silica gel to dry the air down to 10 % RH, respectively. After the defined humidity level was reached, the humidity was kept constant at this value for four hours before starting the test. The normal load was then applied. The reciprocating motion was initiated with a defined velocity for 10 cycles and the friction force was continually recorded during motion. After completion, the reciprocating motion was terminated and the counter body removed from the surface. All experiments were repeated at least three times with a new ball at new locations on the sample surface for each set of test conditions to ensure reproducibility of the results. The tests were conducted by adjusting the relative humidity going from the lowest to the highest level within a test series.

Table 4.5: Test conditions applied in the tribological experiments in EG 3.

Parameter	Humidity tests	Velocity tests
Normal load (mN)	0.2	0.2
Maximum contact pressure (MPa)	72 to 121	72 to 121
Average sliding velocity (µm/s) – frequency (Hz)	50-0.25	25-0.13, 50-0.25, 125-0.63, 300-1.5
Temperature (°C) Relative humidity (% RH)	20 ± 1 10, 30, 50, 70, 90 ± 5	20 ± 1 50 ± 5
Stroke (µm)	100	100
Number of cycles	10	10
Counter body[2] material Ball ø 2 mm	TiC	TiC
Spring constants[3]	Glass spring 2 k_N = 60 ± 3 N/m k_L = 15 ± 0.4 N/m	Glass spring 2 k_N = 60 ± 3 N/m k_L = 15 ± 0.4 N/m
Number of test runs	3	3

[1] The calculation of the contact pressure and the values obtained for each nanostructure tested are given in Appendix A.2.

[2] Specifications of counter bodies are given in Table 4.7

[3] The spring constant was determined as described in section 4.3.1.2. The average value and the standard deviation were determined from 5 measurements.

The TiC coating applied on the balls used in these tests exhibit a partly hydrophobic behaviour: the contact angles were determined to be with 58 ± 2°.

4.3.5 Investigated Surfaces

One goal of thesis was to study the influence of type and size of nanoscaled surface features on the tribological functionality, whereby the performance of the nanostrcutures should be characterised for different test conditions. Since such a detailed tribological study could not be conducted for all identified topographies within the given time frame of this thesis, three

topography types* were selected, namely a pyramid-like (P-r), crater-like (CR) and cone-like (C) structure. The types P-r and C were chosen due to the simplicity with which the size of the topographical feature can be modified in a relatively wide range. Though a more complex correlation between deposition parameter and the evolution of its topography, type CR was included in the tribological studies because surfaces with micro or nano-sized cavities have been reported to support low friction behaviour, especially in lubricated contacts (Khurshudov et al. 1997; Zhou et al. 2003; Gerbig et al. 2003; Petterson 2005).

Table 4.6 gives an overview of which topography types and how many differently-sized structures of each were studied in the individual tests. Furthermore, the references chosen in the individual testes are listed in Table 4.6.

Initially, it was planned to estimate the influence of dimensional variations on the tribological behaviour by testing three different feature sizes for each topography type. However, the understanding and interpretation of certain effects required an adaptation of the number of structured surfaces that need to be tested to confirm experimental results. For example, additional, differently-sized crater-like structured surfaces were tested in the experiments of EG 1 and EG 2 to clarify friction-topography dependence.

For the tests in EG 1 and EG 2, the tribological results obtained for the structured Cr-N surfaces were compared to the data measured on a relatively smooth Cr-N thin film, which acts as the reference surface. In contrast to EG 1 and EG 2, the material of the template chosen as reference in EG 3 is less important as long as it can provide a sufficient mechanical support for the covering layer. A polished silicon (100) wafer having an even lower roughness than the smooth Cr-N film was, therefore, used as reference surface in the tests of EG 3 after being coated with SiO_2 or HFP, respectively.

Detailed information about the topographical appearance of the different structures and references tested is included in Chapter 6 and Appendix A.3.

---

* The topography types are described in section 5.1.

Table 4.6: Investigated nanostructured surfaces in the different test series of the EGs.

EG: Test series	Tested nanostructures	Reference surface
EG 1 and EG 2: LCC tests	4 pyramid-like Cr-N structures 6 crater-like Cr-N structures 3 cone-like Cr-N structures	Smooth Cr-N film
EG 1: LTS tests	4 pyramid-like Cr-N structures 3 crater-like Cr-N structures 3 con-like Cr-N structures	Smooth Cr-N film
EG 1: Friction tests	4 pyramid-like Cr-N structures 6 crater-like Cr-N structures 3 cone-like structures	Smooth Cr-N film
EG 2: Friction tests	Tested with all lubricants: 6 crater-like structures Tested with PAO only: 4 pyramid-like structures 3 cone-like Cr-N structures	Smooth Cr-N film
EG 3: Humidity tests	4 pyramid-like Cr-N structures + HFP 3 crater-like Cr-N structures + HFP 3 cone-like Cr-N structures + HFP 4 pyramid-like Cr-N structures + SiO_2 3 crater-like Cr-N structures + SiO_2 3 cone-like Cr-N structures + SiO_2	Silicon + HFP, Silicon + SiO_2
EG 3: Velocity tests	4 pyramid-like Cr-N structures + SiO_2 3 crater-like Cr-N structures + SiO_2 3 cone-like Cr-N structures + SiO_2 4 pyramid-like Cr-N structures + HFP 3 crater-like Cr-N structures + HFP 3 cone-like Cr-N structures + HFP	Silicon + HFP, Silicon + SiO_2

4.3.6 Specification of Counter Bodies and Lubricants Used in the Tests

The counter bodies in the tribological tests were steel AISI 440C balls coated with titanium carbide (supplier: CSEM SA) and balls made of silicon nitride (supplier: Cerbec, NBD200 Grade 2C). All balls had a diameter of 2 mm. The roughness and mechanical properties of the used counter bodies are given in Table 4.7.

Table 4.7: Selected properties of the counter body used in the microtribological tests.

	Titanium carbide (TiC)	Silicon nitride (Si_3N_4)
Hardness (GPa)	35 ± 2	16 ± 1
Elastic modulus (GPa)	450	320
Poisson's ratio	0.19	0.26
Roughness S_q (nm)	2.8 ± 1	4.0 ± 1

The lubricants used in the microtribological tests were additive-free mineral oils (MO4 to MO200) and an additive-free polyalphaolefine (PAO4). Properties of the applied oils are summarized in Table 4.8.

Table 4.8: Selected properties of the lubricants used in the microtribological tests.

Lubricant	MO4	MO40	MO96	MO200	PAO4
Viscosity at 40 °C (cSt)	4	40	96	200	4
Density at 20 °C (kg/m^3)	0.912	0.919	0.915	0.913	0.909

Chapter 5

Nanostructuring of Surfaces

The ability to modify the geometric appearance and dimensions of the topographical features in a controlled manner (in-process structuring) requires more knowledge than currently exists about the relationship between deposition parameters and the topography of thin films deposited by PVD. In order to gain information about this correlation for chromium nitride thin films, in particular, the research approach was chosen as described in subsequent paragraphs.

First, deposition experiments were carried out, in which a selected set of process parameters were varied in a controlled manner and over a reasonably wide process parameter range. Next, the topographical appearance of the deposited thin films needed to be characterised, and the different topography types that could be obtained predictably were determined. Though special emphasis was placed on the topographical evolution, the microstructural development was also investigated, since the surface functionality of thin films is often restricted by their entirety of topography and microstructure. In this context, the correlation between microstructure and mechanical properties of the different topography types were studied. Then, the key deposition parameters influencing the topographical evolution were identified, and the growth conditions for each type of topography were specified. Finally, there was an investigation into how changes in the process parameters modify the dimen-

sions of the topographical features. For individual surface structures, the reproducibility of their topographical parameters and mechanical properties were evaluated.

Since the deposition experiments and the methods applied to characterise the morphology and mechanical properties of thin films have already been discussed in detail in Chapter 4, the following pages of this chapter concentrate on the morphological evolution of the deposited chromium nitride thin films with special emphasis on the development of their topography as a function of the deposition parameters.

5.1 Classification and Description of Topography Types

Six different main topography types, named Pyramid (P), Grain (G), Cone (C), Crater (CR), Ribbon (R) and Hillock (H), were identified for chromium nitride thin films. The following sections describe the morphological appearance of these types.

5.1.1 Topography Type P (Pyramid)

Type P has pyramid-like surface features, which are caused by V-shaped columns with three-sided, faceted points. SEM and TEM analysis (Fig. 5.1 to 5.4) revealed that the films have a relatively porous microstructure with both, inter- and intra-columnar voids, creating a pronounced dendritic pattern. The crystallites of the columns grow at a certain angle around an axis mostly perpendicular to the substrate surface. With respect to geometry and arrangement of the pyramidal surface features, this topography type can be divided into further subtypes (see below).

The electron diffraction patterns (DP) from all topography P subtypes (see Fig. 5.1 to 5.4) reveal a pronounced spot-pattern, confirming that the grains are rather large and grow in a preferential crystallographic orientation (Era et al. 2005). In order to determine a preferential crystallographic orientation (see also section 2.2.3), the texture coefficients, determined for various films of different subtypes according to equation (4.6), are given in Table 5.1. The crystallographic orientation having the highest texture coefficient represents the preferential orientation of the grains in the films, whereby a texture coefficient equal to unity corre-

sponds to randomly oriented grains (Chalker 1991). As the results indicate, films with topography type P consist of CrN crystallites in which (111) planes are preferentially orientated parallel to the substrate surface. The average crystallite size is 10 to 30 nm for films deposited at $T/T_m = 0.10$, or 20 to 50 nm for higher temperatures.

Table 5.1: Crystallographic texture coefficient for the CrN(111), (200) and (220) crystal planes (parallel to the substrate surface) for films of different subtypes of topography type P and topography type G. The table shows the texture coefficients of the samples presented in the SEM and TEM images.

Orientation	P-r	P-f	P-m	P-s	G
CrN(111)	(111) was the only orientation present in films	2.84	2.02	1.79	0.40
CrN(200)		0.50	0.58	0.75	1.83
CrN(220)		0.27	0.41	0.47	0.77

The subtype P-h is not mentioned separately in this table since it is a particular case of P-f, occurring under very special deposition conditions. Furthermore, P-h is similar to P-f with respect to the crystallographic structure, as analysed by XRD.

5.1.1.1 Subtype P-r (Regular Pyramids)

The morphological appearance of subtype P-r is shown in SEM, TEM and DP images of Figure 5.1. The surface features of type P-r are tetrahedral pyramids with the points placed slightly eccentric to the centre point of their theoretical base plane. The crystallite length of the dendrites decreases continuously towards the top of the column. Usually, each column evolves from a separate nucleation site.

5.1.1.2 Subtype P-f (Fractured Pyramids)

To illustrate the morphology of films belonging to subtype P-f, typical SEM, TEM and DP images are given in Figure 5.2. As in subtype P-r, the points of the tetrahedra are placed slightly eccentric to the centre point of their base plane, but the pyramid sides appear fractured. This might be caused by the splitting of a column into several sub-columns. The orien-

tation of the dendrites to the column axis is slightly misaligned between the newly created sub-columns. The general coarser appearance of the pyramid sides results from a non-proportional length growth of dendrites (dendrite lengths) along certain zones of the column axis.

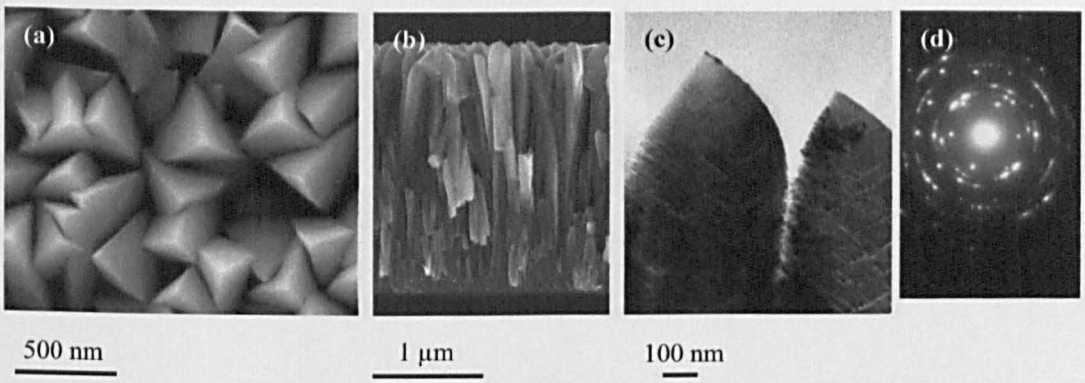

Figure 5.1: Morphological appearance of subtype P-r: (a) SEM micrograph of the topographical features (top view), (b) SEM micrograph of the cleaved cross-section of the film, (c) TEM-bright field (BF) micrograph of column tops, (d) Diffraction pattern (DP) taken by TEM.

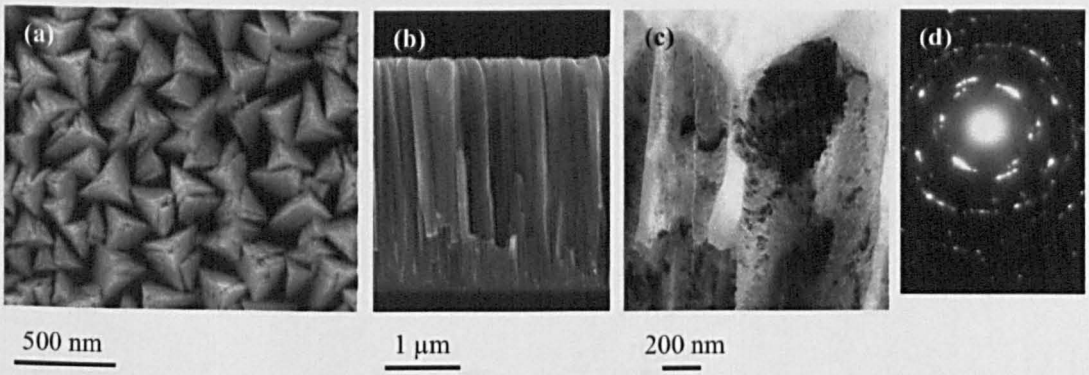

Figure 5.2: Morphological appearance of subtype P-f: (a) SEM micrograph of the topographical features (top view), (b) SEM micrograph of the cleaved cross-section of the film, (c) BF micrograph (TEM) of column tops, (d) DP (TEM).

5.1.1.3 Subtype P-s (Stacked Pyramids)

SEM, TEM and DP images of a representative film with topography type P-s are given in Figure 5.3. These surface features are formed from stacks of pyramids. Here, one side of the pyramid is oriented perpendicular to the base plane. The pyramids seem to penetrate each

other at the edge between the two other (non-perpendicular) planes. These stacks are created by bundles of columns, which start from the same nucleation site and then separate after reaching a certain length (film thickness). Again, the crystallites of the dendrites become shorter towards the top of the column.

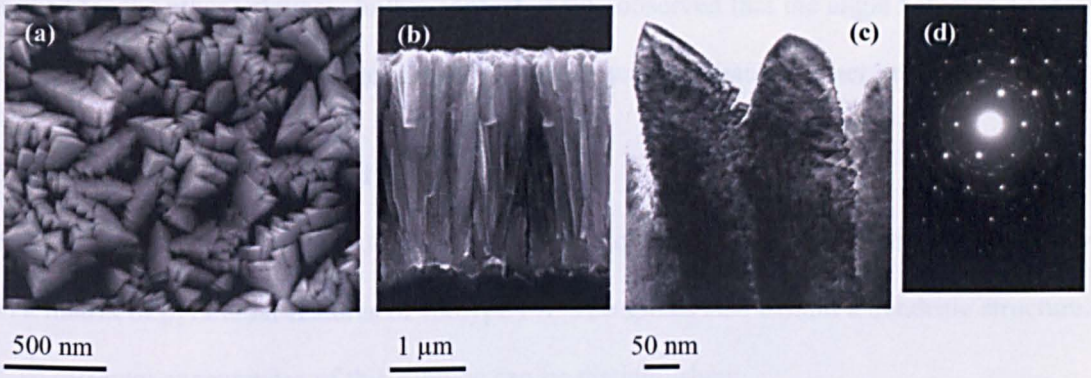

Figure 5.3: Morphological appearance of subtype P-s: (a) SEM micrograph of the topographical features (top view), (b) SEM micrograph of the cleaved cross-section of the film, (c) BF micrograph (TEM) of column tops, (d) DP (TEM).

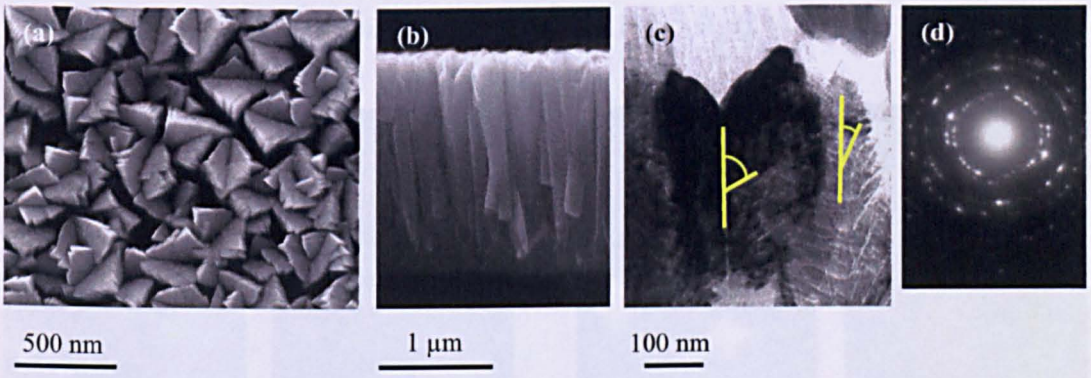

Figure 5.4: Morphological appearance of subtype P-m: (a) SEM micrograph of the topographical features (top view), (b) SEM micrograph of the cleaved cross-section of the film, (c) BF micrograph (TEM) of column tops, (d) DP (TEM).

5.1.1.4 Subtype P-m (Mirrored Pyramids)

The analysis of SEM, TEM and DP images in Figure 5.4 reveals that the appearance of this subtype is characterised by "mirrored" pyramids. In this arrangement, one edge formed between two planes is oriented perpendicularly to the base plane and, thus, the normal through

the point of the pyramid and this edge are in line. Two pyramids are connected (mirrored) to each other along the base line of the side opposite to the perpendicularly oriented edge. The impression of a pair of mirrored pyramids is created since the lengths of the crystallites growing along the grain axis do not change significantly towards the column top, as observed for the other subtypes. In this context, it was observed that the angle between crystallites and the column axis is larger for the mirrored pyramids than for other grains (Fig. 5.4c).

5.1.1.5 Subtype P-h (Hybrid Pyramids)

Here, octahedral grains (spikes) with larger dimensions in height and diameter grow locally in a matrix of pyramidal features of subtype P-f. The spikes also exhibit a dendritic structure. Two different appearances of this subtype can be distinguished:

- P-h(I): The ratio of the length of spikes to the length of the matrix grains is ≥ 3. The spikes cover 80 to 90 % of the total coated area (Fig. 5.5a,b).
- P-h(II): The ratio of the length of spikes to the length of the matrix grains is no more than 1.5. The density of spikes is at most 60 % (Fig. 5.5c,d).

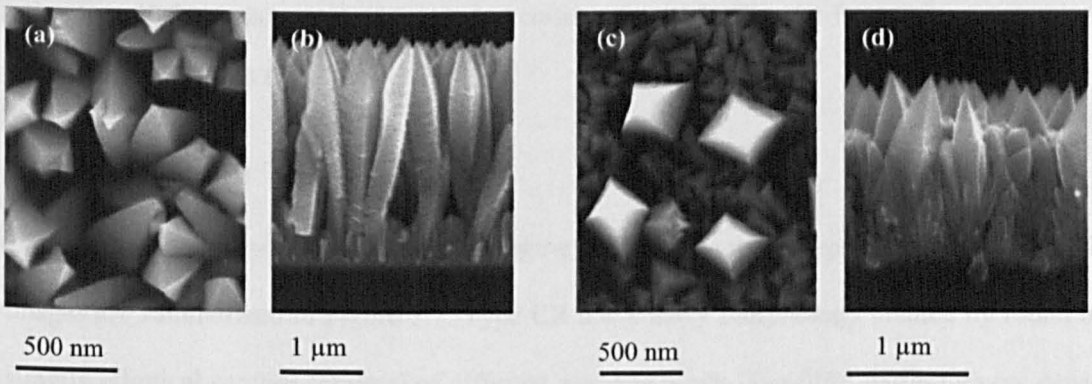

Figure 5.5: SEM micrographs of the morphological appearance of subtype P-h: (a) Top view of P-h(I), (b) Cleaved cross-section of P-h(I), (c) Top view of P-h(II), (d) Cleaved cross-section of P-h(II).

5.1.2 Topography Type G (Grain)

Figure 5.6 depicts SEM, TEM and DP images of a film with type G topography. The surface exhibits a bumpy topography created by small, elliptical surface features. The microstructure is characterised by close-packed, slightly V-shaped columns with rounded tops and separated

by dense grain boundaries. The structure of the single columns as well as of the whole film appears denser than that of topography type P. In comparison to the DP of the type P films, the spots are less pronounced in the DP of films belonging to type G. In other words, the grains are smaller but still grow in a preferential crystallographic orientation. Corresponding to that result, the XRD analysis showed that the films grows preferentially in a (200) or (220) crystallographic orientation parallel to the substrate surface. Table 5.1 (page 84) includes the results of the texture analysis for one typical sample. The size of CrN crystallites slightly decreased to 10 to 20 nm.

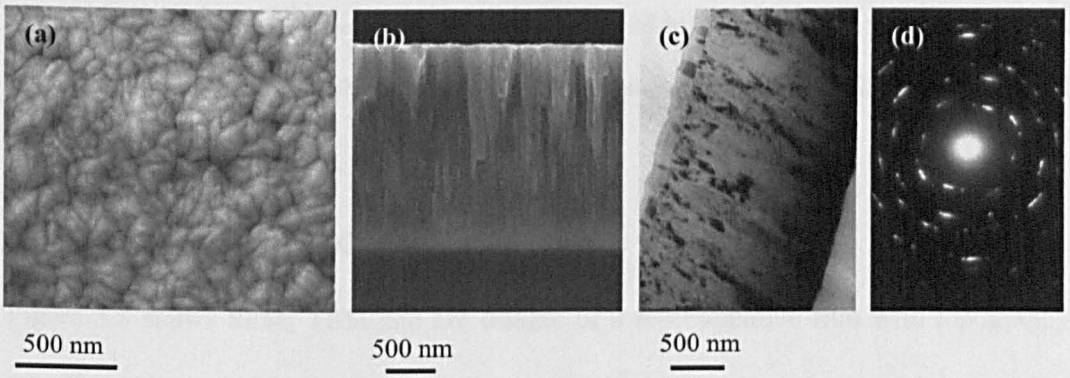

Figure 5.6: Morphological appearance of type G: (a) SEM micrograph of the topographical features (top view), (b) SEM micrograph of the cleaved cross-section of the film, (c) TEM (BF) micrograph of cross-section, (d) DP (TEM).

5.1.3 Topography Type CR (Crater)

To illustrate the morphology of films belonging to this topography type, SEM, TEM and DP images are summarized in Figure 5.7. Type CR has a wavy morphology created by round or slightly elliptical cavities (craters) of different size and depth. The films exhibit a very dense but still columnar structure. Different to films of topography P and G, the DP becomes more diffuse and starts to form a ring pattern. That means that the grains become fine and are more randomly oriented (Era et al. 2005). This result was confirmed by the XRD analysis, where a preferred crystallographic orientation of the films was no longer found. The texture coefficients of the different crystallographic phases and orientations are close to unity (T ~ 0.89 to

1.01). The films with crater-like morphology grow as mixtures of CrN and Cr_2N crystals with crystallite size varying from 5 to 15 nm.

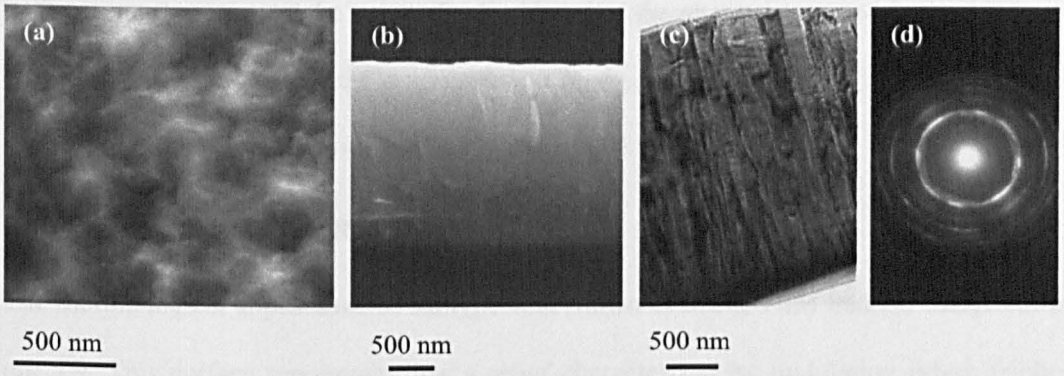

Figure 5.7: Morphological appearance of type CR: (a) SEM micrograph of the topographical features (top view), (b) SEM micrograph of the cleaved cross-section of the film, (c) TEM (BF) micrograph of cross-section, (d) DP (TEM).

5.1.4 Topography Type C (Cone)

Figure 5.8 shows SEM, TEM and DP images of a representative film with topography of type C.

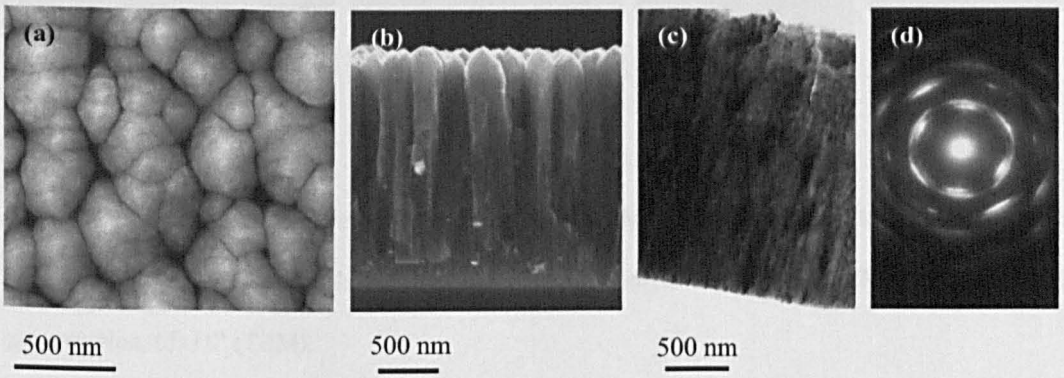

Figure 5.8: Morphological appearance of type C: (a) SEM micrograph of the topographical features (top view), (b) SEM micrograph of the cleaved cross-section of the film, (c) TEM (BF) micrograph of cross-section, (d) DP (TEM).

The films of this type are characterised by a spiky topography due to tightly packed columns with cones as tops. The cones have apex angles of 70 to 80°. The columns are separated by dense boundaries. The columns themselves seem to be bundles of small Cr_2N and CrN crystallites, which have a rather small size of about 5 to 15 nm. Usually, nanocrystalline films

produce halo-like DP patterns. Different to this, a diffuse, but still recognizable spot-pattern was observed in case of the films of type C, which suggests still relatively strong alignment in the textural growth of the small-sized grains. For the phases presented in the XRD spectrum, texture coefficients were determined to be $T_{Cr2N(300)} = 1.41$ for $Cr_2N(300)$, $T_{CrN(220)} = 0.68$ for CrN(220) and $T_{Cr2N(200)} = 0.61$ for $Cr_2N(200)$.

5.1.5 Topography Type R (Ribbon)

The morphological appearance of subtype R is shown in SEM, TEM and DP images of Figure 5.9. This surface topography has a relief characterized by undulating ridges (ribbons) bordered by shallow depressions. The ridges exhibit a substructure of small, dispersed hemispheres. The microstructure appears fibrous. The XRD analysis and the ring-like reflections in DP indicate the growth of randomly oriented Cr_2N crystals of small sizes (5 to 15 nm).

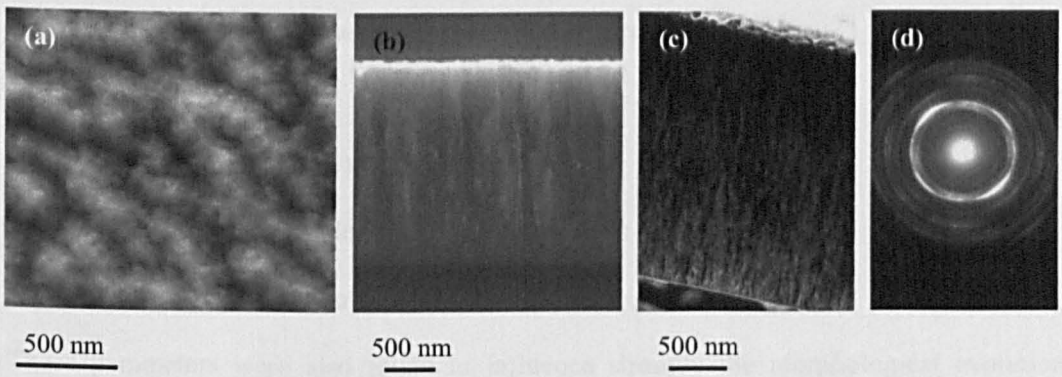

Figure 5.9: Morphological appearance of type R: (a) SEM micrograph of the topographical features (top view), (b) SEM micrograph of the cleaved cross-section of the film, (c) TEM (BF) micrograph of cross-section, (d) DP (TEM).

5.1.6 Topography Type H (Hillock)

The SEM, TEM and DP images in Figure 5.10 reveal the surface features of morphology type H as showing circular to elliptical hillocks. The microstructure of type H has fibrous appearance and consists of randomly oriented Cr_2N nanocrystals (size: 3 to 10 nm).

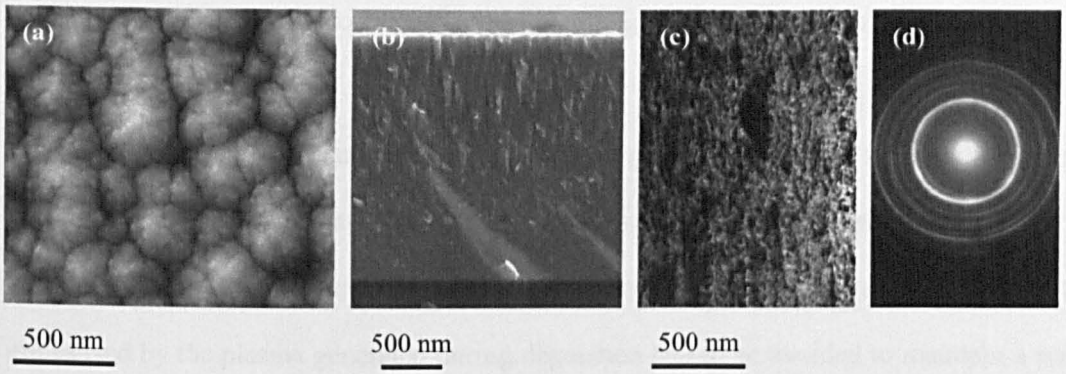

Figure 5.10: Morphological appearance of type H: (a) SEM micrograph of the topographical features (top view), (b) SEM micrograph of the cleaved cross-section of the film, (c) TEM (BF) micrograph of cross-section, (d) DP (TEM).

5.2 Growth Conditions for Topography Types

Preliminary classification of the topography types against deposition parameters indicated that the major ones (i.e. those showing consistent correlation) were:

- Substrate temperature
- Bias voltage (ion energy)
- Deposition rate, calculated according to equation (4.4)
- Ratio of inert gas flow to reactive gas flow (Ar/N_2 ratio).

These parameters were also found to influence strongly the morphological evolution of chromium nitride thin films in other studies, e.g. Hurkmans et al. (1999); Nam, Jung & Han (2000) and Xu, Umehara & Kojima (2002).

Following common usage found in literature (Movchan & Demchishin 1969; Thornton 1977; Messier, Giri & Roy 1984; Musil et al. 1990; Kelly &Arnell 1998; Barna & Adamik 1998), the homologous temperature T/T_m (T_m is the melting temperature of the deposit) is considered instead of the substrate temperature T in the rest of this work. Because the process parameters vary over a wide range, the films obtained can consist of Cr_2N, CrN or mixed phases. Based on data reported in literature (Atzor 1989; Toth 1971), the melting temperature appears to be similar for Cr_2N and CrN and is taken to be T_m = 1500 °C. Hence, the de-

deposition experiments were carried out at homologous temperatures of T/T_m = 0.10, 0.17, 0.23 or 0.30, respectively.

Figure 5.11 shows the occurrence of the defined topography types as function of the bias voltage U_b and deposition rate a_d for different Ar/N_2 ratios and temperatures T/T_m. Since the deposition chamber is not equipped with a cooling system for the substrates, excessive heating caused by the plasma generated during deposition had to be avoided to maintain a stable temperature during the process. Hence, the deposition parameters that influence the plasma generation could only be varied in a limited range, especially in the experiments at low temperatures. The area coloured in grey in the U_b-a_d charts indicate the range of the parameters a_d and U_b investigated in this study. The lines in the charts indicate where the transition between two different topography types might occur based on the observations in the experiments. For reasons of simplicity, a sharp transition is assumed in this model whereas a gradual change between topography types (a transition zone) is more likely to be expected in reality and was also directly observed in a few cases. Figure 5.11 represents an empirical topography-zone model for selecting parameters to generate specific topography types. In the following sections, the growth conditions for creating different topography types of Cr-N thin films are discussed according to this model.

5.2.1 Topography Type P

Generally, coatings with type P topography can be grown at low bias voltage and low to medium deposition rates. At homologous temperatures T/T_m of 0.10 and 0.17, the maximum bias voltage applicable is -85 V. When increasing the homologous temperature to 0.23, the transition voltage ($U_{b,t}$) drops very slightly down to -75 V and remains at this value also for a higher temperatures. The transition deposition rate ($a_{d,t}$) is hardly influenced by the applied bias voltage at $T/T_m \geq 0.23$. For voltages in the range of -50 V to -75 V, $a_{d,t}$ decreases marginally from 1.2 µm/h to 1.1 µm/h.

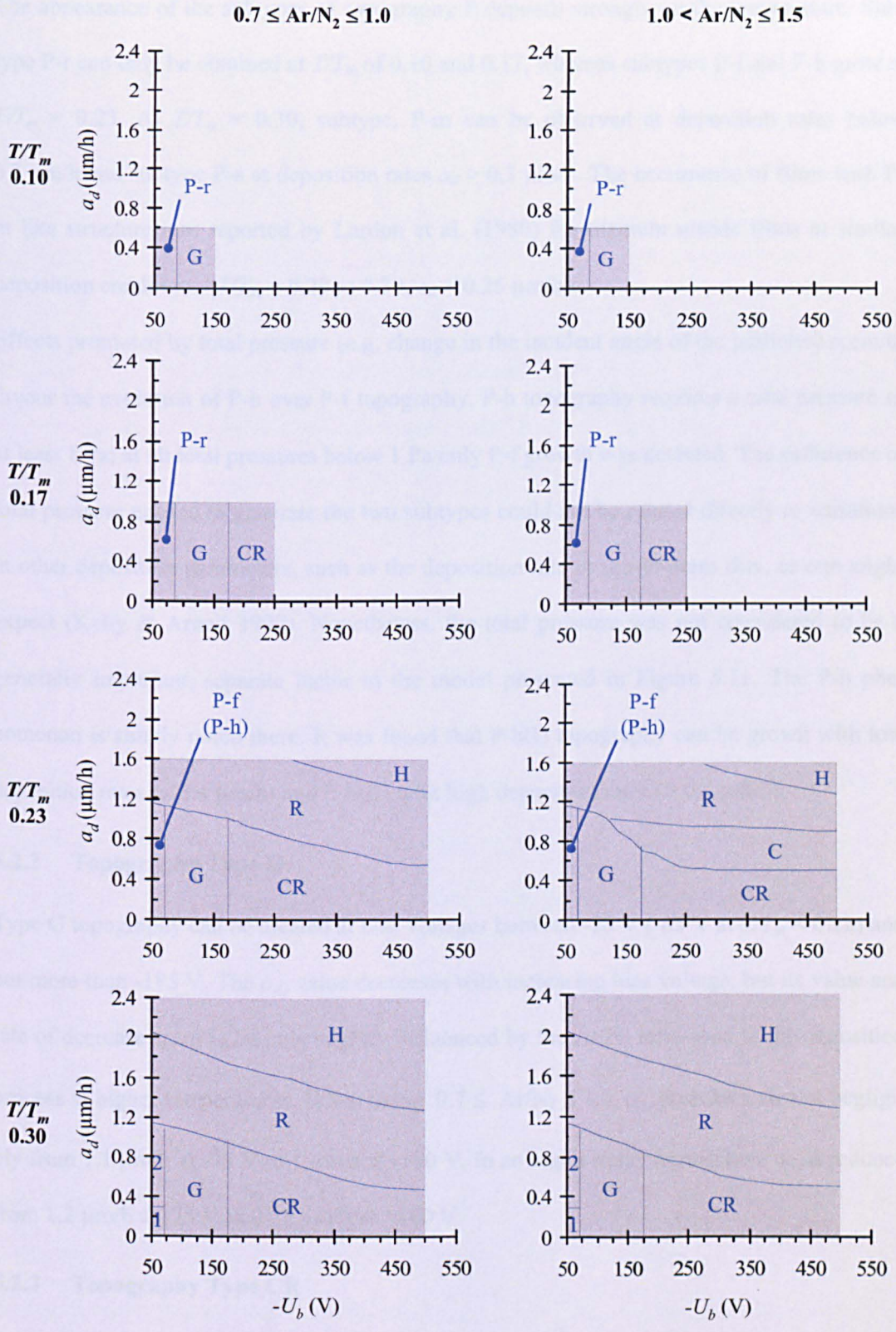

Figure 5.11: Topography-zone model for Cr-N thin films (deposited by UBM sputtering) indicating the occurrence of the different topography types as function of Ar/N_2 ratio, homologous temperature T/T_m, bias voltage U_b and deposition rate a_d (1… P-m, 2…P-s).

The appearance of the subtypes of topography P depends strongly on the temperature. Subtype P-r can only be obtained at T/T_m of 0.10 and 0.17, whereas subtypes P-f and P-h grow at T/T_m = 0.23. At T/T_m = 0.30, subtype, P-m can be observed at deposition rates below 0.3 µm/h and subtype P-s at deposition rates a_d > 0.3 µm/h. The occurrence of films with P-m like structure was reported by Lardon et al. (1980) for titanium nitride films at similar deposition conditions (T/T_m = 0.20 to 0.30, a_d > 0.25 µm/h).

Effects promoted by total pressure (e.g. change in the incident angle of the particles) seem to favour the evolution of P-h over P-f topography. P-h topography requires a total pressure of at least 1 Pa; at all total pressures below 1 Pa only P-f growth was detected. The difference in total pressure needed to generate the two subtypes could not be related directly to variations in other deposition parameters, such as the deposition rate or ion-to-atom flux, as one might expect (Kelly & Arnell 1997). Nonetheless, the total pressure was not considered to be a generally important, separate factor in the model presented in Figure 5.11. The P-h phenomenon is simply noted there. It was found that P-h(I) topography can be grown with low deposition rates (≤ 0.4 µm/h) and P-h(II) with high deposition rates (> 0.4 µm/h).

5.2.2 Topography Type G

Type G topography can be created at bias voltages between -75 V (-85 V at T/T_m < 0.23) and not more than -185 V. The $a_{d,t}$ value decreases with increasing bias voltage, but its value and rate of decrease seem to be only slightly influenced by the Ar/N_2 ratio used in the deposition process at higher temperatures. When using $0.7 \leq Ar/N_2 \leq 1.0$, $a_{d,t}$ decreases almost negligibly from 1.1 µm/h at -75 V to 1 µm/h at -180 V. In an argon richer atmosphere $a_{d,t}$ is reduced from 1.2 µm/h at -75 V to 0.75 µm/h at -180 V.

5.2.3 Topography Type CR

Coatings with crater-like topography can be obtained in the medium to high bias range (U_b > -175 V) at low to medium deposition rates at temperatures of T/T_m > 0.17. Again, it was found that the $a_{d,t}$ value is a function of the applied bias voltage and is also influenced by

the Ar/N_2 ratio. When increasing the bias from -175 V to -500 V, the $a_{d,t}$ value drops from 1.0 µm/h to 0.5 µm/h for $0.7 \leq Ar/N_2$ ratio ≤ 1.0 and from 0.75 µm/h to 0.5 µm/h for $1.0 \leq Ar/N_2$ ratio ≤ 1.5.

5.2.4 Topography Type C

Coatings with topography of type C can be obtained only under a restricted range of intermediate conditions. The occurrence of this topography type was only observed for one temperatures $T/T_m = 0.23$, in an atmosphere with an Ar/N_2 ratio above 1.0 under the condition that the a_d and U_b values fall within a zone located between 1.0 µm/h at -125 V, 0.9 µm/h and 0.5 µm/h, both at -500 V.

5.2.5 Topography Type R

Topography type R appears over the whole bias voltage range investigated when the deposition rate is chosen appropriately and the homologous temperature $T/T_m > 0.17$. The a_d value should be located within the zone stretching between 1.2 µm/h to 2.1 µm/h (1.6 µm/h for $T/T_m = 0.23$) at -50 V, gradually declining to between 0.5 µm/h, and 1.3 µm/h at -500 V. An exception is seen when depositions are carried out at $T/T_m = 0.23$ and $1.0 \leq Ar/N_2 \leq 1.5$. Here, the parameter window for type R narrows at higher bias voltages to between 0.9 µm/h and 1.3 µm/h at -500 V.

5.2.6 Topography Type H

To achieve a type H topography, the deposition rate must be above a certain $a_{d,t}$ value which is a function of the applied bias voltage. Due to the limited parameter range at $T/T_m = 0.23$, type H can be obtained only in a bias voltage range from -300 V to -500 V, whereby $a_{d,t}$ decrease from 1.6 µm/h to 1.3 µm/h when increasing the bias voltage. At $T/T_m = 0.30$, the threshold value increases from 1.3 µm/h to 2.1 µm/h on decreasing the bias voltage from -500 V to -50 V.

5.3 Size Modification of Topographical Features

To estimate the alteration of the feature size induced by controlled variations in the deposition process, topographical parameters were specified to describe the geometrical shape of the surface features sufficiently precisely, but also in a simple manner. Therefore, the height H_x and a lateral dimension L_x were selected for the topography types P, G, C, R and H. The definition of the lateral dimension L_x is shown for each of those topography types and the subtype P-h in Figure 5.12a to f. The height H_x of a surface features of type P, G and C was defined as the distance d from the tip of column to the point where the width $w_c(d)$ of the column does not increase further ($w_c(d = H_p) = w_{c,\,max}$), as illustrated for a column with pyramidal surface feature in Fig. 5.12g. In the case of topography types R and H (non-columnar microstructure), the feature height was measured from the tip of the feature to the point where the feature emerge from the underlying bulk material of the film (Fig. 5.12h).

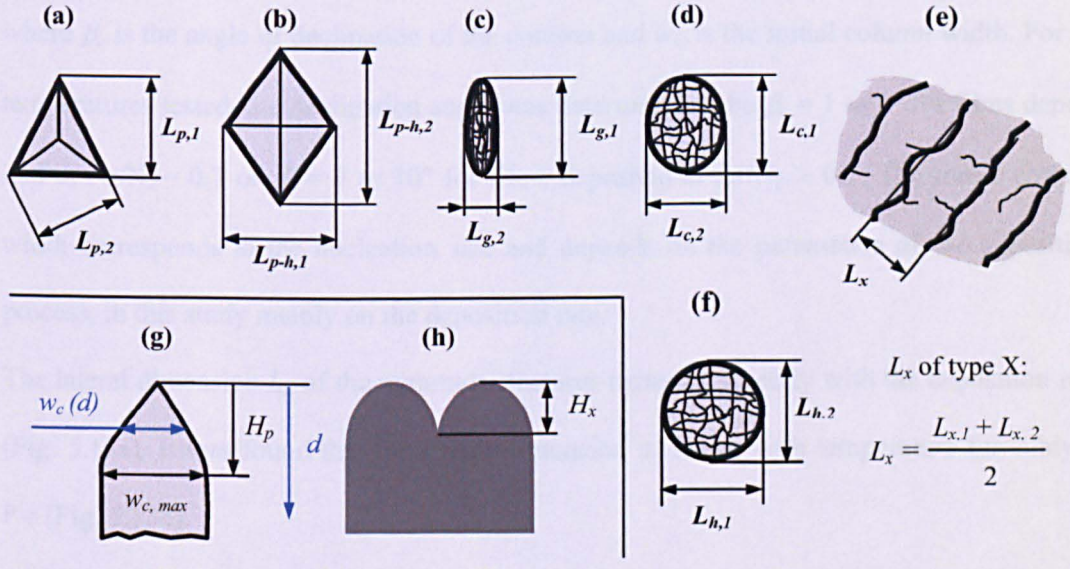

Figure 5.12: Definition of the topographical dimension L_x of the surface features of (a) type P (general), (b) subtype P-h (spike), (c) type G, (d) type C, (e) type R and (f) type H. The determination of the feature height H_x is shown for the topography types P, G and C in (g) and for the types R and H in (h).

The topographical evolution of type CR was quantitatively analysed by determining various parameters (root mean square roughness S_q, skewness S_{sk}, kurtosis S_{ku}, dominant wavelength

λ and the fractal dimension D), since the features of this topography type are less homogenous in shape, size and distribution and, thus, geometrical-simple shapes cannot precisely describe them.

5.3.1 Topography Type P

Since the bias voltage changes only marginally (-50 V to -75 V) in the parameter field of topography type P, the influence of this parameter is assumed to be negligible and, thus, not considered further.

5.3.1.1 Topography Subtypes P-r, P-f, P-s and P-m

Since films of topography type P exhibit V-shaped columnar growth, the width of the pyramidal features w_p can be adjusted over the column length (film thickness t_f)

$$w_p = 2 \cdot \sin \beta_c \cdot t_f + w_{ci} \tag{6.1}$$

where β_c is the angle of declination of the column and w_{ci} is the initial column width. For all temperatures tested, the declination angle was determined to be β_c = 1 to 3° for films deposited at $Ar/N_2 = 0.7$ or β_c = 7 to 10° for films deposited at $Ar/N_2 > 0.7$. The initial column width corresponds to the nucleation size and depends on the parameters of the deposition process, in this study mainly on the deposition rate.

The lateral dimension L_p of the pyramidal features increases linearly with the deposition rate (Fig. 5.13a). It was found that the lateral dimension increases with temperature for subtype P-r (Fig. 5.13b).

The pyramid height increases linearly with the column width (Fig. 5.14). The apex angle of the pyramids remains relatively constant between 60° and 70° for different deposition parameters. The influence of temperature on the lateral dimension could not be investigated for the other subtypes because they occurred at only one investigated temperature (see Fig. 5.11).

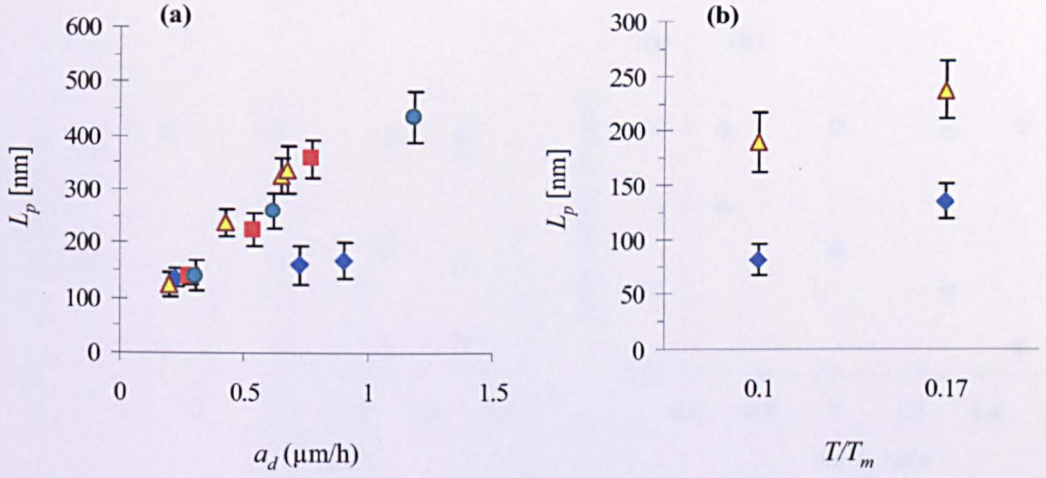

Figure 5.13: Lateral dimension L_p as function of: (a) deposition rate a_d at homologous temperature T/T_m = 0.20 and Ar/N_2 ratios of 0.7 (◆), 1.0 (■),1.3 (●) and 1.5 (△) for subtypes P-r, P-m, P-s, P-f; (b) homologous T/T_m at a Ar/N_2 ratios of 0.7 (◆) and 1.5 (△) for subtype P-r. The bias voltage was set at U_b = -50 V in all experiments.

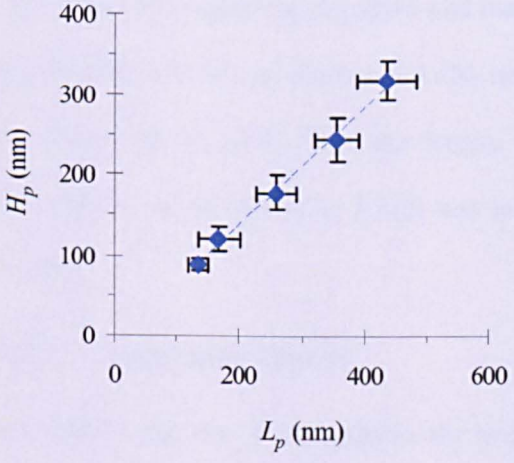

Figure 5.14: Correlation between lateral dimension L_p and height H_p of the surface features of topography type P.

5.3.1.2 Subtype P-h

For this subtype, Ar/N_2 ratio and sputter power (deposition rate) are the only parameters that could be changed to modify the size or density of the spikes. A change in the sputter power modifies the appearance from P-h(I) at deposition rates ≤ 0.4 µm/h to P-h(II) at higher deposition rates, as mentioned earlier.

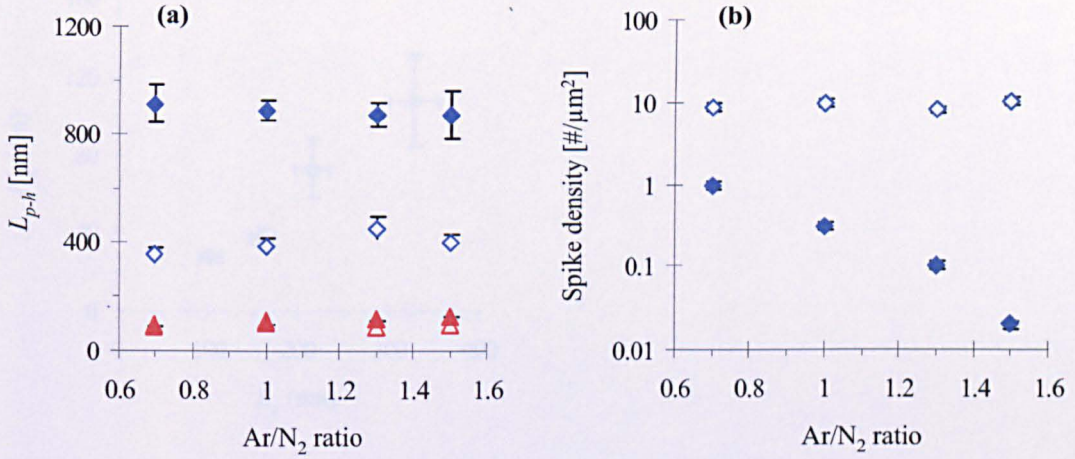

Figure 5.15: Evolution of the topographical features of type P-h as function of Ar/N_2 ratio. (a) Lateral dimension $L_{p\text{-}h}$ of matrix grains of P-h(I) (△) and P-h(II) (▲) and spikes of P-h(I) (◇) and P-h(II) (◆), (b) Spike density for P-h(I) (◇) and P-h(II) (◆), The homologous temperature and the bias voltage were fixed at $T/T_m = 0.23$ or $U_b = -75$ V, respectively.

The lateral dimensions of the spike and matrix grains of subtypes P-h(I) and P-h(II) are not significantly affected by change in Ar/N_2 ratio (Fig. 5.15a).

By increasing the Ar/N_2 ratio, the density of the spikes of subtype P-h(II) can be reduced. The density of the spikes in P-h(I) was not affected by changing the gas flow ratio (Fig. 5.15b).

5.3.2 Topography Type G

As seen for the type P topography, the height of the surface features increase linearly with their lateral dimension (Fig. 5.16).

It appears that the temperature and the Ar/N_2 ratio do not influence significantly the growth of the topographical features (Fig. 5.17a, b). The lateral dimension of the topographical features depends mainly on bias voltage and deposition rate (Fig. 5.17c, d). On increasing the bias voltages, the size of the topographical features decreases, whereas the features expand on increasing the deposition rate.

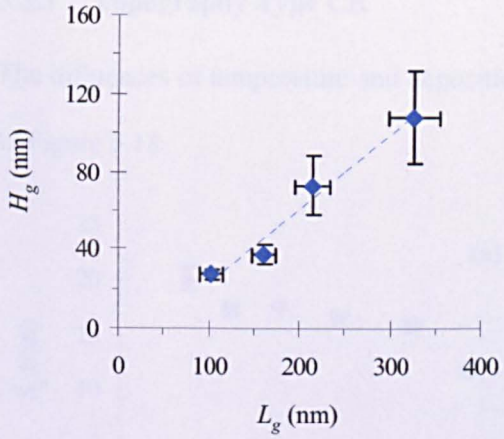

Figure 5.16: Correlation between lateral dimension L_g and height H_g of the surface feature for topography type G.

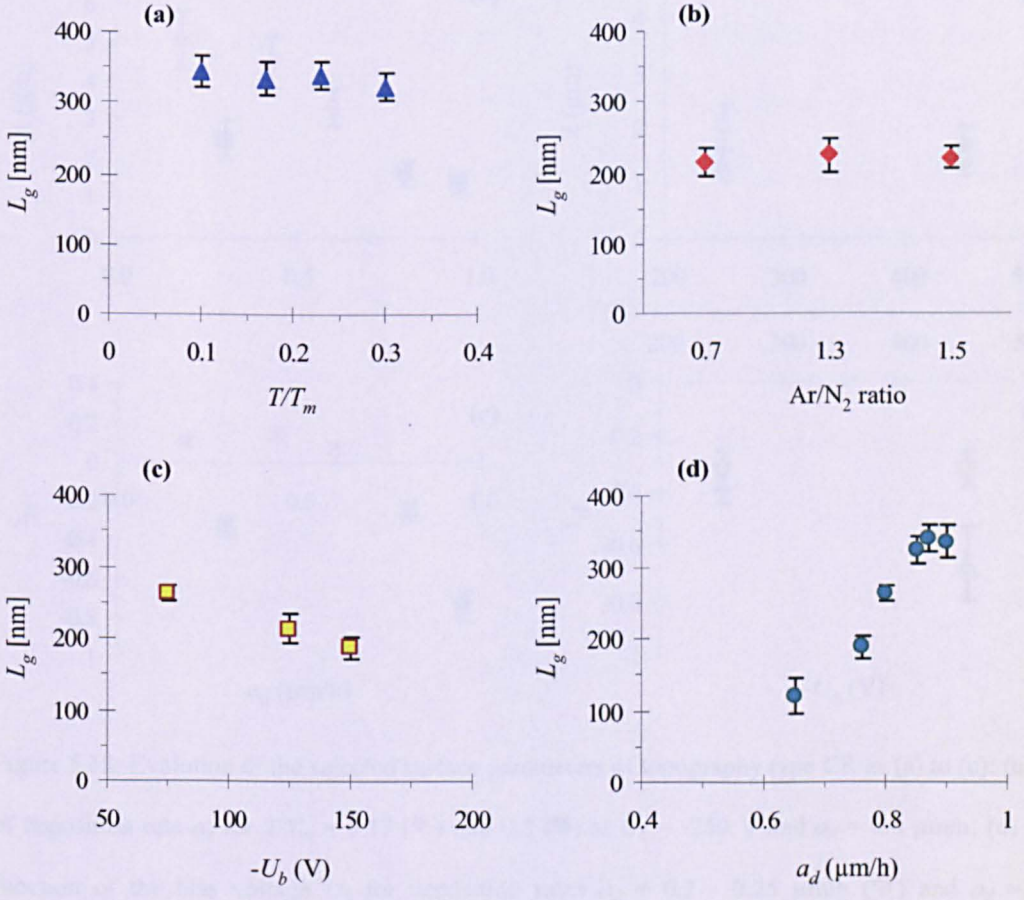

Figure 5.17: Evolution of the morphological features of type G as function of: (a) homologous temperature T/T_m (Ar/N$_2$ = 1.3, U_b = – 75 V, a_d = 0.85 - 0.9 µm/h), (b) Ar/N$_2$ ratio (T/T_m = 0.1, U_b = -125 V, a_d = 0.3 µm/h), (c) bias voltage U_b (T/T_m = 0.23, Ar/N$_2$ = 1.3, a_d = 0.75 - 0.8 µm/h), (d) deposition rate a_d at bias voltages of U_b of -75 V (T/T_m = 0.23, Ar/N$_2$ = 1.3).

5.3.3 Topography Type CR

The influences of temperature and deposition rate on the topographical parameters are shown in Figure 5.18.

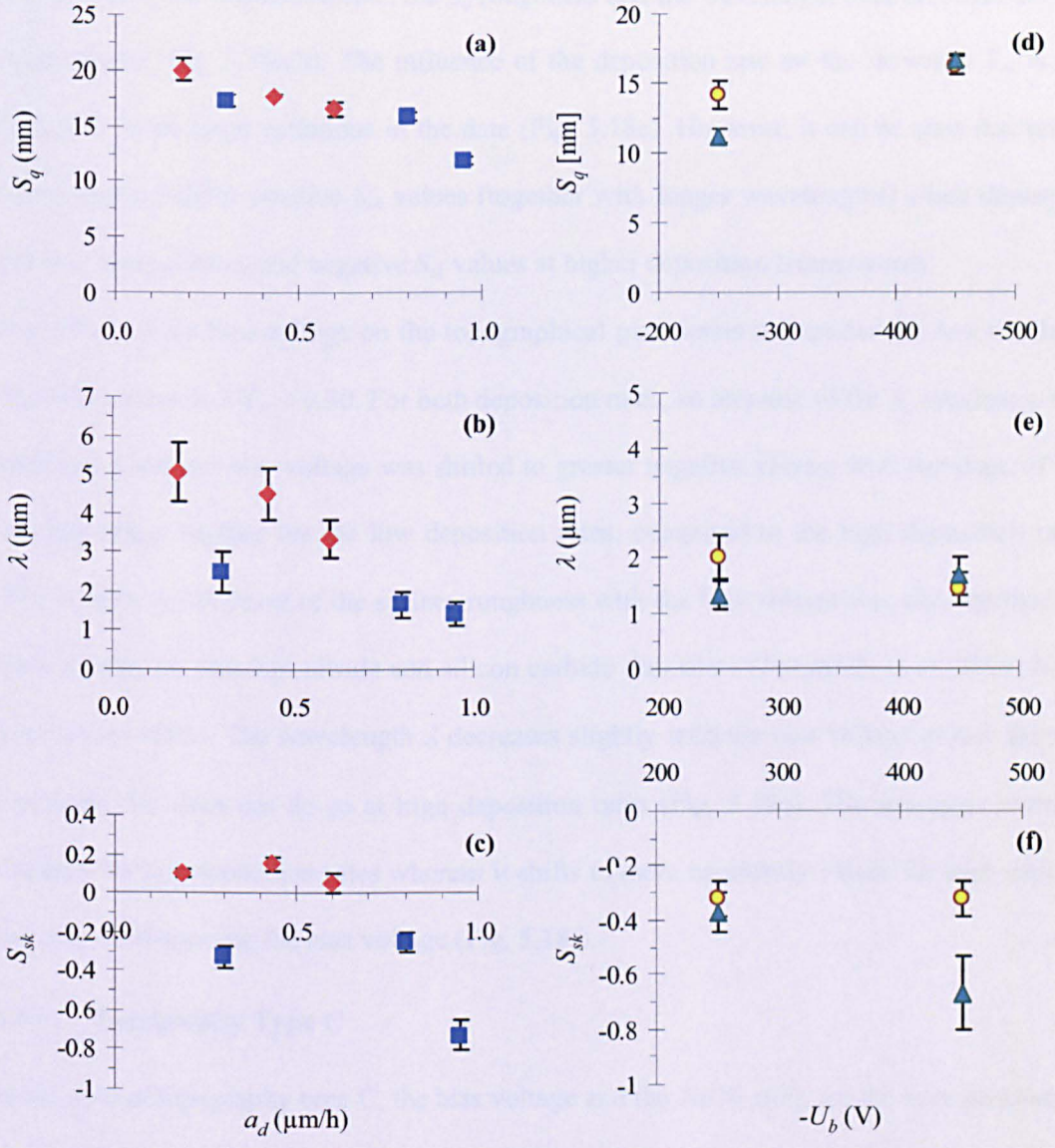

Figure 5.18: Evolution of the selected surface parameters of topography type CR as (a) to (c): function of deposition rate a_d for T/T_m = 0.17 (◆) and 0.3 (■) at U_b = -250 V and a_d = 0.6 µm/h; (d) to (f): function of the bias voltage U_b for deposition rates a_d = 0.2 - 0.25 µm/h (●) and a_d = 0.5 - 0.6 µm/h (▲) at T/T_m = 0.30. The gas flow ratio was fixed at Ar/N_2 = 1.3.

The variations in kurtosis S_{ku} (S_{ku} = 2.8 to 3.6) and fractal dimension D (D = 1.70 to 1.80) across these films are relatively small and, therefore, these surface parameters were not considered further here.

On increasing the deposition rate, the S_q roughness and the wavelength both decrease at both temperatures (Fig. 5.18a,b). The influence of the deposition rate on the skewness S_{sk} is not clear due to the large variations in the data (Fig. 5.18c). However, it can be seen that crater topographies exhibit positive S_{sk} values (together with longer wavelengths) when deposited at lower temperatures and negative S_{sk} values at higher deposition temperatures.

The effect of the bias voltage on the topographical parameters is depicted for low and high deposition rates at T/T_m = 0.30. For both deposition rates, an increase of the S_q roughness was observed when the bias voltage was shifted to greater negative values; with the slope of the increase being smaller for the low deposition rates, compared to the high deposition rates (Fig. 5.18d). An increase of the surface roughness with the bias voltage was also reported by other groups for titanium nitride and silicon carbide thin films (Takahashi et al. 2000; Kim, Kim & Lee 2003). The wavelength λ decreases slightly with the bias voltage at low deposition rates, but does not do so at high deposition rates (Fig. 5.18e). The skewness remains constant for low deposition rates whereas it shifts to more negatively values for high deposition rate on increasing the bias voltage (Fig. 5.18f).

5.3.4 Topography Type C

In the case of topography type C, the bias voltage and the Ar/N_2 ratio are the only parameters that can be freely changed. On increasing the bias voltage, the diameter of the conical features increases in an inverse exponential form and asymptotically approaches a maximum value of about 550 nm (Fig. 5.19). The lateral dimension of the conical features remains nearly constant when raising the Ar/N_2 ratio from 1.3 (L_c = 350 ± 30 nm) to 1.5 (L_c = 336 ± 35 nm) at -300 V bias voltage. Consequently, the Ar/N_2 ratio does not influence L_c.

The apex angle of the cones remains constant between 70° and 80°. The height of the cones appears to increase exponentially with their width (Fig. 5.20).

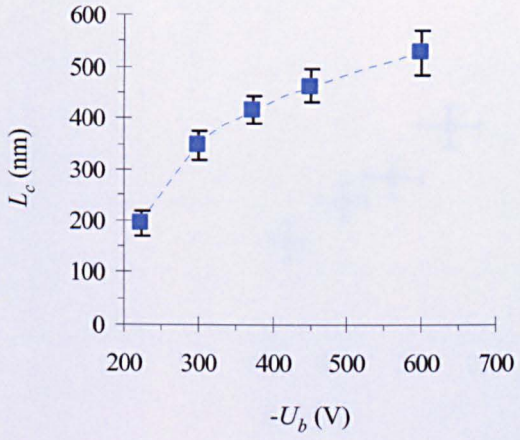

Figure 5.19: Lateral dimension L_c of topography type C as function of bias voltage U_b at $T/T_m = 0.23$, $a_d = 0.75$ - 0.85 µm/h and $Ar/N_2 = 1.3$.

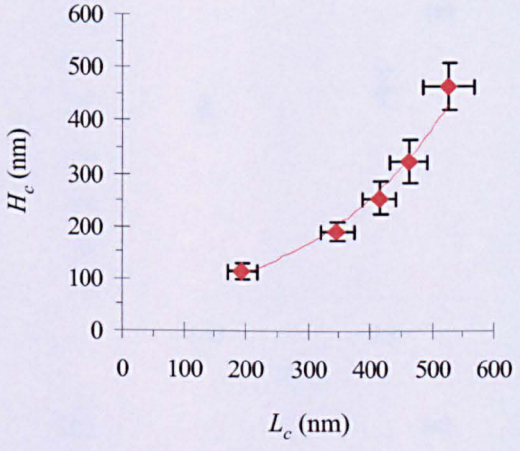

Figure 5.20: Correlation between lateral dimension L_c and height H_c of the surface feature for topography type C.

5.3.5 Topography Type R

The height of the topographical features of type R increases linearly with their lateral dimensions (Fig. 5.21).

As seen for the grain topographies, temperature and Ar/N_2 ratio have no effect on the growth of the features of this topography type (Fig. 5.22a, b). Again, the feature size depends on bias voltage and deposition rate (Fig. 5.22c, d). For all experiments, the lateral dimension increases linearly with increasing bias voltage. On increasing the deposition rate, the dimensions of the features decrease.

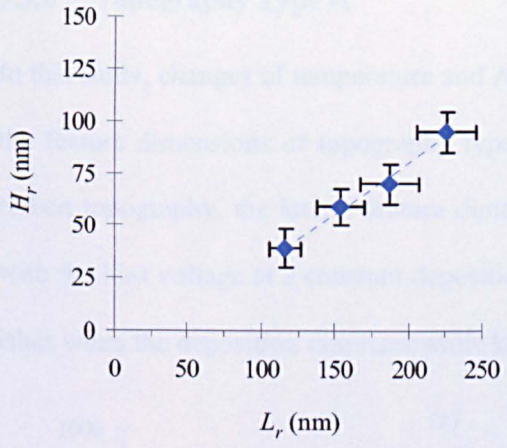

Figure 5.21: Correlation between lateral dimension L_r and height H_r of the surface feature for topography type R.

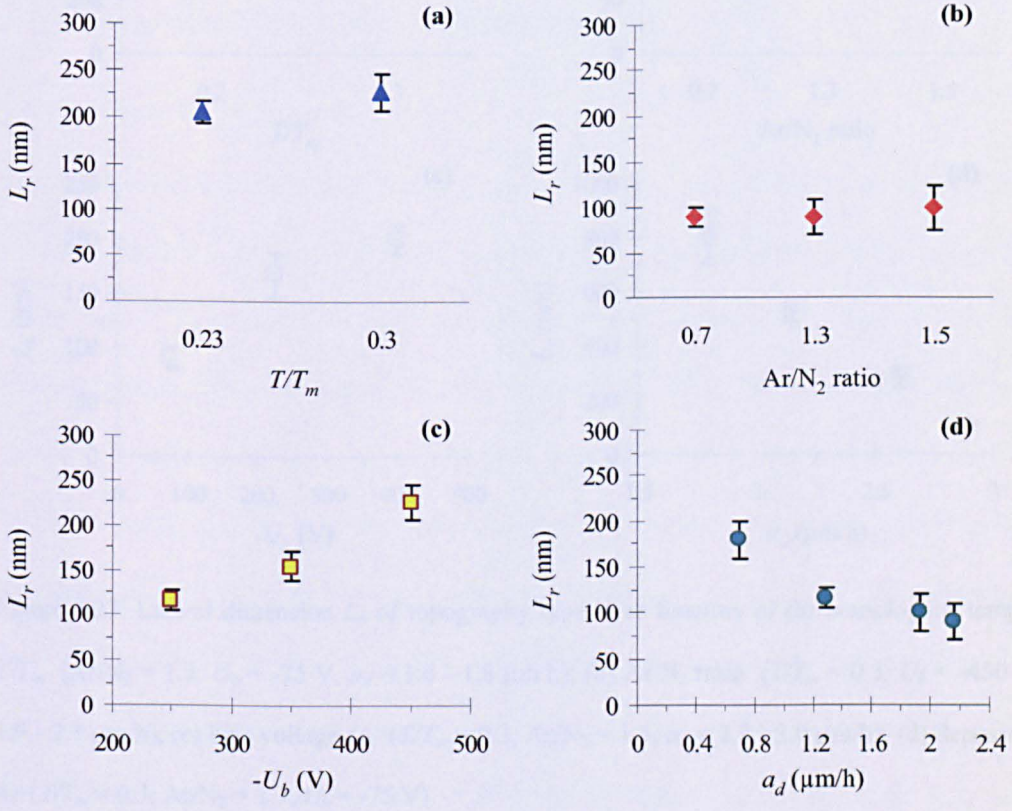

Figure 5.22: Lateral dimension L_r of topography type R as function of (a) homologous temperature T/T_m (Ar/N_2 = 1.3, U_b = -450 V, a_d = 0.9 - 1.0 µm/h); (b) Ar /N_2 ratio (T/T_m = 0.3, U_b = -250 V, a_d = 1.9 - 2.1 µm/h); (c) bias voltage U_b (T/T_m = 0.3, Ar/N_2 = 1.3, a_d = 1.1 – 1.2 µm/h); (d) deposition rate a_d (T/T_m = 0.3, Ar/N_2 = 1.3, U_b = -250 V).

5.3.6 Topography Type H

In this study, changes of temperature and Ar/N_2 ratio seem also to have a negligible effect on the feature dimensions of topography type H (Fig. 5.23a, b). Similarly to the findings for ribbon topography, the lateral feature dimensions of this topography type increases linearly with the bias voltage at a constant deposition rate (Fig. 5.23c). The lateral dimension diminishes when the deposition rate rises while keeping the bias voltage constant (Fig. 5.23d).

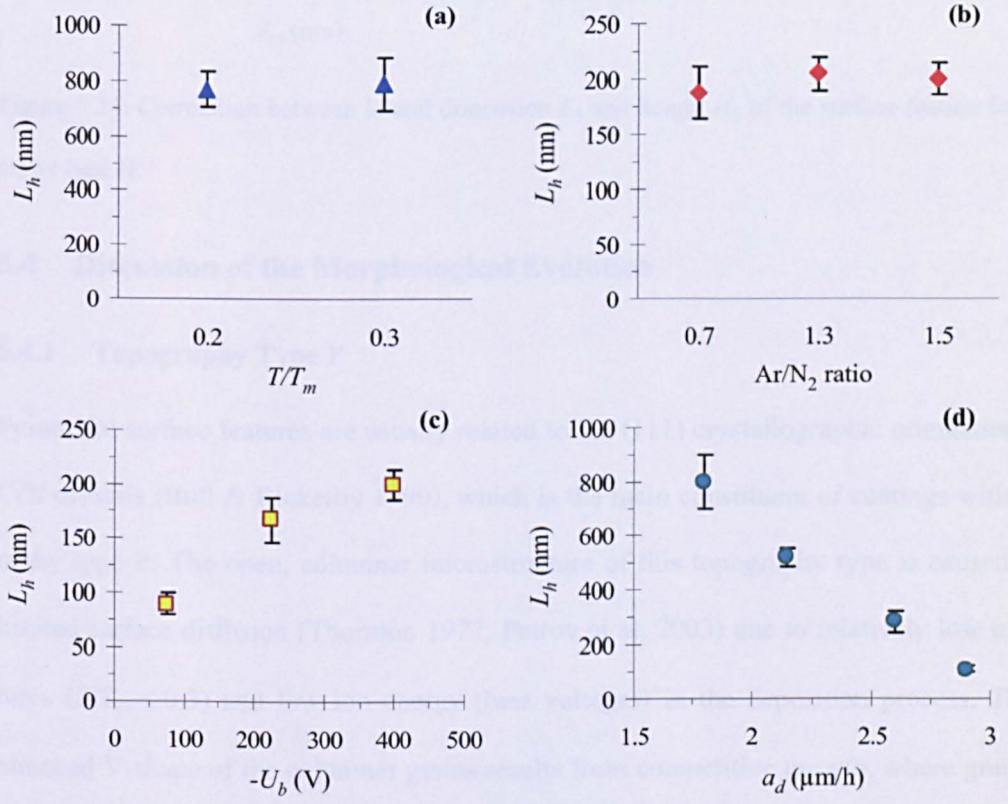

Figure 5.23: Lateral dimension L_h of topography type H as function of (a) homologous temperature T/T_m (Ar/N_2 = 1.3, U_b = -75 V, a_d = 1.6 - 1.8 µm/h); (b) Ar/N_2 ratio (T/T_m = 0.3, U_b = -450 V, a_d = 1.9 - 2.1 µm/h); (c) bias voltage U_b (T/T_m = 0.3, Ar/N_2 = 1.3, a_d = 2.8 - 3.0 µm/h); (d) deposition rate a_d (T/T_m = 0.3, Ar/N_2 = 1.3, U_b = -75 V).

Different to other topography types, the height of the surface features of topography type H remains constant when changing the lateral dimensions (Fig. 5.24).

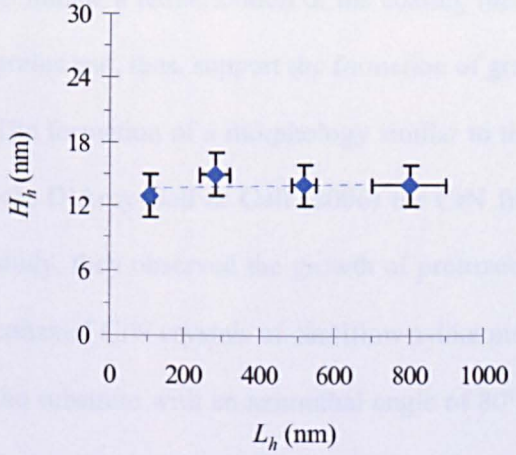

Figure 5.24: Correlation between lateral dimension L_h and height H_h of the surface feature for topography type H.

5.4 Discussion of the Morphological Evolution

5.4.1 Topography Type P

Pyramidal surface features are usually related to the (111) crystallographic orientation of the CrN crystals (Bull & Rickerby 1990), which is the main constituent of coatings with topography type P. The open, columnar microstructure of this topography type is caused by the limited surface diffusion (Thornton 1977; Petrov et al. 2003) due to relatively low temperatures ($T/T_m \leq 0.3$) and low ion energy (bias voltages) in the deposition process. The pronounced V-shape of the columnar grains results from competitive growth, where grains with less preferable orientation are overgrown by orientations with higher flux collection rates (shadowing effects) (Petrov et al. 2003). The difference found in the angle of the V-shaped columns between $Ar/N_2 = 0.7$ and $Ar/N_2 > 0.7$ might be explained by scattering effects at higher inert gas pressures enhancing the flux supply at the column sides and, thus, the lateral growth of the grains (Avelar-Batista et al. 2004).

When increasing the temperature T/T_m above 0.17, bundle-like or stacked growth of grains occurs and, thus, the pyramidal features become less regular (occurrence of subtypes P-f, P-s and P-m). The increase in temperature enhances presumably the adatom mobility sufficiently

to initiate a redistribution of the coating flux to preferable nucleation sites along the sides of grains and, thus, support the formation of grain bundles or stacks.

The formation of a morphology similar to that of P-h was quite recently reported by Frederick, D'Arcy-Gall & Gall (2006) for CrN films deposited on MgO(001) substrates. In their study, they observed the growth of protrusions of triangular lateral shape within a matrix of epitaxial CrN crystals of cauliflower-like morphology, when the deposition flux impinges at the substrate with an azimuthal angle of 80°. They propose that the rough surface generated during the deposition from oblique angles causes the nucleation of misoriented grains that develop into surface protrusions.

The occurrence of topography type P-h might be also related to an enhanced oblique component of the deposition flux, since this type was only obtained at relatively high total pressures. As described in section 2.2.2.2, an increased total pressure promotes the scattering of the particle flux to larger angles. However, in the experiments conducted here, the main effect of the oblique deposition flux is apparently not the creation of a rough surface. Similar rough surfaces were also obtained at lower total pressures. It is rather a question of supplying potential nucleation sites for the spike growth with sufficient deposition flux to initiate the spike growth.

The deposition experiments conducted in this thesis have also shown that the growth of topography P-h requires a careful balance between the surface diffusion, energy, flux and direction of the vapour particles. So the number of spike-forming nuclei is apparently reduced at higher deposition rates (see spike density in Fig. 5.15b). This means that fewer spike crystals can compete in the flux collection and, thus, bigger spikes and faster growing spikes are generated (Fig. 5.25). However, due to the reduced spike density, more flux reaches the slower growing matrix grains, and so the growth rate of these grains also increases. Since the growth rate of matrix grains rises faster than that of the spikes, the ratio of spike length to matrix grain length is reduced at higher deposition rates. The enhanced randomisation of the

flux direction induced by higher Ar/N_2 ratios might further reduce the difference between the two growth rates.

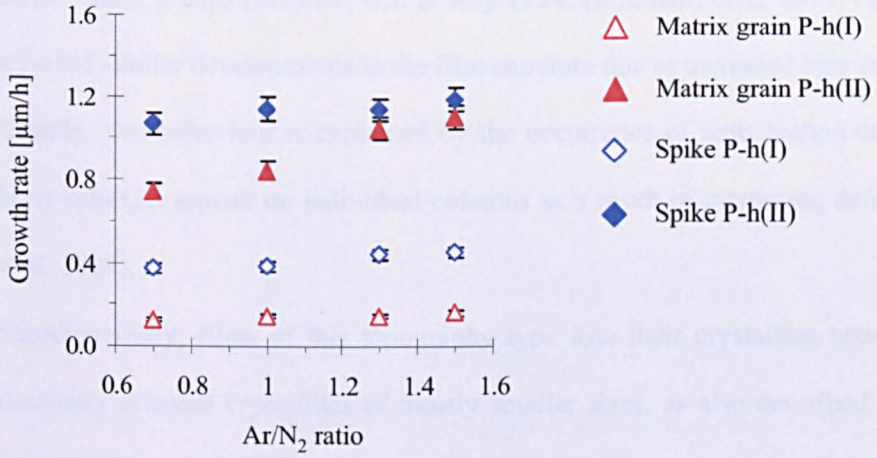

Figure 5.25: Growth rate of matrix grains and spikes of topography subtype P-h. The homologous temperature and the bias voltage were fixed at $T/T_m = 0.23$ or $U_b = -75$ V, respectively.

Since the mechanism for spike formation in this study is not yet completely understood, it is difficult to find a suitable explanation for the reduced spike density at higher deposition rates.

5.4.2 Topography Type G

When the bias voltage is increased above the transition voltage $U_{b,t}$ of type P, the valleys and voids begin to be filled by resputtering of weakly bound material (Müller 1986). This leads to a densification of the film microstructure and a flattening of the topography by eroding the grain facets due to the enhanced ion bombardment (Bland, Kominiak & Mattox 1974). In the case of topography type G, the facets of the grains were rounded by the enhanced ion bombardment and, although the microstructure was still columnar, it changed to closely-packed columns separated by dense grain boundaries (see Fig. 5.6). The observed change in crystallographic orientation of the CrN crystals from (111) to (200) or (220) is also a known result of increased ion bombardment (Cunha et al. 1999; He et al. 2000) and is explained by the lower sputtering yield of (200) and (220) crystal planes compared to the (111) planes (see section 2.2.3).

5.4.3 Topography Type CR

On further increasing the ion bombardment (bias voltage), the microstructure becomes more dense. Other groups (Messier, Giri & Roy 1984; Hurkmans et al. 1999; He et al. 2000) have reported similar developments in the film structure due to increased bias voltage (ion energy). Usually, this behaviour is explained by the occurrence of renucleation due to disruption of local epitaxial growth on individual columns as a result of increasing defect density (Petrov et al. 2003).

Simultaneously, films of this topography type lose their crystalline texture and consist of randomly oriented crystallites of mostly smaller sizes, as also described by Mattox & Kominiak (1971). Furthermore, the Cr/N ratio of this topography type increases at higher bias voltages since the comparatively lighter N atoms are preferentially resputtered from the film by the enhanced ion bombardment (Sugiyama et al. 1994; Gautier & Machet 1997).

When raising the bias voltage, the ion energy and the ion flux towards the substrate increases, which most probably results in a more intensive resputtering (etching), and hence, roughening of the surface of the growing film, as seen in Fig. 5.18d and also observed in other studies (Anderson et al. 1998).

For most topography types, there is a strong tendency to maintain features shapes and so there is also a direct correlation between lateral dimensions and heights. Thus, no detailed discussion of topographic parameterization was needed for this work; it is clear that process parameters can give a degree of control over topographic size. This situation does not apply obviously to CR topographies. However, under most of the conditions, there are experimentally observed correlations between S_q and λ, especially strong at higher temperatures, and fractal dimensions vary only marginally. Thus, for at least the parameter range examined here, there appears to be a tendency for CR topographies also to scale in size in a broadly 'self-similar' manner. The more erratic behaviour of the skewness does not seriously detract form this view, because it can be heavily influenced by a few extreme events in topography. For example, at lower temperatures and energies there could be more opportunity for high,

sharp peaks to grow and survive, leading to positive or only slightly negative values. More generally, a negative skewness could be expected, reflecting the presence of some deep valleys that derive from flaws in the underlying morphology. Higher intensity of surface bombardment is more likely to etch away peaks and perhaps to open up valleys, both shifting the skewness to increasingly negative values.

5.4.4 Topography Type C

Even at high bias voltages, a columnar microstructure appears on increasing the deposition rate. Similar observations were made by Wang & Oki (1990). They reported the growth of $Cr_2N(300)$ films of columnar microstructure and elongated grains. Due to enhanced atom arrival rate, the renucleation effects related to higher bias voltages might be suppressed. Thus, the dense, fibrous film growth observed for type CR is hindered and a columnar microstructure is created instead. The tops of the columns are conical probably due to kinetic roughening, which in combination with atomic shadowing, results in deep cusps between columns and column boundaries (Craig & Harding 1981; Petrov et al. 2003). The increase of the conical surface features (lateral dimension) with bias voltage might be explained by the decreased nucleation rate in the presence of ion bombardment due to depletion of small clusters by resputtering and dissociation (Marinov 1977; Greene et al. 1987).

5.4.5 Topography Types R and H

On further increasing the deposition rate, the microstructure changes again from columnar to fibrous. This modification is probably attributed to the fact that above a certain deposition rate the nucleation density increases which leads to fine-grain microstructure (Ohring 2002). It is assumed that preferential sputtering at the edge of the fibre bundles causes the elliptical or circular appearance of the topographical features of type R or type H, respectively. The variation in the shape of the features (elliptical or circular) can be attributed to preferred orientation or texture of the film and, thus, to differences in the sputtering rate for the specific crystal orientations (You, Brown & Al-Assadi 1993).

Deposits of topography type R and H are almost pure Cr_2N films, whereas a significant content of CrN crystallites was found in the films with CR and C topography. Compared to type CR and C, the main difference in the deposition processes of type R and H is the higher deposition rate, which can be related to higher sputter powers applied in the process. On increasing the power on the chromium targets, the number of sputtered chromium atoms available for the film formation is enlarged and, thus, the Cr/N ratio will augment in the deposited film. An enhanced occurrence of the chromium-rich phases in chromium nitride films as result of increased target power was recently reported by Lim & Lee (2006).

5.5 Mechanical Properties of Topography Types

Table 5.2 summarizes the results of the mechanical characterisation for the various topography types.

Table 5.2: Hardness, Young's modulus and residual stress of different morphology types.

Type	Hardness (GPa)	Young's modulus (GPa)	Residual stress (GPa)*
P	P-r: 2.3 to 4.3 P-f, P-h: 3.0 to 7.0 P-m, P-s: 6.3 to 9.3	P-r: 85 to 130 P-f, P-h: 87 to 190 P-m, P-s: 187 to 247	P-r: 0.053 to 0.085 P-f, P-h: 0.078 to 0.105 P-m, P-s: 0.063 to 0.225
G	12.1 to 20.4	249 to 317	0.213 to 1.002
CR	21.2 to 31.6	296 to 381	-0.356 to -2.685
C	11.5 to 18.6	217 to 286	0.190 to 0.809
R	16.4 to 26.8	274 to 323	-0.139 to -1.534
H	17.3 to 25.3	283 to 351	-0.160 to -1.581

* Negative values for stress correspond to compressive stress, and positive values represent tensile stress.

The here measured values for hardness, Young's modulus and residual stress are in good agreement with results obtained for chromium nitride thin films by other groups. For example, similarly large variations in hardness (4 GPa to 29 GPa) and Young's modulus (125 GPa

to 324 GPa) were found by Cunha et al. (1999). In their study, the bias voltage and temperature were varied from 0 V to -75 V or 150 °C to 380 °C, the sputter power was set to 500 W or 600 W, whereas the Ar/N_2 ratio and total pressure were fixed to a constant value. Also the range of residual stress determined for the different topography types is comparably to variations reported in the literature (Mayrhofer, Tischler & Mitterer 2001; Hoy, Sloof & Janssen 2005; Zhao et al. 2005). Regarding their mechanical properties, some generally significant differences between the topography types were observed. The films of topography type P exhibit the lowest values for hardness and Young's modulus, but also nearly zero to slight tensile stress. Higher tensile stresses as well as higher values for hardness and Young's modulus were measured for samples of topography type G and C. In contrast to this, topography type CR, R and H have medium to high compressive stress. Combined with this, medium to high values for hardness and Young's modulus were determined for these topography types.

Generally, the residual stress correlates to hardness and elasticity of thin films: films with high (compressive or tensile) stress usually also exhibit high hardness and low elasticity (high Young's modulus). The same trend can be seen for the thin chromium nitride films investigated here. The stress in thin films is influenced by their microstructure. So, it was found that dendritic, columnar structures, as seen for the topography type P, have nearly zero stress, since such structures are unable to support large mechanical stress (Shen & Mai 2000; Shen 2003). When the columnar microstructure becomes denser, the tensile stress of the film can increase significantly. A model developed by Finegan and Hoffman (1959) and later supported by simulations (Müller 1987b) explains this increase of tensile stress by the closing of voids in the porous structure due to interatomic attractive forces. Later Knuyt, Lauwerens and Stals (2000) suggested that the transition from zero stress to maximum tensile stress occurs as a consequence of instability in film structure, e.g. rough columns leading to partial contact between neighbouring columns and, or distributions of column diameter. In agreement with these considerations, this study found higher tensile stress in the denser co-

lumnar microstructure of the types G and C compared to type P. Consequently, the hardness of type G and C is higher compared to that of type P. Besides differences in the microstructure, the variations in phase and orientation of the grains found between the topography types might also cause changes in the hardness values. So it was shown by Friedrich (1998) that CrN films with (111) crystallographic texture, as type P, exhibit lower hardness than CrN films growing preferentially in (220) orientation, as films of type G do (see section 5.1.2). Films of type C consists beside of CrN crystals in (220) crystallographic orientation also of Cr_2N phases, which are usually reported to be harder than CrN (111), e.g. Hones, Sanjines & Lévy (1997); Friedrich (1998).

On increasing bias voltage applied in the deposition process, the stress in the films increases from nearly zero (type P) to tensile (type G) and suddenly changes to compressive (type CR). A similar behaviour was seen for tungsten thin films and was related to the transformation from a columnar to fibrous microstructure (Haghiri-Gosnet et al. 1989). Fibrous or even nanocyrstalline morphologies are often associated with compressive stress (Zhao et al. 2005), which can be related back to the mechanisms involved in the creation of such morphologies namely: atomic peening (Thornton & Hoffman 1989; Windischmann 1991; Davis 1993; Kamminga et al. 1998) and entrapment of gas ions in the film lattice (Fang, Jones & Prasad 1993; Paturaud et al. 1999). Since the topography types R and H also exhibit a fibrous, nanocyrstalline microstructure, compressive stress is also expected for these films. For types G, CR, H and R, the stress in the films increases with the bias voltage, which is a known effect in thin film deposition and has been also demonstrated for magnetron sputtered Cr-N thin films, e.g. by He et al. (2000) and Hoy, Sloof & Janssen (2004).

5.6 Reproducibility of Thin Film Properties

The reproducibility of the film properties was estimated by repetition experiment. In these experiments, the Si(100) substrates were coated in three separate experiments carried out under almost identical deposition conditions. The actual value of a process parameter dif-

fered by a maximum of 5 % from the set value in each experiment. The repetition experiments were conducted for three different sets of process conditions A, B and C (see Table 5.3).

Table 5.3: Average value and standard deviation of topographical parameters and mechanical properties determined for the films 1, 2, 3, which were deposited in three separate experiments conducted for each individual set (A, B or C) of deposition conditions.

		Set A		Set B		Set C	
Process parameters	T/T_m (°C)	0.1		0.17		0.23	
	Ar/N_2	1.0		0.7		1.3	
	U_b (-V)	50		250		250	
	Power (kW)	3x2		3x2		3x4	
	Pressure (Pa)	0.4		0.4		0.4	
Topography type		P-r		CR		C	
Surface parameters	L_p	1: 250 ± 25 2: 262 ± 19 3: 272 ± 28	S_q	1: 9.74 ± 0.39 2: 8.75 ± 0.26 3: 9.40 ± 0.28	L_c	1: 229 ± 24 2: 212 ± 27 3: 241 ± 26	
	H_p	1: 122 ± 10 2: 128 ± 9 3: 119 ± 7	S_{sk}	1: -0.188 ± 0.018 2: -0.132 ± 0.006 3: -0.147 ± 0.019	H_c	1. 159 ± 16 2: 149 ± 15 3: 170 ± 15	
			D	1: 1.74 ± 0.01 2: 1.73 ± 0.01 3: 1.72 ± 0.01			
Hardness (GPa)		1: 2.9 ± 0.1 2: 2.8 ± 0.3 3: 2.6 ± 0.2		1: 27.1 ± 2.4 2: 25.9 ± 2.3 3: 28.5 ± 1.6		1: 15.0 ± 1.6 2: 14.8 ± 0.8 3: 16.1 ± 0.9	
Young's modulus (GPa)		1: 112 ± 6 2: 92 ± 4 3: 102 ± 15		1: 375 ± 23 2: 339 ± 32 3: 401 ± 35		1: 258 ± 27 2: 246 ± 32 3: 281 ± 20	
Residual stress (GPa)		1: 0.083 ± 0.003 2: 0.078 ± 0.010 3: 0.085 ± 0.015		1: -2.551 ± 0.250 2: -2.244 ± 0.356 3: -2.814 ± 0.272		1: 0.614 ± 0.037 2: 0.690 ± 0.047 3: 0.453 ± 0.018	

For each set of process conditions, the three films (1, 2, and 3) were produced, whereby each film was deposited in a separate experiment. After the deposition, the topographical parameters and mechanical properties of the films 1, 2 and 3 for each set were determined. Table 5.3 gives the average values with the standard deviations from 10 measurements performed in individual places on the films 1, 2 or 3 for each of the sets A, B and C. Generally, the difference between the films deposited in the three separate experiments is comparable to the variations of the data measured on an individual film. This indicates that the topographical and mechanical properties of the films are under reasonable control in deposition experiments conducted in this work. Furthermore, it can be concluded that the structural characteristics (size, phase and orientation of the grains) of the films are under control as well, otherwise significant differences in the mechanical behaviour and the topographical appearance should be detectable due to their strong correlation to the film morphology.

Chapter 6

Microtribology of Selected Nanostructures

One goal of the thesis is to study the influence of the in-process structuring on the microtribological behaviour of surfaces with special emphasis on investigations in lubricated contacts as well as in humid environment. Furthermore, the resistance of the nanostructures against wear-induced damages has to be considered, since an efficient, functional performance of nanostructured topographies depends strongly of the geometrical stability of their surface features.

Consequently, the microtribological behaviour of nanostructured surfaces needed to be investigated under different test conditions which can be summarized in three main groups of experiments:

The tests conducted in experimental group (EG) 1 concentrate on the wear resistance and the frictional behaviour of different nanostructures as function of the normal load applied and the duration of loading.

In EG 2, the lubrication-efficiency of differently nanostructured surfaces was determined and compared to each other and in comparison to smooth surfaces.

The influence of nanoscale topography and chemical composition of surfaces on their microtribological behaviour in humid environment was studied in EG 3.

6.1 Friction and Wear of Nanostructured Surfaces in Unlubricated Contacts (EG 1)

The tests in EG 1 were carried out to gain information about the frictional behaviour and wear resistance of various nanostructured surfaces with respect to the normal force applied (load carrying capacity, LCC) and the duration of loading (long-term stability, LTS). Here, it was of particular interest to specify when and which kind of wear was observed for the different types and dimensions of nanostructures in wear mapping tests. Furthermore, experiments were conducted as function of the normal force applied under nearly wear-free conditions in order to measure the friction without being significantly affected by wear-related changes in surface topography or chemistry. Different to the friction measurements under nearly wear-free conditions, the LCC and LTS tests were performed with another counter body to ensure more severe tribological loading of the surfaces. The results obtained in these tests are reported and analysed in the following pages. Initially, the investigated nanostructures are described with respect to their mechanical, structural and topographical properties that might be relevant for the evaluation of the tribological data. The details of the tribological experiments carried out in EG 1 are summarized in section 4.3.2. Examples of the tribological measurements are presented in Appendix A.3.

6.1.1 Properties of Nanostructures Investigated in EG 1

The structural (crystallographic phase and texture) and relevant mechanical properties (hardness and Young's modulus) of the surfaces investigated in EG 1 are summarized in Table 6.1. SEM and AFM images of the surfaces tested are shown in Appendix A.3.

Selected topographical parameters of the surfaces are given in Table 6.2. The conditions for measuring the topographical parameters are explicitly described in section 4.2.2.

Table 6.1: Structural and mechanical properties of the nanostructured surface investigated in EG 1 and EG2.

Structure	Phase and preferential, crystallo-graphic orientation of the grains parallel to the substrate surface	Hardness H (GPa)	Young's modulus E_f (GPa)
Ref	CrN (220)	17.3 ± 2.5	295 ± 21
P1	CrN(111)	2.9 ± 0.4	120 ± 23
P2		3.3 ± 0.5	125 ± 25
P3		3.5 ± 0.7	125 ± 15
P4		4.0 ± 0.2	130 ± 18
C1	Cr_2N(300), CrN(220), Cr_2N (200)	17.1 ± 1.6	286 ± 27
C2		15.5 ± 0.8	274 ± 20
C3		13.5 ± 0.9	266 ± 32
CR1	CrN(220), Cr_2N(111), Cr_2N(110)	28.2 ± 2.5	366 ± 35
CR2		29.3 ± 2.4	380 ± 33
CR3		22.2 ± 2.0	286 ± 30
CR4		23.2 ± 1.9	324 ± 38
CR5		25.7 ± 2.2	342 ± 32
CR6		25.5 ± 2.1	338 ± 30

Table 6.2: Topographical parameters of the investigated surfaces: Lateral dimension L_x and height H_x of the surface features, root mean square roughness S_q, skewness S_{sk}, kurtosis S_{ku}, summit curvature S_{sc}, summit density S_{sd}, rms slope σ', surface bearing index S_{bi}, core fluid retention index S_{ci}, valley fluid retention index S_{vi} and fractal dimension D.

	L_x (nm)	H_x (nm)	S_q (nm)	S_{sk}	S_{ku}	S_{sc} (nm)	S_{sd} (#/µm²)	σ'	S_{bi}	S_{ci}	S_{vi}	D
Ref	-	-	5.5 ±0.03	0.403±0.018	3.29± 0.03	98±8	22.8±0.5	0.24±0.01	0.57±0.12	1.73±0.03	0.10±0.02	1.60±0.01
P1	88±8	65±7	17.9±0.2	0.214±0.016	2.71±0.36	5±3	43.0±2.6	0.87±0.09	0.72±0.06	1.48±0.02	0.12±0.01	-
P2	151±18	90±12	31.0±0.7	0.565±0.089	3.16±0.19	6±17	25.5±0.4	0.92±0.07	0.48±0.05	1.28±0.02	0.14±0.01	-
P3	205±15	139±26	57.9±1.2	0.495±0.040	3.08±0.13	6±17	12.2±1.3	1.00±0.06	0.90±0.08	1.41±0.05	0.14±0.01	-
P4	567±48	375±45	77.6± 3.0	0.259±0.026	2.87±0.25	6±17	3.4±0.1	1.37±0.02	0.70±0.15	1.74±0.11	0.10±0.01	-
C1	134±11	89±16	15.3±0.9	0.103±0.039	2.87± 0.14	196±46	28.8±0.7	0.80± 0.05	0.60±0.13	1.55±0.04	0.11±0.01	-
C2	237±32	137±24	40.4±0.6	0.076±0.040	3.16±0.19	373±45	13.3±0.9	0.63±0.03	0.66±0.10	1.55±0.03	0.11±0.01	-
C3	379±39	362±35	64.9±0.8	0.188±0.043	2.75±0.71	465±52	4.6±0.1	0.56±0.05	0.72±0.08	1.44±0.05	0.12±0.01	-
CR1	not defined (see section 4.2.2.1)		9.0±0.9	0.333±0.09	3.05± 0.14	112±46	3.3±0.7	0.21± 0.03	0.45±0.13	1.45±0.04	0.11±0.01	1.72±0.01
CR2			9.4±0.2	-0.373±0.037	3.26±0.07	115±8	3.6±0.2	0.22±0.01	0.67±0.12	1.51±0.03	0.13±0.01	1.72±0.02
CR3			12.0±0.6	-0.650±0.051	3.08±0.71	104±20	3.2±0.1	0.28±0.01	0.82±0.21	1.72±0.05	0.15±0.01	1.72±0.01
CR4			20.3±0.6	0.255±0.024	2.80±0.03	78±12	3.0±0.2	0.35±0.02	0.76±0.22	1.45±0.04	0.11±0.01	1.73±0.03
CR5			22.6±1.0	-0.336±0.077	3.63±0.36	68±7	3.1±0.2	0.42±0.09	0.71±0.13	1.51±0.11	0.13±0.01	1.71±0.03
CR6			22.4±2.0	-0.539±0.060	3.31±0.22	75±17	3.0±0.1	0.37±0.02	0.67±0.08	1.71±0.11	0.10±0.06	1.75±0.02

6.1.2 Frictional Behaviour of Nanostructured Surfaces under Nearly Wear-free Conditions

The friction force F_F was measured as function of the normal load F_N under nearly wear-free conditions on pyramid-like (P1 to P4), cone-like (C1 to C3) and crater-like (CR1 to CR6) nanostructured Cr-N films and on a relatively smooth Cr-N film, which is referred to as the reference surface (Ref) later on.

6.1.2.1 Friction on Nanostructured Surfaces

As seen in Figure 6.1, the friction forces increase on raising the normal load on all tested surfaces. Evaluating the F_F values measured on various surfaces of the same topography type, it was found that:

- for surfaces of topography type P, the friction force decreases when going from surface P1 to P4 (i.e. increasing roughness). On surface P1, stiction was observed even at 15 mN. When stiction occurs, the friction force curve no longer exhibits its typical shape (see Fig. 4.8c), but a saw-tooth-like one. Such behaviour indicates that the friction force has exceeded the stiffness of the spring. Thereby, the mounted ball no longer slides over the surface but sticks on it and the deflection of the spring corresponds to the amplitude of the oscillating sample motion. In this case, the friction force could not be determined and the occurrence of stiction was marked in the F_F-F_N curve instead.
- for surfaces of topography type C, sample C1 exhibits the highest and C3 the lowest friction. Similar to P1, sticking occurred also at the highest normal load on surface C1.
- for surfaces of topography type CR, the lowest friction was measured on surface CR3 and the highest on surface CR4. Generally, the samples CR1 to CR3 show lower friction than the samples CR4 to CR6. However, the differences between the various crater-like structured samples are relatively small and partially within the variation of the test data for one surface. For example, the minimum/maximum F_F values were determined to be for CR1: 2.19/2.25 mN, CR2: 2.15/2.22 mN, CR3: 1.78/1.95 mN, CR4: 2.43/2.55, CR5: 2.40/2.51

mN and CR6: 2.35/2.42 mN in three tests on different places on a sample at 15 mN normal force.

Furthermore, differences in friction force between the reference and certain nanostructured surfaces were observed. Compared to the reference surface, lower friction was measured on the structures P4, C3 and all crater-like structured surfaces, whereas higher friction was obtained on the surfaces P1 to P3 and C1. Among the nanostructured samples, most of the crater-like structured surfaces exhibit lower friction than surfaces of topography type C and P.

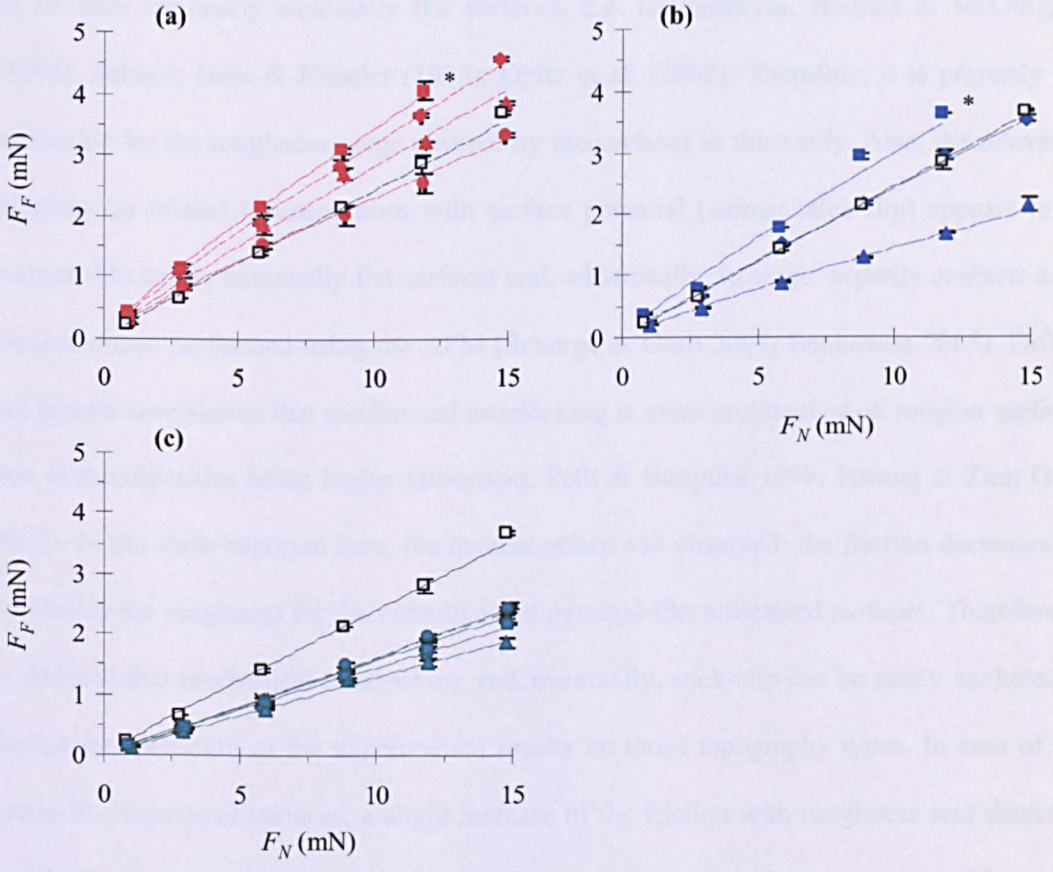

Figure 6.1: Friction force F_F measured as function of the normal force F_N force on the reference (□) and Cr-N thin films with

(a) pyramid-like topography: ■ P1, ◆ P2, ▲ P3, ● P4

(b) cone-like topography: ■ C1, ◆ C2, ▲ C3

(c) crater-like topography: ■ CR1, ◆ CR2, ▲ CR3, ● CR4, ✖ CR5, − CR6.

The sign * indicates the occurrence of stiction in the system. The error bars show the difference between the maximum and minimum value within three tests at the same normal force on one structure.

6.1.2.2 Correlation between Frictional Behaviour and Topographical Parameters

In order to explain the experimental results, it is essential to first identify the mechanisms that induce friction in the investigated systems. As shown in Chapter 3, friction in the micro and nanoscale scale can be generated by the following main mechanisms: stick-slip, wear, capillarity, solid-solid adhesion or combinations thereof.

The occurrence of stick-slip can be attributed to viscosity effects, atomic stick-slip and mechanical interlocking (see section 3.1.3). Stick-slip due to viscosity effects has been reported so far only for nearly atomically flat surfaces, e.g. Israelachivili, Homola & McGuiggan (1988); Schoen, Hess & Diestler (1995); Opitz et al. (2002). Therefore, it is probably not applicable for the roughness range covered by the surfaces in this study. Also, the relevance of stick-slip related to interactions with surface potential (atomic stick-slip) appears to be restricted to nearly atomically flat surfaces and, additionally, to single-asperity contacts as in measurements performed using the AFM (Scherge & Gorb 2001; Bennewitz 2005). Different groups have shown that mechanical interlocking is more pronounced on rougher surfaces due to the asperities being higher (Bouissou, Petit & Barquins 1998; Hwang & Zum Gahr 2003). In the study reported here, the inverse effect was observed: the friction decreases on increasing the roughness for the cone-like and pyramid-like structured surfaces. Therefore, it is deduced that mechanical interlocking and, eventually, stick-slip can be safely excluded in further interpretation of the experimental results on those topography types. In case of the crater-like structured surfaces, a slight increase of the friction with roughness was detected, but there was no reasonable explanation why interlocking should occur on crater-like structured surfaces but not on often rougher surfaces with pyramidal and conical features. So, it was deduced, that interlocking is also not relevant for this type of topography.

Another potential source of friction can be capillarity. In order to judge the relevance of capillarity for friction in the system, the capillary force achievable between the mating surfaces needs to be estimated and compared to the friction forces measured in the tribological tests. A good estimate of the capillary force can be obtained from the results of the tribologi-

cal tests performed in EG 3 (see section 6.3.3.1). There, the friction was measured as function of the relative humidity on hydrophilic samples with nanostructured topographies similar to those of the samples investigated in EG 1. Based on considerations that are explained in more detail in section 6.3, the difference in the friction force determined at 10 % RH and 50 % RH on hydrophilic surfaces was exclusively attributed to capillary effects. Thereby, it was found that the maximum capillary force ranges between nearly 0 mN on crater-like structured surfaces to about 0.03 mN on pyramid-like or cone-like topographies with small-sized surface features. At the lowest normal load applied in EG 1, the friction force exceeds the maximum possible capillary force already by factor of ten on surfaces with small-sized pyramidal or conical features. At higher normal loads the difference between friction force and maximum capillary force become even more significant. Therefore it appears reasonable to assume the capillary force as a minor friction-influencing factor here.

The contribution of wear-induced forces to friction can probably be regarded as being less important since indications of significant wear were not detected while analysing the surface features of the different nanostructures after the tribological tests.

Consequently, the solid-solid adhesion appears to be the dominant factor for generating friction on the investigated surfaces. Since other contributions to the friction are highly probably negligible, equation (3.1) for calculating the friction force F_F reduces to

$$F_F = \tau_a \cdot A_r \tag{6.1}$$

where τ_a is the average shear strength and A_r is the real contact area.

The real contact area is strongly influenced by the normal load F_N, whereby their correlation can be expressed in a general way by (Czischos & Habig 1992)

$$A_r = C_s \cdot F_N{}^c \tag{6.2}$$

The factor C_s considers surface-specific characteristics (e.g. summit density, summit height distribution) and relevant material properties.

When inserting equation (6.2) into equation (6.1), the functional relation between friction force and normal force is given by

$$F_F = \mu \cdot F_N{}^C \text{ where } \mu = \tau_a \cdot C_s \tag{6.3}$$

Different models have been developed to study the dependence of friction force on the normal force for single- and multi-asperity contacts (Johnson 1987; Enachescu et al. 1998; Greenwood 1992; Riedo & Brune 2003) as well as for self-affine surfaces (Persson 2001). For single-asperity contacts a 2/3 power law dependence (C = 2/3) is usually seen whereas a linear dependence (C = 1) appears to be typical for multi-asperity contacts and self-affine surfaces (Riedo et al. 2004). Taking the experimental set-up into account, a multi-asperity contact and, hence, a linear F_F-F_N dependence is most likely in this study. By fitting the F_F-F_N data according to equation (6.3), the values of power C were determined for the differently nanostructured surfaces and the reference. The power C was found to vary between 0.86 to 1.02, with the fitting confidence ranging between 0.98 and 0.99. Thus, as expected, a linear F_F-F_N dependence is clearly indicated for the surfaces investigated here.

Under the presumption that the material properties are not affected by the tribological loading (e.g. by strain hardening), the shear strength can be regarded as being constant within the tests performed at various normal loads on one surface. In consequence, the increase in friction is attributed to an increase in the contact area, as often reported in literature, e.g. Lim & Ashby (1987); Carpick et al. (1996).

With respect to the differences in μ between the various nanostructured surfaces, beside changes in the contact area, diversities in the shear strength have probably to be considered as a reason for these differences. Deliberations involving shear strength are complicated by the fact that several definitions of the shear strength exist in the literature (Straffelini 2001). Some authors consider the shear strength to be proportional to the material yield pressure (Heilman & Rigney 1981; Bowden & Tabor 2001), whereas others believe it to be equal to the shear yield strength (Molinari, Estrin & Mercier 1999). In other theories the shear

strength is assumed to directly depend on the adhesion between the asperities (Zum Gahr 1987; Landherr & de Gee 1991) or to the sum of two contributions, the first related to adhesion and the second to a dissipative term (Tabor 1982). The achievement of reliable values of the shear strength in a contact requires tribological measurements with the mating materials in vacuum (Ott, Michal & Chottiner 1989; Carpick et al. 1996; Piétrement & Troyon 2001). Such tests could not be performed in this study due to instrumental limitations. Therefore, another approach was chosen to estimate the relevance of changes in the contact area to the alteration of friction forces for the investigated surfaces. This approach presumes that variations in the friction force can be entirely related to modifications of the contact area, when samples exhibiting an identical surface chemistry are tested under similar conditions, and when wear or capillarity effects can be neglected in these tests. Experiments confined in such a manner were carried out on the hydrophobic samples in EG 3 (see section 6.3.3.2). Due to variations in the contact area, the friction force measured in EG 3 changes at the ratio of 1 : 1.28 : 1.61 : 2.01 ~ P1 : P2 : P3 : P4 for pyramid-like structured samples, 1 : 1.64 : 2.15 ~ C1 : C2 : C3 for cone-like structured samples, and 1 : 0.93 : 1.10 ~ CR2 : CR4 : CR5 for crater-like structured samples, respectively. Comparable ratios were found in the tribological tests discussed here: 1 : 1.1 : 1.47 : 1.78 ~ P1 : P2 : P3 : P4 for pyramid-like structured samples, 1 : 1.56 : 2.04 ~ C1 : C2 : C3 for cone-like structured samples, and 1 : 0.87 : 1.24 ~ CR2 : CR4 : CR5 for crater-like structured samples. Hence, it was concluded that, similar to the effect explained for those tests in EG 3, the modification of the solid-solid adhesion mainly attributed to changes in the contact area causes the observed diversity in friction.

The differently nanostructured surfaces were compared with respect to the contact area. The contact area is determined by the number of contacts and the size of the individual contact patches. The size of the individual patches certainly grows with increasing normal load due to enhanced deformation. However, the asperities were never deformed to such extent that residual changes of the asperity shape could be detected by SEM (resolution: 15 nm) after the tests.

On raising the normal load, the nominal contact area between sample and counter body (ball) is expected to increase as well, as described in common contact models (Czischos & Habig 1992; Bhushan 1999). In case of spherical counter bodies, an increase in the nominal contact area usually leads to a higher number of contacts under the conditions that (1) the nominal contact area is significantly larger than the average size of the asperities, (2) the distance between the asperities is small compared to the nominal contact area, (3) the asperities are homogenously distributed on the sample surface, and (4) the heights of the asperities is similar. The radius of nominal contact area between counter body (TiC ball) and the sample, a_n, was determined according to the commonly used theory by Hertz (1882)

$$a_n = \left(\frac{3 \cdot R \cdot F_N}{4 \cdot E^*} \right)^{1/3} \tag{6.4}$$

where R is the ball radius, F_N is the normal load and E^* is composite Young's modulus of the two contacting surfaces (see equ. 3.7). The calculation of the E^* values is given for the various nanostructures in Appendix A.2.

The radius of the nominal contact area was found to range from 1.5 µm to 2.0 µm for the lowest (1 mN) and from 3.7 µm to 4.9 µm for the highest (15 mN) normal load applied in the tests. A comparison of the topographical parameters given in Table 6.2 to the values of the nominal contact area A_n ($A_n = \pi \cdot a_n^2$) indicates that the size of the surface features and the distance between them (related to summit density) are much smaller for the three topography types and, thus, requirements (1) and (2) are met. Also, condition (3) and (4) are fulfilled for all topography types, since the deviation of the summit density is relatively small compared to the average value (see Tab. 6.2) and, thus, a certain similarity in the height of the surface features can be assumed. Consequently, changes of the contact area can also be related to variations in the number of contacts.

For rough surfaces, a detailed analysis of the patch growth as function of the nominal load involves application or even development of complex contact models suitable for the various topography types; this would go beyond the topic of this thesis. Therefore, though being

aware, that probable effects related to changes in the patch size are neglected, the further discussion of the experimental data concentrates on the contact number, which is undoubtedly an important parameter in this context.

Since the roughness of the counter body is lower than for the differently nanostructured surfaces, it might be tolerable to simplify the contact between sample and counter body to an interaction between smooth surface (counter body) and a rough one (sample). In this case, the contact number is then proportional to the number of asperities present on the nanostructured surface, which corresponds to the summit density. For pyramid-like and cone-like structured surfaces, the manipulation of the lateral dimensions of the surface features changes the summit density. Whereas, the modification of the crater-like topography is mainly limited to deepening of the cavities, which does not affect significantly the summit density (see Tab. 6.2). The graph in Figure 6.2 plots the coefficient μ as function of the summit density for pyramid-like, cone-like and crater-like structured surfaces and the reference.

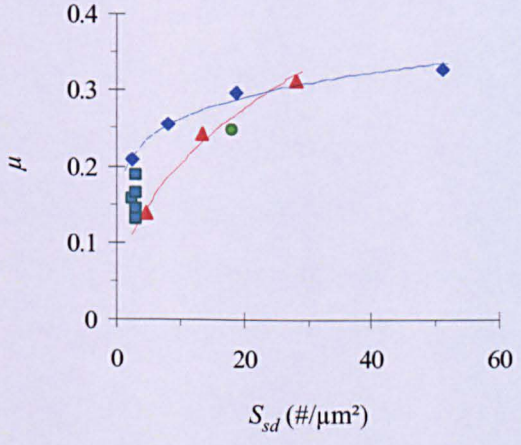

Figure 6.2: μ as function of the summit density S_{sd} for the reference (●) and Cr-N thin films with pyramid-like structured (◆), cone-like structured (▲) and crater-like (■) structured surfaces.

It gives evidence that the difference in the frictional behaviour of the various nanostructured surfaces might be strongly influenced by the summit density. In the case of pyramid-like and cone-like structured surfaces, the friction decreases with the decreasing summit density. The

lower summit number is presumably also the reason for the mostly reduced friction on surfaces with a crater topography compared to samples of other topography types.

However, when the summit density for pyramid- and crater-like surfaces approaches values close to that of crater-like structures, the friction on surfaces with pyramidal or conical surface features becomes similar to the friction forces obtained for crater structures. Nevertheless, even at low summit densities, the friction on the pyramid structure seems to be higher than on cone-like structured surfaces probably due to variations in the dimension of the contact junction and/or the shear strength.

Differences in the actual shape of the contacting asperities and the mechanical properties might also cause the lower sensitivity of μ to changes in the summit density of pyramid-like structures compared to cone-like structures. Interestingly, the friction coefficient of the reference surface is comparable to the μ value of a cone-like structure surface with similar summit density.

Differences in the contact number can not be applied to explain the variations found between the samples CR1 to CR3 and CR4 to CR6, since their summit densities are comparable (see Table 6.2). The samples CR4 to CR6 have higher S_q values than CR1 to CR3. Interlocking was earlier excluded as possible source of friction. Due to higher roughness, more pronounced ploughing of the counter body might cause higher friction in case of sample CR4 with spiky surface features (indicated by positive skewness), but probably not for the surface CR5 and CR6 consisting of bumpy surface features (corresponds to negative skewness).

Beside higher roughness amplitudes, the surfaces CR4 to CR6 have features with smaller curvatures than the samples CR1 to CR3. The shape of the summit and the mechanical properties determine the nature of the contact (elastic, elastic-plastic, plastic). Since the mechanical properties are relatively similar, significant changes in the summit radius, as seen in here, might influence the contact mechanics. Usually, the plasticity index is regarded in order to judge the contact nature of a rough surface (Greenwood & Willamson 1966). The plasticity index is defined according to Chang (1997) as

$$\psi = \frac{2 \cdot E^*}{\pi \cdot KY \cdot H}\left(\frac{\sigma_{asp}}{R_{asp}}\right)^{1/2} \tag{6.5}$$

where H is the hardness, σ_{asp} is the standard deviation of the asperity heights and R_{asp} is the average curvature of the asperity and E^* is composite Young's modulus of the two contacting surfaces (see equ. 3.7). K_Y is the yield coefficient of the sample material, which is a function of Poisson's ratio and can be linearly approximated by (Chang 1997)

$$KY = 1.282 + 1.158 \cdot \nu \tag{6.6}$$

According to Taybei & Polycarpou (2005), the standard deviation of asperity heights σ_{asp} can be related to the standard deviation of the surface heights R_q by

$$R_q{}^2 = \sigma_{asp}{}^2 + \frac{3.717 \cdot 10^{-4}}{\eta_{asp}{}^2 \cdot R_{asp}{}^2} \tag{6.7}$$

where η_{asp} is the area density of asperities and R_{asp} is the average asperity curvature.

Values of the plasticity index $\psi < 0.6$ correspond to mostly elastically deformed asperities. The asperity deformation is predominantly plastic, if $\psi > 1$. For values in the range $0.6 < \psi < 1$, the asperities deform elastically and plastically.

In order to calculate the plasticity index, it is assumed that the parameters R_{asp}, R_q, η_{asp} correspond to the parameters S_{sc}, S_q and S_{sd}, which are used for characterising the surfaces in this study. The mechanical and topographical parameters involved in this calculation are given for the crater-like structured surfaces in Table 6.1 and 6.2 and for the counter body (TiC ball) in Table 4.7.

For the surface CR1 to CR3, the values of ψ ranges from 0.5 to 0.6, which means elastic-plastic deformation of the asperities, whereas a mainly plastic deformation is indicated by the ψ values (1.2 to 1.3) obtained for surface CR4 to CR6. A theory developed by Patton & Bhushan (1999) predicts that plastic contact junctions have larger sizes than purely elastic or elastic-plastic contacts due to the combined effect of normal and tangential force in sliding

motion. The same effect probably leads to larger contact areas and, thus, higher friction on the surfaces CR4 to CR6 compared to CR1 to CR3.

6.1.3 Load-Carrying Capacity (LCC) of Nanostructured Surfaces

In LCC tests, the frictional evolution and the occurrence of wear as a function of the normal load were determined in short-time tests (20 cycles) on pyramid-like (P1 to P4), cone-like (C1 to C3) and crater-like (CR1 to CR6) nanostructured Cr-N films and on a relatively smooth Cr-N film, which serves as reference (Ref.) in these tests.

6.1.3.1 Frictional Evolution on Nanostructured Surfaces

For easier comparison of the variations in friction, the ratio of friction force F_F to normal force F_N was plotted versus the number of cycles n_{cycles} for the differently nanostructured surfaces and the reference sample (see Appendix A.3).

Generally, four main types of curves describing the F_F/F_N-n_{cycles} evolution can be identified and are schematically illustrated in Figure 6.3.

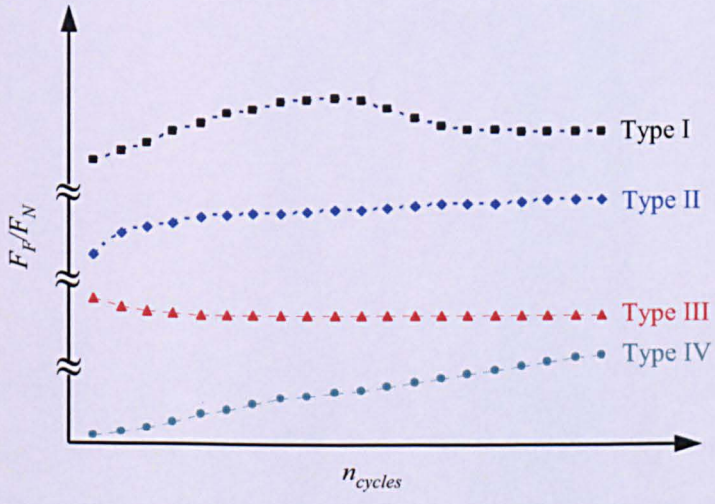

Figure 6.3: Schematic drawing of the main types of F_F/F_N-n_{cycles} curves observed in the LCC tests on nanostructured Cr-N thin films.

In type I, the F_F/F_N ratio increases to a peak value, stagnates, then decrease slightly and may afterwards stabilize. In type II and III, the F_F/F_N ratio increases or decreases rapidly, respec-

tively, and then evolves with a smaller slope or stabilizes. Typical for type IV is a steady increase of the F_F/F_N value with the number of cycles.

The functional correlation between F_F/F_N and n_{cycles} were fitted with a relatively high reliability ($0.78 < R^2 > 0.9$) by the polynomial equation $F_F/F_N = a_3 \cdot n_{cycles}^3 + a_2 \cdot n_{cycles}^2 + a_1 \cdot n_{cycles} + a_0$ for curves of type I or by the polynomial equation $F_F/F_N = a_2 \cdot n_{cycles}^2 + a_1 \cdot n_{cycles} + a_0$ for curves of type II to IV, respectively. However, only the coefficients that are present in both polynomial equations are relevant for comparison purposes, namely a_2, a_1 and a_0.

For the nanostructured surfaces, the coefficient a_2 is usually at least two orders of magnitudes lower than the coefficients a_1 and a_0. Furthermore, the value of a_2 does not vary in a consistent way with the load or topographical parameters for a certain type of topography. As an example, the a_2 values determined for various normal loads are shown for the structures P1 to P4 in Figure 6.4.

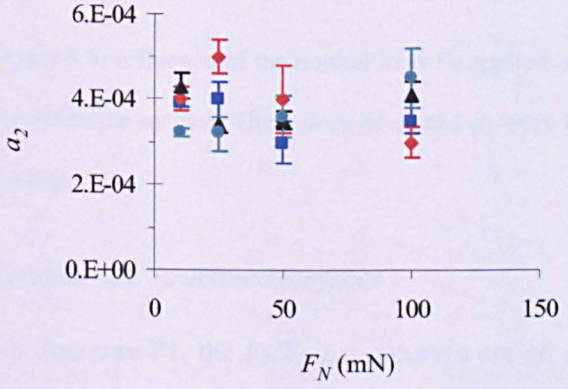

Figure 6.4: The fitting coefficient a_2 determined for various normal loads F_N on the pyramid-like structured surface P1 (■), P2 (◆), P3 (▲) and P4 (●). The vertical bars indicate the difference between the maximum and minimum value determined in three tests.

Therefore, the main interest was focused on the analysis of the coefficients a_1 and a_0. The contribution of a_2 to the evolution of the $F_F/F_N - n_{cycles}$ curve was not considered further, except the mathematical sign of coefficient a_2. The effect of the mathematical sign of coefficient a_2 on the curve shape has been already taken into account in the classification of the

curve types ($a_2 > 0$ if curve is of types I, II or IV, $a_2 < 0$ if curve of type III). The coefficients a_1 and a_0 were set in relation to the normal load to evaluate its influence on the friction.

Reference

The ratio F_F/F_N evolves as function of the cycle number for the various normal loads according to curve type II. At a normal load of 200 and 250 mN, stiction was observed. On raising the normal load, the coefficients a_1 and a_0 increase marginally with the normal load (Fig. 6.5).

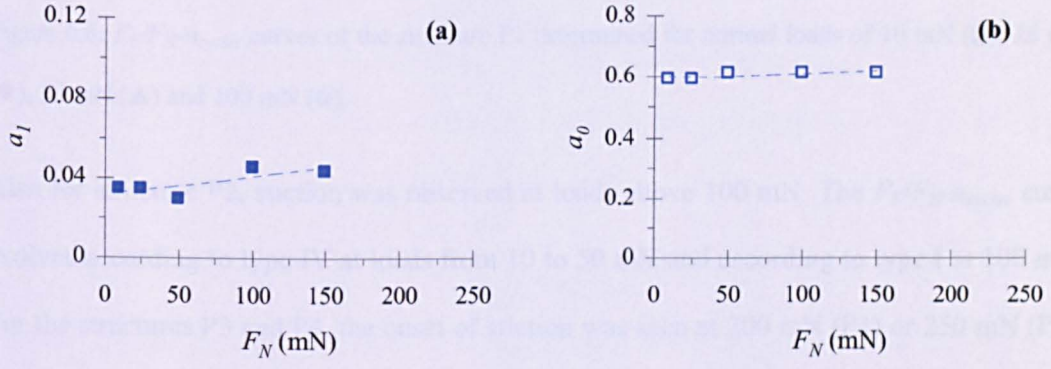

Figure 6.5: Influence of the normal load F_N applied in the LCC tests on the coefficients a_1 and a_0 for the reference surface. The values of a_0 and a_1 were determined only for tests without occurrence of stiction.

Pyramid-like Structured Surfaces

For structure P1, the F_F/F_N-n_{cycles} curves are all of the type I, whereby the friction could be determined only for normal loads ≤ 100 mN due to the occurrence of stiction at higher loads. The height and width of the peak of the F_F/F_N-n_{cycles} curve decrease on increasing the normal load (Fig. 6.6). As seen in Fig 6.6, the F_F/F_N ratio is often > 1. Different to conventional, macroscopic behaviour, the occurrence of such high values is a common feature in micro and nanotribological studies and can be attributed to the enhanced sensitivity of friction generating surface forces (Persson 2000).

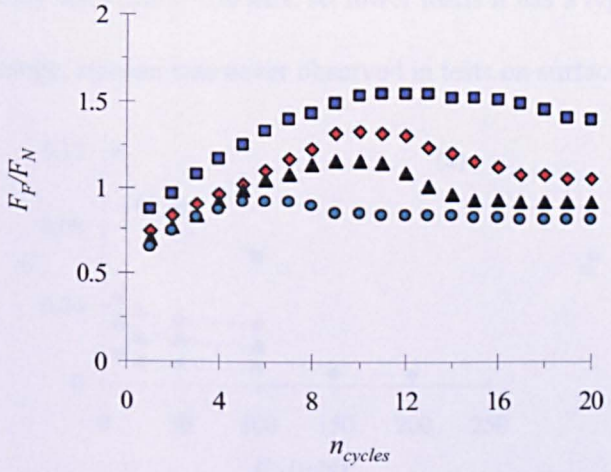

Figure 6.6: F_F/F_N-n_{cycles} curves of the structure P1 determined for normal loads of 10 mN (■), 25 mN (◆), 50 mN (▲) and 100 mN (●).

Also for structure P2, stiction was observed at loads above 100 mN. The F_F/F_N-n_{cycles} curve evolves according to type IV at loads from 10 to 50 mN and according to type I at 100 mN. For the structures P3 and P4, the onset of stiction was seen at 200 mN (P3) or 250 mN (P4), respectively. In the tests at lower loads, the F_F/F_N-n_{cycles} plots behave like type IV for both structures.

The frictional evolution as function of the normal load was compared between the different pyramid-like structured samples only for loads from 10 to 100 mN, since the friction for P1 and P2 could not be determined at higher loads due to stiction. For all pyramid-like structured surfaces, a_1 as well as a_0 decreases when increasing the load (Fig 6.7). Hereby, the decrease can be fitted with a potential equation. The evolution of a_1 and a_0 as function of the normal load shows a similar trend for all pyramid-like structured surfaces, but the actual values of a_1 and a_0 are continuously shifted to lower values on increasing the size of the pyramidal feature.

Cone-like Structured Surfaces

In case of the cone-like structured surfaces C1 and C2, the F_F/F_N ratio evolves according to type IV for loads below 150 mN (C1) or 250 mN (C2). Above these loads, stiction was observed in the tested systems. For surface C3, the F_F/F_N-n_{cycles} curve is also of type IV but

only for loads > 150 mN. At lower loads it has a type III shape. Within the investigated load range, stiction was never observed in tests on surface C3.

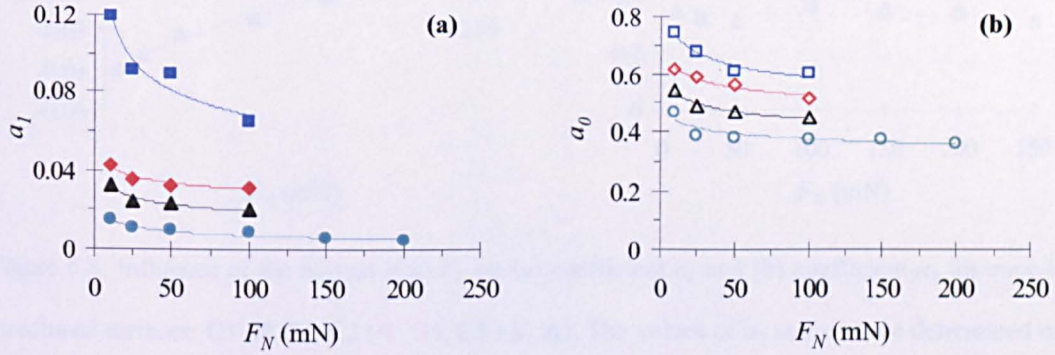

Figure 6.7: Influence of the normal load F_N on (a) coefficient a_1 and (b) coefficient a_0 for pyramid-like structured surfaces: P1 (■, □), P2 (◆, ◇), P3 (▲, △), P4 (●, ○). The values of a_0 and a_1 were determined only for tests without occurrence of stiction.

The frictional evolution as function of the normal load could be compared between C1, C2 and C3 only for loads ranging from 10 to 100 mN due to the early onset of stiction in case of structure C1. In the plots a_1 versus F_N (Fig 6.8a), a similar behaviour of the a_1 value was observed for the structures C1 and C2: At first the value remains nearly constant on increasing the load, whereas it increases above 50 mN. Generally, the a_1 values determined for C1 are slightly higher than the one for C2.

Different to C2 and C1, the a_1 values gradually increase with load for the surface C3. The a_1 values change from negative to positive value due to alteration of the frictional behaviour with time as indicated by the conversion from curve type IV to III.

The coefficient a_0 determined for C1 and C2 decreases almost linearly while increasing the normal load (Fig 6.8b). The difference in the actual value of the coefficient is only marginal between both surfaces. In case of structure C3, the value of a_0 remains nearly constant for all normal loads.

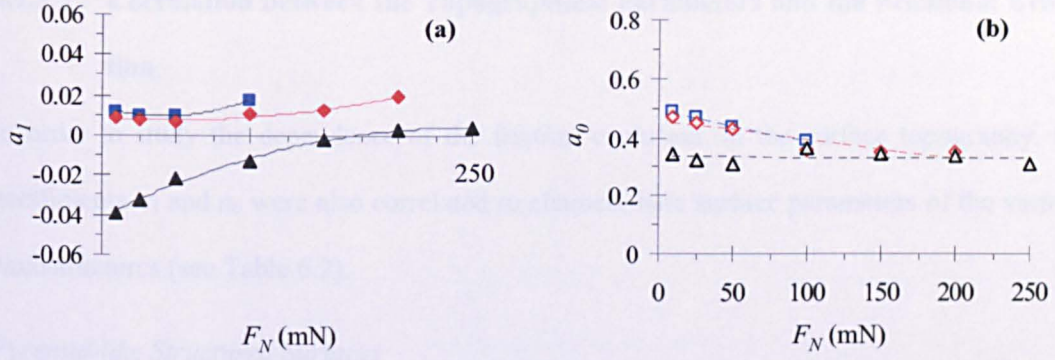

Figure 6.8: Influence of the normal load F_N on (a) coefficient a_1 and (b) coefficient a_0 for cone-like structured surfaces: C1 (■, □), C2 (◆, ◇), C3 (▲, △). The values of a_0 and a_1 were determined only for tests without occurrence of stiction.

Crater-like Structured Surfaces

For all crater-like structured surfaces, the ratio F_F/F_N evolves according to type IV. Stiction was observed at 250 mN only on the surfaces CR1 and CR6. The coefficient a_1 increases nearly linearly with the normal force for all tested surfaces (Fig. 6.9a). The coefficient a_0 changes only marginal with the normal load for the different surfaces (Fig. 6.9b).

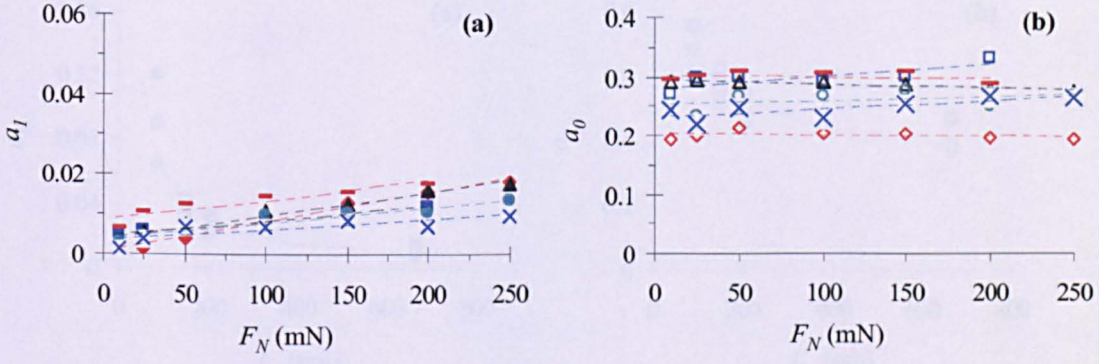

Figure 6.9: Influence of the normal load F_N on (a) coefficient a_1 and (b) coefficient a_0 for crater-like structured surfaces: CR1 (■, □), CR2 (◆, ◇), CR3 (▲, △), CR4 (●, ○), CR5 (✖) and CR6 (−). The values of a_0 and a_1 were determined only for tests without occurrence of stiction.

6.1.3.2 Correlation between the Topographical Parameters and the Frictional Evolution

In order to study the dependence of the friction evolution on the surface topography, the coefficients a_1 and a_0 were also correlated to characteristic surface parameters of the various nanostructures (see Table 6.2).

Pyramid-like Structured Surfaces

As shown in Figure 6.10, the correlation between coefficients a_1 and a_0 and the lateral dimension L_p can be described by equations of the type $a_1 = m_1 \cdot L_p^{-n1}$ and $a_0 = m_0 \cdot L_p^{-n0}$, respectively. For the analysed normal load range, the values of the parameters m_1, n_1, m_0 and n_0 at specific normal loads varied by no more than 15 % from the overall average. The values of parameters were determined to be $m_1 = 5.28 \pm 0.66$, $n_1 = 0.97 \pm 0.04$ and $m_0 = 1.91 \pm 0.28$, $n_0 = 0.24 \pm 0.02$. So, it appears that the actual value of the normal load does not influence significantly the correlation of a_1 and a_0 to L_p.

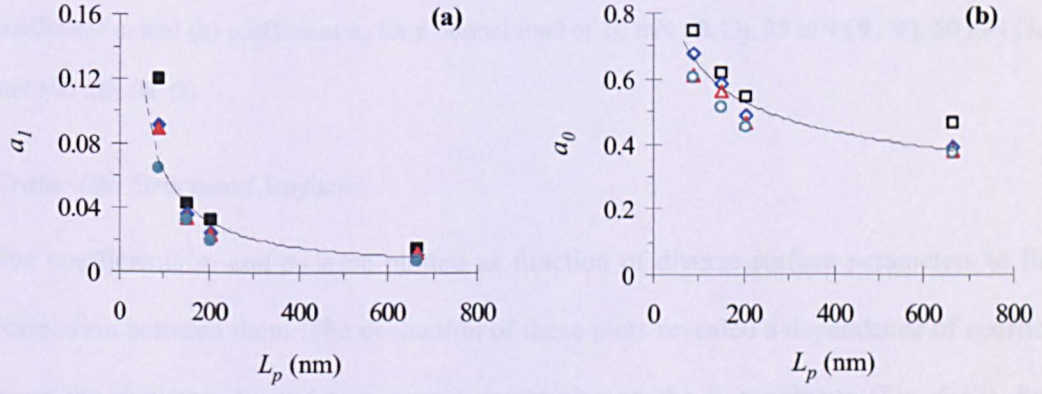

Figure 6.10: Functional correlation of lateral dimension L_p of the pyramidal features with (a) coefficient a_1 and (b) coefficient a_0 for normal loads of 10 mN (■, □), 25 mN (◆, ◇), 50 mN (▲, △) and 100 mN (●, ○).

Cone-like Structured Surfaces

When increasing the lateral dimension L_c from 134 nm to 237 nm, the coefficient a_1 decreases only slightly, whereas it changes quite dramatically for an L_c of 379 nm (Fig. 6.11a). The curves become slightly less steep with increasing load.

The coefficient a_0 is the lower the larger the size of the surface feature is, except for 100 mN normal load. In this case, the a_0 values are nearly identical for the three cone-like structured surfaces (Fig. 6.11b).

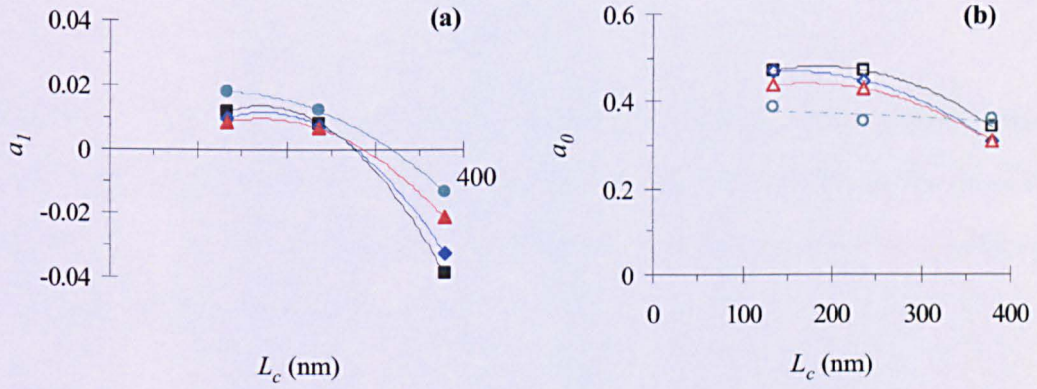

Figure 6.11: Functional correlation between the lateral dimension L_c of the conical features and (a) coefficient a_1 and (b) coefficient a_0 for a normal load of 10 mN (■, □), 25 mN (◆, ◇), 50 mN (▲, △) and 100 mN (●, ○).

Crater-like Structured Surfaces

The coefficients a_1 and a_0 were plotted as function of diverse surface parameters to find a correlation between them. The evaluation of these plots revealed a dependence of coefficient a_1 on the skewness S_{sk} and to a certain extent also on the S_q roughness (Fig. 6.12). For S_q roughness between 9 and 12 nm, while the skewness decreases from positive to negative values, a_1 at first decreases, reaching its minimum value at between -0.3 and -0.4 and then increases. This behaviour was observed only at normal loads ≤ 50 mN. At higher normal loads, the a_1 appears to increase continuously on lowering the skewness values. For higher S_q roughness (20 to 22 nm), the evolution of a_1 with S_{sk} appears not to be influenced by the normal load, although the curves shift to higher values as the load increases. In all tests, a_1

values of surfaces with positive or moderate negative skewness are similar but significantly lower than the ones measured on surface with high negative skewness.

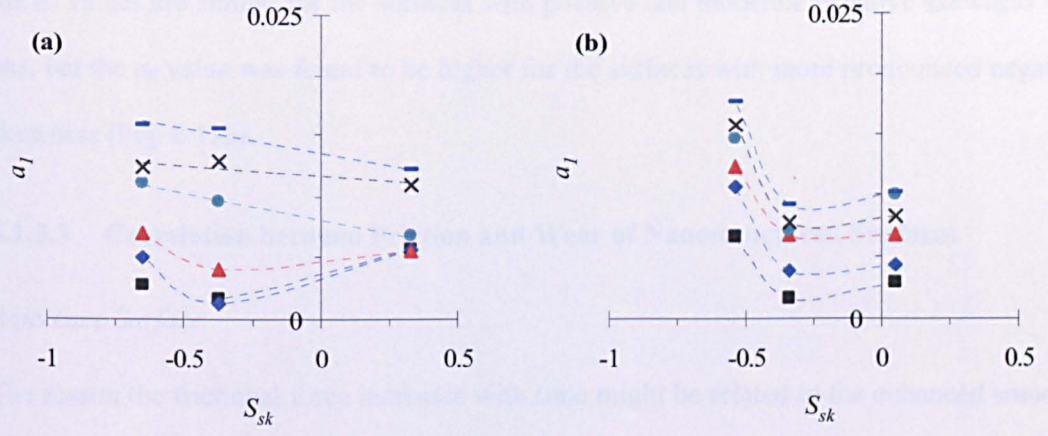

Figure 6.12: Functional correlation between the skewness S_{sk} of the crater-like structured surfaces and coefficient a_1 in the roughness range of (a) 9 nm ≤ S_q ≤ 12 nm (CR1 to CR3) and (b) 20 nm ≤ S_q ≤ 22 nm (CR4 to CR6) for a normal load of 10 mN (■, □), 25 mN (◆, ◇), 50 mN (▲, △), 100 mN (●, ○), 150 mN (✖) and 200 mN (−).

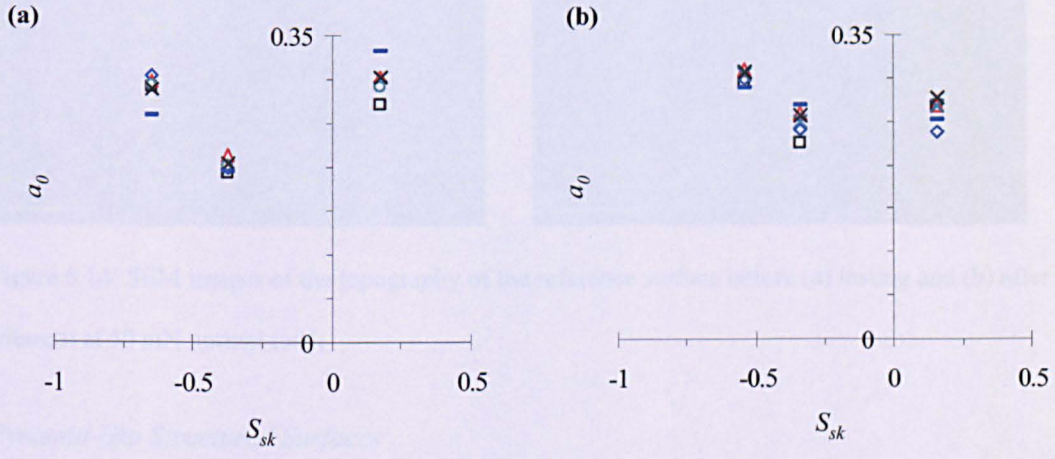

Figure 6.13: Functional correlation between the skewness S_{sk} of the crater-like structured surfaces and coefficient a_0 in the roughness range of (a) 9 nm ≤ S_q ≥ 12 nm (CR1 to CR3) and (b) 20 nm ≤ S_q ≥ 25 nm (CR4 to CR6) for a normal load of 10 mN (■, □), 25 mN (◆, ◇), 50 mN (▲, △), 100 mN (●, ○), 150 mN (✖) and 200 mN (−).

Regarding the coefficient a_0, comparable values were determined for the crater-like structured surfaces with roughness between 9 nm ≤ S_q ≤ 12 nm, despite having different positive

and negative skewness (Fig. 6.13a). The only exception is the samples with skewness of S_{sk} = -0.373, which shows a significantly lower a_0 value. For samples with higher roughness, the a_0 values are similar for the surfaces with positive and moderate negative skewness values, but the a_0 value was found to be higher for the surfaces with more pronounced negative skewness (Fig. 6.13b).

6.1.3.3 Correlation between Friction and Wear of Nanostructured Surfaces

Reference Surface

The reason the frictional force increases with time might be related to the enhanced smoothening of the surface topography induced by deformation and wear processes (Fig 6.14). Thereby, the contact area between the mating surfaces increases and, thus, so does the adhesive friction in the system (see equ. 3.2).

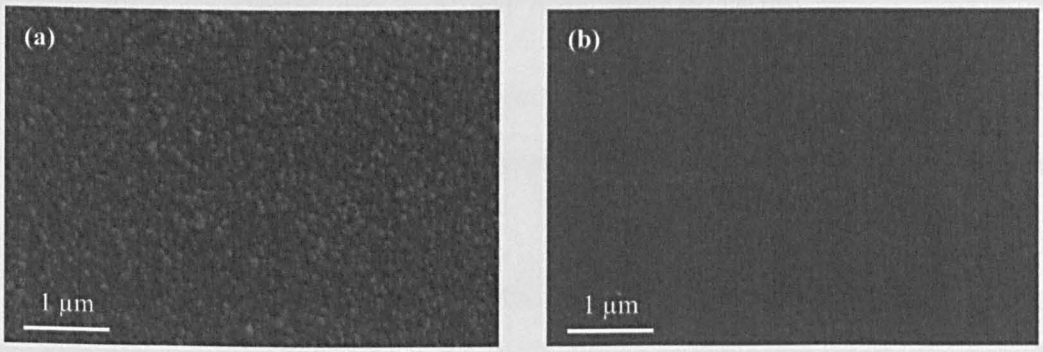

Figure 6.14: SEM images of the topography of the reference surface before (a) testing and (b) after the tribotest at 50 mN normal load.

Pyramid-like Structured Surfaces

The tribological-loaded contact zone of the pyramid-like structured surfaces was analysed by SEM. In case of structure P1, a levelling of the surface features, formation of cracks perpendicular to the sliding direction and even the partial break-off of material of the surface-near region were observed for all loads (Fig. 6.15).

Similar destructions of the surface topography occur also on the other pyramid-like structured surfaces. The severity of wear diminishes with increasing feature size at same normal

loads. So, the onset of cracking is postponed from 10 mN for P1 to 100 mN or 150 mN for P2 and P3, respectively. A cracking of structure P4 was not observed in the range of normal loads investigated here.

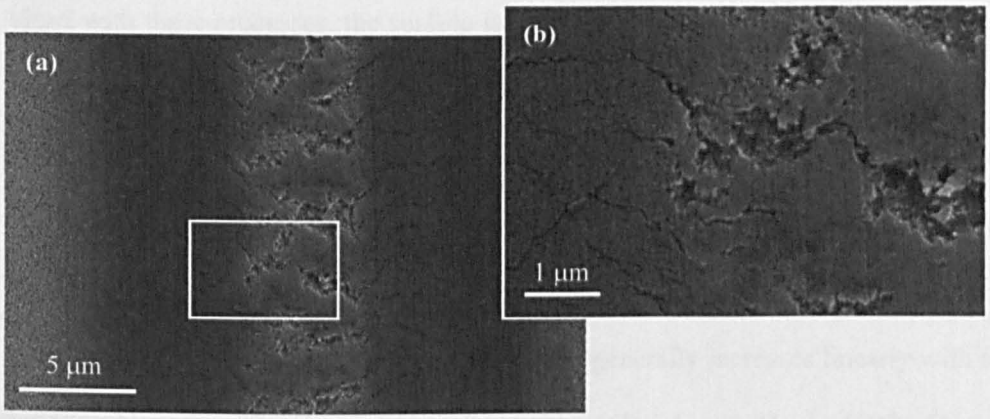

Figure 6.15: SEM images showing the alteration of surface topography of sample P1 in tribologically stressed zone on surface P1 after testing at a normal load of 10 mN. Figure (b) is a micrograph at higher magnification from the region indicated (white-framed box) in (a).

Based on the frictional evolution with time and the analysis of the worn contact zones, the tribolologically induced damage of any pyramid-like structured surfaces is presumed to proceed as follows:

When applying the normal load, the pyramid points are plastically deformed, since the contact stress exceeds the mechanical strength of the material. The deformed material is pushed to the sides of the asperities. Other studies have shown that asperities even at the nanoscale do not break but start to flow under sufficiently high contact pressure (Landman & Luedtke 1993). The deformation of the asperities leads to a levelling of the surface topography. The generation of a flat, closed surface region (layer) above the columnar microstructure of the pyramid-like structured films is probably enhanced through bridging or filling the gaps between the surface features with the material pushed aside from the asperities. The smoothing of the topography results in an enlargement of the real contact area, which certainly augments the adhesive force (see equ. 3.2), thus, increases the friction in the system. Moreover, the lateral sliding of the counter body on the sample surface might support the levelling of

the surfaces by smearing out the deformed material around the asperities or shearing off additional material from the asperities. Perhaps caused by high friction (adhesion) and low shear strength, the surface cracks and material is even broken off (surface fatigue). Combined with these processes, the surface topography is modified again, but this time the contact area diminishes, which causes a reduced friction in the system. Under this presumption a peak in the F_F/F_N–n_{cycles} curve (see Fig. 6.6) marks the transformation from a pyramid-like, rough topography to a flat, smooth one in the (almost) complete nominal contact area.

Usually, a linear relationship between friction and normal load can be expected in adhesion-dominated systems, since the real area of contact generally increases linearly with the normal load in plastic contacts for multiasperity contacts (Czichos & Habig 1992). However, Williamson et al. (cited in Azushima et al. 2006) propounded a theory of plastic contact which took into account the redistribution of material displaced from deformed asperities and showed a non-linear increase of the contact area with the normal load for surfaces with closely spaced asperities. In case of pyramid-like structured surfaces, a non-linear correlation between contact area and normal load can probably be also assumed due to the formation of closed surface layer on top of the film. Beside this, the lowering of the peak in the F_F/F_N-n_{yncles} curve with higher loads (see Fig. 6.6) might be attributed to the fact that the proportion of the zone exhibiting a smooth surface structure on the total contact zone decreases with increasing the normal load (Fig. 6.16) and, thus, the contribution of the adhesion to the friction force might be lower. The narrowing of the friction peak at higher normal loads is probably caused by accelerated surface fatigue with the result that the phase of a smooth surface topography and, thus, high friction is passed through more quickly.

The earlier occurrence of surface fatigue induced damage at increased normal loads seems probable since the initiation of cracks is strongly influenced by tangential stress related to the contact mechanics and the frictional work generated in the system (Szolwinski & Farris 1996). Therefore, the peak vertex is shifted to lower F_F/F_N ratios when increasing the normal load on an individual pyramid-like structure.

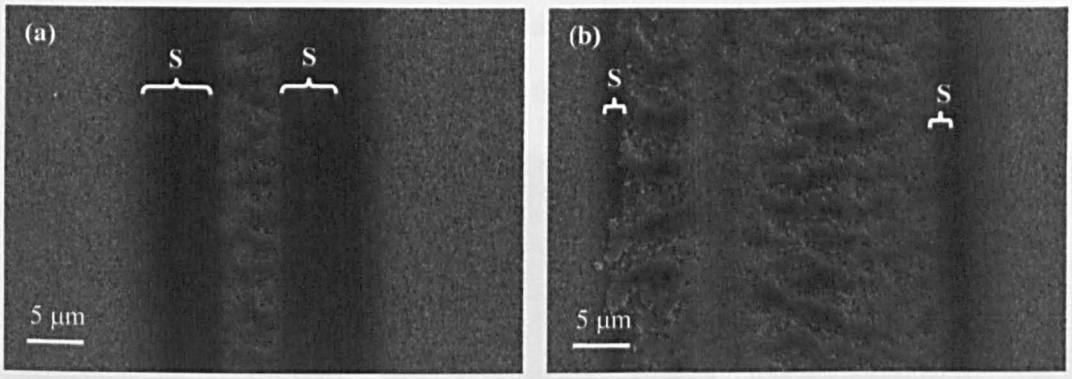

Figure 6.16: SEM images of the tribologically stressed zone of the pyramid-like structured surface P1 after testing at different normal loads of (a) 10 mN and (b) 100 mN. The bracket marked with S represents the width of the wear track exhibiting a smoothened surface topography.

On increasing the size of the pyramidal features, the generation of a closed surface is hindered or inhibited due to the larger gaps between the asperities. Therefore, the increase of friction is less pronounced; hence, the values of a_1 and a_0 are smaller on surfaces with larger lateral feature dimensions.

Cone-like Structured Surfaces

For all cone-like structured surfaces, a flattening of the surface features was observed as result of deformation and wear. The flattening is more pronounced for higher normal loads (Fig. 6.17).

From the experimental data the following explanation of wear and connected to this the frictional behaviour of cone-like structured surfaces was deduced: By shearing-off material from the conical asperities, the contact area is expanded: Thereby, adhesion and, thus, the friction in the system increase, which results in positive a_1 values. On increasing the normal load, accelerated wear should enhance the increase of friction and, thus, the increase of a_1. Beside the augmentation of adhesion forces, loose particles, that were generated in the wear process and were not trapped in the gaps between the asperities, might negatively affect sliding and cause additional friction in the system. However, an increase of the a_1 coefficient, which might correspond to such effects, was only observed while applying normal loads above

50 mN for C1 and C2. The reason for that might be that the wear of the asperities proceeded sufficiently to be detected by changes in the friction only at higher loads.

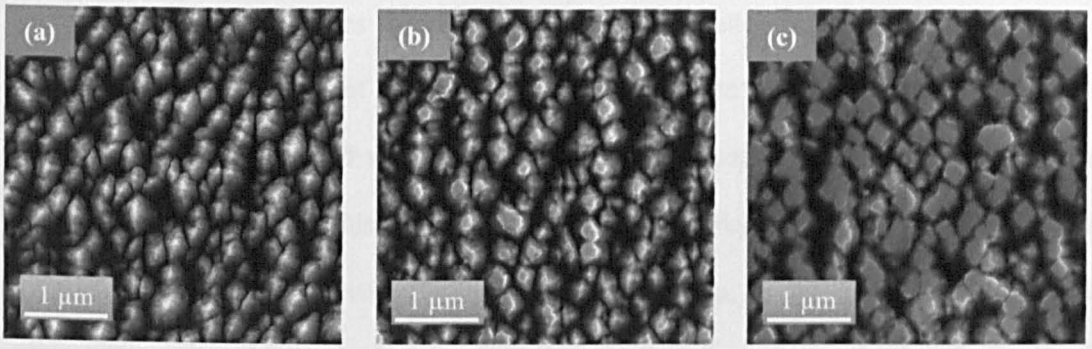

Figure 6.17: SEM images of the topography of structure C3 before testing (a), after testing at a normal load of 10 mN (b) and 250 mN (c).

This elucidation does not explain the experimental data found for C3. For this structure, the friction decreases and then stabilizes after a certain time. The time to establish stable friction decreases with higher normal loads (shifting of a_1 to less negative values). Probably due to the large dimensions of the surface features and their moderately high hardness, the asperities might firstly act as obstacles for the sliding motion of the mating surfaces and, therefore, cause higher friction at the beginning of the tests. During the first cycles in the tests the asperities tops are worn off and the friction decreases as result of the smoothened surface. Finally, the friction remains nearly constant when a stable surface topography is created in the contact zone. This stage seems to be reached when the shearing of material from the truncated asperities requires more energy than supplied by the system. At higher loads, the conversion to this stable topography is obtained faster due to the accelerated truncation of the asperity tops. However, if the normal loads exceeds a certain value (~ 150 mN for C3), the energy in the contact zone is sufficiently high for a continuous shearing of the material. In this case the friction and wear evolution might follow the principles as described for structures C1 and C2.

Crater-like Structured Surfaces

The described variation in frictional behaviour with changing skewness and roughness of crater-like structured surfaces might be explained in the following way. At low loads, the wear related modifications of the surface topography of the crater-like structured surfaces can presumably be excluded since no indication of damages of the surface structures was observed by SEM. Under this condition, the relatively spiky topography of surfaces with positive skewness, as schematically shown in Figure 6.18a, might support ploughing and wear on the counter body which can cause higher friction than a less spiky surface, e.g., surfaces with negative skewness.

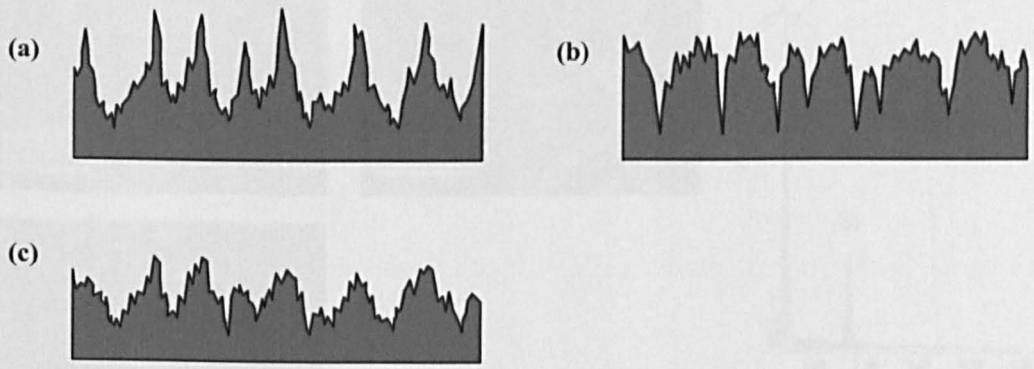

Figure 6.18: Schematic profile of surfaces with (a) positive skewness, (b) highly negative skewness and (c) moderate negative skewness.

The assumption, that the counterbody was worn in this case rather than the sample, was confirmed by an EDS analysis of particles found in the cavities of the crater topography (see Fig. 6.19). In this analysis, the chemical elements the particle material consists of were identified as silicon, oxygen and nitrogen. The occurrence of oxygen is presumably related to oxidation of the counter body material (Si_3N_4).

High friction might also occur on a surface with highly negative skewness (Fig. 6.18b) due to an increased real contact area, thus, probably enhanced adhesion in the system. A topography of moderate negative skewness (Fig. 6.18c) appears to present an optimum surface under such considerations, as seen in the tribological tests.

At higher loads, indications of wear were found by analysing the crater-like structured surfaces by SEM (Fig. 6.19). It is assumed that the onset of wear causes the alteration in the a_l-S_{sk} correlation at normal loads above 50 mN. The spiky features of surfaces with positive skewness are flattened to a certain level due to wear processes. Caused by topographical changes in the contact zone, ploughing might be reduced or eliminated in favour of adhesion. Wear induced flattening of the surface features was observed also on surfaces with moderate and highly negative skewness.

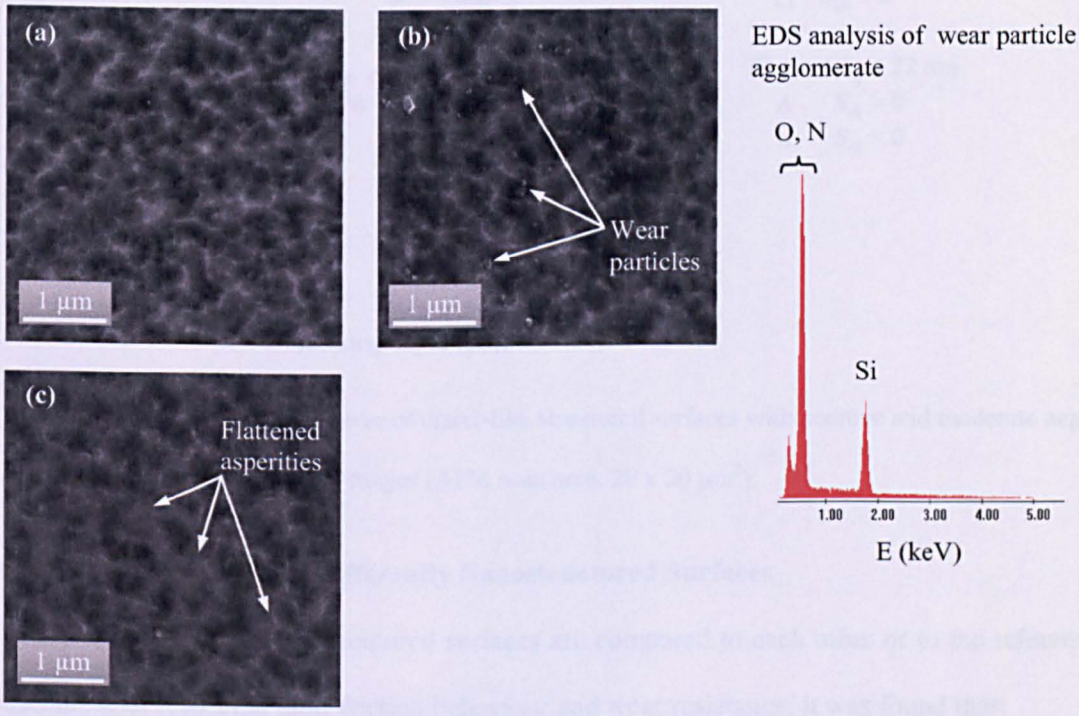

Figure 6.19: SEM images of the topography of crater-like structured surface CR5 (a) before testing (a) and after testing at a normal load of (b) 10 mN and (c) 100 mN (c). The figure shows also an element spectrum obtained by EDS of agglomerates of wear particles.

Under the condition that the wear rate is similar for the different crater-like structured samples, the increase in the wear depth results in a more pronounced expansion of the contact area on surfaces with negative skewness than for samples with positive one. To illustrate this, a part of the Abbott-Firestone curve (see Appendix A.1) is shown for surfaces with positive and moderate negative skewness in Figure 6.20. In this context it is assumed that the surface area obtained after wearing the sample down to certain wear depth is equal to the

bearing area at the corresponding depth level. For the rougher surfaces, the difference in the a_1 value between positive and moderate negative surface appears to be less pronounced because of the similarity between samples with positive and moderate negative skewness with respect to their Abbot-Firestone curves.

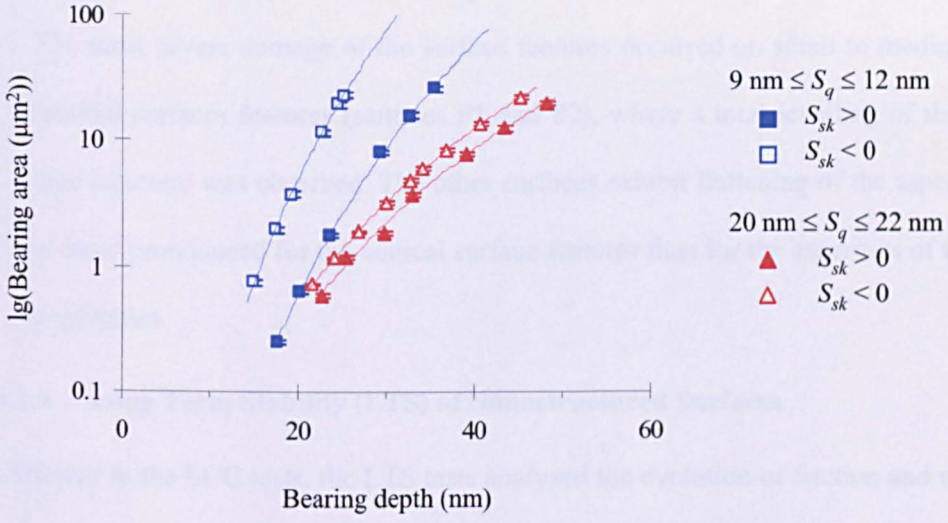

Figure 6.20: Abbot-Firestone curve of crater-like structured surfaces with positive and moderate negative skewness in two roughness ranges (AFM scan area: 20 x 20 µm²).

6.1.3.4 Comparison of Differently Nanostructured Surfaces

When the differently nanostructured surfaces are compared to each other or to the reference surface with respect to their friction behaviour and wear resistance, it was found that:

- Except for surface P1, lower friction was always measured on the nanostructured surfaces than on the reference.
- Amongst the nanostructured surfaces, the crater-like topographies exhibit the lowest friction, and pyramid-like topographies the highest friction. By increasing the lateral dimension of the pyramidal or conical features, friction can be reduced and approaches the values obtained for crater-like structured surfaces.
- The friction generated on crater-like structured surfaces and the reference is less sensitive to the actual value of the normal load than on pyramid-like and cone-like structured sur-

faces; this is attributed to the higher wear resistance of the crater-like structured surface and the reference.

- In the experimental set-up of this study, wear was detected already at 10 mN normal load on all pyramid-like and cone-like structured surfaces, whereas indications of wear were found only at loads of at least 50 mN on crater-like surfaces and the reference.
- The most severe damage of the surface features occurred on small to medium sized pyramidal surfaces features (samples P1 and P2), where a total levelling of the initial surface structure was observed. The other surfaces exhibit flattening of the asperities, which is more pronounced for the conical surface features than for the asperities of the crater topographies.

6.1.4 Long Term Stability (LTS) of Nanostructured Surfaces

Different to the LCC tests, the LTS tests analysed the evolution of friction and wear over an extended test duration (20, 50, 100, 500, 1000 and 2000 cycles) for three selected normal loads (10, 50 and 150 mN) on pyramid-like (P1 to P4), cone-like (C1 to C3) and crater-like (CR1, CR3, CR4 and CR6) nanostructured Cr-N films and on a relatively smooth Cr-N film (Ref). Though having different roughness and skewness, all crater-like structured surfaces show a similar behaviour in these tests. Therefore, the tests were not extended to a larger number of samples with crater-like topography.

For better illustration of the experimental data, the F_F/F_N ratio was plotted versus the logarithm of n_{cycles} for the differently nanostructured surfaces and the reference sample tested at three normal loads. For all investigated surfaces, the F_F/F_N ratio increases steadily with the logarithm of the cycle number, as shown in Figure 6.21. This is related to the enhanced levelling of the surface topography and, thus, the augmentation of adhesive friction.

Also here, relatively high friction coefficients were determined in some tests. As mentioned earlier, the occurrence of such high μ values in microtribological tests is attributed to the enhanced sensitivity of friction generating surface forces, e.g. adhesion as in this study.

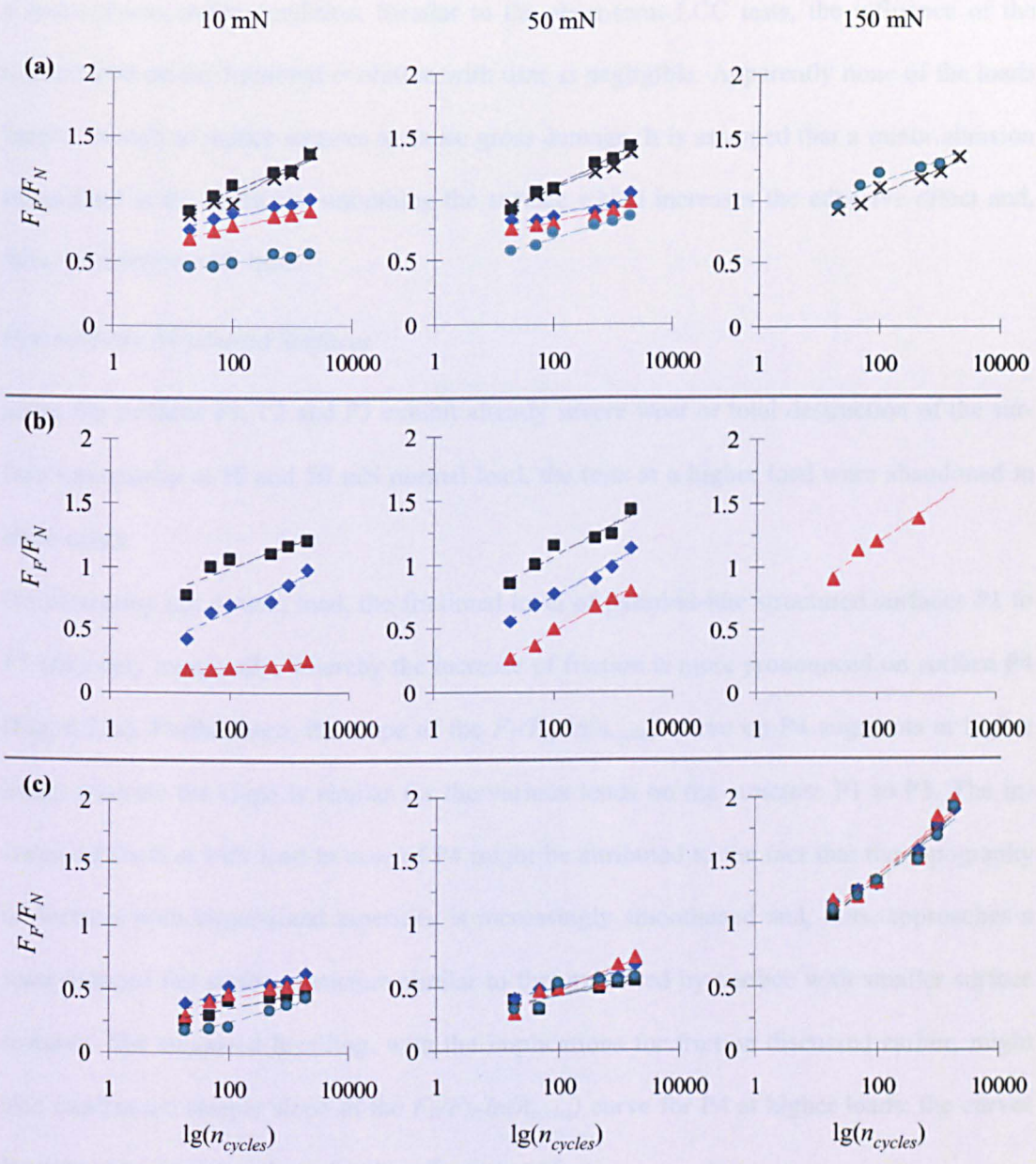

Figure 6.21: Dependence of F_F/F_N on the logarithm of cycle number n_{cycles} at normal loads of 10, 50 and 150 mN for the reference surface, marked as ✖ in (a), and Cr-N films with

(a) pyramid-like structured surfaces: ■ P1, ◆ P2, ▲ P3, ● P4

(b) cone-like structured surfaces: ■ C1, ◆ C2, ▲ C3

(c) crater-like structured surfaces: ■ CR1, ◆ CR3, ▲ CR4, ● CR6.

Reference

The steady increase of friction against a log scale means that there is an asymptotic behaviour against the number of cycles (Fig. 6.21a), suggesting wear of the residual topography to

a more-or-less stable condition. Similar to the short-term LCC tests, the influence of the normal load on the frictional evolution with time is negligible. Apparently none of the loads here is enough to induce stresses to cause gross damage. It is assumed that a minor abrasion component is the agent for smoothing the surface which increases the adhesive effect and, thus, the friction with time.

Pyramid-like Structured Surfaces

Since the surfaces P1, P2 and P3 exhibit already severe wear or total destruction of the surface topography at 10 and 50 mN normal load, the tests at a higher load were abandoned in these cases.

On increasing the normal load, the frictional level of pyramid-like structured surfaces P1 to P3 rises only marginally, whereby the increase of friction is more pronounced on surface P4 (Fig. 6.21a). Furthermore, the slope of the F_F/F_N-$ln(n_{cycles})$ curve on P4 augments at higher loads, whereas the slope is similar for the various loads on the structure P1 to P3. The increase of friction with load in case of P4 might be attributed to the fact that the topography of surfaces with larger-sized asperities is increasingly smoothened and, thus, approaches a wear-induced flat surface structure similar to that exhibited by surface with smaller surface features. The enhanced levelling, with the implications for friction discussed earlier, might also explain the steeper slope of the F_F/F_N-$ln(n_{cycles})$ curve for P4 at higher loads: the curves become very similar to those for the reference surface.

Cone-like Structured Surfaces

Compared to the tests at 10 mN, the friction level rises on cone-like structured surfaces at higher normal loads, whereby the friction changes more significantly on C3 compared to C1 and C2 (Fig. 6.21b). High friction causes stiction in the tests at 150 mN on cone-like structured samples. The stiction occurs after 500 cycles on sample C3 but at much lower numbers in the cases of C1 and C2, which is why their results are not shown for that load.

Additionally, an increase of the slope of the F_F/F_N-$ln(n_{cycles})$ curve was seen for surface C3 when a normal load of 50 mN was applied in stead of 10 mN. The slope of C3 becomes very similar to those for the reference surface. However, the slope does not change further at a normal load of 150 mN, but the friction values are all shifted upwards.

Mechanisms similar to those discussed for pyramid-like structured samples, might apply here to the varying frictional behaviour of sample C3. A higher normal load is required to generate a wear-induced smoothening of the surface structure similar to that seen on the surface C1 and C2.

Crater-like Structured Surfaces

Similar to the pyramid-like and cone-like structured surfaces, the friction measured on the crater-like structured surfaces increase with the normal load applied (Fig. 6.21c). The slope of the F_F/F_N-$ln(n_{cycles})$ curve is similar for 10 and 50 mN normal load, but it has a higher value for 150 mN. Also here, the difference in friction between the crater-like structured surfaces diminishes in the tests at higher normal loads probably due to the functionally relevant features of the wear-induced topographies of the various samples becoming more similar and approximating those of a 'smooth' surface.

6.1.4.1 Comparison of Differently Nanostructured Surfaces

Similar to the nanostructured surfaces, friction measured on the reference sample rises steadily with the number of cycles. However, the friction on the reference surface hardly changes while increasing load or cycle number, probably because the surface topography changes only marginally by deformation or shearing-off asperities. The surface features of the nanostructured surfaces are larger-sized and, thus, alterations of the asperities might affect the friction much more strongly in these cases. Nevertheless, the friction recorded on nanostructured surfaces is mostly lower than on the reference surface. Nevertheless, it appears that the nanostructured surfaces are preferentially applicable at low loads ($\leq$ 10 mN under the conditions applied in this study) to avoid serious damages of the surface features and, thus, nega-

tive effects on the frictional behaviour. In the test at 10 mN normal load, the sample C3 exhibits the lowest friction and, further, the smallest increase in friction with time.

6.2 Comparison of Nanostructured Surfaces in Lubricated Contacts (EG 2)

The goal of these experiments was to study whether nanostructuring can influence the lubrication effects, namely the reduction of friction and the minimization of wear, in the system compared to a relatively smooth reference surface. The correlation between friction force and nanostructure was analysed at various normal loads, sliding velocities and for oils with different viscosities.

The results obtained in these tests are summarized and discussed on the following pages. Examples of the friction measurements are shown in Appendix A.3. The details of the tribological experiments conducted in EG 2 are given in more detail in section 4.3.3.

6.2.1 Surfaces Investigated in EG 2

The structural (phase and crystallographic texture of the thin film) and relevant mechanical properties of the surfaces investigated in EG 2 are summarized in Table 6.1. Selected topographical parameters of the surfaces are given in Table 6.2. SEM and AFM images of the nanostructures tested are presented in Appendix A.3.

6.2.2 Microfrictional Behaviour of Nanostructured Surfaces in Lubricated Contacts

Figure 6.22 shows a typical evolution of the friction force recorded over 20 cycles. It can be seen that after a brief running-in period of about 5 cycles, the friction amplitude became stabilized and remained constant afterwards. The friction force was determined from the stable stage as indicated in Figure 6.22.

For all the conditions used in this work, the friction force was well represented by taking it to be linearly proportional to the applied normal load. In worst case, the fitting confidence has a value of $R^2 = 0.95$, whereas the R^2 value is usually around 0.98. Figure 6.23 shows an example of a typical measurement. Therefore, the coefficients of friction μ were determined by performing a linear fit to the friction-load curves and recording the slope of the curves.

The friction coefficients were measured on the PAO lubricated reference surface and the differently structured surfaces with pyramid-like topography (P1 to P4), cone-like topogra-

phy (C1 to C3) and crater-like topography (CR1 to CR6). These results were compared to the data obtained in tests on unlubricated surfaces (EG 1).

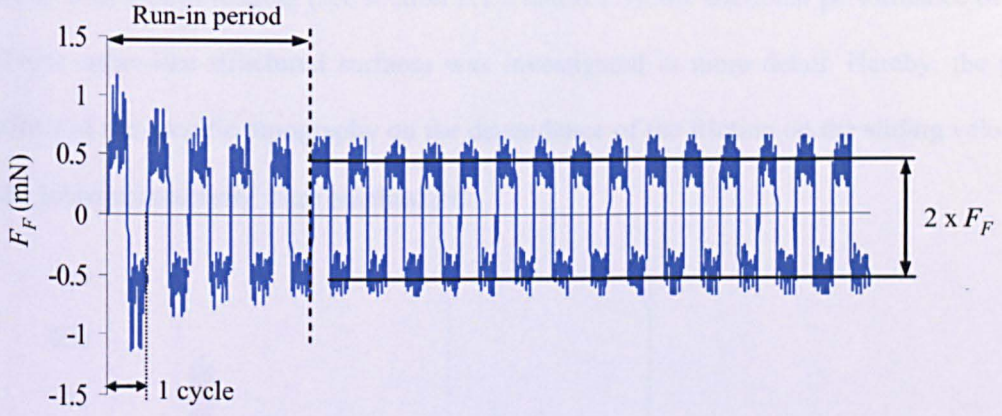

Figure 6.22: Friction force F_F evolution as function of cycle number. The example shows a friction curve recorded on structure CR6 (lubricated with MO40, speed 25 µm/s, normal load 3 mN, cycle period 13 s).

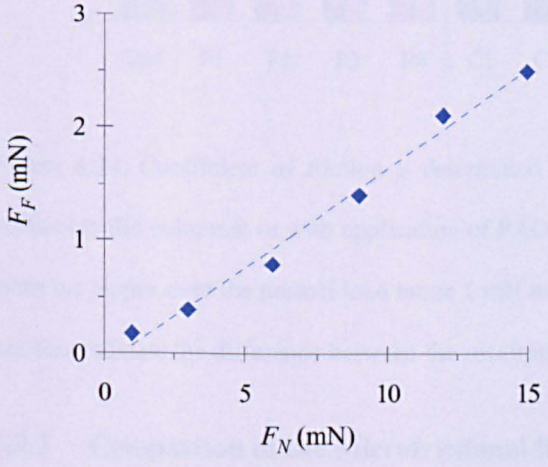

Figure 6.23: Friction force F_F measured as function of the normal force F_N on the reference sample lubricated with MO4 in a test at a sliding speed of 300 µm/s.

As Figure 6.24 shows, applying a lubricant diminished the friction on all surfaces, whereby no specific surface has more than 20 % reduction from lubrication. Most significant lowering in friction was observed on the reference and the nanostructured surfaces P1 (20 %), CR2 (17 %), CR4 (17 %) and C3 (20 %). Nevertheless, the reference, pyramid and cone-like

structured surfaces, except sample C3, do not reach the friction level generated on the crater-like structured surfaces. Since the crater-like topography was found to exhibit a higher stability to tribological loading (see section 6.1.2 and 6.1.3), the frictional performance of the different crater-like structured surfaces was investigated in more detail. Hereby, the possible effect of the specific topography on the dependence of the friction on the sliding velocity and the lubricant viscosity were emphasized.

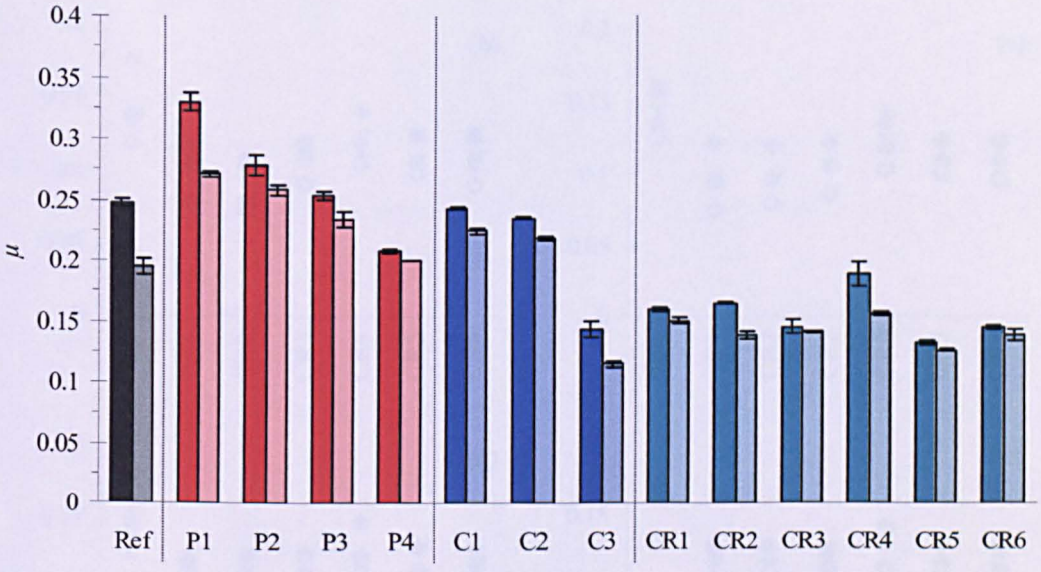

Figure 6.24: Coefficient of friction μ determined for various nanostructured surfaces in tests with without (solid columns) or with application of PAO oil (striped columns). The μ values were obtained from the slopes over the normal load range 1 mN to 15 mN at a sliding velocity of 25 µm/s. The vertical bars indicate the difference between the maximum and minimum μ value determined in three tests.

6.2.3 Comparison of the Microfrictional Behaviour of Lubricated, Crater-like Structured Surfaces at Low Loads

6.2.3.1 Influence of Crater-like Structure on Friction

The friction measured on the crater-like structured surfaces, CR1 to CR6, is generally lower than on the reference surface for all oil viscosities tested and for all sliding velocities (see Fig. 6.25).

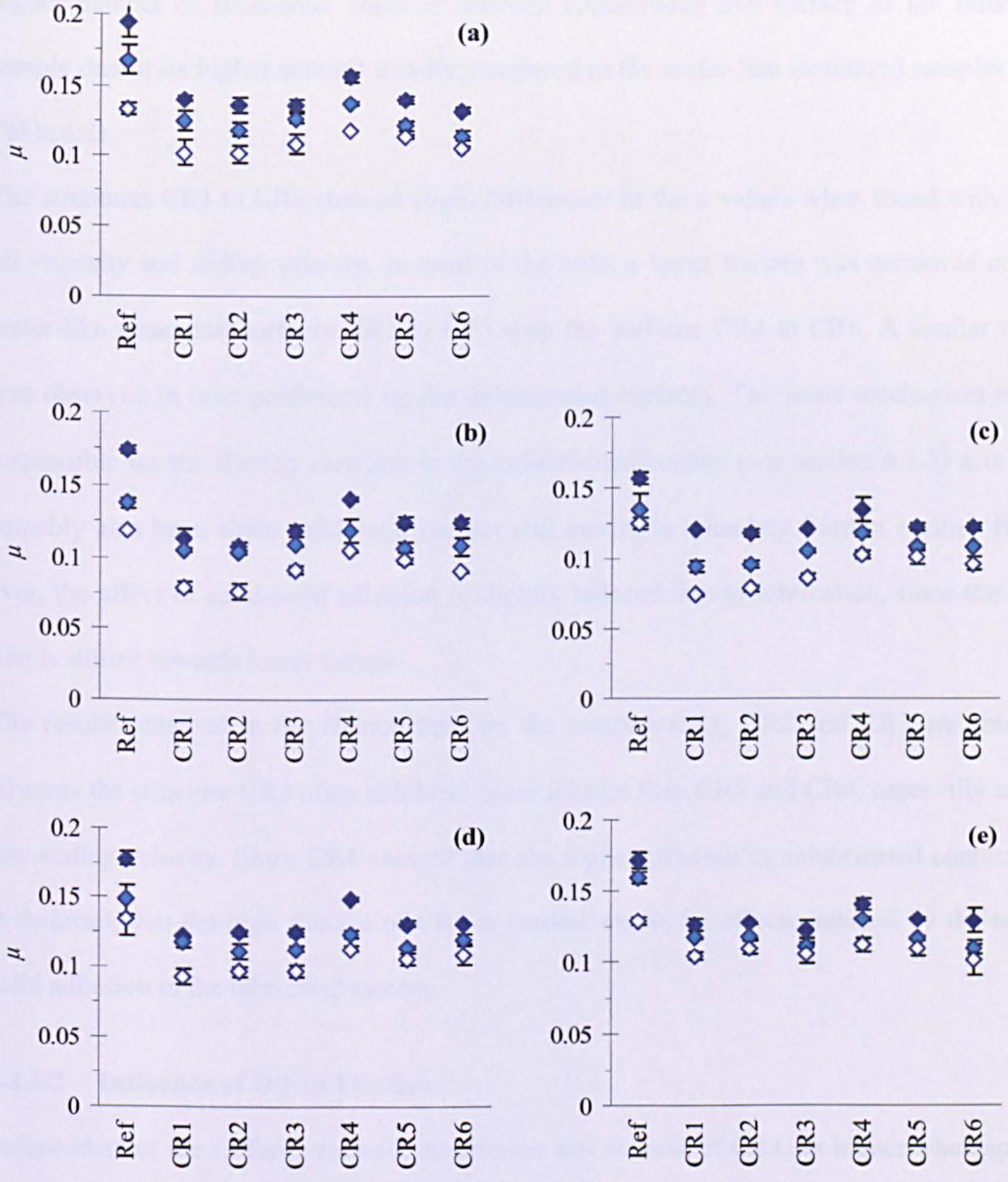

Figure 6.25: Coefficient of friction μ determined on the reference and crater-likes structured surfaces (CR1 to CR6) lubricated with oil (a) PAO, (b) MO4, (c) MO40, (d) MO96 and (e) MO200 and tested at sliding velocities of 25 µm/s (◆), 300 µm/s (◈) and 500 µm/s (◇).The vertical bars indicate the difference between the maximum and minimum μ value determined in three tests.

Based on the μ values determined, it is assumed that the system is operating in the boundary lubrication regime. Hence, the solid-solid adhesion might dominate over the contribution of the liquid shearing to the friction in the system, especially at low sliding velocities. Taking this into account, the higher friction on the reference can be explained by the occurrence of a

higher number of solid-solid contacts between counterbody and surface of the reference sample due to its higher summit density compared to the crater-like structured samples (see Table 6.2).

The structures CR1 to CR6 showed slight differences in the μ values when tested with each oil viscosity and sliding velocity. In most of the tests, a lower friction was measured on the crater-like structured surfaces CR1 to CR3 than the surfaces CR4 to CR6. A similar trend was observed in tests performed on the unlubricated surfaces. The same mechanism being responsible for the friction variation in the unlubricated contact (see section 6.1.2) acts presumably also here, since solid-solid contact still occurs in boundary friction regime. However, the effect of solid-solid adhesion is slightly reduced due to lubrication, since the friction is shifted towards lower values.

The results obtained in the friction tests on the samples CR1, CR2 and CR3 are similar, whereas the structure CR4 often exhibits higher friction than CR5 and CR6, especially at the low sliding velocity. Since CR4 showed also the highest friction in unlubricated contacts, it is deduced, that the high friction of CR4 is caused, again, by effects induced by the solid-solid adhesion in the lubricated system.

6.2.3.2 Influence of Oil on Friction

Independent of the surface structure, the friction was in most of the tests higher when applying PAO instead of one of the mineral oils (Fig. 6.26). When comparing the various mineral oils, the μ values recorded on all surfaces was lower when lubricated with less viscous oils (4, 40 cSt) than with ones that are more viscous (96, 200 cSt).

The majority of practical situations follow the Stribeck curve, in which an increase in viscosity generally leads to reduced friction due to enhanced pressure support of the more viscous oils. The present observations contradict this model. It appears that at the conditions used in this particular work, relatively low sliding velocity and low normal forces, the pressure capability of the lubricant is less important for the development of friction. Further evidence for this conclusion is seen in the linear increase of the friction force with the normal load

(see Fig. 6.23). In the case of a pressure dependence of the friction, the friction is expected to decrease with increasing pressure. In this study, the friction seems to be more influenced by shearing forces occurring in the lubricant. The shear losses, and therefore the friction, can be expected to be larger for higher viscous oils.

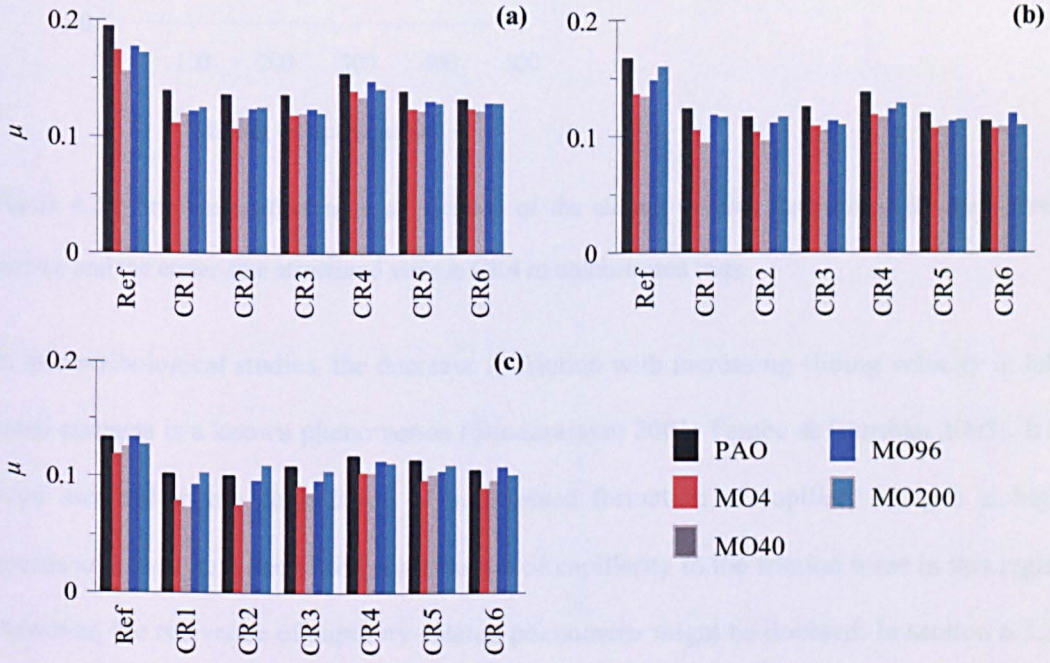

Figure 6.26: Coefficient of friction μ measured on the reference and different crater-like structured surfaces (CR1 to CR6) in test with sliding speeds of (a) 25, (b) 300 and (c) 500 µm/s and lubricated with various oils. (Data are redrawn from Figure 6.25).

6.2.3.3 Influence of Sliding Velocity on Friction

For the reference and all rough surfaces, the values of μ decreases at higher sliding velocities (see Fig. 6.25). The friction is reduced by 13 to 30 % while increasing the sliding velocity from 25 to 500 µm/s. There is no systematic evidence that the friction-velocity dependence might be connected to the viscosity of the oil applied in the systems.

The alteration of the friction can probably be attributed to mechanisms requiring the presence of a liquid, since the friction remains unaffected in tests with varied velocities in unlubricated contacts (see Fig. 6.27).

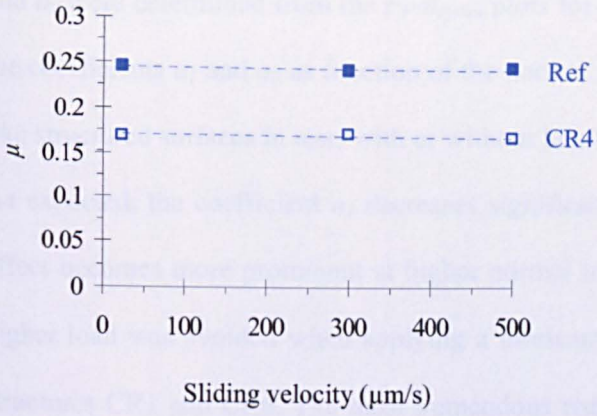

Figure 6.27: Friction coefficient μ as function of the sliding velocity determined for the reference surface and the crater-like structured sample CR4 in unlubricated tests.

In microtribological studies, the decrease in friction with increasing sliding velocity in lubricated contacts is a known phenomenon (Sundararajan 2001; Tambe & Bhushan 2005). It has been ascribed to the degradation or suppressed formation of capillary bridges at higher speeds and, thus, to a decreased contribution of capillarity to the friction force in this regime. However, the relevance of capillary-related phenomena might be doubted. In section 6.3.3.1, effects of water capillary bridges were hardly detected on hydrophilic crater-like structured surfaces due to their low summit density. Therefore, it is reasonable to assume that capillarity can be neglected here. Moreover, oils are likely to have lower surface tension than water and, thus, the capillary force of the lubricants should be lower than that generated by water (see equ. 3.4). If this is true, the reduction of friction might be related to a shift from the boundary to the mixed lubrication regime.

6.2.4 Comparison of the Microfrictional Behaviour of Lubricated, Crater-like Structured Surfaces at Higher Loads

Similar to the experiments performed in the LCC study (see section 6.1.3), friction measurements were carried out on the reference (Ref) and the crater-like structured surfaces CR1 to CR6 lubricated with PAO. In all experiments the F_F-n_{cycles} curves follows an evolution corresponding to type II or IV (see Fig. 6.3). As described in section 6.1.3, the coefficients a_1

and a_0 were determined from the F_F-n_{cycles} plots for various normal loads. Figure 6.28 shows the coefficients a_1 and a_0 as function of the normal load applied for the reference and crater-like structured surfaces in tests with or without lubrication.

As expected, the coefficient a_1 decreases significantly when the contact is lubricated. That effect becomes more prominent at higher normal loads. Consequently, stiction occurring at higher load was avoided when applying a lubricant on the reference surface and the crater structures CR1 and CR6. The most tremendous reductions for the coefficient caused by lubrication were observed in tests on the reference surface. Nevertheless, the a_1 values of the reference are still higher than that of most of the crater structures. The average of the a_1 values of the reference is in the range of the coefficients obtained for CR1, CR2 and CR4, which show mostly the highest values for a_1 among the crater-like structured surfaces in lubricated contacts.

For all surfaces, the values obtained for a_0 are slightly lower than in unlubricated contacts. Also here, higher values of a_0 were measured on the reference surfaces compared to most of the crater-like structured surfaces.

In the experiments conducted in non-lubricated contacts, a correlation between the evolution of a_1 and a_0 and the skewness S_{sk} of the surfaces was found. Given that the system is operated in boundary lubrication regime, topographical parameters being important for dry contacts, e.g. S_{sk}, cannot be neglected here. Therefore, an attempt was made to correlate to the coefficients a_1 and a_0 to the skewness of the surfaces in a first approach.

For easier comparison, the mean values of a_1 and a_0, $a_{1,mean}$ or $a_{0,mean}$, were determined for a surface by averaging the results obtained in tests with different normal loads on this surface. When comparing the evolution of the mean values as a function of S_{sk}, different trends were observed for lubricated and non-lubricated conditions (see Fig 6.29). In the non-lubricated contact, higher $a_{1,mean}$ values were determined on the surface with a highly negative skewness than on surfaces with positive or moderate negative skewness for both roughness ranges.

When applying a lubricant, the inverse effect was seen. The general evolution of $a_{0,mean}$ as function of S_{sk} was not affected by lubrication.

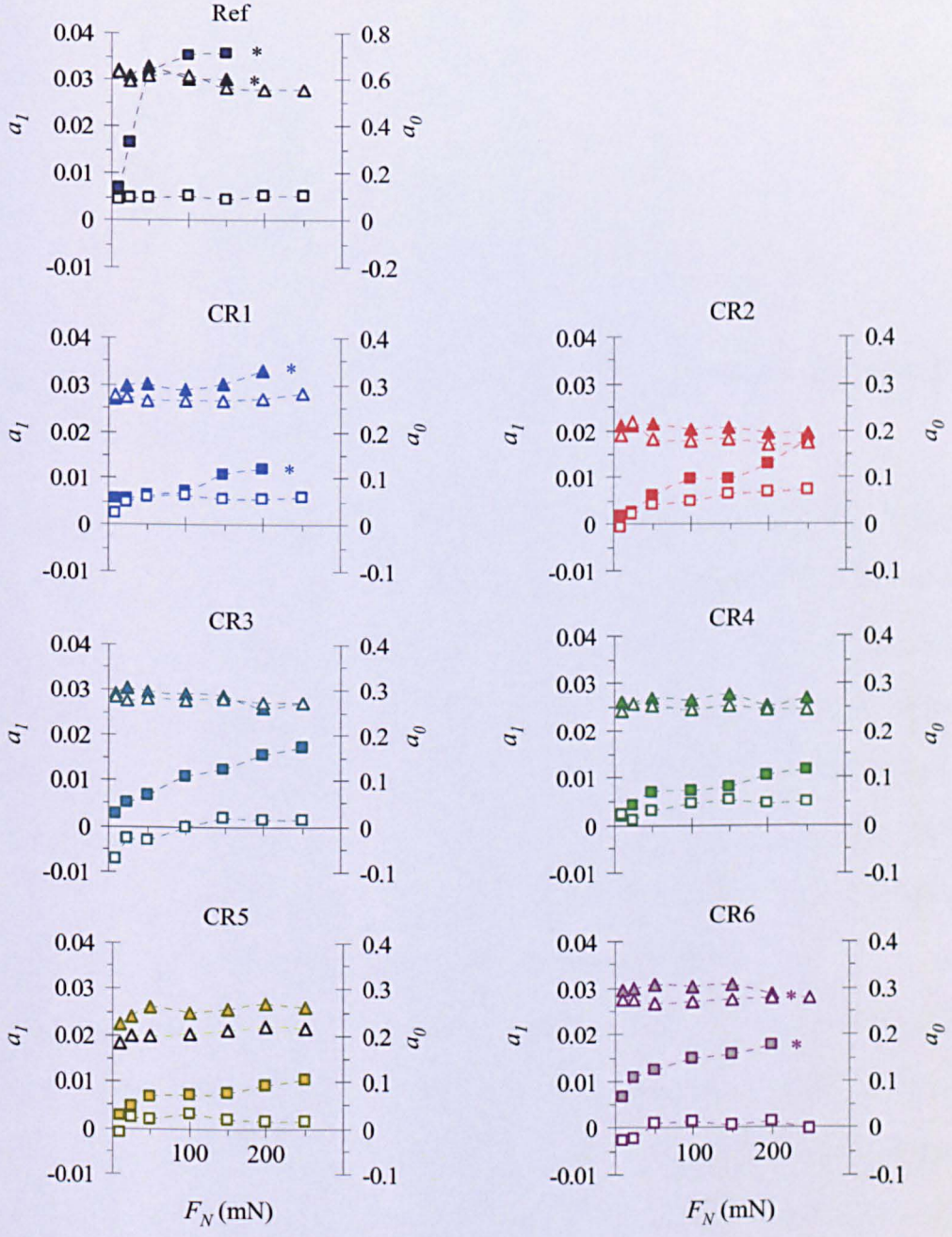

Figure 6.28: Evolution of a_1 and a_0 as function of the normal load applied for the reference and the crater-like structured surfaces CR1 to CR6 in non-lubricated and lubricated contacts (oil PAO). The values of a_1 are marked as full squares in non-lubricated conditions and as empty squares in lubricated tests. The values of a_0 are marked as full triangles in non-lubricated conditions and as empty triangles in lubricated tests. The occurrence of stiction in the non-lubricated tests is indicated by *.

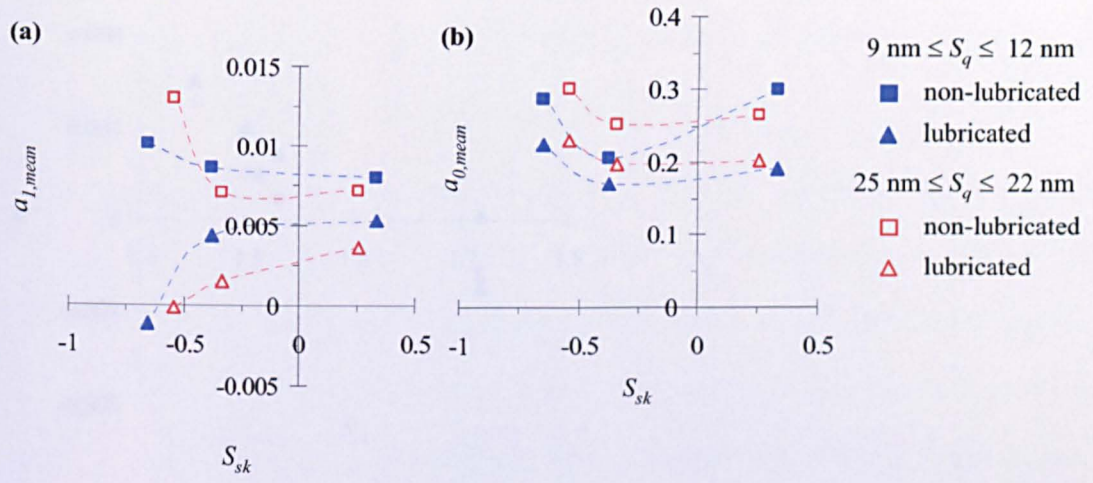

Figure 6.29: Mean values of coefficients a_1 and a_0 plotted versus the skewness S_{sk} of crater-like structured surfaces in two S_q roughness ranges.

In lubricated contacts, topographical parameters characterising the lubrication efficiency of surfaces also needs to be considered. Since the surface topography was not worn during the test, the core fluid retention index S_{ci} might be of larger importance for the interpretation of the results than valley fluid retention index S_{vi}. There is evidence of systematic relationships between S_{ci} and a_1 for the lubricated crater-like structured surfaces investigated here. The a_1 value decreases on increasing the S_{ci} value (Fig. 6.30). This appears reasonable since larger S_{ci} values indicate that more lubricant might be stored in the surface cavities with the result that enhanced lubrication and, thus, lower friction occurs in the contact.

However, skewness and the valley fluid retention index vary simultaneously and in a correlated way (lower S_{sk}, higher S_{ci}): so, the effect of the skewness on a_1 might not only be related to variation of skewness itself but can be also caused by superimposed change of the S_{ci} value. In case of coefficient a_0, the variation of the value can probably related to changes in S_{sk}, since it follows the same trend as seen also for unlubricated contacts, where the parameter S_{ci} looses its relevance for the frictional behaviour.

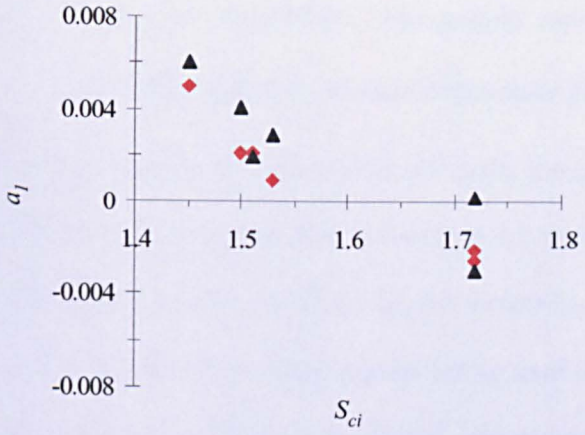

Figure 6.30: Coefficient a_1 plotted versus the core fluid retention index S_{ci} for normal load of 25 mN (◆) and 50 mN (▲). For better a illustration, a_1-S_{ci} data were presented only for selected normal loads.

Finally, it is reasonable to assume that the coefficient a_1 is mainly influenced by parameter S_{ci}, whereas the coefficient a_0 is more related to S_{sk}. That can be attributed to the fact that the a_0 represents the friction at the start of the test, corresponding to static friction, which is often less influenced by the presence of a lubricant than the dynamic friction.

Different to the tests conducted in unlubricated contacts, wear was not observed when a lubricant was applied

6.3 Effect of Nanoscale Topography and Chemical Composition of Surfaces on Their Microfrictional Behaviour (EG 3)

It is important to gain knowledge about the influence of the shape as well as the dimension of nanoscaled topographical features on the functionality of hydrophilic and hydrophobic surfaces with special emphasis on the wettability with water and the microtribological behaviour. Details of the experimental set-up used in the tests referred to here are described in section 4.3.4. Examples of the friction measurements recorded on differently structured hydrophobic and hydrophilic surfaces are shown in Appendix A.3.

6.3.1 Surfaces Tested in EG 3

For this study, the rough-interlayer method has been applied to modify the surface chemistry of nanostructured chromium nitride thin films. To alter the chemical behaviour from hydrophilic to hydrophobic, the reference (polished Si wafer) and the nanostructured Cr-N thin films were coated with either silicon oxide (SiO_2) to make them hydrophilic or with hexafluoropropene (HFP) to render them hydrophobic. The roughness values of the surfaces coated with SiO_2 are comparable to the values obtained after HFP deposition. Therefore, the average roughness values, listed in Table 6.3, were calculated from hydrophilic as well as hydrophobic samples. Beside the commonly used S_q values, the summit density S_{sd} is given, since these parameters appear to be the most relevant in this context. For the pyramid-like and cone-like structured samples, increase of the surface roughness is related to larger but fewer surface features within the same scan area. For the crater-like samples, deeper craters result in increase of surface roughness whereas the number of surface features remains relatively constant.

6.3.2 Influence of Nanostructure on Wettability

The average values for advancing (θ_A) and receding (θ_R) contact angle measured on the various nanostructured surfaces after coating with SiO_2 or HFP are given in Table 6.3. Additional data of the contact angle measurements are given in Appendix A.3.

The changed surface chemistry caused by the deposition of the SiO_2 or HFP layer results, as expected, in different water wettability: hydrophilic or hydrophobic, respectively. When coated with SiO_2, the reference sample and the three samples with a crater-like topography exhibit similar θ_A and θ_R values that lie between 40° and 51°, whereas the pyramid-like and cone-like structures show contact angles of only 9° to 10°. This implies that the pyramid-like and cone-like structures are more hydrophilic compared to the reference and crater-like structures. Comparing the samples having the same type of topographical structure but differently sized surface features against each other revealed that the wettability does not appear to be influenced by the size of the surface features.

Table 6.3: Mean values of root mean square roughness (S_q) and asperity density S_{sd}, advancing (θ_A) and receding (θ_R) contact angles determined on the smooth reference (Ref), the pyramid-like (P1 to P4), cone-like (C1 to C3) and crater-like (CR1 to CR3) structures coated with 10 nm thick SiO_2 or HFP layers. Since the topographical parameters are similar for the SiO_2 and HFP coated surfaces, the average value calculated from measurements from hydrophilic and hydrophobic sample are given.

Structure	S_q (nm)	S_{sd} (#/µm²)	+ SiO_2 layer		+ HFP layer	
			θ_A (deg.)	θ_R (deg.)	θ_A (deg.)	θ_R (deg.)
Ref	2.1 ± 0.2	18.1 ± 1.2	51 ± 2	40 ± 1	100 ± 2	60 ± 2
P1	17.9 ± 0.7	49.7 ± 3.1	10 ± 1	10 ± 1	142 ± 2	30 ± 2
P2	34.4 ± 0.5	22.0 ± 2.2	9 ± 1	10 ± 2	136 ± 2	34 ± 2
P3	59.6 ± 0.6	10.7 ± 1.9	10 ± 1	10 ± 1	138 ± 2	30 ± 2
P4	78.4 ± 0.4	3.1 ± 0.2	10 ± 1	10 ± 1	116 ± 2	75 ± 2
C1	17.6 ± 1.1	26.2 ± 0.6	9 ± 1	9 ± 1	120 ± 2	74 ± 2
C2	35.8 ± 3.1	12.5 ± 2.3	9 ± 1	9 ± 1	124 ± 2	80 ± 2
C3	55.9 ± 1.2	4.1 ± 0.1	10 ± 1	10 ± 1	128 ± 2	82 ± 2
CR1	9.6 ± 0.2	3.3 ± 0.5	50 ± 2	45 ± 2	112 ± 2	68 ± 2
CR2	15.6 ± 0.9	3.1 ± 0.3	49 ± 1	42 ± 2	108 ± 2	66 ± 2
CR3	30.3 ± 1.0	3.3 ± 0.2	50 ± 3	45 ± 2	108 ± 2	70 ± 2

Usually, the contact angle of SiO_2 surfaces is expected to be below 10°. Compared to this value, the contact angles measured on silicon oxide in this study are quite high. However, similarly high contact angles were found in the literature (Bregliozzi 2006). The variation in the wettability of silicon oxide is commonly explained by difference in the preparation method and the altering of the surfaces properties by adsorption of organic material (Takeda & Fukawa 2003; Bregliozzi 2006). In this context it is interesting to note that significantly smaller contact angles were measured on the SiO_2 covered pyramid structures than for smooth and crater-like structured samples with identical surface chemistry. The enhanced wetting of spiky surfaces was also observed by Bico, Thiele & Quéré (2002) and was attributed to the enhanced sucking of liquid into the surface cavities on this type of surface structure. It is assumed that a similar effect causes the observed difference in the wettability of the various surfaces.

With the HFP layer, θ_A values between 100° and 116° and θ_R values between 60° and 75° were recorded on the smooth reference, all crater-like structures and the pyramid-like structure P4. The other pyramid-like structured samples P1 to P3 had θ_A values of 136° to 142° and θ_R values in the range of 30° to 34°. On the surfaces C1 to C3, θ_A values between 120° and 128° and θ_R values between 74° and 82° were measured. No other effect of the size of the surface features on wettability could be detected on these hydrophobic samples. A comparison of the θ_A values measured on the different surface topographies revealed that tapered surface features are required to gain an increase in the water contact angle. This is in good agreement with the work of other groups (Youngblood & McCarthy 1999; Miwa et al. 2000) who observed higher contact angles for uniformly distributed, sharp protuberances. It has been suggested (Youngblood & McCarthy 1999; Miwa et al. 2000; Kulinich & Farzaneh 2005) that the air trapped between the protuberances supports the bottom of the water droplet leading to a transition from nanocomposite surface (completely liquid-solid interface = Wenzel regime) to a composite surface (including trapped air = Cassie regime).

6.3.3 Influence of Structure on Frictional Behaviour

6.3.3.1 Hydrophilic Surfaces

Figure 6.31 shows the friction force F_F measured in different relative humidities for hydrophilic samples of the reference surface (Ref), the pyramid-like structures P1 to P4, the cone-like structures C1 to C3 and crater-like structures CR1 to CR3.

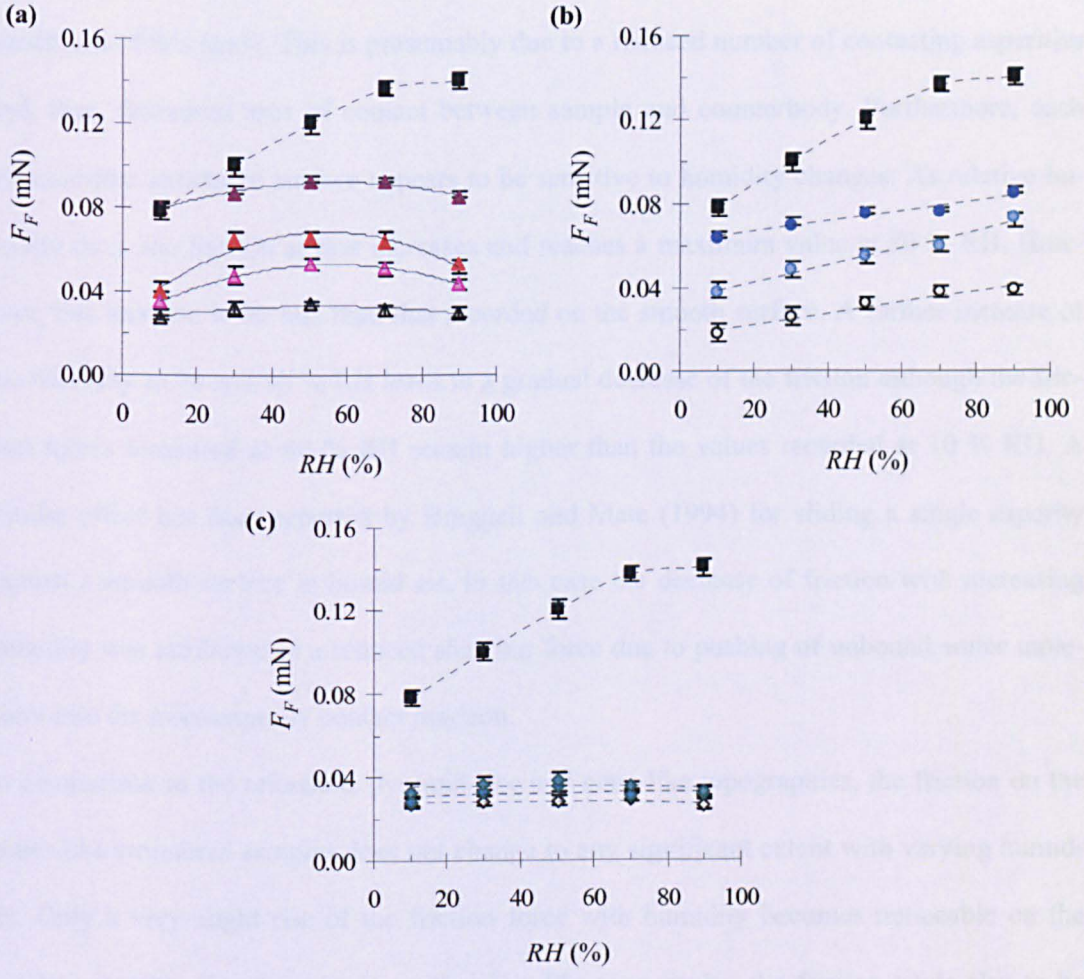

Figure 6.31: Friction force F_F as function of the relative humidity RH measured for a normal load of 0.2 mN on hydrophilic surfaces with

(a) pyramid-like topography: ▲ P1, ▲ P2, △ P3, △ P4

(b) cone-like topography: ● C1, ● C2, ○ C3

(c) crater-like topography: ◆ CR1, ◆ CR2, ◇ CR3

and compared to a smooth reference surface (■). The vertical bars represent the variation between the minimum and maximum value in these tests.

At all humidities tested, the friction measured on the smooth reference surface is considerably higher than on any of the structured surfaces, with the sole exception of an insignificant difference for structure P1 at 10 % RH. On the reference surface, the friction increases with the relative humidity until reaching 70 % RH. On increasing the humidity to 90 % RH, the friction remains at a similar level as obtained for 70 % RH.

With increasing size of the pyramidal surface features, friction decreases under the given test conditions of this study. This is presumably due to a reduced number of contacting asperities and, thus, decreased area of contact between sample and counterbody. Furthermore, each pyramid-like structured surface appears to be sensitive to humidity changes. As relative humidity rises, the friction at first increases and reaches a maximum value at 50 % RH. However, this increase is far less than that recorded on the smooth surface. A further increase of the humidity to 70 and 90 % RH leads to a gradual decrease of the friction although the friction forces measured at 90 % RH remain higher than the values recorded at 10 % RH. A similar effect has been reported by Binggeli and Mate (1994) for sliding a single asperity against a smooth surface in humid air. In this case the decrease of friction with increasing humidity was attributed to a reduced shearing force due to pushing of unbound water molecules into the microasperity contact junction.

In comparison to the reference, pyramid-like and cone-like topographies, the friction on the crater-like structured samples does not change to any significant extent with varying humidity. Only a very slight rise of the friction force with humidity becomes noticeable on the rougher samples. For the samples with crater-like topography, the friction tends also to be consistently lower with increasing roughness although the variation is marginal and perhaps insignificant.

Unlike the pyramid structures, the number of asperities does not change with modifying the surface roughness of the crater topography (see Tab. 6.3). That means that the area of contact remains nearly constant for the different crater-like structures.

An increase in size of the conical surface features leads to reduced friction, comparable to the observations made on the pyramid-like structures. Also for the cone-like structured surfaces, friction is influenced by the humidity of the environment, whereby a nearly linear increase of the friction with humidity was seen in this case.

Generally, the lowest friction was recorded on the crater-like topographies and the highest friction on pyramid-like structures among the structured samples. This could be due to the different number and shape of asperities.

6.3.3.2 Hydrophobic Surfaces

The friction force measured in different relative humidities is shown for the different nanostructured surfaces in comparison to the reference surface in Figure 6.32.

In all cases, the friction measured on the smooth reference surfaces is higher than on any of the structured surfaces.

The friction force determined on the pyramid-like structures P1 to P4 and the cone-like structures C1 to C3 decreases with increasing roughness, the same pattern as seen with hydrophilic samples of the same topography. It is assumed, that, as described for the hydrophilic samples, the decrease in the area of contact might cause a lower friction on rougher surfaces. Again, no significant effect of the surface roughness on the frictional behaviour was observed for the crater-like structured surfaces.

The crater-like structures CR1 to CR3 as well as the pyramid-like structured surface P4 and the cone-like structured surface C3 showed the lowest forces in these experiments.

There was no significant variation of friction force with humidity in any of the tests. A similar result was also reported by Scherge and Gorb (2001) on silicon surfaces coated with hydrophobic an self-assembled monolayer (SAM).

Compared to the hydrophilic sample with identical surface structure, the friction force was rather lower on the hydrophobic sample.

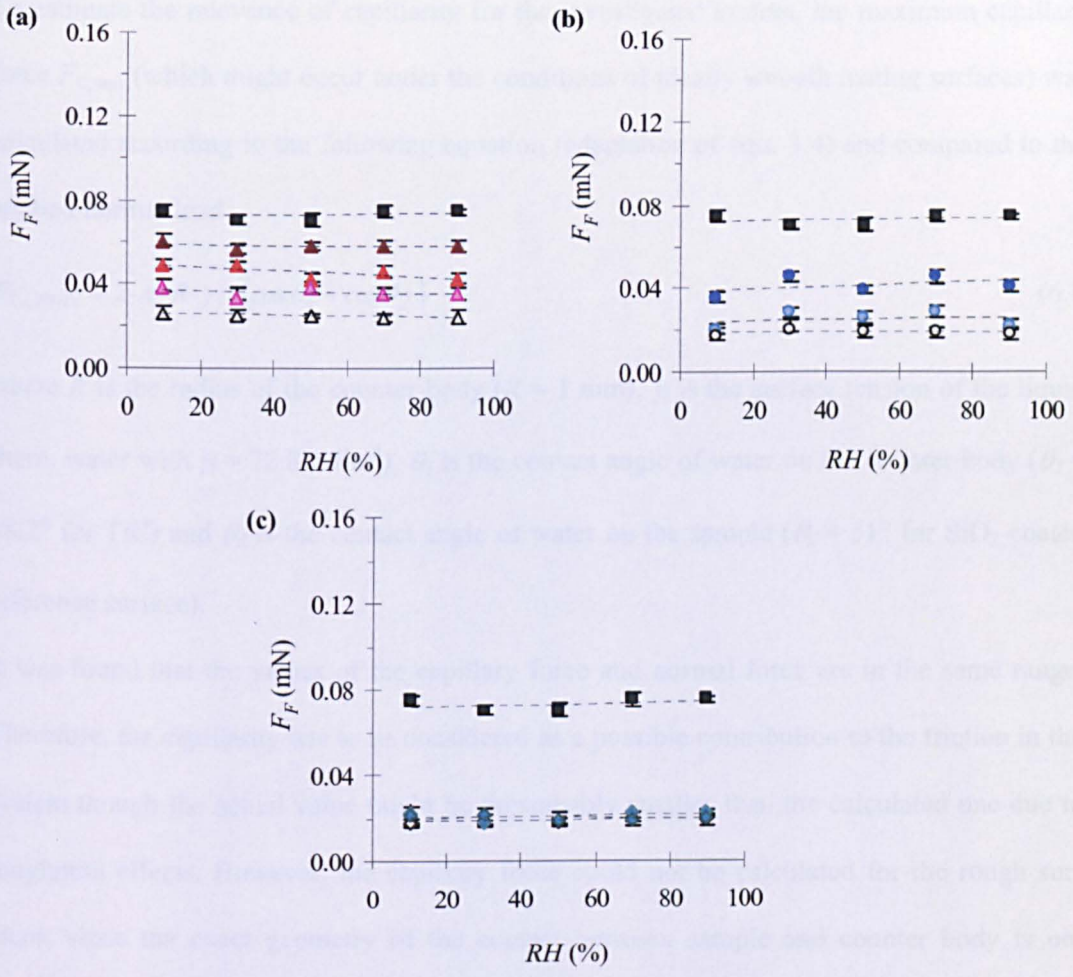

Figure 6.32: Friction force F_F as function of the relative humidity RH measured for a 0.2 mN normal force on hydrophobic surfaces with

(a) pyramid-like topography: ▲ P1, ▲ P2, △ P3, △ P4

(b) cone-like topography: ● C1, ● C2, ○ C3

(c) crater-like topography: ◆ CR1, ◆ C2, ◇ CR3

and compared to a smooth reference surface (■). The vertical bars represent the variation between the minimum and maximum value in these tests.

6.3.4 Comparison between Friction on Hydrophilic and Hydrophobic Surfaces

The underlying mechanism of friction reduction of structured surfaces due to varying contact areas may be interlocking effects (Bhushan 2002) or capillarity (Israelachvili 1992) or even solid-solid adhesion (bonding) between the two surfaces (Tabor 1977), or combinations thereof.

To estimate the relevance of capillarity for the investigated system, the maximum capillary force $F_{C,max}$ (which might occur under the conditions of ideally smooth mating surfaces) was calculated according to the following equation (adaptation of equ. 3.4) and compared to the applied normal load

$$F_{C,max} = 2 \cdot \pi \cdot R \cdot \gamma_l \cdot (\cos\theta_1 + \cos\theta_2) \tag{6.8}$$

where R is the radius of the counter body (R = 1 mm), γ_l is the surface tension of the liquid (here: water with γ_l = 72.8 mJ/m^2), θ_1 is the contact angle of water on the counter body (θ_1 = 58.2° for TiC) and θ_2 is the contact angle of water on the sample (θ_2 = 51° for SiO_2 coated reference surface).

It was found that the values of the capillary force and normal force are in the same range. Therefore, the capillarity has to be considered as a possible contribution to the friction in the system though the actual value might be presumably smaller than the calculated one due to roughness effects. However, the capillary force could not be calculated for the rough surfaces, since the exact geometry of the contact between sample and counter body is not known.

Another potential surface of friction is probably interlocking. Interlocking effects are usually more pronounced on rougher samples. The surface roughness of the nanostructured samples is higher than on the reference. Consequently, the effect of interlocking should be much higher on the rougher structured samples than on the smooth reference. If interlocking is a major effect in the system, the friction should be higher on these surfaces than on the reference sample in experiments performed on hydrophobic surfaces at low relative humidity. Such behaviour was not observed (see Fig. 6.31 and 6.32), suggesting that interlocking effects do not play a significant role in this study.

Solid-solid adhesion cannot be neglected, since for the hydrophobic samples the contact mechanisms seems to influence the friction force and presumably cause the found variation in friction between the different pyramid-like and cone-like structured samples. However,

variations in solid-solid adhesion caused by differences in material of the surface layer appear to be of minor importance. Otherwise, a difference in the friction force values should be measurable between SiO_2 coated (hydrophilic) and HP coated (hydrophobic) samples at low humidity, but the friction force values are similar at 10 % RH for most of the investigated structures. Therefore, it seems that under the given test conditions, for smooth surfaces the capillarity occurring between asperities on samples and counter body strongly contributes to the friction in the system. The hydrophilic surface can adsorb more water in a more humid environment, leading to higher friction forces. However, at a certain point (in this case above 70 % RH) the thickness of the adsorbed water film keeps constant and the friction force saturates (Scherge & Gorb 2001).

The question is whether capillarity is also the main mechanism in structured surfaces. Generally, a higher friction was recorded on the pyramid-like structure than on cone-like or crater-like structured surfaces. This might be explained, beside differences in the contact area, with the higher probability of liquid bridging on the pyramid-like topography than on the cone-like and crater-like structures due to higher numbers of surface asperities on the former topography type. An increase of the number of asperities (nearly) contacting the counter-body, which corresponds to a higher summit density, causes an increased effect of the capillary bridging and leads, therefore, to a higher capillary forces and, thus, higher friction force, as described in the model developed by Riedo, Lévy & Brune (2002) for friction evolution in nanoscopic sliding.

Capillary effects might also be the reason for the measured difference in friction between hydrophilic and hydrophobic samples with the same structure (compare Fig. 6.31 and 6.32) because the variation in material (SiO_2 or HFP) seems not to affect the friction force. On hydrophobic samples, capillary force is expected to be significantly lower than on the hydrophilic surfaces. The results of the study indicate that the capillarity appears to be even negligible for hydrophobic samples because a humidity-dependence of the friction force was not observed. Therefore, it is assumed that the difference in the friction force between hydro-

phobic and hydrophilic surface corresponds to the missing (not detectable) contribution of a capillary force.

Furthermore, capillary effects may explain why the difference between hydrophilic and hydrophobic samples is less pronounced with increasing surface roughness of the pyramid structures. Since the P1 structure exhibits a higher number of asperities than the other structures, and more locations for capillary bridging are thus available, the capillary effects are detectable already at lower humidities on this surface structure. On samples with fewer asperities (P2, P3, P4), a higher amount of water (higher humidity) is required to build the capillary bridges in sufficient number to measurably influence the friction in the tribosystem.

6.3.5 Correlation between Surface Wettability and Frictional Behaviour

As expected, the study showed that wettability has a significant effect on the frictional behaviour of the smooth reference surface well as the nanostructured samples: the hydrophobic samples exhibit lower friction force values than the hydrophilic ones (see Fig. 6.31 and 6.32). However, conventional contact angle measurements appear to be less suitable for correlating wettability and frictional behaviour of differently structured surfaces with identical surface chemistry. Regarding the friction measurements on the different hydrophilic samples, it seems that the friction is more strongly influenced by the roughness than by the actual wettability. For example, the reference surface shows higher values for the contact angles (is less hydrophilic) than the pyramid-like structures although lower friction occurred on the latter ones.

A comparison between hydrophobic samples with different structures is complicated by the fact that the pyramid-like structures exhibit higher θ_A values, but at the same time lower θ_R values than the reference and both other structure types. In this case, it might be helpful to consider only the hysteresis of the contact angles (θ_A-θ_R): values obtained were between 38° and 46° for the reference, the crater-like and cone-like structures, but between 108° and 112° for the pyramid-like structures. Although a larger hysteresis corresponds to lower water-

repellence of the surface (Chen et al. 1999), the pyramid-like structures maintain lower friction than the smooth surface probably due to the previously mentioned roughness effect.

A clear correlation between wettability and the friction force measurements on differently structured surfaces with identical surface chemistry, which one might expect to see, could not be found in this study. That might be due, in part, to the fact that conventional contact angle measurements are not sufficiently sensitive to topographical changes in the nanoscale range.

6.3.6 Influence of Sliding Velocity on Friction of Different Surface Structures

6.3.6.1 Hydrophilic Surfaces

Based on the results reported in literature (Gnecco et al. 2000; Liu, Ahmed & Scherge 2001; Tambe & Bhushan 2005), a logarithmic variation of the friction force F_F with the sliding velocity v is to be expected for the investigated velocity range and was also observed in this work (see Fig. 6.33)

The linear variation of the friction force with the logarithm of the velocity is usually expressed as follows (Riedo, Lévy & Brune 2002; Tambe & Bhushan 2005):

$$F_F = F_0 + F_1 \cdot ln(v(\mu m/s)) \tag{6.9}$$

where F_F is the friction force, F_1 is the slope and F_0 is the force at a consistently-used, arbitrary reference speed (here, 1 μm/s) determined from the linear line fits of the F_F versus ln(v) plot, as shown in Figure 6.33. The values of F_1 and F_0 for the hydrophilic samples of the different structures are summarized in Table 6.4.

For all hydrophilic samples of type P and C, a negative slope was determined, which means that the friction force decreases when increasing the sliding velocity. This behaviour of hydrophilic surfaces has been already described by other groups (Scherge & Gorb 2001; Riedo, Lévy & Brune 2002; Gnecco et al. 2000; Liu, Ahmed & Scherge 2001; Tambe & Bhushan 2005) and is explained by the diminishing influence of the capillary force on the friction

force due to the reduced or inhibited formation of stable capillary bridges at higher speeds (Scherge & Gorb 2001; Liu, Ahmed & Scherge 2001; Tambe & Bhushan 2005).

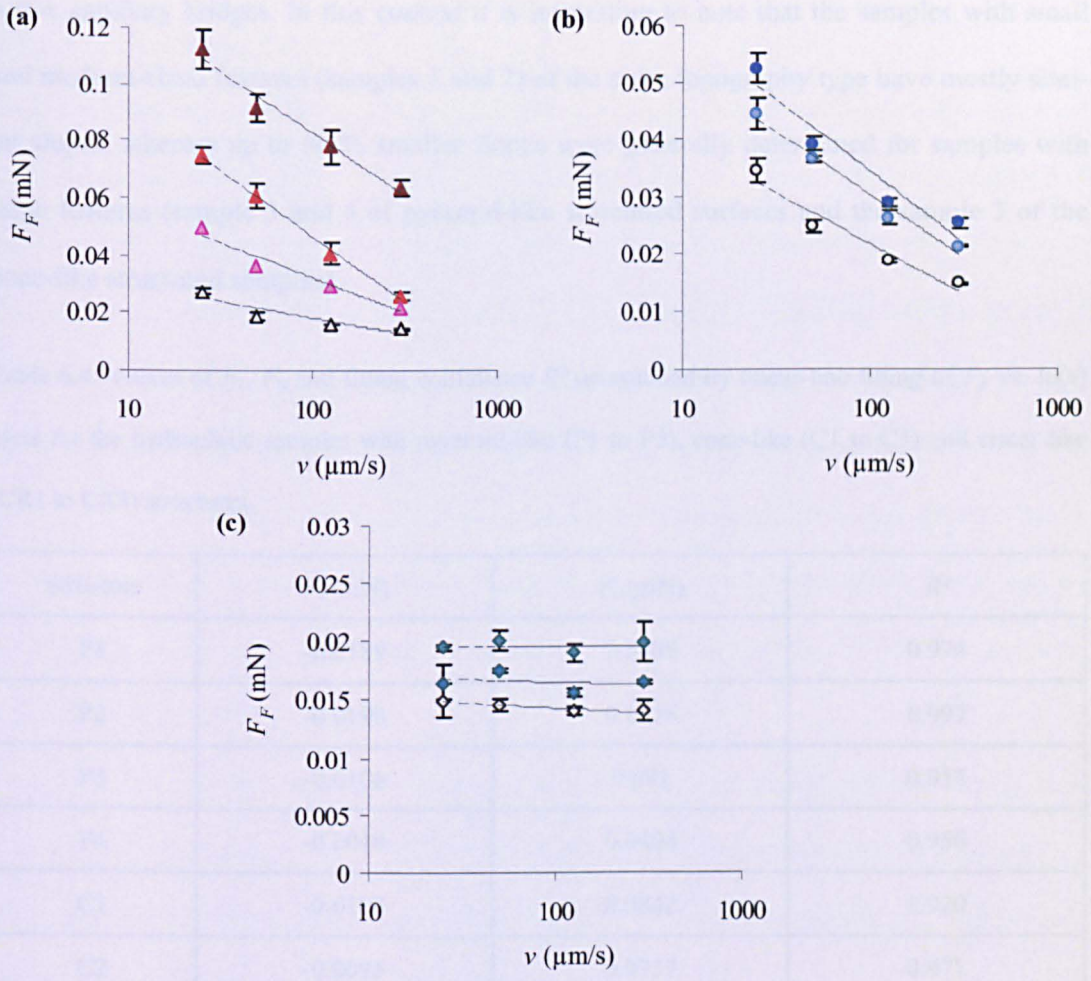

Figure 6.33: Friction force F_F as function of sliding speed v for hydrophilic surfaces with

(a) pyramid-like topography: ▲ P1, ▲ P2, △ P3, △ P4

(b) cone-like topography: ● C1, ● C2, ○ C3

(c) crater-like topography: ◆ CR1, ◆ C2, ◇ CR3

The velocity is plotted in logarithmic scale. The lines mark the least square linear-line fits to the data points. The vertical bars represent the variation between the minimum and maximum value in these tests.

The topography types show a different sensitivity to changes in the sliding speed. The pyramid-like structures have a larger slope than the cone-like structures that exhibit a larger slope than the crater-like ones, which exhibit only a marginal slope. That can be explained by the

fact that the contribution of the capillary forces on the friction forces diminishes going from pyramid-like to cone-like to crater-like structured surfaces due to the reduced number of active capillary bridges. In this context it is interesting to note that the samples with small and medium-sized features (samples 1 and 2) of the same topography type have mostly similar slopes, whereas up to 60 % smaller slopes were generally determined for samples with large features (sample 3 and 4 of pyramid-like structured surfaces and the sample 3 of the cone-like structured samples).

Table 6.4: Values of F_1, F_0 and fitting confidence R^2 determined by linear-line fitting of F_F vs. ln(v) plots for the hydrophilic samples with pyramid-like (P1 to P3), cone-like (C1 to C3) and crater-like (CR1 to CR3) structures.

Structure	F_1 (mN)	F_0 (mN)	R^2
P1	-0.0189	0.1695	0.974
P2	-0.0198	0.1376	0.997
P3	-0.0106	0.081	0.957
P4	-0.0048	0.0404	0.956
C1	-0.0108	0.0842	0.920
C2	-0.0095	0.0737	0.977
C3	-0.0076	0.0566	0.940
CR1	-0.0004	0.0209	0.917
CR2	-0.0002	0.0176	0.964
CR3	-0.0004	0.0162	0.913

Comparing the F_0 values; the same trend as described for the friction experiments in varied humidity (see section 6.3.3.1) can be observed: The highest value for F_0 is measured on the pyramid-like and the lowest intercept is determined on crater-like structured samples. When increasing the size of the surface features, the F_0 values decrease for all three structure types.

Compared to the friction tests in varied humidity, differences between the crater-like structures are more pronounced regarding their F_0 values.

6.3.6.2 Hydrophobic Surfaces

To investigate the correlation between friction force and sliding velocity on hydrophobic surfaces, diamond-like carbon (DLC) films (Riedo, Lévy & Brune 2002; Liu, Ahmed & Scherge 2001; Tambe & Bhushan 2005) or self-assembled monolayers (SAMs) (Gnecco et al. 2000; Liu, Ahmed & Brune 2001; Tambe & Bhushan 2005; Hild 2005; Bregliozzi 2006) have been widely used as model surfaces in nano and microtribological studies. For DLC films, an increase of the friction force with the sliding speeds was reported for an investigated speed range from 1 µm/s to 10 mm/s and is related to atomic stick slip effects (Tambe & Bhushan 2005). In case of SAMs, a realignment of the molecular chains in the contact zone is suggested to cause the increase of friction with sliding velocity (Tambe & Bhushan 2005; Bregliozzi 2006).

In this study a different behaviour was observed for the hydrophobic surfaces presumably due to the different nature of the hydrophobic surface layer (in this case plasma polymerised fluorocarbon). The experiments indicate that the friction force remains relatively stable while increasing the sliding velocity from 25 to 300 µm/s (Tab. 6.5).

However, the crater-like structured samples show the lowest friction and the pyramid-like structured samples have the highest friction in these tests. Among samples of the same structure type, rougher samples show lower friction than less rough ones presumably due to changes in the contact area.

Table 6.5: Friction force as function of the sliding velocity, measured for 0.2 mN normal force, on pyramid-like (P1 to P4), cone-like (C1 to C3) and crater-like (CR1 to CR3) structured, hydrophobic samples.

Structure	Friction force F_F (mN) measured at various sliding speeds v			
	v = 25 µm/s	v = 50 µm/s	v = 125 µm/s	v = 300 µm/s
P1	0.126	0.125	0.124	0.127
P2	0.062	0.061	0.060	0.062
P3	0.042	0.045	0.045	0.046
P4	0.022	0.023	0.021	0.020
C1	0.091	0.090	0.089	0.090
C2	0.047	0.051	0.050	0.049
C3	0.031	0.028	0.027	0.030
CR1	0.030	0.033	0.032	0.032
CR2	0.028	0.30	0.028	0.026
CR3	0.020	0.024	0.022	0.021

Chapter 7

Summary, Conclusions and Outlook

7.1 Nanostructuring of Thin Films (In-Process Structuring)

The study has shown that a wide range of different topography types can be achieved and, moreover, that the dimensions of the topographical features of thin chromium nitride films can be reproducibly modified in a controlled way by in-process structuring. The type of topography type evolving in a deposition experiments depends on the appropriate adjustment of four major process parameters, namely bias voltage U_b and deposition rate a_d, Ar/N_2 ratio and homologous temperature T/T_m. The following table summaries the effect of the major process parameters on the evolution of the lateral dimension of the various topography types.

Table 7.1: Effect of process parameters homologous temperature T/T_m, Ar/N_2 ratio, bias voltage U_b and deposition rate a_d on the evolution of lateral dimension L_x on different topography types of chromium nitride thin films.

Parameter	Type P	Type G	Type CR	Type C	Type R	Type H
T/T_m	↑	→	→	-	→	→
Ar/N_2	↑	→	→	-	→	→
U_b	-	↓	↑	↑	↑	↑
a_d	↑	↑	↓	→	↓	↓

↑ ... increase in parameter increases L_x, ↓ ... increase of parameter decreases L_x,
→ ... no effect of parameter on L_x, - ... invariable parameter

Summarising it can be stated, that in-process structuring can provide a path for better exploitation (optimization) of topography-related properties of thin crystalline films and, thus, shows potential as a new approach for nanostructuring of surfaces.

7.1.1 Applicability of In-Process Structuring

In-process structuring uses the correlation between microstructure (e.g. size, crystallographic orientation and phase) of the thin films to their topographical appearance in order to influence the surface structure. The microstructure of thin films, and hence their topographical evolution, is controlled by the appropriate adjustment of the parameters in the deposition process. Conversely, it has to be considered, when applying this technique for nanostructuring of surfaces that topography variations of thin films might be coupled to changes in their microstructure and, thus, can possibly affect their microstructure-dependent properties. Changes in mechanical and tribological behaviour due to changes in the microstructures were also observed in some cases in this study (see section 5.5 and wear mapping tests reported in sections 6.1.3 and 6.1.4). In this regard, the application of in-process-structuring might be most suitable to thin films for which functionality depends mainly on their topography and less on their mechanical properties, e.g. superhydrophobic layers in microfluidic systems (McNeely et al. 1999; Feng et al. 2003; Zhan et al. 2006) or calibration standards for AFM tips (Seah et al. 1999).

Other applications for in-process structuring might be the production of nanostructured masters for replication processes, as applied for structuring of polymer surfaces (Heyderman et al. 2001; Cui & Veres 2006), or templates used for further surface functionalization. For example, the hydrophobicity of a fluoro-carbon layer is enhanced by depositing it on nanostructured surfaces, as seen in this study (see section 6.3) or in (Gerbig, Phani & Haefke 2005; Lacroix et al. 2005).

When changing the dimensions of the surface features of a specific topography type, the microstructure varies only marginally in most of the cases. Consequently, in-process structuring could be a useful tool in applications where the efficiency and performance of

surfaces depends on the appropriate adjustment of the feature dimensions. In this context, the results about the size modification of pyramidal features might be of special interest, for example, for optical coatings. Nowadays, attempts are made to create so-called moth-eye surface structure, which are equivalent to topography type P-r, in order to increase the energy output of optical coatings (Iwaya et al. 2006; Burmeister et al. 2005).

7.1.2 Validity of Topography-Zone Model for Other Coating Materials

Although this study has intensively investigated the technique of in-process structuring exclusively for chromium nitride thin films, the knowledge gained about the correlation between microstructure and topographical evolution is probably applicable to other materials exhibiting a crystallographic structure comparable to that of Cr-N, especially binary nitrides formed by metals from the IV, V, VI groups of the element table (Hones 2000). So, for example, a similarity in the microstructural evolution and growth behaviour was found between Cr-N and Ti-N thin films (Schell et al. 2003), which are often applied as coatings on surgical instruments and implants (Coll & Jacquot 1988; Park et al. 2003, Piscanec et al. 2004). Nevertheless, the topography-zone model developed here, namely the position of the boundaries between the different zones, needs to be adapted when using another coating material and/or another PVD process than unbalanced magnetron sputtering, since the interrelationship between process parameter and film growth depends to a certain extent on the material deposited and the deposition process (Ohring 2002; Mattox 1998).

7.2 Microtribological Behaviour of In-Process Structured Surfaces

The potential of in-process structuring of thin films has been explicitly investigated for application in the field of microtribology (see Chapter 6). In this part of the work, the influence of size and type of the nanoscaled surface features on the microtribological behaviour was studied for three selected topography types, Pyramid (P), Cone (C) and Crater (CR), under different test conditions in three experimental groups (EG). Generally, it was found:

- A significantly lower friction can be obtained by surface nanostructuring in comparison to smooth surfaces. Hereby, the amount of the friction reduction depends on the type of the topography.
- A strong correlation between density of the asperities (expressed by S_{sd}) and the friction in the system was found: the friction was lower at lower S_{sd} in all experiments. Low friction was measured on surfaces having an asperity density of around 3 #/µm² in this study. Such asperity densities were exhibited by all crater-like structured surfaces tested. In case of topography types P and C, this S_{sd} value, hence low friction, was reached by increasing the lateral dimension of the surface features.
- Beside the asperity density, also the shape of the asperities appears to influence the friction to a certain extent. The relevance of individual topographical parameters to the tribological behaviour of a surface depends on the test conditions applied and, thus, the main mechanisms generating friction in the system. Therefore, they are summarized in below by experimental group:

  EG 1: Friction and Wear of Nanostructured Surfaces in Unlubricated Contacts

  When testing under nearly wear-free conditions, the differences detected between the nanostructured surfaces were correlated to the changes in contact area which finally results in variations in solid-solid adhesion. For the different samples with pyramid-like and cone-like topography, the diversities in contact area are caused by changes in the summit density. In case of crater-like structured surfaces, dissimilarities in the contact nature due to varied summit curvature lead to changes in the contact area.

  Also when applying higher normal forces (LCC and LTS tests), the dominant component of friction is solid-solid adhesion. Since the surface topography and, hence, the contact area are significantly modified by wear, the wear behaviour plays an important role for the evolution of adhesion and friction. The evolution of wear as function of time and load is influenced by density, shape (skewness) and size of the surface features, but also by the mechanical properties. This topography specific correlation between surface properties

and microtribological behaviour determines the application range where an individual surface structure can be operated without inducing wear-related increase in friction.

EG 2: Comparison of Nanostructured Surfaces in Lubricated Contacts

The experiments of this experimental group were conducted in boundary lubrication regime. Therefore, the contribution of the solid-solid adhesion to the friction force in the systems is still relatively high. Consequently, the same topographical parameters important for the friction generation in unlubricated contacts are also relevant in this regime. Additionally, a correlation was found between friction and core fluid retention index, which judges the functionality of surface with respect to lubrication efficiency.

EG 3: Influence of Nanoscale Topography and Chemical Composition of Surfaces on Their Microfrictional Behaviour

Here, capillarity and solid-solid adhesion appear to play a dominant role in defining the friction behaviour of the smooth as well as the structured surfaces. Changes in sliding speed and relative humidity of the environment influence mainly the capillarity component of the friction force. The activation of capillary effects and solid-solid adhesion depends strongly on the asperity density. Consequently, the dependence of friction on humidity and sliding velocity can be reduced by appropriate nanostructuring.

When varying the topographical parameters of a topography type within the range achievable by in-process structuring (which means by changing parameters of the deposition process), the microtribological behaviour differs less for topography type CR than for type P and C in the tests conducted in this study. This indicates that the functional performance of crater-like structured surfaces is less sensitive to modification in the deposition process, which means consequently higher production dependability when embedding this technique in a production process. Another advantage of the crater-like structured surfaces is the higher wear resistance due to their superior mechanical properties, mainly hardness, compared to surfaces of topography type P and C. Since the deposition parameters can be relatively freely

changed without significant effects on the tribological behaviour, crater-like structured films can be deposited at voltages from the lower end of the bias range of this topography type in order to avoid high residual stress in the thin films which might create problems to fragile structures as found in MEMS (Romig Jr., Dugger & McWorther 2003; Iborra et al. 2004; Guillén et al. 2005). Otherwise, the stress of topography type CR but also R and H can be reduced by different methods for stress relaxation (Fitz, Fukarek & Möller 2002; Debelle et al. 2006).

7.3 Future Work

7.3.1 Extension of Topography-Zone-Model

The suitability of the found topography-zone model for high atom-flux ratios ($J_i/J_a > 2$) might be an interesting subject for further studies, since the higher ion fluxes are reported to affect the crystallographic texture of thin films and the porosity of their microstructure (Inoue et al. 2002; Petrov et al. 2003), which certainly influenced the presence and/or growth conditions of the topography types. Also the extension of the topography-zone model beyond the investigated parameter field should be considered in future, especially experiments at low nitrogen concentrations. Under such conditions, additional chromium phases, beside CrN and/or Cr_2N, can occur (see Fig. 2.9) and are expected to influence the topographical appearances (Zhao et al. 2005).

Since the importance of the topography for the functionality of thin films has been recognized recently, the interest in controlling their topographical appearance grows continuously. In this context, it is worth to dedicate further studies to the development topography-zone models for other thin film materials and to the modification of the dimensions of their topographical features by in-process structuring.

7.3.2 Further Microtribological Studies on In-Process Structured Surfaces

In the microtribological study reported here just three types of topographies were investigated due to reasons discussed earlier. In order to gain more knowledge, especially in

regards to the effect of the feature shape on the friction evolution, the other topography types should be included in further tribological experiments. For example, it would be worthwhile to compare samples with pyramidal, conical and hillock-like features with regard to the influence of the feature shape on the friction-humidity or friction-speed dependence of hydrophilic surfaces (see section 6.3), or the correlation between friction and asperity shape as well as asperity density in unlubricated but also lubricated contacts (see section 6.1, 6.2). Other topics worth being investigated emerge from the rough interlayer approach applied in section 6.3, which combines functional surface layers with in-process structured surfaces in order to enhance the functionality of the layer. In this context, microtribological studies might be of special interest on nanostructured surfaces coated with SAMs, which find wide use in antistiction applications in microsystems, or coated with bounded lubricants (oils or solid materials) in lubricated contacts. The purpose of the nanostructure could be to improve the hydrophobicity in combination of hydrophobic SAMs or to reduce the contact area, hence, static friction in the latter case.

Nevertheless, the microtribological experiments already performed show clearly the importance of performing investigations dedicated to friction optimization by nanostructuring and that in-process structuring can be a useful technique to create nanostructures in order to enhance the microtribological behaviour of surfaces.

References

Achanta, S., Drees, D., Celis, J.-P. (2005), "Friction and nanowear of hard coatings in reciprocating sliding at milli-Newton loads", *Wear*, 259, 719-729

Adamik, M., Barna, P.B. (1996), "Role of underlayers in the development of evolutionary texture in polycrystalline thin films", *Surf. Coat. Technol.*, 80, 109-112

Adamik, M., Barna, P.B. (1999), "Applicability of the new structure zone models for the diagnosis of polycrystalline thin film technologies" in *Proc. of the 2nd COST 516 Tribology Symposium*, Antwerpen, 20-21 May, 78-83

Allamed, S.M., Shrotriya, P., Butterwick, A., Brown, S.B., Soboyejo, W.O. (2003), "Surface topography evolution and fatigue fracture in polysilicon MEMS structure", *J. Microelectromech. S.*, 12, 313-324

Almer, J., Oden, M., Hultman, L., Håkanson, G. (2000), "Microstructural evolution during tempering of arc-evaporated Cr-N coatings", *J. Vac. Sci. Technol. A*, 18, 121-130

Amontons, G. (1699), "De la résistance causée dans les machines", *Mémoires de l'Académie Royale A*, 257-282

Anderson, C.A., Bown, N.M.D., Cui, N., Liu, Z., McKinley, A., Walker, C.G.H. (1998), "Studies of the evolution of the topography of selected materials as a function of etching in reactive and non-reactive r.f. plasmas", *Surf. Coat. Technol.*, 106, 82-89

Ando, Y., Ino, J. (1998), "Friction and pull-off forces on submicron-size asperities", *Wear*, 216, 115-122

Ando, Y. (2000), "The effect of relative humidity on friction and pull-off forces measured on submicron-size asperity arrays", *Wear*, 238, 12-19

Aouadi, S.M., Schultze, D.M., Rohde, S.L., Wong, K.-C., Mitchell, K.A.R. (2001), "Growth and characterization of Cr_2N/CrN multilayer coatings", *Surf. Coat. Technol.*, 140, 269-277

Aouadi, S.M., Gorishnyy, T.Z., Schultze, D.M., Rohde, S.L. (2002), "Control and monitoring of growth of chromium nitride coatings using in-situ spectroscopic ellipsometry", *Surf. Coat. Technol.*, 153, 1-9

Atzor, M. (1989), *Aspekte des Magnetronsputterns zur Herstellung verschleiss- und korrosionsbeständiger Schichten auf Chrombasis*, VDI-Fortschrittsbericht Reihe 5, Vol. 156, (Düsseldorf: VDI)

Avelar-Batista, J.C., Wilson, A.D., Davison, A., Matthews, A., Fancey, K.S. (2004), "Gas scattering effects and microstructural evaluation of electron beam evaporated titanium coatings in neon and argon at different gas pressures", *Vacuum*, 72, 225-232

Azushima, A., Kuba, S., Tani, S., Olsson, D.D. (2006), "Direct observation of asperity deformation of specimens with random rough surfaces in upsetting and indentation processes", *Wear*, 260, 243-248

Baac, H., Lee, J.-H., Seo, J.-M., Park, T.H., Chung, H., Lee, S.-D., Kim, S.S. (2004), "Submicron-scale topographical control of cell growth using holographic surface relief grating", *Mat. Sci. Eng. C*, 24, 209-212

Bales, G.S., Zangwill, A. (1991), "Macroscopic model for columnar growth of amorphous films by sputter deposition", *J. Vac. Sci. Technol. A*, 9, 145-149

Barna, P.B., Adamik, M. (1998), "Fundamental structure forming phenomena of polycrystalline films and the structure zone models", *Thin Solid Films*, 317, 27-33

Barthlott, W., Neinhuis, C. (1997), "Purity of the sacred lotus or escape from contamination in biological surfaces", *Planta*, 202, 1-8

Beerschwinger, U., Abrecht, T., Mathieson, D., Reuben, R.L., Yang, S.J., Taghizadeh, M. (1995), "Wear at microscopic scales and light loads for MEMS applications", *Wear*, 181-183, 426-435

Benien, H., Maushart, J., Meyer, M., Suchentrunk, R. (1991), "D.C. magnetron sputtering of oxidation-resistant chromium and CrN films monitored by optical emission spectrometry", *Mater. Sci. Eng. A*, 139, 126-131

Bennewitz, R. (2005), "Friction force microscopy", *Mater. Today*, 8 (5), 42-48

Berg, J.C., ed. (1993), *Wettability* (New York: Dekker)

Berg, G., Friedrich, C., Broszeit, E., Berger, C. (1996), "Development of chromium nitride coatings substituting titanium nitride", *Surf. Coat. Technol.*, 86-87, 184-191

Bertrand, G., Savall, C., Meunier, C. (1997), "Properties of reactively sputtered RF magnetron-sputtered chromium-nitride coatings", *Surf. Coat. Technol.*, 96, 323-329

Bertrand, G., Mahdjoub, H., Meunier, C. (2000), "A study of the corrosion behaviour and protection quality of sputtered chromium nitride coatings", *Surf. Coat. Technol.*, 126, 199-209

Bhushan, B. (1999), *Principles and applications of tribology* (New York: John Wiley & Sons)

Bhushan, B. (2002), *Introduction to tribology* (New York: John Wiley & Sons)

Bhushan, B. (2005), "Nanotribology and nanomechanics", *Wear*, 259, 1507-1531

Bhushan, B., Venkatesan, S. (2005), "Effective mechanical properties of layered rough surfaces", *Thin Solid Films*, 473, 278-295

Bi, X., Xu, H., Gong, S. (2000), "Investigation of the failure mechanism of thermal barrier coatings prepared by electron beam physical vapor deposition", *Surf. Coat. Technol.*, 130, 122-127

Bico, J., Thiele, U., Quéré, D. (2002), "Wetting of textured surfaces", *Colloid Surface A*, 206, 41-46

Bilby, B.A., Cottrell, A.H., Swinden, F.R.S., Swinden, K.H. (1963), "The spread of plastic yield from a notch", *Proc. R. Soc. London Ser. A*, 272, 304-314

Binggeli, M., Christoph, R., Hintermann, H.E., Marti, O. (1993), "Atomic-scale tribometer for friction studies in a controlled atmosphere", *Surf. Coat. Technol.*, 62, 523-528

Binggeli, M., Mate, C.M. (1994), "Influence of capillary condensation of water on nanotribology studied by force microscopy", *Appl. Phys. Lett.*, 65, 415-417

Bland, R.D., Kominiak, G.J., Mattox, D.M. (1974), "Effect of ion bombardment during deposition of thick metal and ceramic deposits", *J. Vac. Sci. Technol.*, 11, 671-674

Bolse, W., Bolse, T., Dais, C., Etissa-Debissa, D., Elsanousi, A., Feyh, A., Kalafat, M., Paulus, H. (2005), "Modification of ceramic coatings by swift heavy ions", *Surf. Coat. Technol.*, 200, 1430-1435

Booth, H.J. (2004), "Recent applications of pulsed lasers in advanced materials processing", *Thin Solid Films*, 453-454, 450-457

Bouaidat, S., Winther-Jensen, B., Flygenring Christensen, S., Jonsmann, J. (2004), "Plasma-polymerized coatings for bio-MEMS applications", *Sensor. Actuat. A-Phys. A*, 110, 390-394

Bouissou, S., Petit, J.P., Barquins, M. (1998), "Normal load, slip rate and roughness influence on the polymethylmethacrylate dynamics of sling 1. Stable sliding to stick-slip-slip transition", *Wear*, 214, 156-164

Bouquet, L., Charlaix, E., Cilibreto, S., Crassous, J. (1998), "Moisture-induced ageing in granular media and the kinetics of capillary condensation", *Nature*, 396, 735-737

Bowden, F.P., Tabor, D. (2001), *The friction and lubrication of solids* (Oxford: Clarendon Press)

Bradley, R.M., Harper, J.M.E., Smith, D.A. (1986), "Theory of thin-film orientation by ion bombardment during deposition", *J. Appl. Phys.*, 60, 4160-4164

Brandon D.D., Kaplan, W.D. (1999), *Microstructural characterization of materials*, (Chichester: John Wiley & Sons)

Bregliozzi, G. (2006), "Microtribology of functional surfaces for microengineering applications", Ph.D. diss., (University of Perugia, Italy)

Broszeit, E., Friedrich, C., Berg, G. (1999), "Deposition, properties and applications of PVD Cr_xN coatings", *Surf. Coat. Technol.*, 115, 9-16

Brundle, C.R., Evans, Jr., C.A., Wilson, S. (eds.) (1992), *Encyclopedia of materials characterization - Surfaces, interfaces, thin films* (Boston: Butterworth-Heinemann)

Bull, S.J., Rickerby, D.S. (1990), "Compositional, microstructural and morphological effects on the mechanical and tribological properties of chromium nitride films", *Surf. Coat. Technol.*, 43/44, 732-744

Bunshah, R.F., Deshpandey, C. (1990), "Plasma-assisted deposition techniques for hard coatings", *Vacuum*, 41, 2190-2195

Burmeister, F., Kohn, C., Kuebler, R., Kleer, G., Bläsi, B., Gombert, A. (2005), "Applications of TiAlN- and TiO_2-coatings with nanoscale surface topographies", *Surf. Coat. Technol.*, 200, 1555-1559

Busch, C. (2001), "Solid lubrication" in T. Mang, W. Dresel (eds.) *Lubricants and lubrication* (Weinheim: Wiley-VCH) pp. 647-667

Carcia, P.F., French, R.H., Reilly, M.H., Lemon, M.F., Jones, D.J. (1997), "Optical superlattices-a strategy for designing phase-shift masks for photolithography at 248 and 193 nm: Application to AlN/CrN", *Appl. Phys. Lett.*, 70, 2371-2373

Carpick, R.W., Agraït, N., Ogletree, D.F., Salmeron, M. (1996), "Variation of the interfacial shear strength and adhesion of a nanometer-sized contact", *Langmuir*, 12, 3334-3340

Cassie, A.B.D., Baxter, S. (1944), "Wettability of porous surfaces", *Trans. Faraday. Soc.*, 40, 516-551

Chalker, P.R. (1991), "Characterisation of coatings and interfaces", in D.S. Rickerby, A. Matthews (eds.) *Advanced surface coatings: A handbook of surface engineering* (Glasgow: Blackie & Sons) pp. 278-314

Chang, W.R. (1997), "An elastic-plastic contact model for a rough surface with an ion-plated soft metal coating", *Wear*, 212, 229-237

Chekour, L., Nouveau, C., Chala, A., Labidi, C., Rouag, N., Djouadi, M.A. (2005), "Growth mechanism for chromium nitride films deposited by magnetron and triode sputtering methods", *Surf. Coat. Technol.*, 200, 241-244

Chen, W., Fadeev, A.Y., Hsieh, M.C., Öner, D., Youngblood, J., McCarthy, T.J. (1999), "Ultrahydrophobic and ultralyophobic surfaces: Some comments and examples", *Langmuir*, 15, 3395-3399

Chen, S., Liu, L., Wang, T. (2005), "Investigation of the mechanical properties of thin films by nanoindentation, considering the effect of thickness and different coating-substrate combinations", *Surf. Coat. Technol.*, 191, 25-32

Chun, J.-S., Petrov, I., Greene, J.E. (1999), "Dense fully 111-textured TiN diffusion barriers: Enhanced lifetime through microstructure control during layer growth", *J. Appl. Phys.*, 86, 3633-3641

Coll, B.F., Jacquot, P. (1988), "Surface modification of medical implants and surgical devices using TiN layers", *Surf. Coat. Technol.*, 36, 867-878

Collaud Coen, M., Lehmann, R., Groening, P., Schlapbach, L. (2003), "Modification of the micro-and nanotopography of several polymers by plasma treatments", *Appl. Surf. Sci.*, 207, 276-286

Coulomb, C.A. (1785), "Théorie des machines simples en ayant égard au frottement de leurs parties et à la raideur des cordages" in *Mémoires de Mathématique et de Physique de l'Académie Royale des Sciences*, Vol. X, Paris, 161-342

Craig, S., Harding, G.L. (1981), "Effects of argon pressure and substrate temperature on the structure and properties of sputtered copper films", *J. Vac. Sci. Technol.*, 19, 205-215

Cui, B., Veres, T. (2006), "Pattern replication of 100 nm to millimetre-scale features by thermal nanoimprint lithography", *Microelectron. Eng.*, 83, 902-905

Cunha, L., Andritschky, M., Pischow, K., Wang, Z. (1999), "Microstructure of CrN coatings produced by PVD techniques", *Thin Solid Films*, 355-356, 465-471

Cunha, L., Andritschky, M., Pischow, K., Wang, Z., Zarychta, A., Miranda, A.S., Cunha, A.M. (2000), "Performance of chromium nitride and titanium nitride coatings during plastic injection moulding", *Surf. Coat. Technol.*, 153, 160-165

Curtis, L.J. (1984), "Lifetime measurements in highly ionised atoms", *Phys. Scr.*, 78, 77-83

Czichos, H., Habig, K.-H. (1992), *Tribologie Handbuch: Reibung und Verschleiss* (Braunschweig: Vieweg)

Dalby, M.J., Childs, S., Riehle, M.O., Johnstone, H.J.H., Affrossman, S., Curtis, A.S.G. (2003), "Fibroplast reaction to island topography: changes in cytoskeleton and morphology with time", *Biomaterials*, 24, 927-935

Daniel, C., Mücklich, F., Liu, Z. (2003), "Periodical micro-nano-structucuring of metallic surfaces by interfering laser beams", *Appl. Surf. Sci.*, 208-209, 317-321

Davidse, P.D. (1967), "Theory and practice of RF sputtering", *Vacuum*, 17, 139-145

Davis, C.A. (1993), "A simple model for the formation of compressive stress in thin films by ion bombardment", *Thin Solid Films*, 226, 30-34

Debelle, A., Michel, A., Abadias, G., Jaouen, C. (2006), "Ion-irradiation induced stress relaxation in metallic thin films and multilayers grown by ion beam sputtering", *Nucl. Instrum. Meth. B*, 242, 461-465

Diss, P., Brendlé, M. (1997), "A general approach to discontinuous transfer films: influence of sliding speed and stick-slip phenomena", *Wear*, 203-204, 564-572

Djouadi, M.-A., Nouveau, C., Banakh, O., Sanjiés, R., Lévy, F., Nouet, G. (2002), "Stress profiles and thermal stability of Cr_xN_y films deposited by magnetron sputtering", *Surf. Coat. Technol.*, 151-152, 510-514

Dobrev D. (1982), "Ion-beam-induced texture formation in vacuum-condensed thin metal films", *Thin Solid Films*, 92, 41-53

Dong, W.P., Sullivan, P.J., Stout, K.J. (1994a), "Comprehensive study of parameters for characterising three-dimensional surface topography III: Parameters for characterising amplitude and some functional properties," *Wear*, 178, 29-43

Dong, W.P., Sullivan, P.J., Stout, K.J. (1994b), "Comprehensive study of parameters for characterising three-dimensional surface topography IV: Parameters for characterising spatial and hybrid properties", *Wear*, 178, 45-60

Donnet, C., Erdemir, A. (2004), "Historical developments and new trends in tribological and solid lubricant coatings", *Surf. Coat. Technol.*, 180-181, 76-84

Dresel, W. (2001), "Synthetic base oils", in T. Mang, W. Dresel (eds.) *Lubricants and lubrication* (Weinheim: Wiley-VCH) pp. 61-84

Dvorak, S.D., Woodland, D.D., Unertl, W.N. (1998), "Nanotribometer: a new instrument for nano-scale to micron-scale friction and wear measurements", *Tribol. Lett.*, 4, 199-204

Enachescu, M., Van den Oetelaar, R.J.A., Carpick, R.W., Ogletree, D.F., Flipse, C.F., Salmeron, M. (1998), "Atomic force microscopy study of an ideally hard contact: the diamond(111)/tungsten carbide interface", *Phys. Rev. Lett.*, 81, 1877-1880

Era, H., Ide, Y., Nino, A., Kishitake, K. (2005), "TEM study on chromium nitride coatings deposited by reactive sputter method", *Surf. Coat. Technol.*, 194, 265-270

Erdemir, A. (2005), "Review of engineered tribological interfaces for improved boundary lubrication", *Tribol. Int.*, 38, 249-256

Esaka, F., Furuya, K., Shimada, H., Imamura, M., Matsubayashi, N., Sato, H., Nishijima, A., Kawana, A., Ichimura, H., Kikuchi, T. (1997), "Comparison of surface oxidation of titanium nitride and chromium nitride films studied by x-ray absorption and photoelectron spectroscopy", *J. Vac. Sci. Technol. A*, 15, 2521-2528

Fang, C.C., Jones, F., Prasad, V. (1993), "Effects of gas impurity and ion bombardment on stresses in sputter-deposited thin films: A molecular-dynamics approach", *J. Appl. Phys.*, 74, 4472-4482

Favia, P., Cicala, G., Micella, A., Palombo, F., Rossigni, P., d'Agostino, R. (2003), "Deposition of super-hydrophobic fluorocarbon coatings in modulated RF glow discharges", *Surf. Coat. Technol.*, 169-170, 609-612

Fayer, A., Glozman, O., Hoffman, A. (1995), "Deposition of continuous and well adhering diamond films on steel", *Appl. Phys. Lett.*, 67, 2299-2301

Feng, Y., Zhou, Z., Ye, X., Xiong, J. (2003), "Passive valves based on hydrophobic microfluidics", *Sensor Actuat. A-Phys.*, 108, 138-143

Finegan, J.D., Hoffman, R.W. (1959), "Stress anisotropy in evaporated iron films", *J. Appl. Phys.*, 30, 597-598

Fischer-Cripps, A.C. (2002), *Nanoindentation* (New York: Springer)

Fitz, C., Fukarek, W., Möller, W. (2002), "Stress relaxation and phase stability of cubic boron nitride films during ion post implantation and annealing", *Thin Solid Films*, 408, 155-159

Flater, E.E., Corwin, A.D., de Boer, M.P., Carpick, R.W. (2006), "In situ wear studies of surface micromachined interfaces subjected to controlled loading", *Wear*, 260, 580-593

Friedrich, C. (1998), *Tribologische Problemlösungen mit PVD-Hartstoffschichten zum Verschleissschutz* (Aachen: Shaker)

Frederick, J.R., D'Arcy-Gall, J., Gall, D. (2006), "Growth of epitaxial CrN on MgO(001): role of deposition angle on surface morphological evolution", *Thin Solid Films*, 494, 330-335

Fujita, F.E. (1958), "Dislocation theory of fracture of crystals", *Acta Metall.*, 6, 543-555

Fouvry, S., Kapsa, P. (2001), "An energy description of hard coating wear mechanisms", *Surf. Coat. Technol.*, 138, 141-148

Gåhlin, R., Bromark, M., Hedenqvist, P., Hogmark, S., Håkansson, G. (1995), "Properties of TiN and CrN coatings deposited at low temperature using reactive arc-evaporation", *Surf. Coat. Technol.*, 76-77, 174-180

Gall, D., Kodambaka, S., Wall, M.A., Petrov, I., Greene, J.E. (2003), "Pathways of atomistic processes on TiN(001) and (111) surfaces during film growth: an ab initio study", *J. Appl. Phys.*, 93, 9086-9094

Gautier, C., Machet, J. (1997), "Study of the growth mechanisms of chromium nitride films deposited by vacuum arc evaporation", *Thin Solid Films*, 295, 43-52

Gerbig, Y., Dumitru, G., Romano, V., Spassov, V., Haefke, H. (2003), "Effects of laser texturing on technical surfaces", *Mater. Res. Soc. Proc.*, Vol. 750, Y5.37.1 – Y5.37.6

Gerbig, Y.B., Phani, A.R. Haefke, H. (2005), "Influence of nanoscale topography on the hydrophobicity of fluoro-based polymer thin films", *Appl. Surf. Sci.*, 242, 251-255

Gerbig, Y.B., Ahmed, S.I.-U., Chetwynd, D.G., Haefke, H. (2005), "Topography-related effects on the lubrication of nanostructured hard surfaces", *Tribol. Int.*, in press. [Online through Science Direct]. Available: http://www.sciencedirect.com/

Glocker, D.A., Shah, S.I. (eds.) (1995), *Handbook of Thin Film Process Technology* (Bristol: IOP Publishing)

Glozman, O., Hoffman, A. (1997), "Adhesion improvement of diamond films on steel substrates using chromium nitride interlayers", *Diam. Relat. Mater.*, 6, 796-801

Gnecco, E., Bennewitz, R., Gyalog, T., Loppacher, C., Bammerlin, M., Meyer, E., Güntherodt, H.J. (2000), "Velocity dependence of atomic friction", *Phys. Rev. Lett.*, 84, 1172-1175

Gnecco, E., Bennewitz, R., Socoliuc, A., Meyer, E. (2003), "Friction and wear on the atomic scale", *Wear*, 254, 859-862

Graf, W., Brucher, F., Höhl, M., Tröscher, T., Wittwer, V., Herlitze, L. (1997), "Development of large area sputtered solar absorber coatings", *J. Non-Cryst. Solids*, 218, 380-387

Graper, E.B. (1995), "Thermal evaporation", in D.A. Glocker, S.I. Shah (eds.) *Handbook of thin film process technology* (Bristol: IOP Publishing) pp. A1.0:1-A1.5:11

Grattan, K.T.V, Sun, D.T. (2000), "Fiber optic sensor technology: an overview", *Sensor. Actuator.*, 82, 40-61

Greene, J.E., Motooka, T., Sundgren, J.-E., Lubben, D., Gorbatkin, S., Barnett, S.A. (1987), "The role of ion/surface interactions and photo-induced reactions during film growth from the vapour phase", *Nucl. Instrum. Methods B*, 27, 226-242

Greene, J.E., Sundgren, J.-E., Hultmann, L., Petrov, I., Bergstrom, D.B. (1995), "Development of preferred orientation in polycrystalline TiN layers grown by ultrahigh vacuum reactive magnetron sputtering", *Appl. Phys. Lett.*, 67, 2928-2930

Greenwood, J.A., Williamson, J.B.P. (1966), "Contact of nominally flat surfaces", *Proc. R. Soc. London A*, 295, 300-319

Greenwood, J.A. (1992), *Fundamentals of friction* (Dordrecht: Kluwer)

Grovenor, C.R.M., Hentzell, H.T.G., Smith, D.A. (1984), "The development of grain structure during growth of metallic films", *Acta metall.*, 32, 773-781

Gschwender, L.J., Kramer, D.C., Lok, B.K., Sharma, S.K., Snyder, Jr., C.E., Sztenderowicz, M.L. (2001), "Liquid lubricants and lubrication", in B. Bhushan (ed.) *Modern Tribology Handbook*, Vol. I (Boca Raton: CRC Press) pp. 361-382

Guillén, F.J.H., Janischowsky, K., Kusterer, J., Ebert, W., Kohn, E. (2005), "Mechanical characterization and stress engineering of nanocrystalline diamonds films for MEMS applications", *Diam. Relat. Mater.*, 14, 411-415

Haghiri-Gosnet, A.M., Ladan, F.R., Mayeux, C., Launois, H., Joncour, M.C. (1989), "Stress and microstructure in tungsten sputtered thin films", *J. Vac. Sci. Technol. A*, 7, 2663-2669

Han, S., Lin, J.H., Guo, X.J., Tsai, S.H., Su, Y.O., Huang, J.H., Lu, F.-H., Shih, H.C. (2000), "The effect of Cr interlayer on the microstructure of CrN coatings on steel", *Thin Solid Films*, 377-378, 578-584

Han, Z., Tian, J., Lai, Q., Yu, X., Li, G. (2003), "Effect of N_2 partial pressure on the microstructure and mechanical properties of magnetron sputtered CrN_x films", *Surf. Coat. Technol.*, 162, 189-193

Hanein, Y., Pan, Y.V., Ratner, B.D., Denton, D.D., Böhringer, K.F. (2001), "Micromachining of non-fouling coatings for bio-MEMS applications", *Sensor. Actuat. B-Chem.*, 81, 49-54

He, X.-M., Baker, N., Kehler, B.A., Walter, K.C., Nastasi, M., Nakamura, Y. (2000), "Structure, hardness, and tribological properties of reactive magnetron sputtered chromium nitride films", *J. Vac. Sci. Technol. A*, 18, 30-36

Heidemeyer, J. (1981), "Influence of the plastic deformation of metals during mixed friction on their chemical reaction rate", *Wear*, 66, 379-387

Heilmann, P., Rigney, D.A. (1981), "An energy-based model of friction and its application to coated systems", *Wear*, 72, 195-217

Hertz, H. (1882), "Über die Berührung fester elastischer Körper", *J. Reine Angew. Math.*, 92, 156-171

Heyderman, L.J., Schift, H., David, C., Ketterer, B., Auf der Maur, M., Gobrecht, J. (2001), "Nanofabrication using hot embossing lithography and electroforming", *Microelectron. Eng.*, 57-58, 375-380

Hild, W. (2005), "Schmiermechanismen von Mikrosystemen unter Berücksichtigung der Benetzbarkeit", Ph.D. diss. (Technische Universität Ilmenau, Germany)

Hoffman, D.W., Thornton, J.A. (1977), "Internal stresses in sputtered chromium", *Thin Solid Films*, 14, 355-363

Hölscher, H., Schwarz, U.D., Wiesendanger, R. (1996), "Simulation of a scanned tip on a NaF(001) surface in friction force microscopy", *Europhys. Lett.*, 36, 19-24

Hones, P., Sanjines, R., Lévy, F. (1997), "Characterization of sputter-deposited chromium nitride thin films for hard coatings", *Surf. Coat. Technol.*, 94-95, 398-402

Hones, P. (2000), "Structural and electronic properties of transition metal nitrides with emphasis on chromium nitride based thin films", Ph.D. diss. (Ecole Polytechnique Fédérale de Lausanne, Switzerland)

Hoy, R., Sloof, W.G., Janssen, G.C.A.M. (2004), "Hard dense CrN_x coatings on three-dimensional objects", *Surf. Coat. Technol.*, 179, 215-222

Hsu, S.M. (2004), "Nano-lubrication: concept and design", *Tribol. Int.*, 37, 537-545

Hu, Z.M., Dean, T.A. (2000), "A study of the surface topography, friction and lubricants in metalforming", *Int. J. Mach. Tool. Manu.*, 40, 1637-1649

Huber, E., Hofmann, S. (1994), "Oxidation behaviour of chromium-based nitride coatings", *Surf. Coat. Technol.*, 68/69, 64-69

Hultman, L., Münz, W.D., Musil, J., Kadlec, S., Petrov, I., Greene, J.E. (1991), "Low-energy (~100 eV) ion irradiation during growth of TiN deposited by reactive magnetron sputtering: Effects if ion flux on film microstructure", *J. Vac. Sci. Technol. A*, 9, 434-438

Hultman, L., Sundgren, J.-E., Greene, J.E., Bergstrom, D.B., Petrov, I. (1995), "High-flux low-energy (20 eV) N^{2+} ion irradiation during TiN deposition by reactive magnetron sputtering: Effects on microstructure and preferred orientation", *J. Appl. Phys.*, 78, 5395-5403

Hurkmans, T., Lewis, D.B., Paritong, H., Brooks, J.S., Münz, W.D. (1999), "Influence of ion bombardment on structure and properties of unbalanced magnetron grown CrN_x coatings", *Surf. Coat. Technol.*, 114, 52-59

Huq, M.Z., Celis, J.-P. (2002), "Expressing wear rate in sliding contacts based on dissipated energy" *Wear*, 252, 375-383

Hwang, D.-H., Zum Gahr, K.-H. (2003), "Transition from static to kinetic friction of unlubricated or oil lubricated steel/steel, steel/ceramic and ceramic/ceramic pairs", *Wear*, 255, 365-375

Iborra, E., Olivares, J., Clement, M., Vergara, L., Sanz-Hervás, A., Sangrador, J. (2004), "Piezoelectric properties and residual stress of sputtered AlN thin films for MEMS applications", *Sensor. Actuat. A-Phys.*, 115, 501-507

Ino, K., Shinohara, T., Ushiki, T., Ohmi, T. (1997), "Ion energy, ion flux, and ion species effects on crystallographic and electrical properties of sputter-deposited Ta thin films", *J. Vac. Sci. Technol. A*, 15, 2627-2635

Inoue, Y., Yoshimura, Y., Ikeda, Y., Kohno, A. (2000), "Ultra-hydrophobic fluorine polymer by Ar-ion bombardment", *Colloid Surface B*, 19, 257-261

Inoue, S., Okada, F., Koterazawa, K. (2002), "CrN films deposited by rf reactive sputtering using a plasma emission monitoring control", *Vacuum*, 66, 227-231

Inoue, S., Saeki, T., Uchida, H., Koterazawa, K., Iwasa, M. (2002), "Effects of ion flux on the properties of dc magnetron-sputtered stainless steel films", *Vacuum*, 66, 257-261

Israelachvili, J.N., Homola, A.M., McGuiggan, P.M. (1988), "Dynamic properties of molecularly thin liquid films", *Science*, 240, 189-191

Israelachvili, J.N. (1992), "Adhesion forces between surfaces in liquids and condensable vapours", *Surf. Sci. Rep.*, 14, 109-159

Israelachvili, J.N., Chen, Y.-L., Yoshizawa, H. (1994), "Relationship between adhesion and friction forces", *J. Adhesion Sci. Technol.*, 8, 1231-1249

Israelachvili, J.N. (1995), "Surface forces and microrheology of molecular thin liquid films", in B. Bhushan (ed.) *Handbook of Micro/Nanotribology* (Boca Raton: CRC Press) pp. 267-319

Iwaya, M., Kasugai, H., Kawashima, T., Iida, K., Honshio, A., Miyake, Y., Kamiyama, S., Amano, H., Akasaki, I. (2006), "Improvement in light extraction efficiency in group III nitride-based light-emitting dioades using moth-eye structure", *Thin Solid Films*, in press, [Online through Science Direct]. Available: http://www.sciencedirect.com/

Johnson, K.L. (1987), *Contact mechanics* (Cambridge: University Press)

Jung, M.J., Nam, K.H., Jung, Y.M., Han, J.G. (2002), "Nucleation and growth behaviour of chromium nitride films deposited on various substrates by magnetron sputtering", *Surf. Coat. Technol.*, 171, 59-64

Kadlec, S., Musil, J., Valvoda, V., Münz, W.-D., Petersein, H., Schroeder, J. (1990), "TiN films grown by reactive magnetron sputtering with enhanced ionization at low discharge pressures", *Vacuum*, 41, 2223-2238

Kadlec, S., Musil, J., Vyskočil, J. (1992), "Growth and properties of hard coatings prepared by physical vapour deposition methods", *Surf. Coat. Technol.*, 54-55, 287-296

Kamminga, J.D., de Keijser, T.H., Delchz, R., Mittemeijer, E.J. (1998), "A model for stress in thin layers induced by misfitting particles: An origin for growth stress", *Thin Solid Films*, 317, 169-172

Kelly, P.J., Arnell, R.D. (1997), "Characterization studies of the structure of Al, Zr, and W coatings deposited by closed-field unbalanced magnetron sputtering", *Surf. Coat. Technol.*, 97, 595-602

Kelly, P.J., Arnell, R.D. (1998), "Development of a novel structure zone model", *J. Vac. Sci. Technol. A*, 16, 2858-2869

Kelly, P.J., Arnell, R.D. (2000), "Magnetron sputtering: a review of recent developments and applications", *Vacuum*, 56, 159-172

Khurshudov, A., Knigge, B., Talke, T.E., Baumgart, P., Tam, A. (1997), "Tribology of laser textured and mechanically textured media", *IEEE Transaction on Magnetics*, 31, 3190–3194

Kim, C.-J., Choi, C.-H. (2006), *Superhydrophobic surfaces*. (American Institute of Physics) [Online] Available: http://www.aip.org/png/2006/247.htm. [Accessed 13th February 2006]

Kim, B., Kim, K., Lee, B.T. (2003), "Radio frequency bias power effect on surface roughness of silicon carbide plasma etching", *Appl. Surf. Sci.*, 217, 261-267

Kirov, K.I., Ivanov, N.A., Atanasova, E.D., Minchev, G.M. (1976), "DC magnetron system for cathode sputtering", *Vacuum*, 26, 237-241

Klett, A., Freudenstein, R., Plass, M.F., Kulisch, W. (1999), "Stress of c-BN thin films: a parameter investigation", *Surf. Coat. Technol.*, 116-119, 86-92

Knapp, H.F., Guckenberger, R., Stemmer, A. (1998), "AFM imaging of biological samples using hydrophobic tips", *Probe Microscop.*, 1, 247-257

Knapp, H.F., Stemmer, A. (1999), "Preparation, comparison and performance of hydrophobic AFM tips", *Surf. Interface Anal.*, 27, 324-331

Knuyt, G., Quaeyhaegens, C., D'Haen, J., Stals, L.M. (1995), "A quantitative model for the evolution from random orientation to a unique texture in PVD thin film growth", *Thin Solid Films*, 258, 159-169

Knuyt, G., Lauwerens, W., Stals, L.M. (2000), "A unified theoretical model for tensile and compressive residual film stress", *Thin Solid Films*, 370, 232-237

Komvopoulos, K. (1996), "Surface engineering and micotribology for microelectromechanical systems", *Wear*, 200, 305-327

Kulinich, S.A., Farzaneh, M. (2005), "On wetting behavior of fluorocarbon coatings with various chemical and roughness characteristics", *Vacuum*, 79, 255-264

Kuruppu, M.L., Negrea, G., Ivanov, I.P., Rohde, S.L. (1998), "Monolithic and multilayer Cr/CrN, Cr/Cr_2N and Cr_2N/CrN on hard and soft substrates", *J. Vac. Sci. Technol. A*, 16, 1949-1955

Labidi, C., Collet, R., Nouveau, C., Beer, P., Nicosia, S., Djouadi, M.A. (2005), "Surface treatments of tools used in industrial wood machining", *Surf. Coat. Technol.*, 200, 118-122

Lacroix, L.-M., Lejeune, M., Ceriotti, L., Kormunda, M., Meziani, T., Colpo, P., Rossi, F., (2005), "Tuneable rough surfaces: A new approach for elaboration of superhydrophobic films", *Surf. Sci.*, 592, 182-188

Lakshmipathy, R., Sagar, R. (1992), "Effect of die surface topography on die-work interfacial friction in open die forging", *Int. J. Mach. Tool Manu.*, 32, 685-693

Landheer, D., de Gee, A.W.J. (1991), "Adhesion, friction and wear", *Mater. Res. Soc. Bull.*, 16, 36-40

Landman, U., Luedtke, W.D. (1993), "Interfacial junctions and cavitation", *Mater. Res. Soc. Bull.*, 18, 36-45

Landolt, D., Chauvy, P.-F., Zinger, O. (2003), "Electrochemical micromachining, polishing and surface structuring of metals: fundamental aspects and new developments", *Electrochim. Acta*, 48, 3185-3201

Lansdown, A.R. (2004), *Lubrication and lubrication selection: A practical guide* 3rd ed. (Bury St Edmunds: Professional Engineering Publications)

Lardon, M., Buhl, R., Signer, H., Moll, E., Pulker, H.K. (1980), "Influence of the substrate temperature and the discharge voltage on the structure of titanium films produced by ion-plating", *Vacuum*, 30, 255-260

Larsson, M., Hedenqvist, P., Hogmark, S. (1996), "Deflection measurements as method to determine residual stress in thin hard coatings on tool materials", *Surf. Eng.*, 12, 43-48

Ledermann, N., Baborowski, J., Muralt, P., Xantopoulos, N., Tellenbach, J.-M. (2000), "Sputtered silicon carbide thin films as protective coating for MEMS applications", *Surf. Coat. Technol.*, 125, 246-250

Li, W., Li, D.Y. (2006), "Influence of surface morphology on corrosion and electronic behaviour", *Acta Mater.*, 54, 445-452

Lim, S.C., Ashby, M.F. (1987), "Wear-mechanisms maps", *Acta metal.*, 35, 1-24

Lim, J., Lee, C. (2006), "The rf-power dependence of the deposition rate, the hardness and the corrosion-resistance of the chromium nitride film deposited by using a dual ion beam sputtering system", *Mat. Chem. Phys.*, 95, 164-168

Liu, H., Ahmed, S.I.-U., Scherge, M. (2001), "Microtribological properties of silicon and silicon coated with diamond like carbon, octadecyltrichlorosilane and stearic acid cadmium salt films: a comparative study", *Thin Solid Films*, 381, 135-142

Lo, S.W., Horng, T.C. (1999), "Lubricant permeation from micro oil pits under intimate contact condition", *J. Tribol-T ASME*, 121, 633-638

Logothetidis, S., Patsalas, P., Sarakinos, K., Charitidis, S., Metaxa, C. (2004), "The effect of crystal structure and morphology on the optical properties of chromium nitride thin films", *Surf. Coat. Technol.*, 180-181, 637-641

Lousa, A., Romero, J., Martinez, E., Esteve, J., Montalà, F., Carreras, L. (2001), "Multilayered chromium/chromium nitride coatings for use in pressure die-casting", *Surf. Coat. Technol.*, 146-147, 268-273

Lu, Y., Chen., S.C. (2004), "Micro and nano-fabrication of biodegradable polymers for drug delivery", *Adv. Drug Deliver. Rev.*, 56, 1621-1633

Lugscheider, E., Bobzin, K. (2003), "Wettability of PVD compound materials by lubricants", *Surf. Coat. Technol.*, 165, 51-57

Maboudian, R. (1998), "Adhesion and friction issues associated with reliable operation of MEMS", *Mater. Res. Soc. Bull.*, 23, 47-51

Maboudian, R., Ashurst, W.R., Carraro, C. (2000), "Self-assembled monolayers as anti-stiction coatings for MEMS: characteristics and recent developments", *Sensor. Actuator.*, 82, 219-223

Machelin, E.S. (1995), *Material science in microelectronics-the relationship between thin film processing and structure* (Croton-on Hudson: Giro Press)

Mahan, J.E. (2000), *Physical vapour deposition of thin films* (New York: John Wiley & Sons)

Mainsah, E., Stout, K.J., Thomas, T.R. (2001), "Surface measurements and characterization", in Mainsah, E., Greenwood, J.A., Chetwynd, D.G. (eds.) *Metrology and properties of engineering surfaces* (Boston: Kluwer Academic Publishers) pp. 1-42

Mang, T. (2001), "Base oils" in Mang, T., Dresel, W. (eds.) *Lubricants and lubrication* (Weinheim: Wiley-VCH) pp. 32-60

Mang, T., W. Dresel, W. (eds.) (2001) *Lubricants and lubrication* (Weinheim: Wiley-VCH)

Marinov, M. (1977), "Effect of ion bombardment on the initial stages of thin film growth", *Thin Solid Films*, 46, 267-274

Martinez, E., Sanjinés, R., Banakh, O., Lévy, F. (2004), "Electrical, optical and mechanical properties of sputtered CrN_y and $Cr_{1-x}Si_xN_{1.02}$ thin films", *Thin Solid Films*, 447-448, 332-336

Mastrangelo, C.H. (1997), "Adhesion-related failure mechanisms in micromechanical devices", *Tribol. Lett.*, 3, 223-238

Mattox, D.M., Kominiak, G.J. (1971), "Structure modification by ion bombardment during deposition", *J. Vac. Sci. Technol.*, 9, 528-532

Mattox, D.M. (1998), *Handbook of physical vapour deposition (PVD) processing* (Westwood: Noyes publications)

Mayrhofer, P.H., Tischler, G., Mitterer, C. (2001), "Microstructure and mechanical/thermal properties of Cr-N coatings deposited by reactive unbalanced magnetron sputtering", *Surf. Coat. Technol.*, 142-144, 78-84

McNeely, M.R., Sputea, M.K., Tusneemb, N.A., Oliphant, A.R. (1999), "Sample processing with hydrophobic microfluidics", *J. Assoc. Lab. Autom.*, 4 (4), 30-33

Merlijn van Spengen, W. (2003), "MEMS reliability from a failure mechanisms perspective", *Microelectron. Reliab.*, 43, 1049-1060

Messier, R., Giri, A.P., Roy, R.A. (1984), "Revised structure zone model for thin film physical structure", *J. Vac. Sci. Technol. A*, 2, 500-503

Milosev, I., Abels, J.M., Strehblow, H.-H., Navinšek, B., Metikoš-Hukovič, M. (1996), "High temperature oxidation of thin CrN coatings deposited on steel", *J. Vac. Sci. Technol. A*, 14, 2527-2534

Miwa, M., Nakajima, A., Fujishima, A., Hashimoto, K., Watanabe, T. (2000), "Effect of the surface roughness on sliding angles of water droplets on superhydrophobic surfaces", *Langmuir*, 16, 5754-5760

Mølgaard, J. (1976), "Die Entwicklung von Verschleissprozessthesen", *Schmiertech. Tribol.*, 23, 126-130

Molinari, A., Estrin, Y., Mercier, S. (1999), "Dependence of the coefficient of friction on the sliding conditions in the high velocity range", *ASME J. Tribol.*, 121, 35-41

Mollenhauer, O., Ahmed, S.I.-U., Spiller, F., Haefke, H. (2003), "High precision positioning and measurement systems for microtribotesting" in Proc. *of Symposium TRIMIS 2003: Microtribology - Tribology in Microsystems,* Neuchâtel, 1-3 June, 2003, CD

Movchan, B.A., Demchishin, A.V. (1969), "Study of the structure and properties of thick vacuum condensates of nickel, titanium, tungsten, aluminium oxide and zirconium dioxide", *Fiz. Metal. Metalloved,* 28, 653-660

Mrotzek, S., Harnisch, A., Hungenbach, G., Strahl, H., Hulsenberg, D. (2003), "Processing techniques for photostructurable glasses", *Glass Sci. Technol.*, 76, 22-27

Müller, K.-H. (1985), "Dependence of thin-film microstructure on deposition rate by means of a computer simulation", *J. Appl. Phys.*, 58, 2573-2576

Müller, K.-H. (1986), "Model for ion-assisted thin-film densification", *J. Appl. Phys.*, 59, 2803-2807

Müller, K.-H. (1987a), "Ion-beam-induced epitaxial vapour-phase growth: A molecular-dynamics study", *Phys. Rev. B*, 35, 7906-7913

Müller, K.H. (1987b), "Stress and microstructure of sputter-deposited thin films: Molecular dynamics investigations", *J. Appl. Phys.*, 62, 1796-1799

Munnik, F., Benninger, F., Mikhailov, S., Bertsch, A., Renaud, P., Lorenz. H., Gmür, M. (2003), "High aspect ratio, 3D structuring of photoresist materials by ion beam LIGA", *Microelectron. Eng.*, 67-68, 96-103

Münz, W.-D. (1991), "The unbalanced magnetron: current status of development", *Surf. Coat. Technol.*, 48, 81-94

Münz, W.-D., Hauzer, F.J.M., Schulze, D., Buil, B. (1991), "A new concept for the physical vapour deposition coating combining the methods of arc evaporation and unbalanced-magnetron sputtering", *Surf. Coat. Technol.*, 49, 161-167

Musil, J., Kadlec, S., Valvoda, V., Kužel, Jr., R., Černy, R. (1990), "Ion-assisted sputtering of TiN films", *Surf. Coat. Technol.*, 43-44, 259-269

Nam, K.H., Jung, M.J., Han, J.G. (2000), "A study on the high rate deposition of CrN_x films with controlled microstructure by magnetron sputtering", *Surf. Coat. Technol.*, 131, 22-227

Navinšek, B., Panjan, P. (1993), "Oxidation resistance of PVD Cr, Cr-N and Cr-N-O hard coatings", *Surf. Coat. Technol.*, 59, 244-248

Navinšek, B., Panjan, P., Milošev, I. (1997), "Industrial application of CrN(PVD) coatings, deposited at high and low temperatures", *Surf. Coat. Technol.*, 97, 182-191

Novák, R., Kvasnička, I., Nováková, D., Malá, Z. (1999), "Study of hard PVD coatings on strongly curved surfaces", *Surf. Coat. Technol.*, 114, 65-69

NTC (2005), *Ultrahydrophobic fibers: Lotus approach*, NTC Online Research Project Database, Available: http://www.ntcresearch.org/projectapp/index.cfm?project=C04-L06&topic=state_of_the_art. [Accessed: Sept. 1, 2005]

Nyman, P., Mäki, R., Olsson, R., Ganemi, B. (2006), "Influence of surface topography on friction characteristics in wet clutch applications", *Wear*, 261, 46-52

Ohring, M. (2002), *Materials science of thin films* (San Diego: Academic Press)

Oliver, W.C., Pharr, G.M. (1992), "An improved technique for determining hardness and elastic modulus using load and displacement sensing indentation experiments", *J. Mater. Res.*, 7, 1564-1583

Olsson, H., Åström, K.J., Canudas de Witt, C., Gäfvert, M., Lischinsky, P. (1997), *Friction models and friction compensation*, [online] Available: http://www.control.lth.se/~kja/friction.pdf.[Accessed: 6th December 2005]

Onda, T., Shibuichi, S., Satoh N., Tsujii, K. (1996), "Super-water-repellent fractal surfaces", *Langmuir*, 12, 2125-2127

Opitz, A., Ahmed, S.I.-U., Schaefer, J.A., Scherge, M. (2002), "Friction of thin water films: a nanotribological study", *Surf. Sci.*, 504, 199-207

Ortmann, S., Savan, A., Gerbig, Y., Haefke, H. (2003), "In-process structuring of CrN coatings, and its influence on friction in dry and lubricated sliding", *Wear*, 254, 1099-1105

Ostermeyer, G.P., Müller, M. (2006), "Dynamic interaction of friction and surface topography in brake systems", *Tribol. Int.*, 39, 370-380

Ott, J.P., Michal, G.M., Chottiner, O.S. (1989), "Shear strength of aluminium-sapphire interfaces", *Mater. Lett.*, 8, 481-485

Pandey, K.N., Chand, S. (2003), "An energy based fatigue crack growth model", *Int. J. Fatigue*, 25, 771-778

Panjan, P., Cvahte, P., Čekada, M., Navinšek, B., Urankar, I. (2001), "PVD CrN coatings for protection of extrusion dies", *Vacuum*, 61, 241-244

Park, J., Kim, D.-J., Kim, Y.-K., Lee, K.-H., Lee, K.-H., Lee, H., Ahn, S. (2003), "Improvement of the biocompatibility and mechanical properties of surgical tools with TiN coating by PACVD", *Thin Solid Films*, 435, 102-107

Patton, S.T., Bhushan, B. (1999), "Origins of friction and wear of the thin metallic layer of metal evaporated magnetic tape", *Wear*, 224, 126-140

Paturaud, C., Farges, G., Sainte Catherine, M.C., Machet, J. (1999), "Correlation between hardness and embedded argon content of magnetron sputtered chromium films", *Thin Solid Films*, 347, 46-55

Pelleg, J., Zevin, L.Z., Lungo, S., Croitoru, N. (1991), "Reactive-sputter-deposited TiN films on glass substrates", *Thin Solid Films*, 197, 170-173

Penfold, A.S. (1995), "Magnetron sputtering", in D.A. Glocker, S.I. Shah (eds.) *Handbook of thin film process technology* (Bristol: IOP Publishing) pp. A3.2:1-A3.2:27

Penning, F.M. (1936), "Die Glimmentladung bei niedrigem Druck zwischen koaxialen Zylindern in einem axialen Magnetfeld", *Physica III*, 9, 873-894

Persson, B.N.J. (2000), *Sliding friction- Physical principles and applications* 2nd ed. (Berlin: Springer)

Persson, B.N.J. (2001), "Elastoplastic contact between randomly rough surfaces", *Phys. Rev. Lett.*, 87, 116101-1 – 116101-4

Petrov, I., Barna, P.B., Hultman, L., Greene, J.E. (2003), "Microstructural evolution during film growth", *J. Vac. Sci. Technol.* A, 21, S117-S128

Pettersson, U. (2005), "Surfaces designed for high and low friction", Ph.D. diss. (Uppsala University, Sweden)

Piétrement, O., Troyon, M. (2001), "Study of the interfacial shear strength on carbon fibers surface at the nanometer scale", *Surf. Sci.*, 490, L592-L596

Piscanec, S., Colombi Ciacchi, L., Vessilli, E., Comelli, G., Sbaizero, O., Meriani, S., De Vita, A. (2004), "Bioactivity of TiN-coated titanium implants", *Acta Mater.*, 52, 1237-1245

Quéré, D. (2002), "Rough ideas on wetting", *Physica A*, 313, 32-46

Rabinowicz, E. (1995), *Friction and wear of materials* 2nd ed. (New York: John Wiley & Sons)

Radhakrishnan, G., Robertson, R.E., Adams, P.M., Cole, R.C. (2002), "Integrated TiC coatings for moving MEMS", *Thin Solid Films*, 420-421, 553-564

Rajan, N., Zorman, A., Mehregany, M., DeAnna, R., Harvey, R.J. (1998), "Effect of MEMS-compatible thin film hard coatings on the erosion resistance of silicon micromachined atomizers", *Surf. Coat. Technol.*, 108-109, 391-397

Ranjan, R., Lambeth, D.N., Tromel, M., Goglia P., Li, Y. (1991), "Laser texturing for low-flying-height media", *J. Appl. Phys.*, 69, 5745–5747

Rebholz, S., Ziegele, H., Leyland, A., Matthews, A. (1999), "Structure, mechanical and tribological properties of nitrogen-containing chromium coatings prepared by reactive magnetron sputtering", *Surf. Coat. Technol.*, 115, 222-229

Rickerby, D.S., Jones, A.M., Bellamy, B.A. (1989), "X-ray diffraction studies of physically vapour-deposited coatings", *Surf. Coat. Technol.*, 37, 111-137

Riedo, E., Lévy, F., Brune, H. (2002), "Kinetics of capillary condensation in nanoscopic sliding friction", *Phys. Rev. Lett.*, 88, 185505-1- 185505-4

Riedo, E., Brune, H. (2003), "Young modulus dependence of nanoscopic friction coefficient in hard coatings", *Appl. Phys. Lett.*, 83, 1986-1988

Riedo, E., Palaci, I., Boragno, C., Brune, H. (2004), "The 2/3 power law dependence of capillary force on normal load in nansocopic friction", *J. Phys. Chem. B*, 108, 5324-5328

Romig, Jr., A.D., Dugger, M.T., McWorther, P.J. (2003), "Materials issues in microelectromechanical devices: science, engineering, manufacturability and reliability", *Acta Mater.*, 51, 5837-5866

Rosenfield, A.R. (1981), "A dislocation theory approach to wear", *Wear*, 72, 97-103

Rossnagel, S.M. (1991), "Uses of plasmas in deposition technologies", in D.S. Rickerby, A. Matthews (eds.) *Advanced surface coatings: A handbook of surface engineering* (Glasgow: Blackie & Sons Ltd.) pp. 14-40

Sanders, J.V. (1971), "Structure of evaporated metal films", in J.R. Anderson (ed.) *Chemisorption and Reactions on Metallic Films*, Vol. I, (London: Academic Press) pp. 1-38

Sanjinés, R., Hones, P., Lévy, F. (1998), "Hexagonal nitride coatings: electronic and mechanical properties of V_2N, Cr_2N and δ-MoN", *Thin Solid Films*, 332, 225-229

Sayles, R.S., Thomas, T.R. (1978), "Surface topography as a nonstationary random process", *Nature*, 271, 431-434

Schargott, M., Popov, V. (2006), "Diffusion as a model of formation and development of surface topography", *Tribol. Int.*, 39, 431-436

Scheideler, L., Geis-Gerstorfer, J., Kern, D., Pfeiffer, F., Rupp, F., Weber, H., Wolburg, H. (2003), "Investigation of cell reactions to microstructured implant surfaces", *Mat. Sci. Eng. C*, 23, 455-459

Schell, N., Matz, W., Bøttiger, J., Chevallier, J., Kringhøj, P. (2002), "Development of texture in TiN films by use of in situ synchrotron X-ray scattering", *J. Appl. Phys.*, 91, 2037-2044

Schell, N., Petersen, J.H., Bøttiger, J., Mücklich, A., Chevallier, J., Andreasen, K.P., Eichhorn, F. (2003), "On the development of texture during growth of magnetron-sputtered CrN", *Thin Solid Films*, 426, 100-110

Scherge, M., Ahmed I., Mollenhauer, O., Spiller, F. (2000), "Detection of microNewton forces in tribology", *tm*, 7-8, 324-327

Scherge, M., Gorb, S.N. (2001), *Biological micro- and nanotribology* (Berlin: Springer)

Schift, H., David, C., Gabriel, M., Gobrecht, J., Heyderman, L.J., Kaiser, W., Köppel, S., Scandella, L. (2000), "Nanoreplication in polymers using hot embossing and injection molding", *Microelectron. Eng., 53*, 171-174

Schoen, M., Hess, S., Diestler, D.J. (1995), "Rheological properties of confined thin films", *Phys. Rev. E*, 52, 2587-2602

Schwarz, U.D., Zwörner, O., Köster, P., Wiesendanger, R. (1997), "Quantitative analysis of the frictional properties of solid materials at low loads I. Carbon compounds", *Phys. Rev. B*, 56, 6987-6996

Seah, M.P., Spencer, S.J., Cumpson, P.J., Johnstone, J.E. (1999), "Cones formed during sputtering of InP and their use in defining AFM tip shapes", *Appl. Surf. Sci.*, 144-145, 151-155

Seekamp, J., Zankovych, S., Helfer, A.H., Maury, P., Sotomayor Torres, C.M., Böttger, G., Liguada, C., Eich, M., Heidar, B., Montelius, L., Ahopelto, J. (2002), "Nanoimprinted passive optical devices", *Nanotechnology*, 13, 581-586

Shah, S.I. (1995), "Sputtering", in D.A. Glocker, S.I. Shah (eds.) Handbook *of thin film process technology* (Bristol: IOP Publishing) pp. A3.0:1-A3.0:22

Shen, Y.G., Mai, Y.W. (2000), "Effect of deposition conditions on internal stresses and microstructure of reactively sputtered tungsten nitride films", *Surf. Coat. Technol.*, 127, 238-245

Shen, Y.G. (2003), "Effect of deposition conditions on mechanical stresses and microstructure of sputter-deposited molybdenum and reactively sputter-deposited molybdenum nitride films", *Mat. Sci. Eng. A*, 359, 158-167

Sibilia, J.P. (ed.) (1996), *A guide to materials characterization and chemical analysis* 2nd ed. (New York: John Wiley & Sons)

Sikkens, M., van Herreveld, A.A.M.T., Vogelzang, E., Boose, C.A. (1983), "The development of high performance, low-cost solar-selective absorbers", *Thin Solid Films*, 108, 229-238

Singer, I.L., Pollock, H.M. (1992), *Fundamental of friction: macroscopic and microscopic processes* (Dordrecht: Kluwer)

Sproul, W.D., Rudnick, P.J., Graham, M.E., Rohde, S.L. (1990), "High rate reactive sputtering in an opposed cathode closed-field unbalanced magnetron sputtering system", *Surf. Coat. Technol.*, 43-44, 270-278

Stoney, G.G. (1909), "The tension of metallic films deposited by electrolysis", *Proc. R. Soc. (London) A*, 82, 172-175

Straffelini, G. (2001), "A simplified approach to the adhesive theory of friction", *Wear*, 249, 79-84

Su, Y.L., Yao, S.H., Leu, Z.L., Wei, C.S., Wu, C.T. (1997), "Comparison of tribological behaviour of three films-TiN, TiCN and CrN-grown by physical vapour deposition", *Wear*, 213, 165-174

Sugiyama, K., Hayashi, K., Sasaki, J., Ichiko, O., Hashiguchi, Y. (1994), "Microstructure and wear behaviour of chromium nitride films formed by ion-beam-enhanced deposition", *Surf. Coat. Technol.*, 66, 505-508

Sundararajan, S. (2001), "Micro/nanoscale tribology and mechanics of components and coatings for MEMS", Ph.D. diss. (The Ohio State University, USA)

Sundgren, J.-E., Johansson, B.-O., Hentzell, H.T.G., Karlsson, S.-E. (1983), "Mechanisms of reactive sputtering of titanium nitride and titanium carbide III: Influence of substrate bias on composition and structure", *Thin Solid Films*, 105, 385-393

Szolwinksi, M.P., Farris, T.N. (1996), "Mechanics of fretting fatigue crack formation", *Wear*, 198, 93-107

Tabor, D. (1977), "Surface forces and surface interactions", *J. Colloid. Interface Sci.*, 58, 2-13

Tabor, D. (1982), "The role of surface and intermolecular forces in thin film lubrication", in J.M. Georges (ed.) *Microscopic aspects of adhesion and lubrication*, Tribology Series 7 (Amsterdam: Elsevier)

Takahashi, T., Masugata, K., Kawai, H., Kontani, S., Yamamoto, J. (2000), "Surface morphology of TiN films reactively deposited by bias sputtering", *Vacuum*, 59, 777-784

Takeda, S., Fukawa, M. (2003), "Surface OH groups governing surface chemical properties of SiO_2 thin films deposited by RF magnetron sputtering", *Thin Solid Films*, 444, 153-157

Tambe, N.S., Bhushan, B. (2005), "Friction model for the velocity dependence of nanoscale friction", *Nanotechnology*, 16, 2309-2324

Tang, C., Alexander, S., Bruinzma, R. (1990), "Theory for the growth of amorphous films", *Phys. Rev. Lett.*, 64, 772-775

Tang, H., Wang, L-P., Gui, J., Kuo, D. (2000), "Experimental and analytical studies of dynamic friction at the head/disk interface", *Tribol. Int.*, 33, 343-351

Tao, Z., Bhushan, B. (2005), "Bonding, degradation, and environmental effects on novel perfluoropolyether lubricants", *Wear*, 259, 1352-1361

Tayebi, N., Polycarbou, A.A. (2005), "Reducing the effects of adhesion and friction in microelectromechanical systems (MEMSs) through surface roughening: Comparison between theory and experiments", *J. Appl. Phys.*, 98, 073528-1 – 073528-13

Thomas, T.R. (1999), *Rough surfaces*, 2nd ed. (London: Imperial College Press)

Thornton, J.A. (1977), "High rate thick film growth", *Ann. Rev. Mater. Sci.*, 7, 239-260

Thornton, J.A., Hoffman, D.W. (1989), "Stress-related defects in thin films", *Thin Solid Films*, 171, 5-31

Tomlinson, G.A. (1929), "A molecular theory of friction", *Phil. Mag. Series*, 7, 905-939

Toth, L.E. (1971), *Transition metal carbides and nitrides* (New York: Academic Press)

Tricoteaux, A., Jouan, P.Y., Guerin, J.D., Martinez, J., Djouadi, A. (2003), "Fretting wear properties of CrN and Cr_2N coatings", *Surf. Coat. Technol.*, 174-175, 440-443

Tsuboi, S., Kotsuji, S., Yoshihara, T., Suzuki, K. (1997), "Low-stress sputtered chromium-nitride hardmasks for x-ray mask fabrication", *J. Vac. Sci. Technol. B*, 15, 2228-2231

Tu, J.-N., Duh, J.-G., Tsai, S.-Y. (2000), "Morphology, mechanical properties, and oxidation behavior of reactively sputtered Cr-N films", *Surf. Coat. Technol.*, 133-134, 181-185

Uelzen, T., Müller, J. (2003), "Wettability enhancement by rough surfaces generated by thin film technology", *Thin Solid Films*, 434, 311-315

Ürgen, M., Fuat Çakir, A. (1997), "The effect of heating on corrosion behaviour of TiN- and CrN-coated steels", *Surf. Coat. Technol.*, 96, 236-244

Usui, S., Umehara N., Kato, K. (2000), "The effect of surface energy on pull-off force transition in relation to humidity", *Proc. of International Tribology Conference*, Nagasaki , 29 October - 2 November, Vol. 1, 739-744.

Van der Drift, A. (1967), "Evolutionary selection, A principle governing growth orientation in vapour-deposited layers", *Philips Res. Repts*, 22, 267-288

Van Wyk, G.N., Smith, H.J. (1980), "Crystalline reorientation due to ion bombardment", *Nucl. Instrum. Methods*, 170, 433-439

Vetter, J., Knaup, R., Dwuletzki, H., Schneider, E., Vogler, S. (1996), "Hard coatings for lubrication reduction in metal forming", *Surf. Coat. Technol.*, 86-87, 739-747

Vladimirov, V.I. (1976), *Einführung in die physikalische Theorie der Plastizität und Festigkeit* (Leipzig: Verlag für Grundstoffindustrie)

Walze, G., Nitz, P., Ell, J., Georg, A., Gombert, A., Hossfeld, W. (2005), "Combination of microstructures and optically functionally coatings for solar control glazing", *Sol. Energ. Mat. Sol. C.*, 89, 233-248

Walzer, K., Toccoli, T., Pallaoro, A., Verucchi, R., Fritz, T., Leo, K., Boschetti, A., Iannotta, S. (2004), "Morphological and optical properties of titanyl phthalocyanine films deposited by supersonic molecular beam epitaxy (SuMBE)", *Surf. Sci.*, 573, 346-358

Wang, D., Oki, T. (1990), "The morphology and orientation of Cr-N films deposited by reactive ion plating", *Thin Solid Films*, 185, 219-230

Wang, M., Miyake, S., Matsunuma, S. (2005), "Nanowear studies of PFPE lubricant on magnetic perpendicular recording DLC-film-coated disk by lateral oscillation tests", *Wear*, 259, 1332-1342

Warren, B. E. (1990), *X-ray diffraction* (New York: Dover Publications)

Webb, R., Kerford, M., Way, A. (1999), "Computer simulation of sputtering of gold targets using Sb and Sb_2 ions", *Nucl. Instrum. Meth. B*, 153, 309-313

Wellman, R.G., Deakin, M.J., Nicholls, J.R. (2005), "The effect of TBC morphology on the erosion rate of EB PVD TBCs", *Wear*, 258, 349-356

Wenzel, R.N. (1936), "Resistance of solid surfaces to wetting by water", *Ind. Eng. Chem.*, 28, 988-994

Westwood, W.D. (1988), "Sputter deposition process", *Mater. Res. Soc. Bull.*, December, 46-51

Whitehead, K.A., Colligon, J., Verran, J. (2005), "Retention of microbial cells in substratum surface features of micrometer and sub-micrometer dimensions", *Colloid Surface B*, 41, 129-138

Wiklund, D., Wihlborg, A., Rosén, B.-G. (2004), "Evaluation of surface topography parameters for friction prediction in stamping", *Wear*, 257, 1296-1300

Williams, J.A (2001), "Friction and wear of rotating pivots in MEMS and other small scale devices", *Wear*, 251, 965-972

Windischmann, H. (1991), "Intrinsic stress in sputtered thin films", *J. Vac. Sci. Technol. A*, 9, 2431-2436

Window, B., Savvides, N. (1986), "Charged particle flux from planar magnetron sputtering sources", *J. Vac. Sci. Technol. A*, 4, 196-202

Wuttke, W. (1986), *Tribophysik: Reibung und Verschleiss von Metallen* (Leipzig: Fachbuch-verlag)

Xiao, L., Rosen, B.-G., Amini, N., Nilsson, P.H. (2003), "A study on the effect of surface topography on rough friction in roller contact", *Wear*, 254, 1162-1169

Xu, J., Umehara, H., Kojima, I. (2002), "Effect of deposition parameters on composition, structures, density and topography of CrN films deposited by r.f. magnetron sputtering", *Appl. Surf. Sci.*, 201, 208-218

Xu, Z.-H., Rowcliffe, D. (2004), "Finite element analysis of substrate effects on indentation behaviour of thin films", *Thin Solid Films*, 447-448, 399-405

Yao, S.H., Su, Y.L. (1997), "The tribological potential of CrN and Cr(C,N) deposited by multi-arc PVD process", *Wear*, 212, 85-94

Ying, F., Smith, R.W., Srolovitz, D.J. (1996), "The mechanism of texture formation during film growth: The roles of preferential sputtering and shadowing," *Appl. Phys. Lett.*, 69, 3007-3009

You, H.-X., Brown, N.M., Al-Assadi, K.F. (1993), "Radio-frequency (RF) plasma etching of graphite with oxygen: a scanning tunnelling microscope study", *Surf. Sci.*, 284, 263-272

Young, T. (1805), "An essay on the cohesion of fluids", *Phil. Trans. Roy. Soc. Lond.*, 95, 65-87

Youngblood, J.P., McCarthy, T.J. (1999), "Ultrahydrophobic polymer surfaces prepared by simultaneous ablation of polypropylene and sputtering of poly(tetrafluoroethylene) using radio frequency plasma", *Macromolecules*, 32, 6800-6806

Zhan, Z., Xiao, J., Pan, M., Runzhang, Y. (2006), "Characteristics of droplet and film water motion in the flow channels of polymer electrolyte membrane fuel cell", *J. Power Sources*, in press. [Online through Science Direct]. Available: http://www.sciencedirect.com/

Zhang, S.-W., Lan, H.-Q. (2005), "Development in tribological research on ultrathin films", *Tribol. Int.*, 35, 321-327

Zhang, W., Meng, G., Li, H. (2005), "Electrostatic micromotor and its reliability", *Micro-electron. Reliab.*, 45, 1230-1242

Zhao, Z.B., Rek, Z.U., Yalisove, S.M., Bilello, J.C. (2005), "Nanostructured chromium nitride films with a valley of residual stress", *Thin Solid Films*, 472, 96-104

Zhou, L., Kato, K., Umehara, N., Miyake, Y. (2000), "Friction and wear properties of hard coating materials on textured hard disk sliders", *Wear*, 243, 133-139

Zhou, L., Kato, K., Vurens, G., Talke, F.E. (2003), "The effect of slider texture on flyability and lubricant migration under near contact conditions", *Tribol. Int.*, 36, 269-277

Zum Gahr, K.H. (1987), *Microstructure and wear of materials*, Tribology Series 10 (Amsterdam: Elsevier)

Zum Gahr, K.H. (1988), "Modelling of two-body abrasive wear", *Wear*, 124, 87-103

Appendix

A.1 Definition of Topographical Parameters

For correlating the topography with the tribological functional of nanostructures, the surface profiles recorded by AFM were mathematically analysed to determine application-relevant topographical parameters. The mathematically definitions of the surface parameters selected for the data evaluation in the thesis are given on the following pages. The surface parameters were selected according to recommendations in literature, e.g. Dong, Sullivan & Sullivan 1994a, 1994b, Mainsah, Stout & Thomas (2001), and under consideration of the data processing facilities available.

An equally spaced digitised 3D surface can be denoted by a function $z(x_i, y_j)$ with $x_i = i\Delta x$ and $y_j = j\Delta y$, whereby $i = 1, 2, \ldots, M$ and $j = 1, 2, \ldots, N$. Δx and Δy are the sampling intervals. M and N represent the number of sampling points in the x and y directions, respectively. The 3D parameters are based on the residual surface $\eta(x, y)$, which is the difference between the original surface $z(x_i, y_j)$ and a reference datum $f(x_i, y_j)$.

Root Mean Square Deviation

The root mean square (RMS) deviation (roughness) S_q is a statistical amplitude parameter defined as the root-mean square value of surface asperity departures from the reference datum within the sampling area. The RMS deviations of a continuous and as discrete surface are given by:

$$S_q = \left[\frac{1}{l_x l_y} \int_0^{l_x} \int_0^{l_y} \eta^2(x,y)dxdy \right]^{1/2} \approx \left[\frac{1}{MN} \sum_{j=1}^{N} \sum_{i=1}^{M} \eta^2(x_i, y_j) \right]^{1/2} \quad \text{(A1.1)}$$

where l_x and l_y are the side lengths of the sampling area.

Skewness and Kurtosis

The skewness S_{sk} is the measure of asymmetry of surface deviation about the mean plane. For a surface with symmetric height distribution, the skewness is zero (Dong, Sullivan & Sullivan 1994a). For asymmetric height distribution the skewness can have negative or positive values.

$$S_{sk} = \frac{1}{S_q^3} \int_{-\infty}^{\infty} \int_{-\infty}^{\infty} \eta^3(x,y)p(\eta)dxdy \approx \frac{1}{M \cdot N \cdot S_q^3} \sum_{j=1}^{N} \sum_{i=1}^{M} \eta^3(x_i, y_j) \quad \text{(A1.2)}$$

The kurtosis S_{ku} characterizes the spread of the height distribution. A Gaussian surface has a kurtosis of 3.0, a surface with a narrow distribution has a kurtosis larger than 3 whilst that of a broad distribution is less than three.

$$S_{ku} = \frac{1}{S_q^4} \int_{-\infty}^{\infty} \int_{-\infty}^{\infty} \eta^4(x,y)p(\eta)dxdy \approx \frac{1}{M \cdot N \cdot S_q^4} \sum_{j=1}^{N} \sum_{i=1}^{M} \eta^4(x_i, y_j) \quad \text{(A1.3)}$$

Power Spectrum

The power spectrum shows a histogram of power and frequencies for profile data and, thus, it reveals the absolute and relative contributions of different wavelength (frequency) components to the mean square height of surfaces. The power spectrum can be obtained from a Fourier transform analysis of the profile.

When the power spectrum plot falls off gradually, the surface is characterized by roughness (i.e. it has important content from short wavelengths, or higher spatial frequencies), whereas a quick fall off of the plot shows a dominance of waviness.

RMS Height and RMS Slope

The RMS height σ corresponds to the RMS deviation S_q. The RMS slope σ' represent the RMS value of the surface slope within the sampling area, respectively. They can be evaluated via direct computation on spatial derivatives of the residual surface, see also equation (A1.12). Subject to certain restrictions associated with random process theory, the RMS height σ and RMS slope σ' can be also obtained from the power spectrum, as seen in equations (A1.4) and (A1.5), respectively.

$$\sigma = \sqrt{\int_{\varpi_l}^{\varpi_h} P(\varpi) d\varpi} = \sqrt{C_P}\, \varpi_l^{-(2-D)} \tag{A1.4}$$

$$\sigma' = \sqrt{\int_{\varpi_l}^{\varpi_h} \varpi^2 \cdot P(\varpi) d\varpi} = \sqrt{C_P}\, \varpi_h^{(D-1)} \tag{A1.5}$$

where ω_l is the low frequency cut offs, ω_h is the high frequency cut off and D is the fractal dimension. The low frequency cut off is equal to the reciprocal of the sampling length L_s ($\omega_l = 1/L_s$). The high frequency cut off is equal to $\omega_h = 1/2\tau_s$, where τ_s is the distance between two adjacent points of the data sampling.

Fractal Dimension

For a fractal surface profile, the power spectrum follows a power law of the form:

$$P(\varpi) = \frac{C_P}{\varpi^{(5-2D)}} \tag{A1.6}$$

where ω is the frequency, D is the fractal dimensions of the profile and C_P is a scaling constant which depends on the amplitude of the rough surface.

The fractal dimension D can be obtained from the slope from a log-log plot power vs. frequency. The scaling constant C_P can then be obtained from equation (A1.6).

Surface Bearing Area Ratio (Abbott-Firestone Curve)

The surface bearing area ratio S_{tp}, or Abbott-Firestone curve, is the ratio of the total contacting area, obtained by truncating the surface summits by a plane parallel to the mean plane at a given truncation level, over the sampling area. The surface bearing area ratio is given by

$$\begin{aligned} &0 \le \left(S_{tp}(h) = \frac{A(h_n)}{(M-1)\cdot(N-1)\cdot\Delta x\cdot\Delta y} \right) \le 1 \\ &-\left| \frac{\eta_{min}(x,y)}{S_q} \right| \le h_n \le \frac{\eta_{max}(x,y)}{S_q} \end{aligned} \tag{A1.7}$$

where $A(h_n)$ is the bearing area at the normalised height h_n, which is expressed by

$$h_n = \frac{\eta(x,y)}{S_q} \tag{A1.8}$$

Surface Bearing Index, Core Fluid Retention Index and Valley Fluid Retention Index

The surface bearing index S_{bi} is the ratio of the RMS deviation over the surface height at 5 % bearing area.

$$S_{bi} = \frac{1}{h_{n0.05}} \tag{A1.9}$$

where $h_{n0.05}$ is the normalised surface height at 5 % bearing area.

For a Gaussian surface, the S_{bi} can be shown to be about 0.608. It tends to fall in the range 0.3 to 2.0 for a wide range of engineering surfaces.

The core fluid retention index S_{ci} is the ratio of the void volume per unit sampling area at the core zone over the RMS deviation and, thus, is a measure of the amount of fluid that can be retained after normal run-in wear.

$$S_{ci} = \left(\frac{V_v(h_{n0.05}) - V_v(h_{n0.8})}{(M-1)\cdot(N-1)\cdot\Delta x\cdot\Delta y} \right) / S_q \tag{A1.10}$$

where $V_v(h_{n0.05})$ and $V_v(h_{n0.8})$ are the void volumes at a normalised heights at 5 % and 80 % bearing area, respectively.

A large S_{ci} indicates a good fluid retention property in the core zone. For a Gaussian surface the core fluid retention index is about 1.56. Generally for all surfaces, there is a relation $0 < S_{ci} < 0.95\ (h_{n0.05}\text{-}h_{n0.8})$ (Mainsah, Stout & Thomas 2001).

The valley fluid retention index, S_{vi}, is a measure of the amount of fluid a surface can retain even after the worst amount of wear.

$$S_{vi} = \left(\frac{V_v(h_{n0.8})}{(M-1)\cdot(N-1)\cdot\Delta x\cdot\Delta y} \right) / S_q \tag{A1.11}$$

For a Gaussian surface, this index is 0.11. For all surfaces, it falls within the range $0 < S_{vi} < 0.2\ (h_{n0.8}\text{-}h_{nmin})$ (Mainsah, Stout & Thomas 2001).

Summit Number and Summit Density

A point is defined as a summit if the difference between the point and the highest of its four adjacent neighbours is greater than the summit threshold value. The summit number N_s is the total number of summits found in the sampling area. The summit density is the total number of summits contained in a unit sampling area. It is given by the formula

$$S_{sd} = \frac{N_s}{(M-1)\cdot(N-1)\cdot\Delta x\cdot\Delta y} \tag{A1.12}$$

Summit curvature is defined as an average of the principal curvatures of the summits within the sampling area.

$$S_{sc} = -\frac{1}{2}\cdot\frac{1}{N_s}\cdot\sum_{k=1}^{N_s}\left| \frac{\delta\eta^2(x_i, y_j)}{\delta x_i{}^2} + \frac{\delta\eta^2(x_i, y_j)}{\delta y_j{}^2} \right| \text{ for any summit} \tag{A1.13}$$

A.2 Calculation of Contact Pressure in Tribological Tests

For comparison of the test conditions applied in this work with those used in other studies or in special applications, the contact pressure is an important factor. Therefore, the Tables 4.4 and 4.5 list, beside the normal load, also the range of the maximum contact pressure determined for the minimum and maximum normal load in the tribological tests on the various nanostructures.

The following paragraphs describe how the contact pressure given in those tables was calculated.

Based on the Hertz' theory the maximum contact pressure p_{max} for a contact between a sphere (counter body) and a plane (sample) is expressed by

$$p_{max} = \frac{1}{\pi} \cdot \left(\frac{6 \cdot E^{*2} \cdot F_N}{R^2} \right)^{\frac{1}{3}} \tag{A2.1}$$

where F_N is the normal load, R is the radius of the counter body, E^* is the composite Young's modulus considering the Young's modulus and Poisson's ratio of counter body and sample. The value of E^* was calculated according to equation (3.7)

$$\frac{1}{E^*} = \left(\frac{1-\nu_1^2}{E_1} + \frac{1-\nu_2^2}{E_2} \right)$$

using the relevant mechanical properties of the counter body (ν_1, E_1) as given in Table 4.7 and of the sample (ν_2, E_2). In this study, the sample is not a bulk material but a compound

consisting of a Cr-N film on top of a Si(100) substrate. Therefore, the Young's modulus of the compound needs to be inserted in equation (3.7). According to a model proposed by Bhushan & Venkatesan (2005), the Young's modulus of film-substrate compound (E_2) can be evaluated by

$$E_2 = E_S \cdot \left[1 + \left(\frac{E_f}{E_S} - 1 \right) exp\left(- \left(\frac{\delta}{t_f} \right)^{0.5} \cdot \left(\frac{E_f}{E_S} \right)^{0.2} \right) \right] \text{ if } E_f/E_s > 1 \quad \text{(A2.2)}$$

$$E_2 = E_S \cdot \left[1 + \left(\frac{E_f}{E_S} - 1 \right) exp\left(- \left(\frac{\delta}{t_f} \right)^{1.0} \cdot \left(\frac{E_f}{E_S} \right)^{0.1} \right) \right] \text{ if } E_f/E_s < 1 \quad \text{(A2.3)}$$

where E_s is the Young's modulus of the substrate, E_f is the Young's modulus of the film, t_f is the film thickness and δ is the plastic deformation under the counter body.

For the calculation of the E_2 values it was assumed that:

- The Young's modulus E_s of the substrate Si(100) is about 169 GPa (Klett et al. 1999)
- The Poisson's ratios of the substrate and the film are similar.
- The ratio δ/t_f is about 0.02.

The Young's modulus E_f of the Cr-N films is given in Table 6.1. The thickness of the Cr-N films t_f is usually 2 µm. In the tests performed at a normal load of 0.2 mN (EG 3), the film-substrate compounds and the reference (Si wafer) were additionally covered with 10 nm thick SiO_2 or HFP layer (see section 4.3.5). For simplicity, it was supposed that the influence of these layers on the mechanical properties of the compound or the reference can be neglected.

Table A3.1 summarizes the Young's modulus and the maximum contact pressure determined for the contact between various nanostructured samples and the counter bodies (Si_3N_4 and TiC ball) for the minimum and maximum normal load applied in the different tribological experiments (see section 4.3.2).

Table A2.1: Young's modulus E_2 of the film-substrate compound and the maximum contact pressure p_{max} calculated for tribological tests performed with TiC and Si_3N_4 counter bodies at various normal loads F_N.

		p_{max} (MPa) calculated for TiC counter body at F_N			p_{max} (MPa) calculated for Si_3N_4 counter body at F_N		
Sample	E_2 (GPa)	0.2 mN	1 mN	15 mN	10mN	150 mN	250 mN
Ref	295	86*	188	464	371	914	1083
P1	120	72	123	304	253	625	741
P2	125	74	126	311	258	637	755
P3	125	74	126	311	258	637	755
P4	130	75	124	317	263	649	770
C1	286	109	186	458	366	904	1072
C2	274	107	182	450	361	890	1055
C3	266	105	180	444	357	880	1044
CR1	366	119	204	504	398	982	1164
CR2	380	121	207	511	403	994	1178
CR3	286	109	186	458	366	904	1ß72
CR4	329	114	195	481	383	944	1119
CR5	342	116	198	491	390	961	1139
CR6	338	116	198	481	388	957	1135

* in these tests (EG 3): $E_2 \approx E_s = 169$ GPa

A.3 Examples of Analysis Data Obtained for Nanostructures

The nanostructures analysed in the microtribological studies were deposited in UBM sputtering process under the following conditions:

Table A.1: Process conditions for depositing the nanostructures tested in different experiment groups.

Tested in	Structure	T (°C)	U_b (V)	Ar/N_2	p (Pa)	P (kW)
EG 1 & 2	Ref	350	-75	1.3	0.4	10
EG 1 to 3	P1	150	-50	1.5	1.0	2
EG 1 to 3	P2	150	-50	1.5	0.4	2
EG 1 to 3	P3	200	-50	1.3	1.0	6
EG 1 to 3	P4	250	-50	1.3	0.4	6
EG 1 to 3	C1	350	-150	1.3	0.4	4
EG 1 to 3	C2	350	-250	1.3	0.4	4
EG 1 to 3	C3	350	-350	1.3	0.4	4
EG 1 & 2	CR1	250	-200	0.7	0.4	2
EG 1 & 2	CR2	450	-200	1.0	1.0	2
EG 1 & 2	CR3	450	-300	1.0	0.4	4
EG 1 & 2	CR4	350	-200	1.5	1.0	2
EG 1 & 2	CR5	350	-250	1.0	0.4	4
EG 1 & 2	CR6	350	-300	1.0	0.4	6
EG 3	CR1	250	-200	0.7	0.4	2
EG 3	CR2	350	-350	1.5	0.4	4
EG 3	CR3	350	-450	1.5	0.4	2

In EG 3, crater-like structured surfaces and references different to those analysed in EG 1 and 2 were investigated. In order to distinguish the samples, the crater-like structured surfaces tested in EG 3 were labelled as CR1-EG3, CR2-EG3, CR3-EG3 and Ref-EG3 in the following text.

Reference

Micrographs to illustrate the topography of reference surface taken by (a) SEM and (b) AFM.

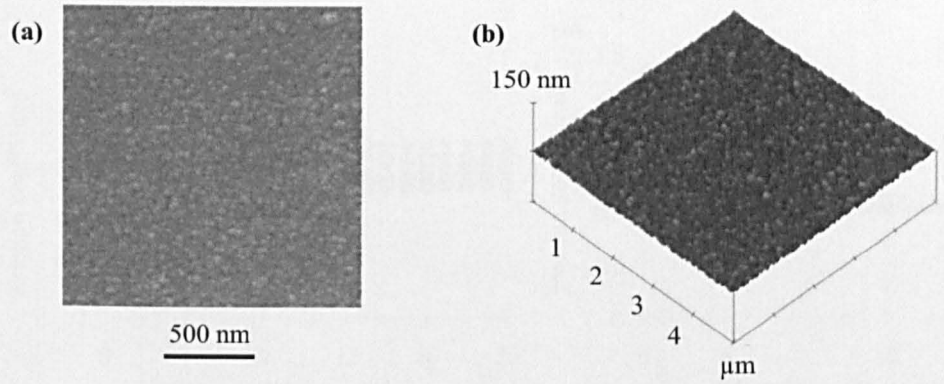

Load-penetration curve measured on reference surface in nanoindentation tests.

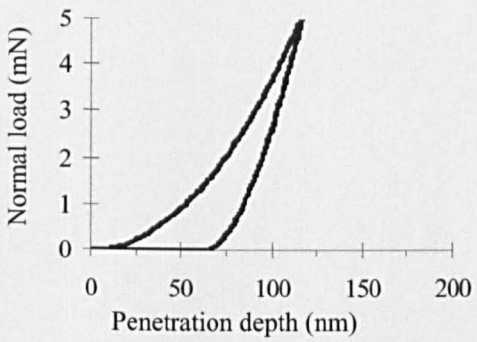

Friction force evolution as function of cycle number recorded on reference surface at F_N = 6 mN and v = 25 µm/s (a) under unlubricated conditions (friction tests EG 1) and (b) when applying PAO oil (friction tests EG 2).

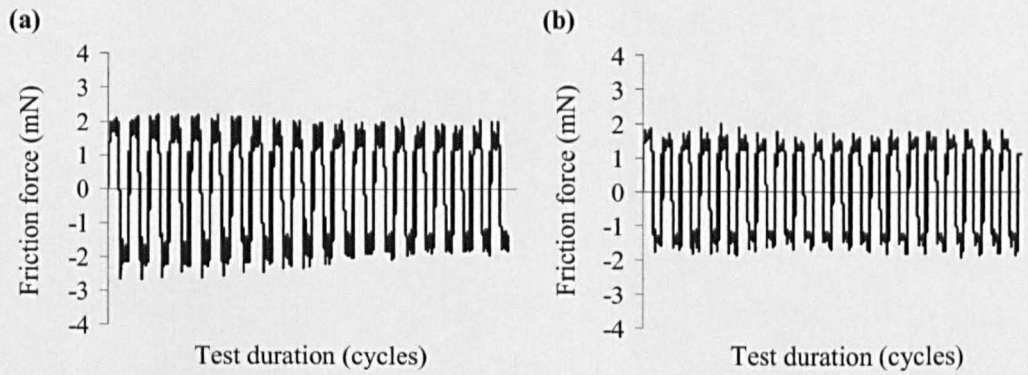

Friction coefficient as function of the test duration obtained on nanostructure P1 in LCC tests of EG 2 for normal loads of 10 mN (■), 25 mN (◆), 50 mN (△), 100 mN (●),150 mN (×), 200 mN (+) and 250 mN (–).

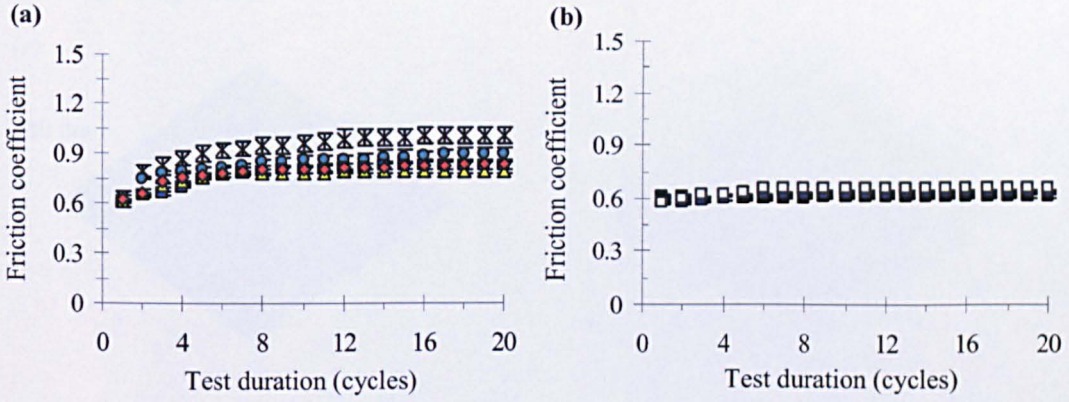

References Ref-EG3

Micrographs to illustrate the topography of a hydrophilic (a) and hydrophobic (b) reference surface taken by AFM.

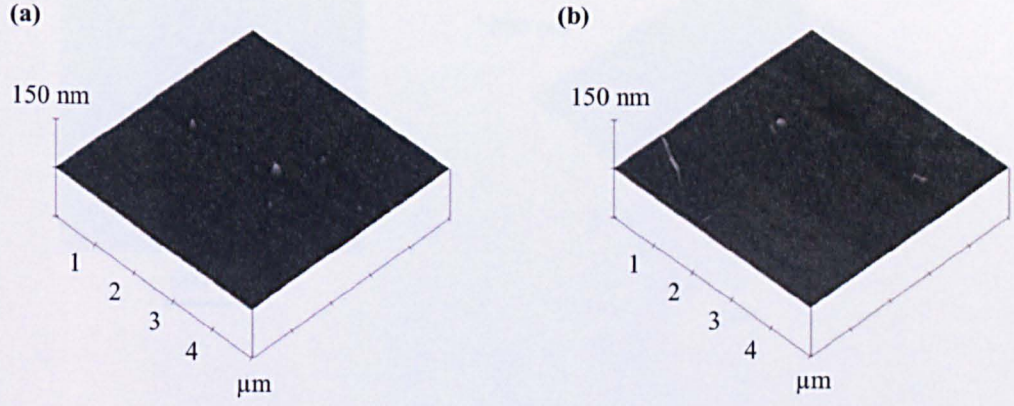

Data of the wettability measurements on references with different surface chemistry. Figure (a) presents values of the advancing (◆) and receding (◇) contact angles on hydrophilic sample as well as advancing (▲) and receding (△) contact angles on hydrophobic sample. Figure (b) shows the photograph of a water drop on the hydrophobic surfaces.

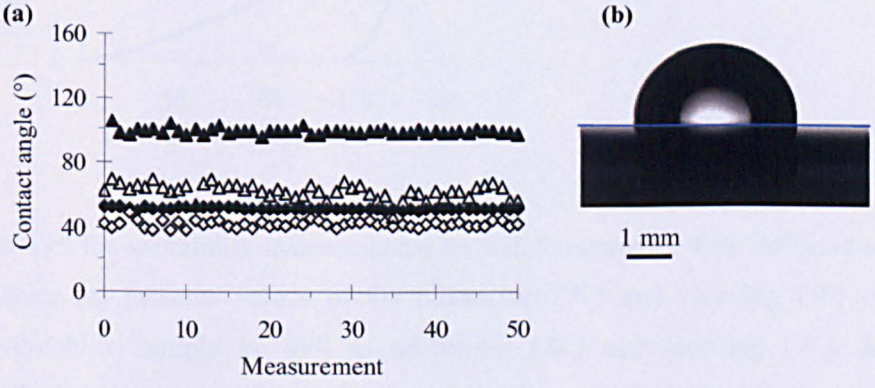

Friction force as function of cycle number recorded in EG 3 at 50 % RH and v = 50 µm/s on (a) hydrophilic and (b) hydrophobic reference sample.

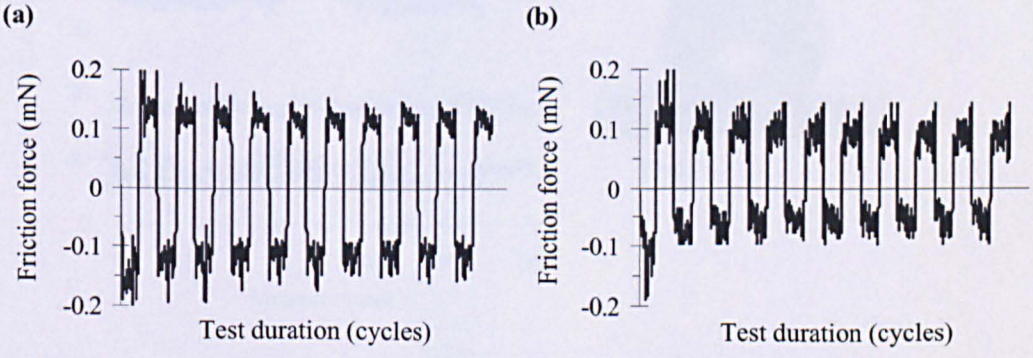

Nanostructure P1

Micrographs to illustrate the topography of nanostructure P1 taken by (a) SEM and (b) AFM.

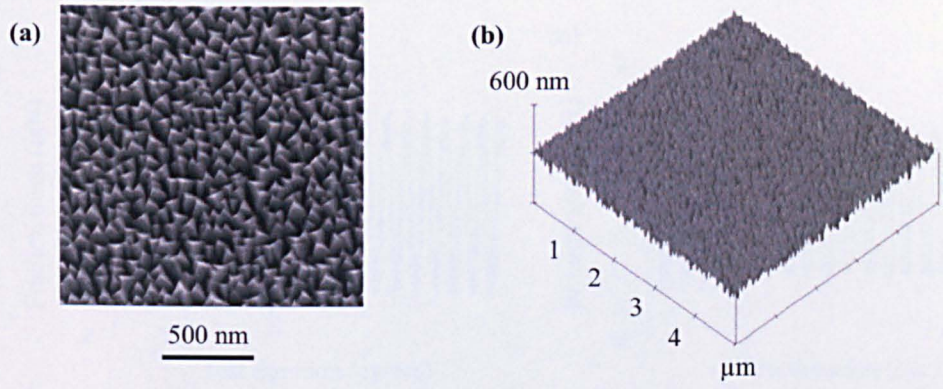

Load-penetration curve measured on nanostructure P1 in nanoindentation tests.

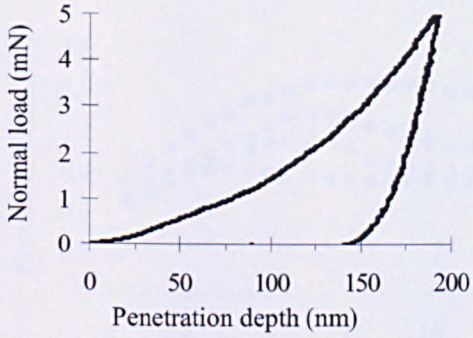

Data of the wettability measurements on nanostructure P1 with different surface chemistry. Figure (a) presents values of the advancing (◆) and receding (◇) contact angles on hydrophilic sample as well as advancing (▲) and receding (△) contact angles on hydrophobic sample. Figure (b) shows the photograph of a water drop on the hydrophobic surfaces.

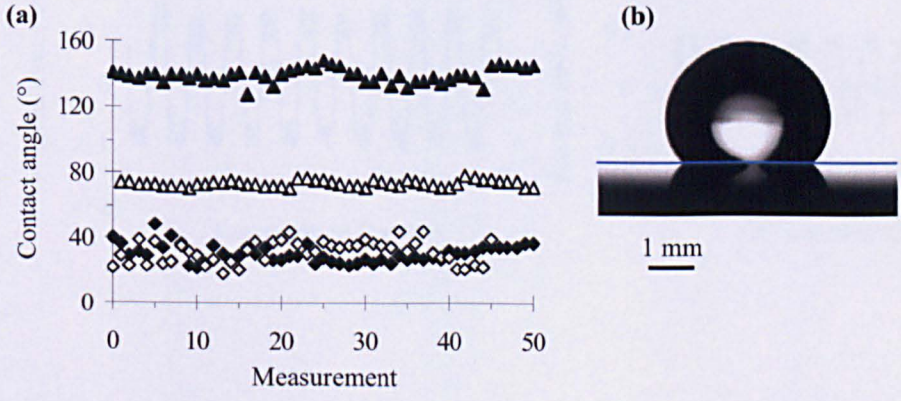

Friction force evolution as function of cycle number recorded on nanostructure P1 at F_N = 6 mN and v = 25 µm/s (a) under unlubricated conditions (friction tests EG 1) and (b) when applying PAO oil (friction tests EG 2).

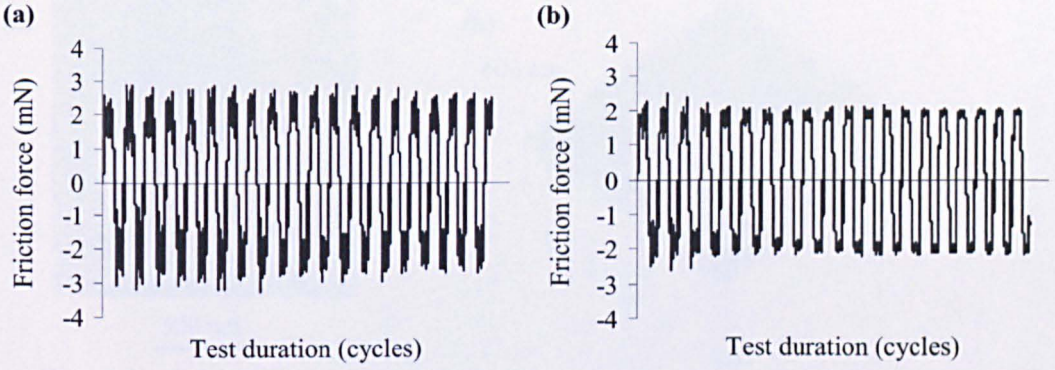

Friction coefficient as function of the test duration obtained on nanostructure P1 in LCC tests of EG 2 for normal loads of 10 mN (■), 25 mN (◆), 50 mN (▲) and 100 mN (●).

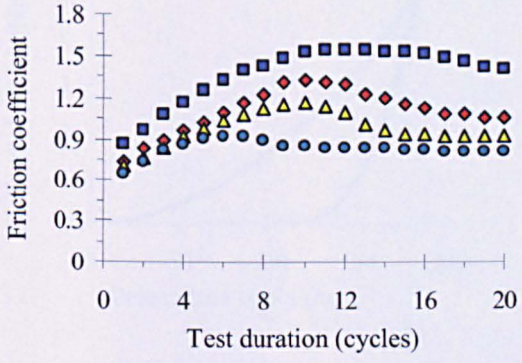

Friction force as function of cycle number recorded in EG 3 at 50 % RH and v = 50 µm/s on (a) hydrophilic sample and (b) hydrophobic surface of nanostructure P1.

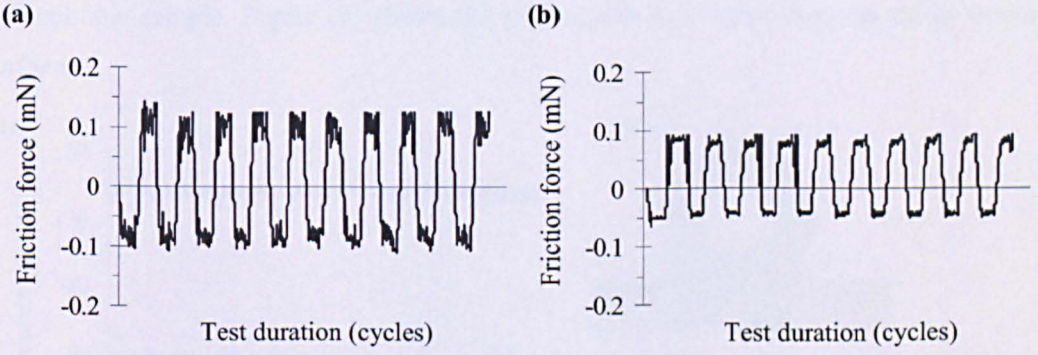

Nanostructure P2

Micrographs to illustrate the topography of nanostructure P2 taken by (a) SEM and (b) AFM.

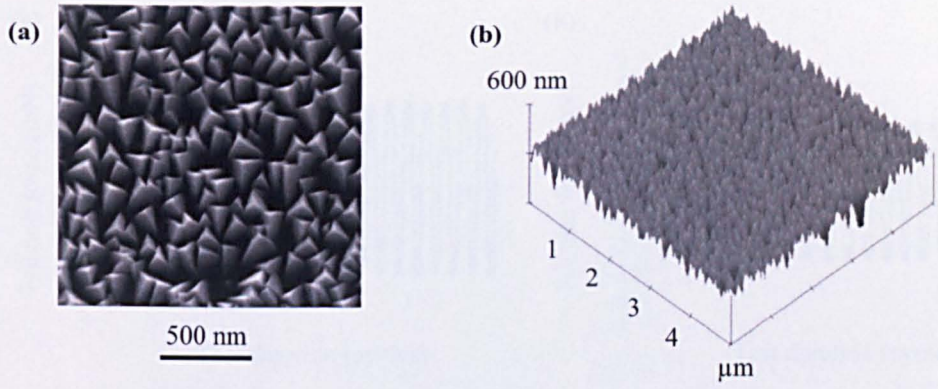

Load-penetration curve measured on nanostructure P2 in nanoindentation tests.

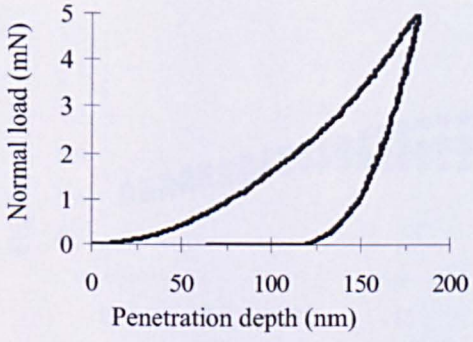

Data of the wettability measurements on nanostructure P2 with different surface chemistry. Figure (a) presents values of the advancing (◆) and receding (◇) contact angles on hydrophilic sample as well as advancing (▲) and receding (△) contact angles on hydrophobic sample. Figure (b) shows the photograph of a water drop on the hydrophobic surfaces.

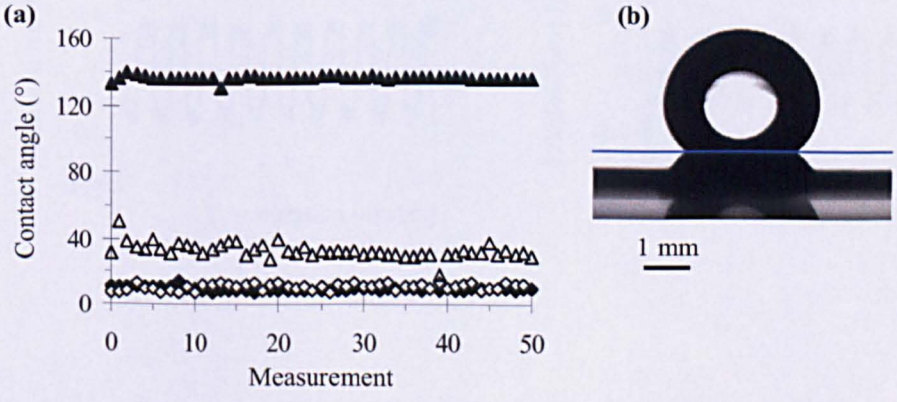

Friction force evolution as function of cycle number recorded on nanostructure P2 at F_N = 6 mN and v = 25 µm/s (a) under unlubricated conditions (friction tests EG 1) and (b) when applying PAO oil (friction tests EG 2).

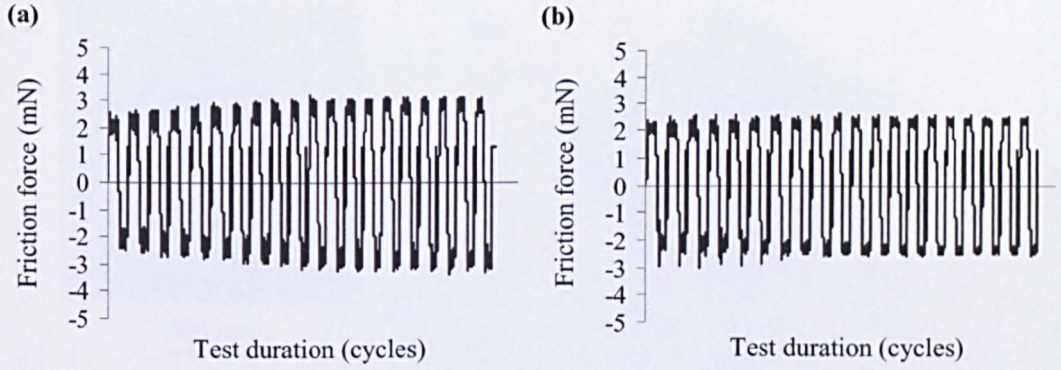

Friction coefficient as function of the test duration obtained on nanostructure P2 in LCC tests of EG 2 for normal loads of 10 mN (■), 25 mN (◆), 50 mN (△) and 100 mN (●).

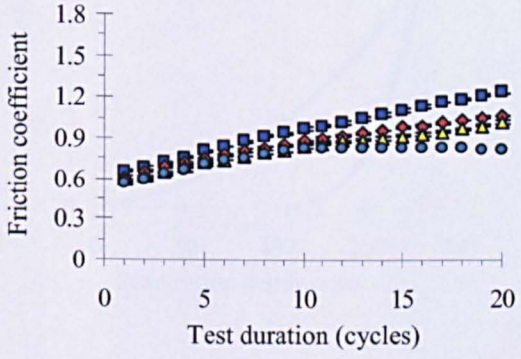

Friction force as function of cycle number recorded in EG 3 at 50 % RH and v = 50 µm/s on (a) hydrophilic sample and (b) hydrophobic surface of nanostructure P2.

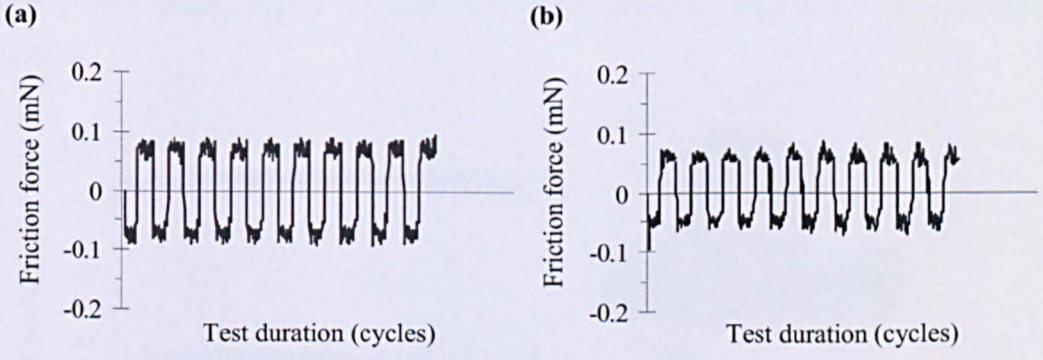

Nanostructure P3

Micrographs to illustrate the topography of nanostructure P3 taken by (a) SEM and (b) AFM.

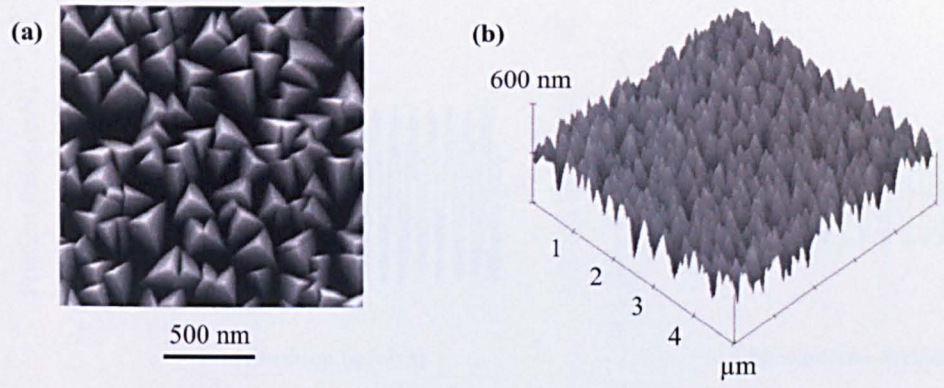

Load-penetration curve measured on nanostructure P3 in nanoindentationtests.

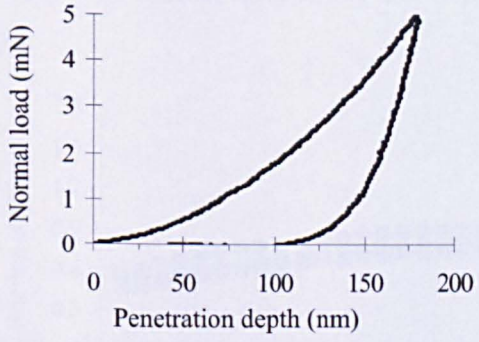

Data of the wettability measurements on nanostructure P3 with different surface chemistry. Figure (a) presents values of the advancing (◆) and receding (◇) contact angles on hydrophilic sample as well as advancing (▲) and receding (△) contact angles on hydrophobic sample. Figure (b) shows the photograph of a water drop on the hydrophobic surfaces.

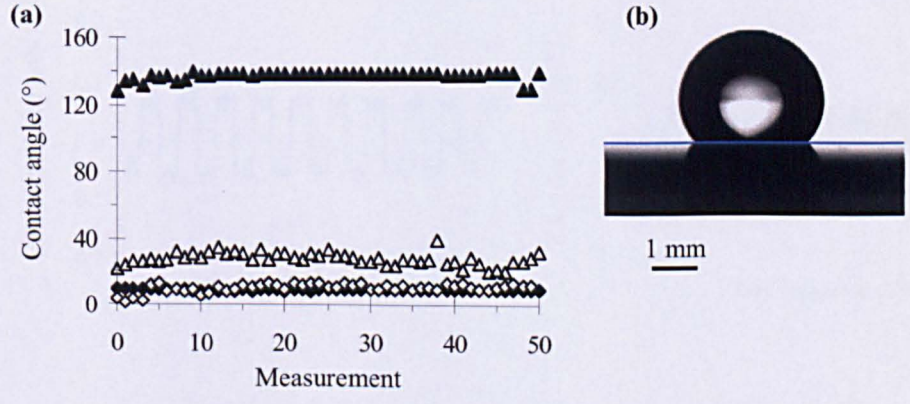

Friction force evolution as function of cycle number recorded on nanostructure P3 at F_N = 6 mN and v = 25 µm/s (a) under unlubricated conditions (friction tests EG 1) and (b) when applying PAO oil (friction tests EG 2).

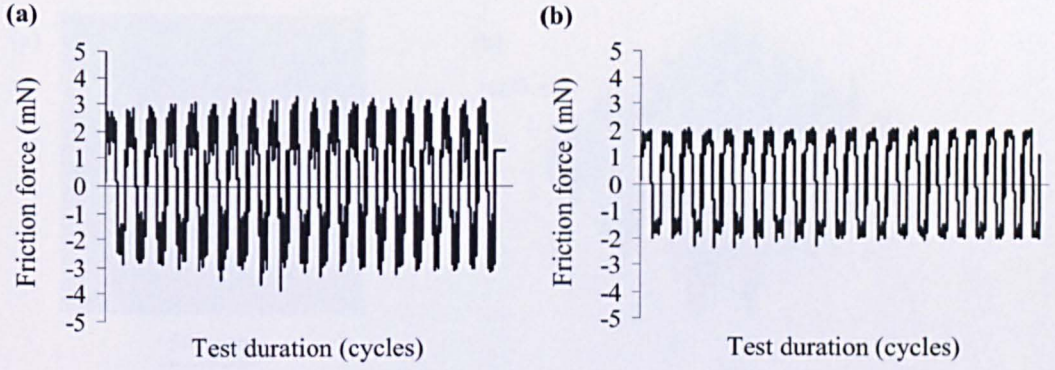

Friction coefficient as function of the test duration obtained on nanostructure P3 in LCC tests of EG 2 for normal loads of 10 mN (■), 25 mN (◆), 50 mN (△), 100 mN (●) and 150 mN (×).

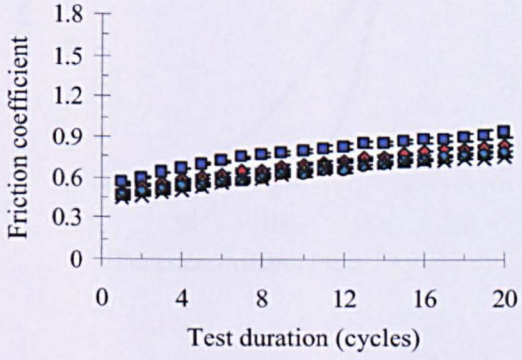

Friction force as function of cycle number recorded in EG 3 at 50 % RH and v = 50 µm/s on (a) hydrophilic sample and (b) hydrophobic surface of nanostructure P3.

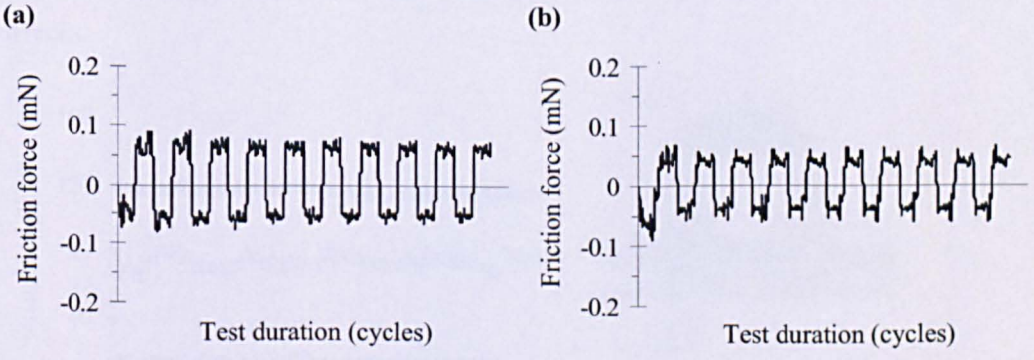

Nanostructure P4

Micrographs to illustrate the topography of nanostructure P4 taken by (a) SEM and (b) AFM.

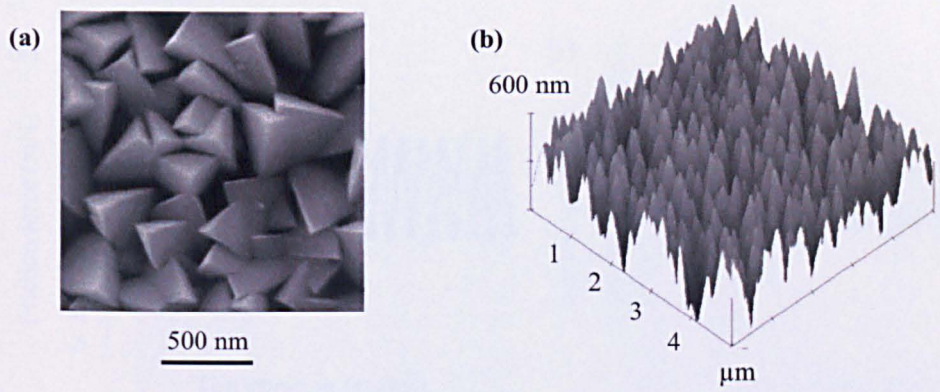

Load-penetration curve measured on nanostructure P4 in nanoindentation tests.

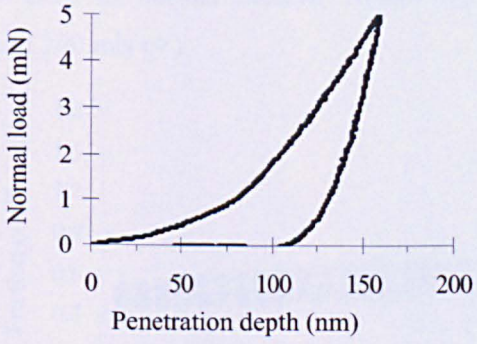

Data of the wettability measurements on nanostructure P4 with different surface chemistry. Figure (a) presents values of the advancing (◆) and receding (◇) contact angles on hydrophilic sample as well as advancing (▲) and receding (△) contact angles on hydrophobic sample. Figure (b) shows the photograph of a water drop on the hydrophobic surfaces.

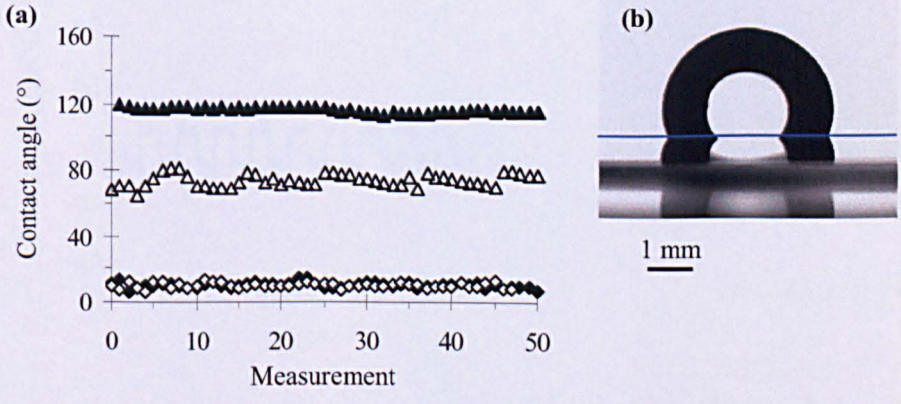

Friction force evolution as function of cycle number recorded on nanostructure P4 at F_N = 6 mN and v = 25 µm/s (a) under unlubricated conditions (friction tests EG 1) and (b) when applying PAO oil (friction tests EG 2).

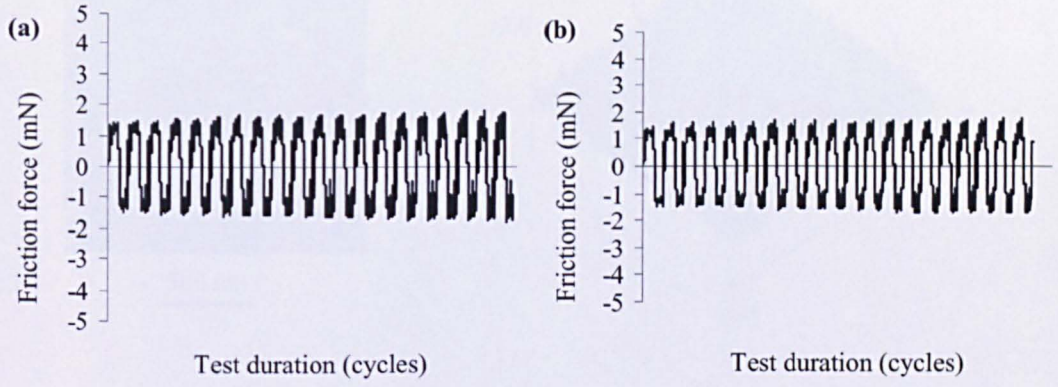

Friction coefficient as function of the test duration obtained on nanostructure P4 in LCC tests of EG 2 for normal loads of 10 mN (■), 25 mN (◆), 50 mN (△), 100 mN (●), 150 mN (×) and 200 mN (+).

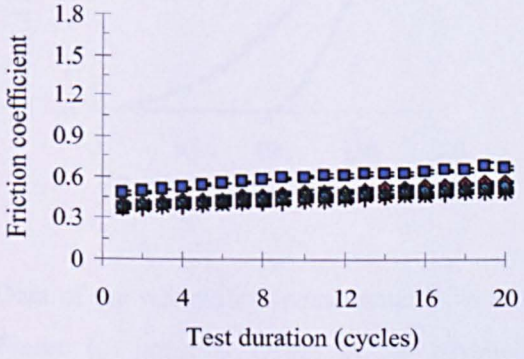

Friction force as function of cycle number recorded in EG 3 at 50 % RH and v = 50 µm/s on (a) hydrophilic sample and (b) hydrophobic surface of nanostructure P4.

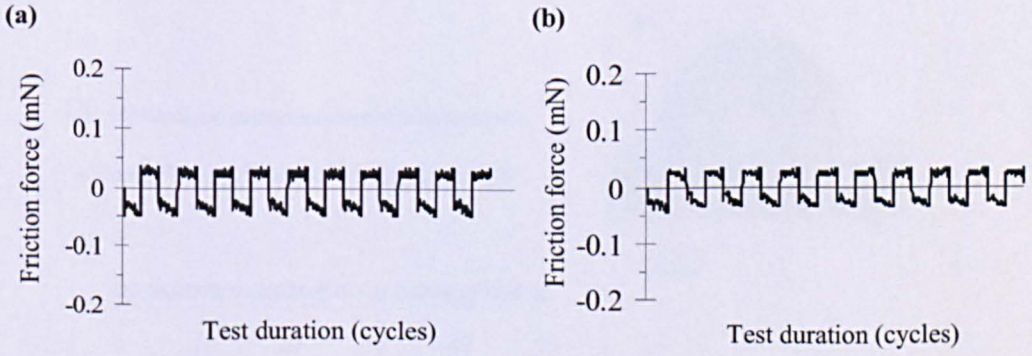

Nanostructure C1

Micrographs to illustrate the topography of nanostructure C1 taken by (a) SEM and (b) AFM.

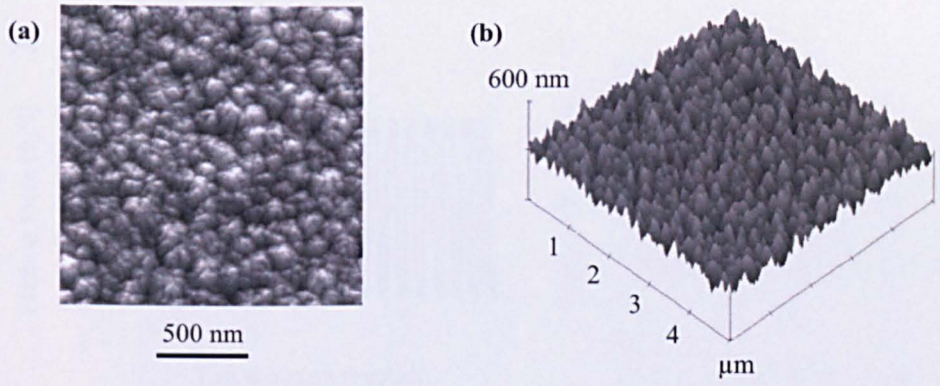

Load-penetration curve measured on nanostructure C1 in nanoindentation tests.

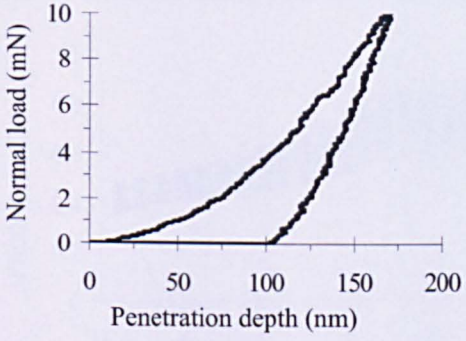

Data of the wettability measurements on nanostructure C1 with different surface chemistry. Figure (a) presents values of the advancing (◆) and receding (◇) contact angles on hydrophilic sample as well as advancing (▲) and receding (△) contact angles on hydrophobic sample. Figure (b) shows the photograph of a water drop on the hydrophobic surfaces.

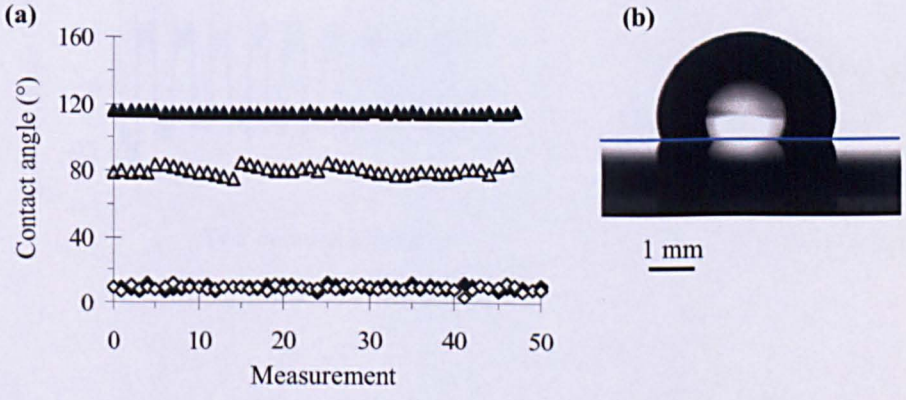

Friction force evolution as function of cycle number recorded on nanostructure C1 at F_N = 6 mN and v = 25 µm/s (a) under unlubricated conditions (friction tests EG 1) and (b) when applying PAO oil (friction tests EG 2).

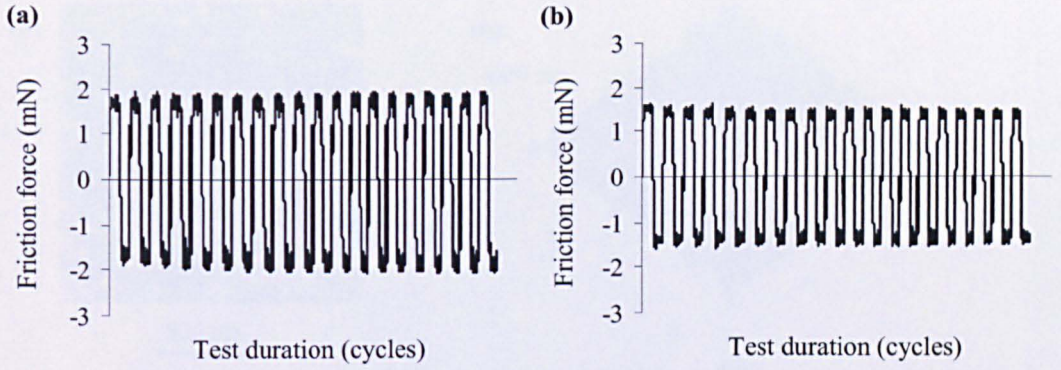

Friction coefficient as function of the test duration obtained on nanostructure C1 in LCC tests of EG 2 for normal loads of 10 mN (■), 25 mN (◆), 50 mN (△) and 100 mN (●).

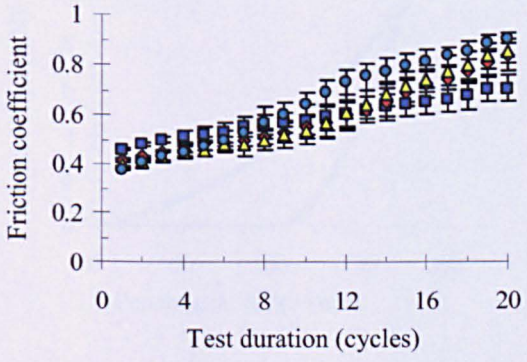

Friction force as function of cycle number recorded in EG 3 at 50 % RH and v = 50 µm/s on (a) hydrophilic sample and (b) hydrophobic surface of nanostructure C1.

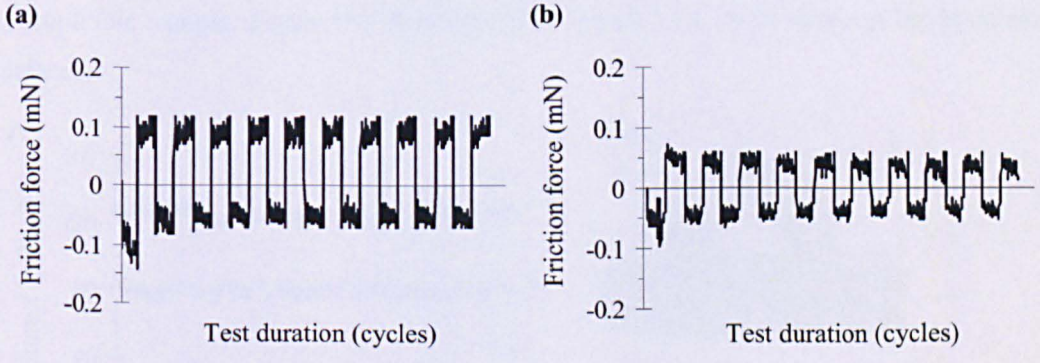

Nanostructure C2

Micrographs to illustrate the topography of nanostructure C2 taken by (a) SEM and (b) AFM.

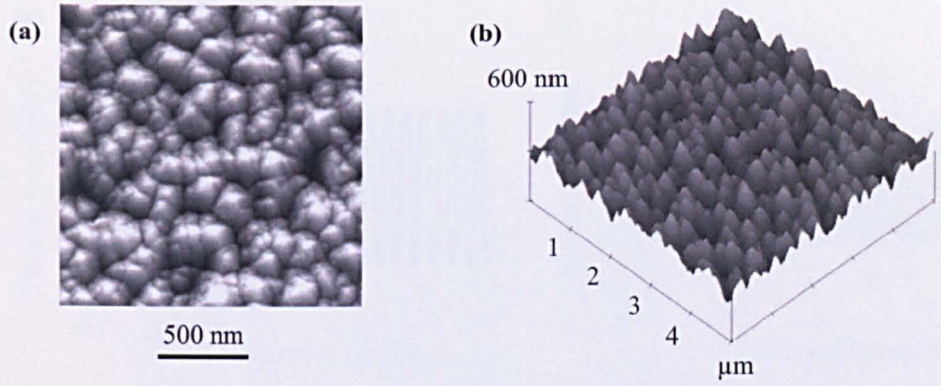

Load-penetration curve measured on nanostructure C2 in nanoindentation tests.

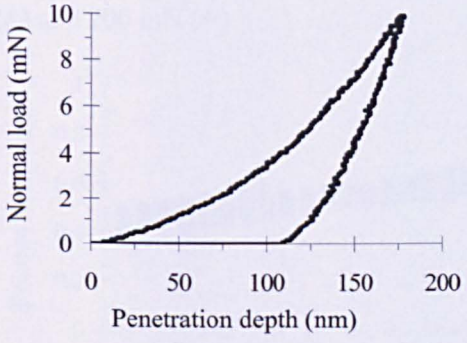

Data of the wettability measurements on nanostructure C2 with different surface chemistry. Figure (a) presents values of the advancing (◆) and receding (◇) contact angles on hydrophilic sample as well as advancing (▲) and receding (△) contact angles on hydrophobic sample. Figure (b) shows the photograph of a water drop on the hydrophobic surfaces.

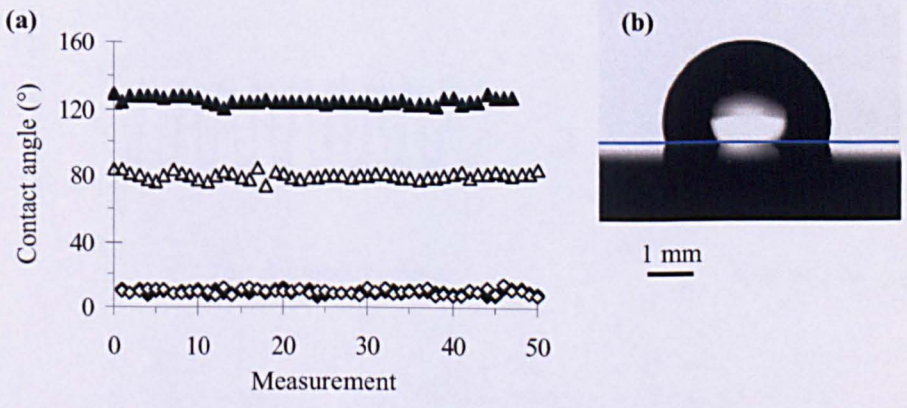

Friction force evolution as function of cycle number recorded on nanostructure C2 at F_N = 6 mN and v = 25 µm/s (a) under unlubricated conditions (friction tests EG 1) and (b) when applying PAO oil (friction tests EG 2).

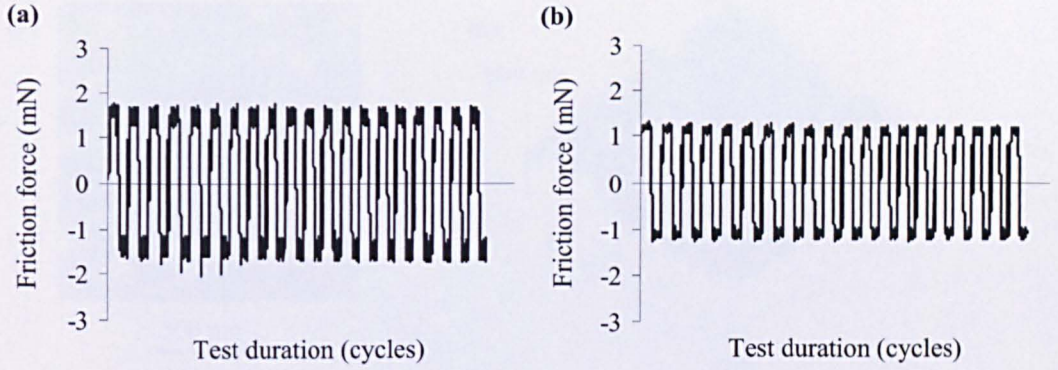

Friction coefficient as function of the test duration obtained on nanostructure C2 in LCC tests of EG 2 for normal loads of 10 mN (■), 25 mN (◆), 50 mN (▲), 100 mN (●),150 mN (×) and 200 mN (+).

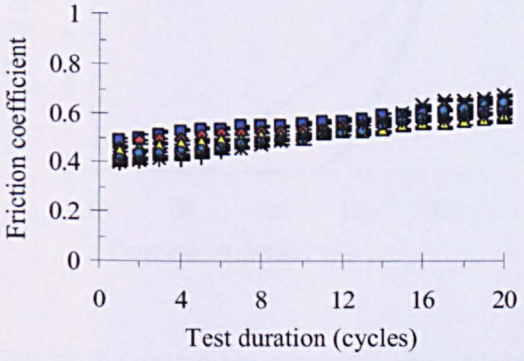

Friction force as function of cycle number recorded in EG 3 at 50 % RH and v = 50 µm/s on (a) hydrophilic sample and (b) hydrophobic surface of nanostructure C2.

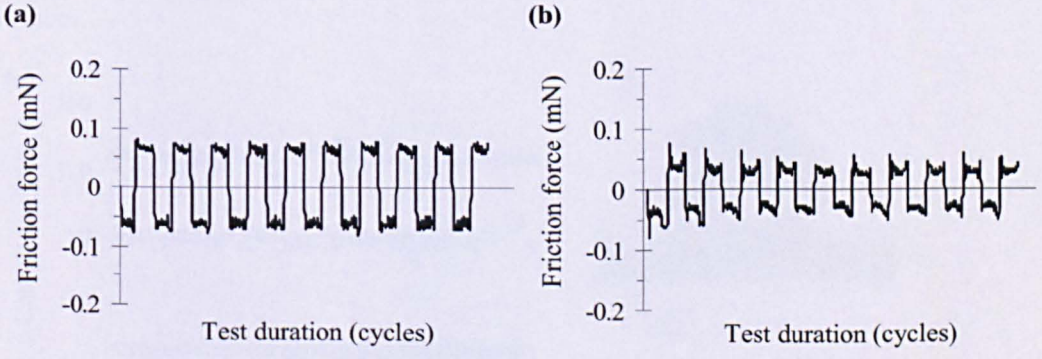

Nanostructure C3

Micrographs to illustrate the topography of nanostructure C3 taken by (a) SEM and (b) AFM.

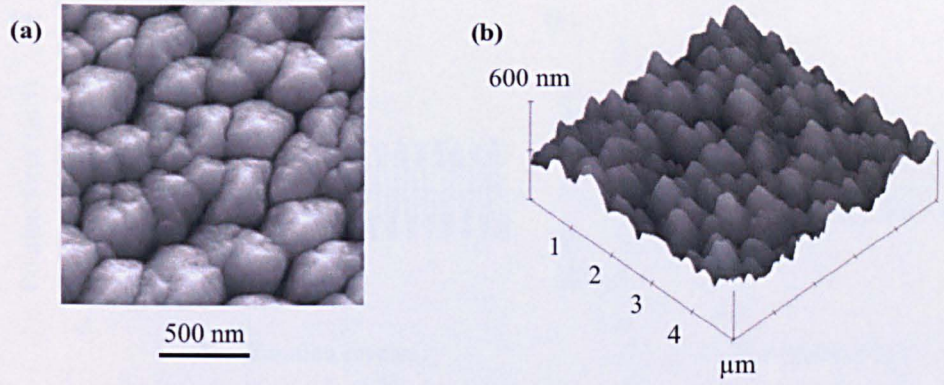

Load-penetration curve measured on nanostructure C3 in nanoindentation tests.

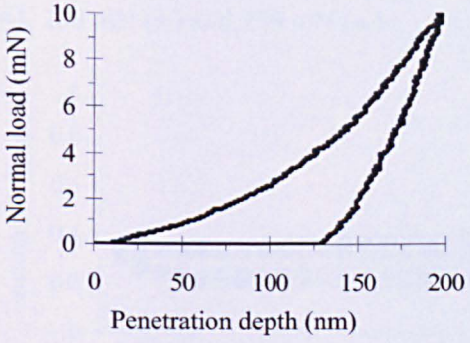

Data of the wettability measurements on nanostructure C3 with different surface chemistry. Figure (a) presents values of the advancing (◆) and receding (◇) contact angles on hydrophilic sample as well as advancing (▲) and receding (△) contact angles on hydrophobic sample. Figure (b) shows the photograph of a water drop on the hydrophobic surfaces.

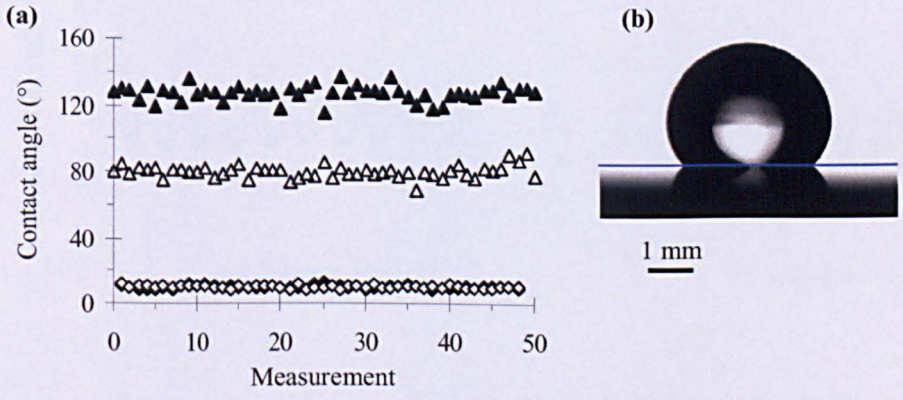

Friction force evolution as function of cycle number recorded on nanostructure C3 at F_N = 6 mN and v = 25 µm/s (a) under unlubricated conditions (friction tests EG 1) and (b) when applying PAO oil (friction tests EG 2).

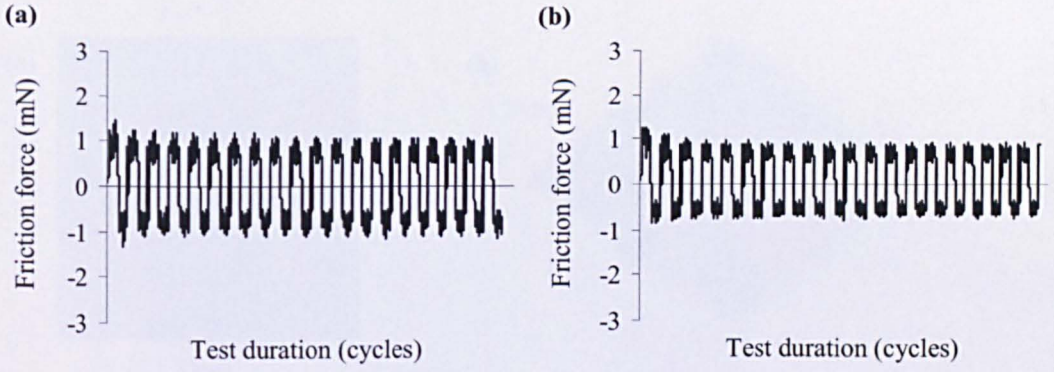

Friction coefficient as function of the test duration obtained on nanostructure C3 in LCC tests of EG 2 for normal loads of 10 mN (■), 25 mN (◆), 50 mN (△), 100 mN (●),150 mN (×), 200 mN (+) and 250 mN (–).

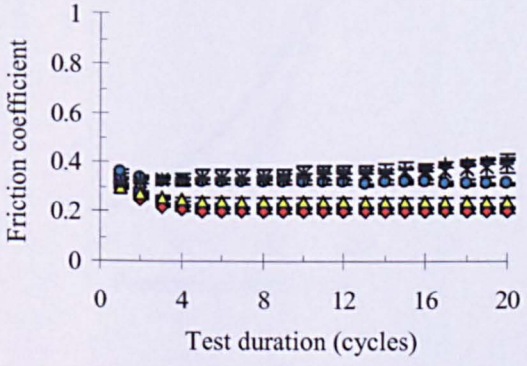

Friction force as function of cycle number recorded in EG 3 at 50 % RH and v = 50 µm/s on (a) hydrophilic sample and (b) hydrophobic surface of nanostructure C3.

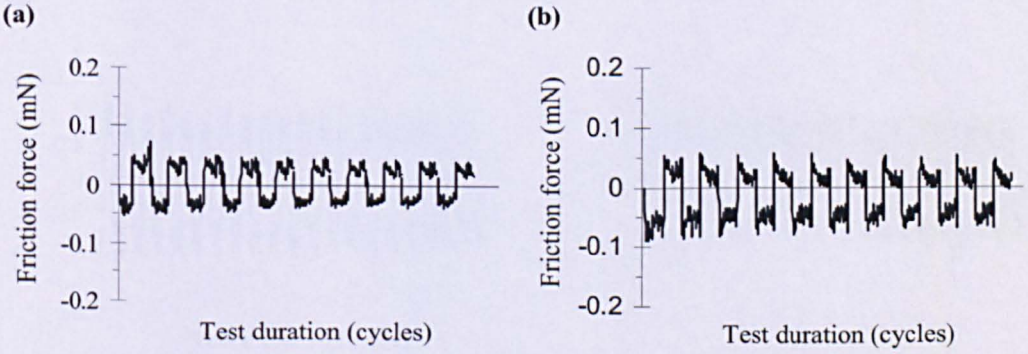

Nanostructure CR1

Micrographs to illustrate the topography of nanostructure CR1 taken by (a) SEM and (b) AFM.

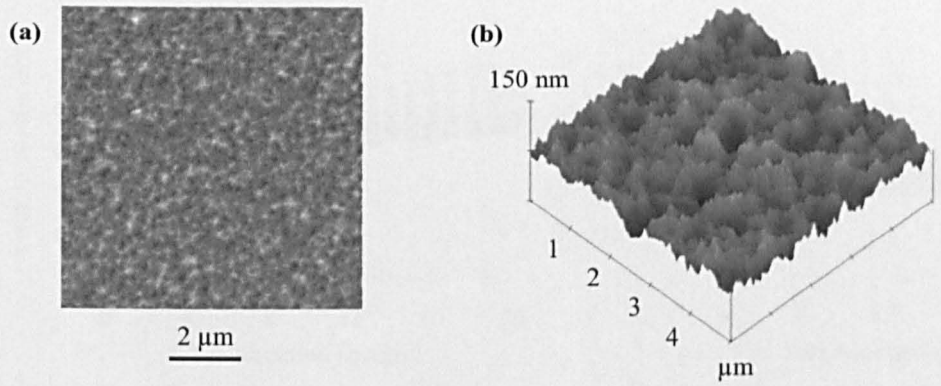

Load-penetration curve measured on nanostructure CR1 in nanoindentation tests.

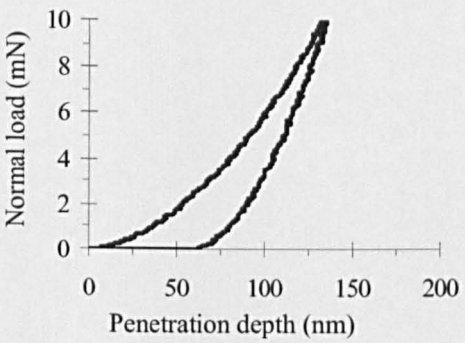

Friction force evolution as function of cycle number recorded on nanostructure CR1 at F_N = 6 mN and v = 25 µm/s (a) under unlubricated conditions (friction tests EG 1) and (b) when applying PAO oil (friction tests EG 2).

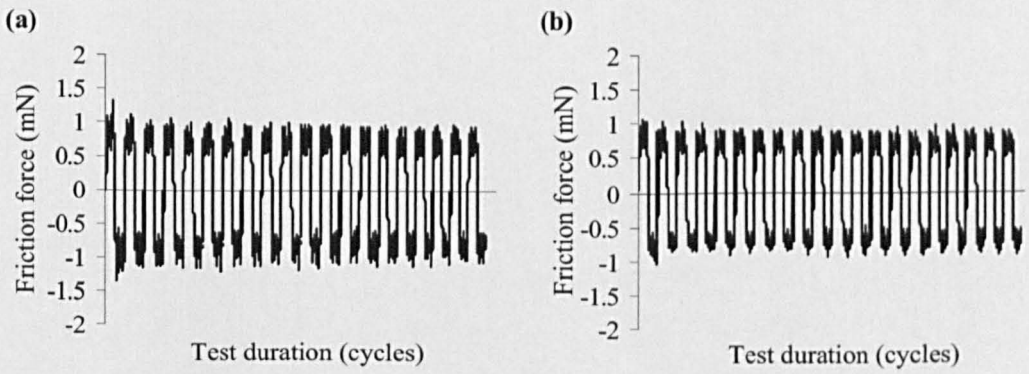

Friction coefficient as function of the test duration obtained on nanostructure CR1 in unlubricated (a) and lubricated (b) LCC tests of EG 2 for normal loads of 10 mN (■), 25 mN (◆), 50 mN (△), 100 mN (●), 150 mN (×), 200 mN (+) and 250 mN (–).

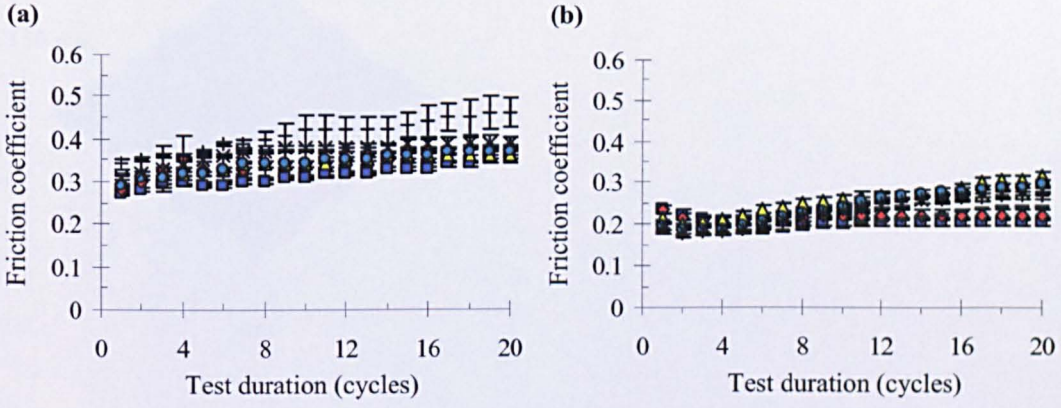

Nanostructure CR1-EG3

Micrographs to illustrate the topography of hydrophilic structure CR1-EG3 taken by AFM.

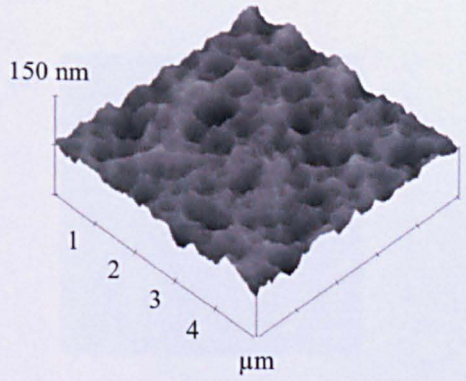

Data of the wettability measurements on nanostructure CR1-EG3 with different surface chemistry. Figure (a) presents values of the advancing (◆) and receding (◇) contact angles on hydrophilic sample as well as advancing (▲) and receding (△) contact angles on hydrophobic sample. Figure (b) shows the photograph of a water drop on the hydrophobic surfaces.

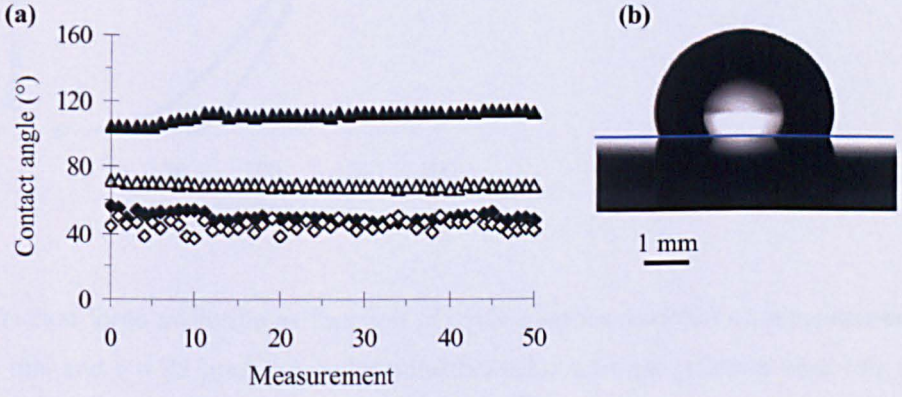

Friction force as function of cycle number recorded in EG 3 at 50 % RH and v = 50 µm/s on (a) hydrophilic and (b) hydrophobic sample of nanostructure CR1-EG3.

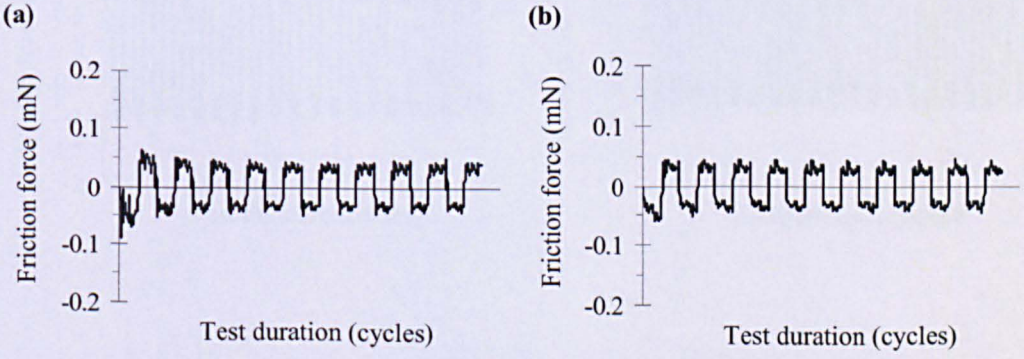

Nanostructure CR2

Micrographs to illustrate the topography of nanostructure CR2 taken by (a) SEM and (b) AFM.

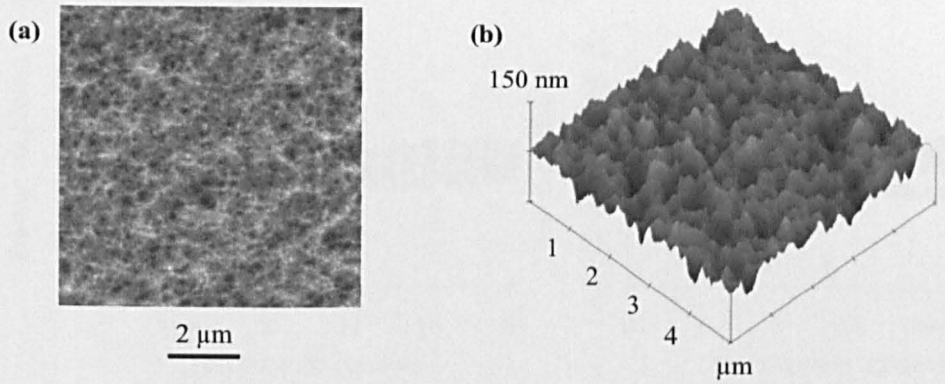

Load-penetration curve measured on nanostructure CR2 in nanoindentation tests.

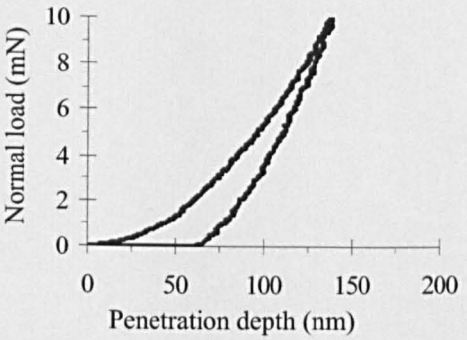

Friction force evolution as function of cycle number recorded on nanostructure CR2 at F_N = 6 mN and v = 25 µm/s (a) under unlubricated conditions (friction tests EG 1) and (b) when applying PAO oil (friction tests EG 2).

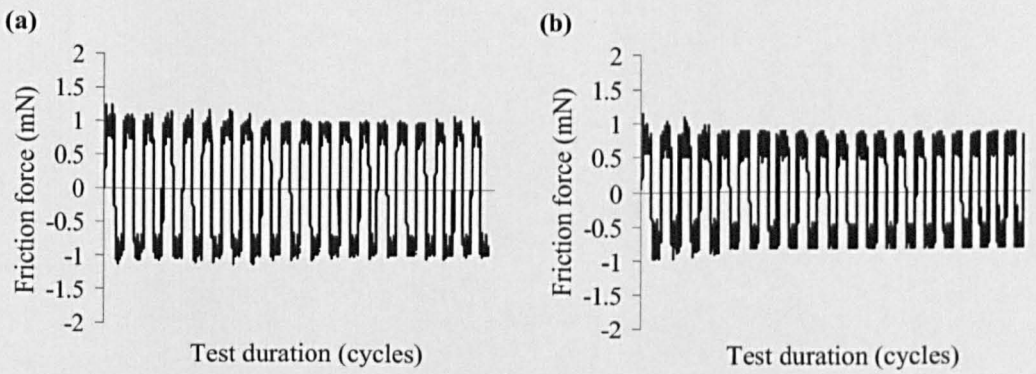

Friction coefficient as function of the test duration obtained on nanostructure CR2 in unlubricated (a) and lubricated (b) LCC tests of EG 2 for normal loads of 10 mN (■), 25 mN (◆), 50 mN (△), 100 mN (●), 150 mN (×), 200 mN (+) and 250 mN (–).

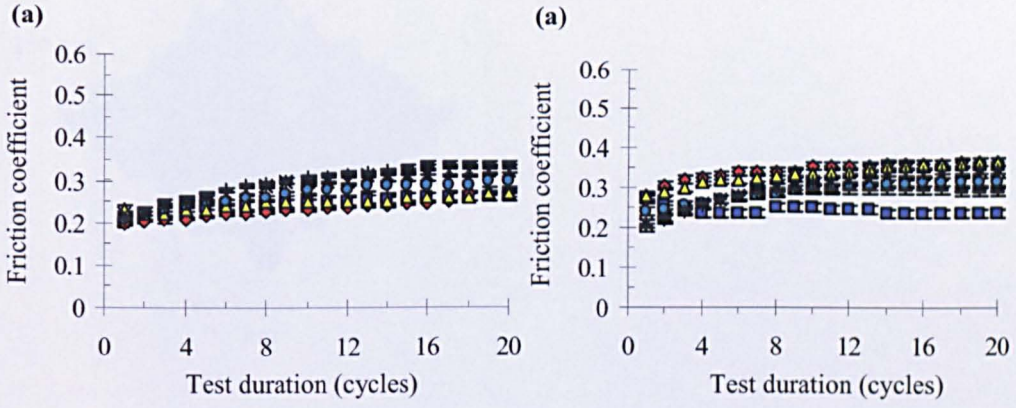

Nanostructure CR2-EG3

Micrographs to illustrate the topography of hydrophilic structure CR2-EG3 taken by AFM.

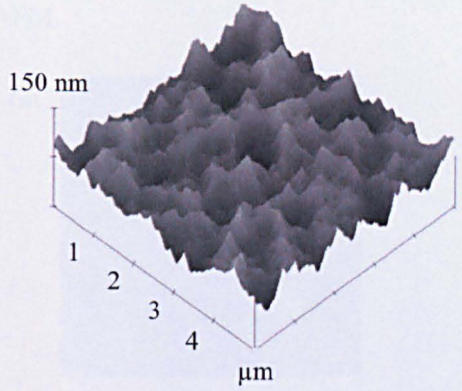

Data of the wettability measurements on nanostructure CR2-EG3 with different surface chemistry. Figure (a) presents values of the advancing (◆) and receding (◇) contact angles on hydrophilic sample as well as advancing (▲) and receding (△) contact angles on hydrophobic sample. Figure (b) shows the photograph of a water drop on the hydrophobic surfaces.

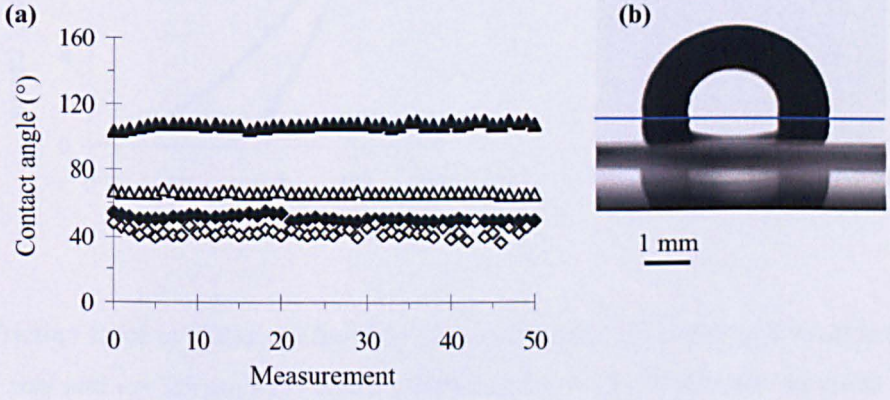

Friction force as function of cycle number recorded in EG 3 at 50 % RH and v = 50 µm/s on (a) hydrophilic sample and (b) hydrophobic surface of nanostructure CR2-EG3.

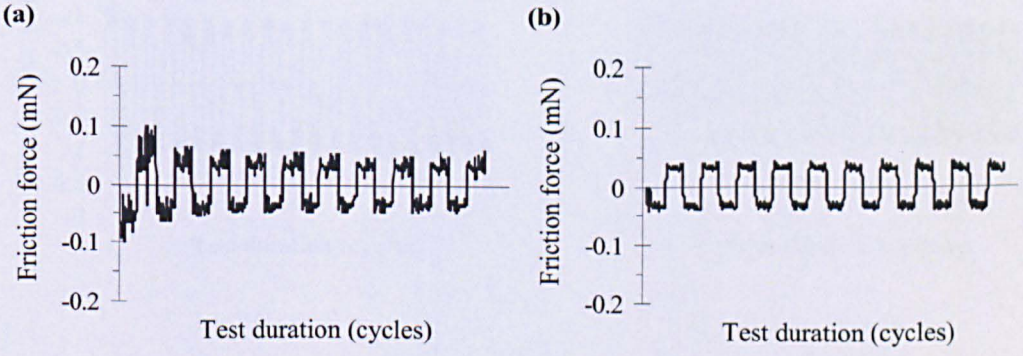

Nanostructure CR3

Micrographs to illustrate the topography of nanostructure CR3 taken by (a) SEM and (b) AFM.

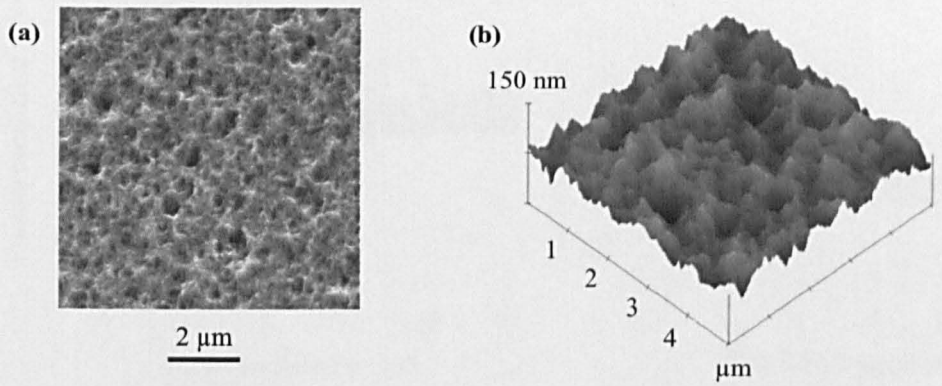

Load-penetration curve measured on nanostructure CR3 in nanoindentation tests.

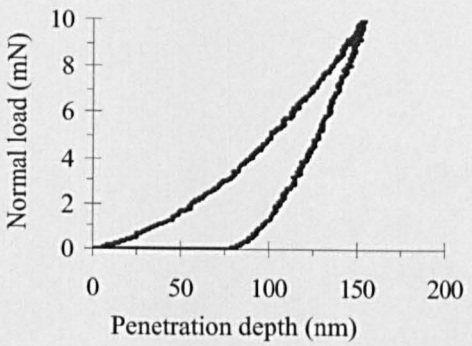

Friction force evolution as function of cycle number recorded on nanostructure CR3 at F_N = 6 mN and v = 25 µm/s (a) under unlubricated conditions (friction tests EG 1) and (b) when applying PAO oil (friction tests EG 2).

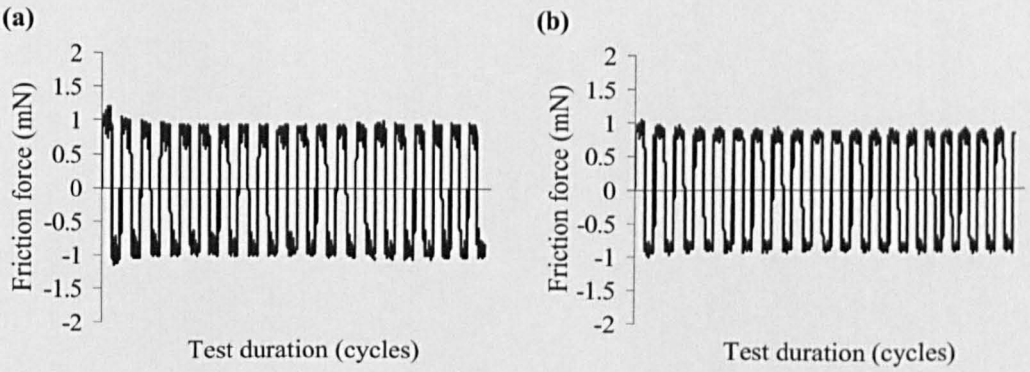

Friction coefficient as function of the test duration obtained on nanostructure CR3 in unlubricated (a) and lubricated (b) LCC tests of EG 2 for normal loads of 10 mN (■), 25 mN (◆), 50 mN (△), 100 mN (●), 150 mN (×), 200 mN (+) and 250 mN (–).

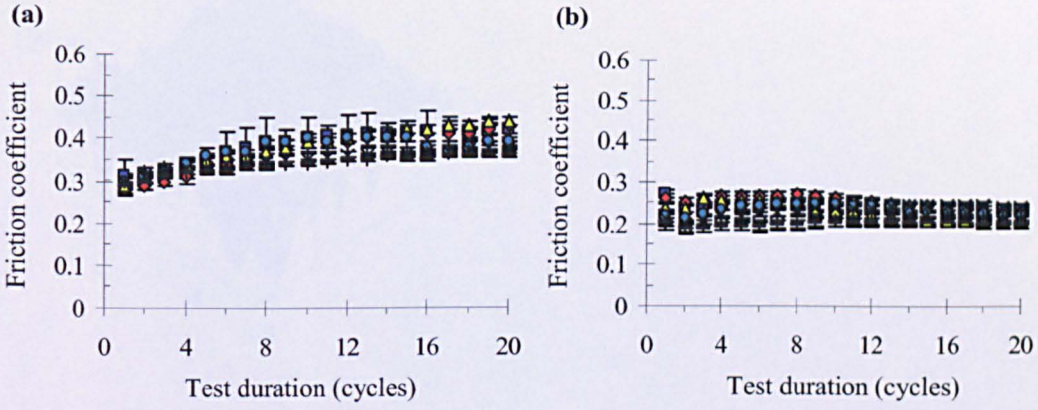

Nanostructure CR3-EG3

Micrographs to illustrate the topography of hydrophilic structure CR3-EG3 taken by AFM.

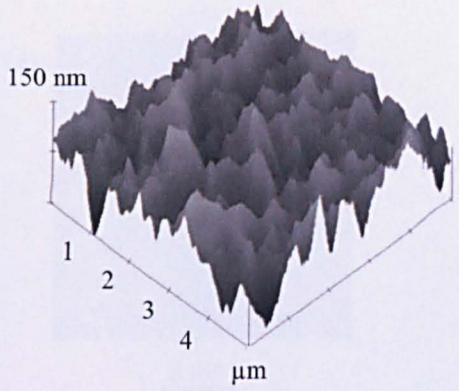

Data of the wettability measurements on nanostructure CR3-EG3 with different surface chemistry. Figure (a) presents values of the advancing (◆) and receding (◇) contact angles on hydrophilic sample as well as advancing (▲) and receding (△) contact angles on hydrophobic sample. Figure (b) shows the photograph of a water drop on the hydrophobic surfaces.

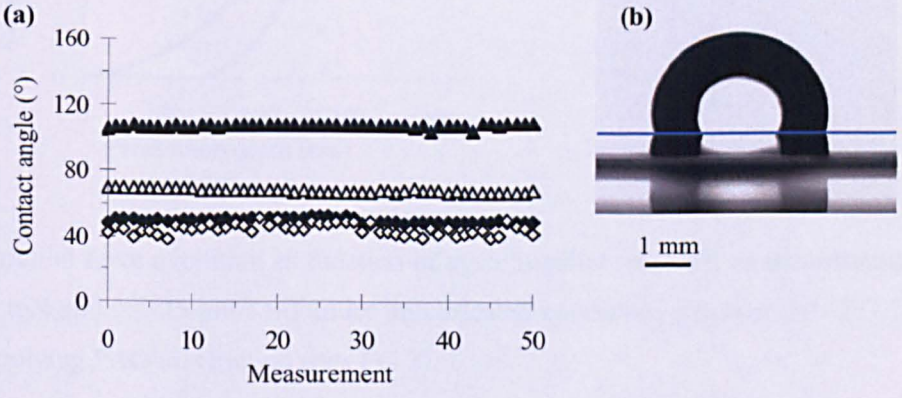

Friction force as function of cycle number recorded in EG 3 at 50 % RH and v = 50 µm/s on (a) hydrophilic sample and (b) hydrophobic surface of nanostructure CR3-EG3.

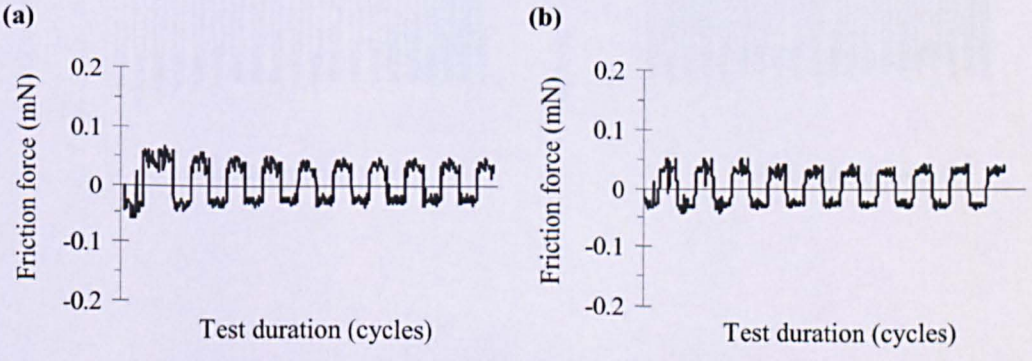

Nanostructure CR4

Micrographs to illustrate the topography of nanostructure CR4 taken by (a) SEM and (b) AFM.

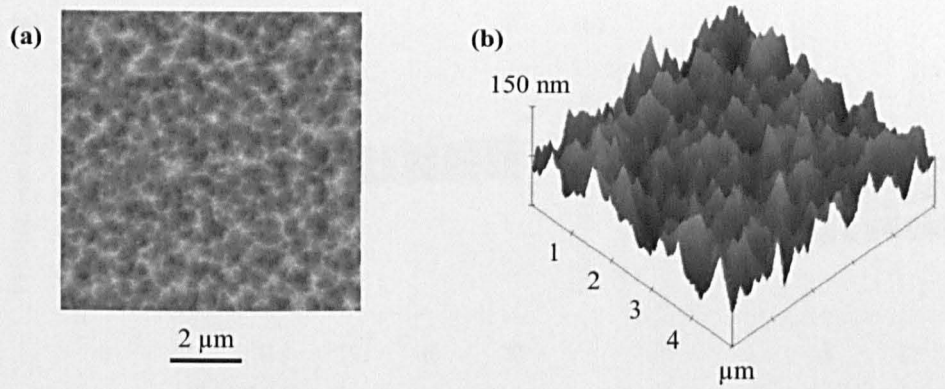

Load-penetration curve measured on nanostructure CR4 in nanoindentation tests.

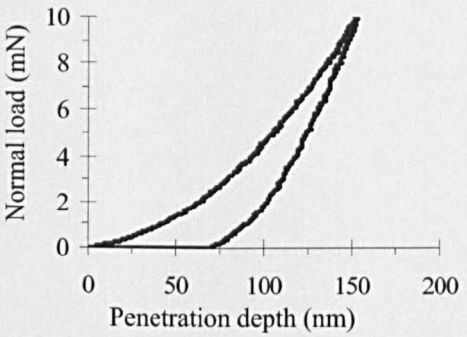

Friction force evolution as function of cycle number recorded on nanostructure CR4 at F_N = 6 mN and v = 25 µm/s (a) under unlubricated conditions (friction tests EG 1) and (b) when applying PAO oil (friction tests EG 2).

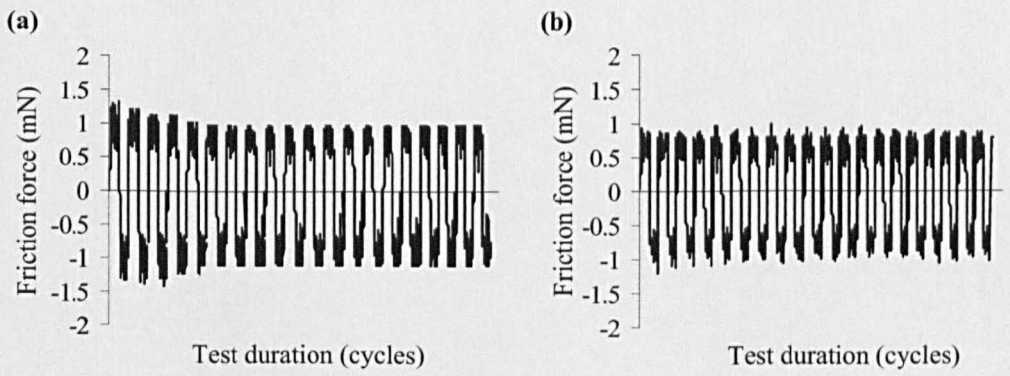

Friction coefficient as function of the test duration obtained on nanostructure CR4 in unlubricated (a) and lubricated (b) LCC tests of EG 2 for normal loads of 10 mN (■), 25 mN (◆), 50 mN (△), 100 mN (●), 150 mN (×), 200 mN (+) and 250 mN (–).

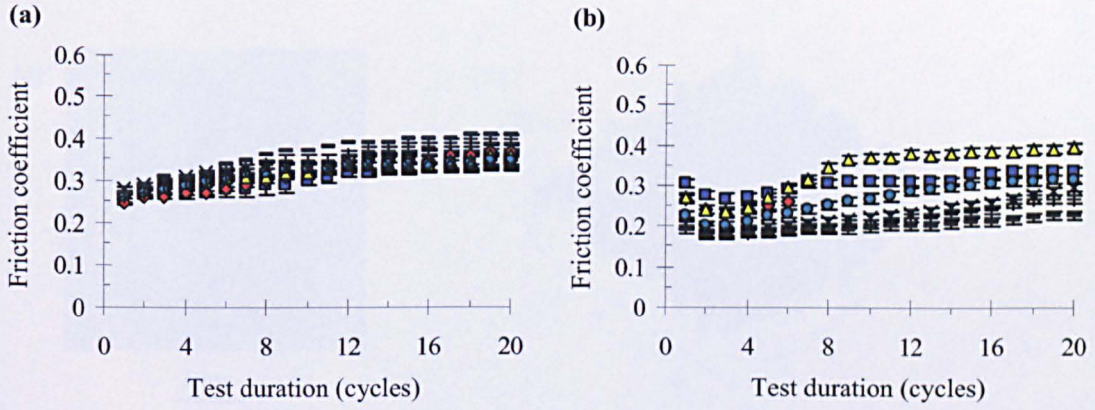

Nanostructure CR5

Micrographs to illustrate the topography of nanostructure CR5 taken by (a) SEM and (b) AFM.

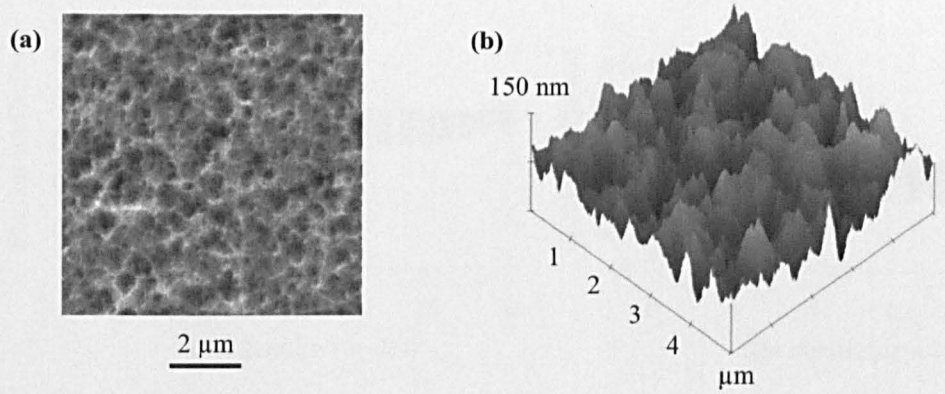

Load-penetration curve measured on nanostructure CR5 in nanoindentation tests.

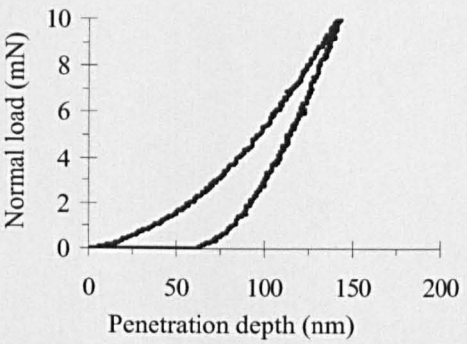

Friction force evolution as function of cycle number recorded on nanostructure CR5 at F_N = 6 mN and v = 25 µm/s (a) under unlubricated conditions (friction tests EG 1) and (b) when applying PAO oil (friction tests EG 2).

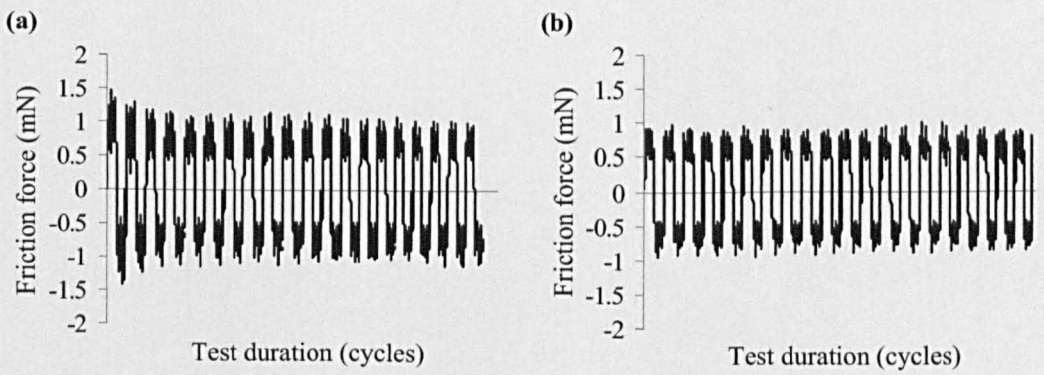

Friction coefficient as function of the test duration obtained on nanostructure CR5 in unlubricated (a) and lubricated (b) LCC tests of EG 2 for normal loads of 10 mN (■), 25 mN (◆), 50 mN (△), 100 mN (●), 150 mN (×), 200 mN (+) and 250 mN (–).

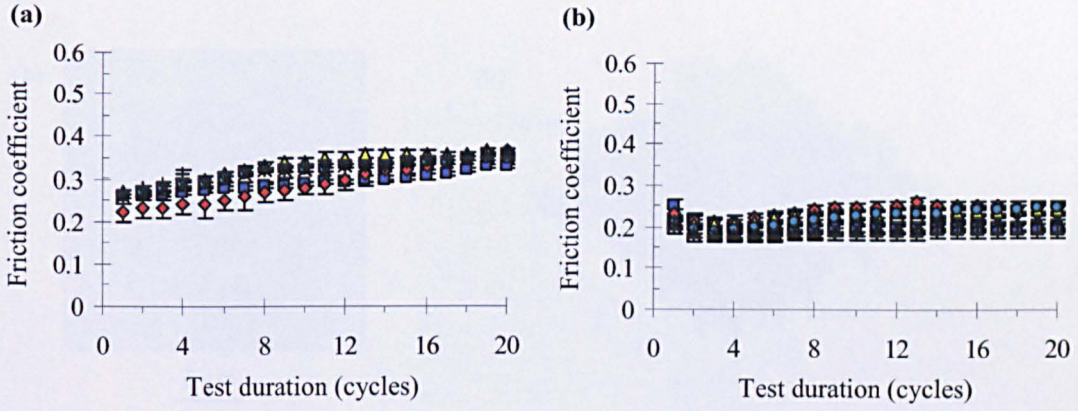

Nanostructure CR6

Micrographs to illustrate the topography of nanostructure CR6 taken by (a) SEM and (b) AFM.

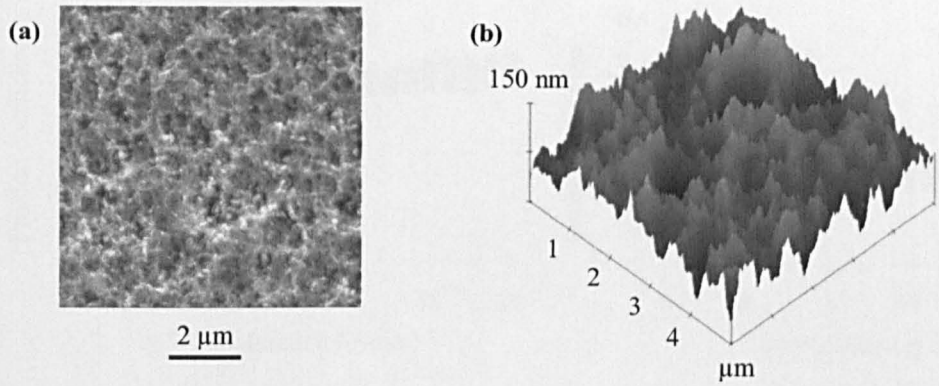

Load-penetration curve measured on nanostructure CR6 in nanoindentation tests.

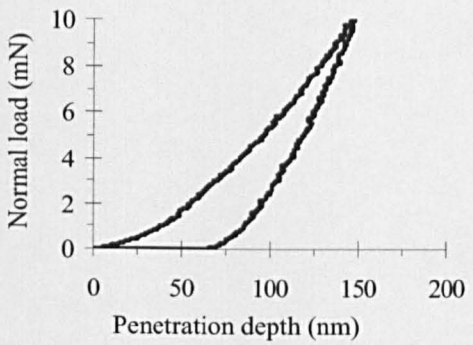

Friction force evolution as function of cycle number recorded on nanostructure CR6 at F_N = 6 mN and v = 25 µm/s (a) under unlubricated conditions (friction tests EG 1) and (b) when applying PAO oil (friction tests EG 2).

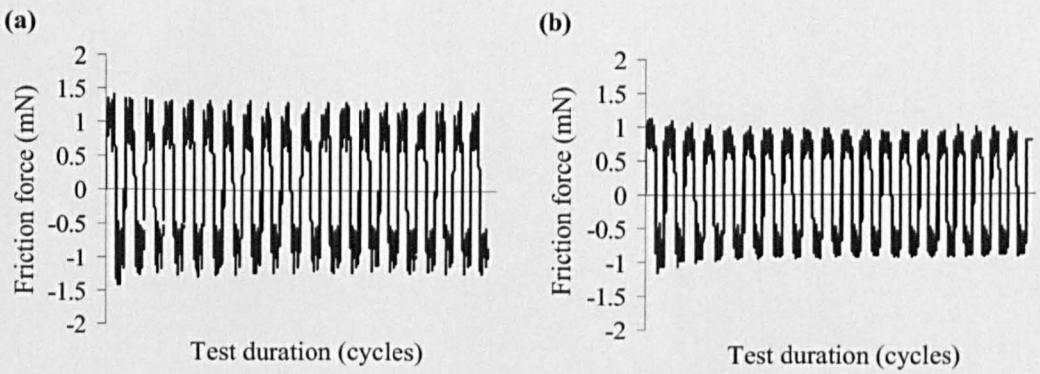

Friction coefficient as function of the test duration obtained on nanostructure CR6 in unlubricated (a) and lubricated (b) LCC tests of EG 2 for normal loads of 10 mN (■), 25 mN (◆), 50 mN (△), 100 mN (●), 150 mN (×), 200 mN (+) and 250 mN (–).

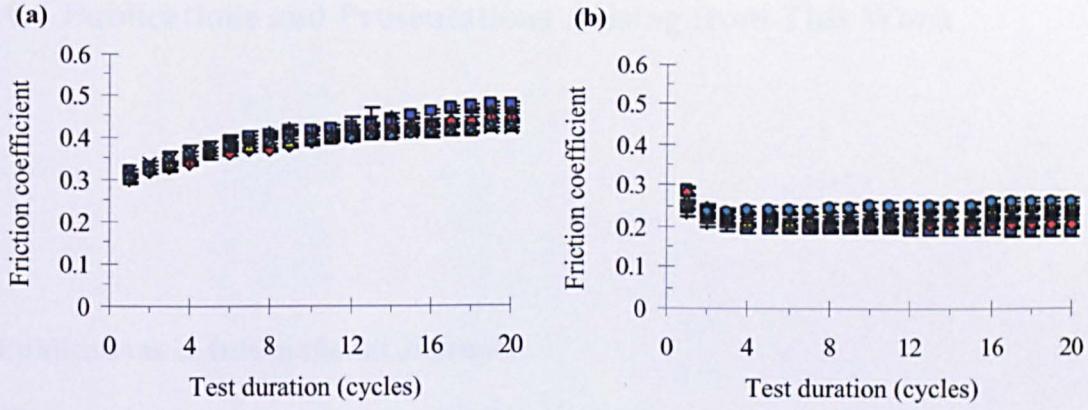

A.4 Publications and Presentations Arising from This Work

Publications in International Journals

"Topographical evolution of sputtered Cr-N thin films"
Y. B. Gerbig, V. Spassov, A. Savan, D.G. Chetwynd
submitted to *Thin Solid Films* in January 2006

"Effect of nanoscale topography and chemical composition of surfaces on their microfrictional behaviour"
Y.B. Gerbig, S.I.-U. Ahmed, D.G. Chetwynd, H. Haefke
Tribology Letters, 21 (2006) 161-168

"Topography-related effects on the lubrication of nanostructured hard surfaces"
Y.B. Gerbig, S.I.-U. Ahmed, S.I.-U., D.G. Chetwynd, H. Haefke
accepted for publication in *Tribology International* in September 2005, online available since November 2005 through Science Direct (http://www.sciencedirect.com)

"Influence of nanoscale topography on the hydrophobicity of fluoro-based polymer thin films"
Y. Gerbig, A.R. Phani, H. Haefke
Applied Surface Science, 242 (2005) 251-255

"In-process structuring of CrN coatings, and its influence on friction in dry and lubricated sliding"
S. Ortmann, A. Savan, Y, Gerbig. H. Haefke
Wear, 254 (2003) 1099-1105

Papers to Published Conferences

"A comparison of lubricants for randomly nanotextured surfaces in micro-contacts"
Y. B. Gerbig, S. I-U. Ahmed, D. G. Chetwynd
Proc. of 6th International Conferenceof European Society of Precision Engineering and Nanostructuring (euspen), 28th May - 1st June 2006, Baden, Austria Vol. II, 409-412

"Influence of the nanoscale topography on the microfriction of hydrophilic and hydrophobic surfaces"
Y.B. Gerbig, S.I.-U. Ahmed, D.G. Chetwynd, H. Haefke,
Proc. of 15th International Colloquium Tribology Automotive and Industrial Lubrication, CD, 17-19 January 2006, Stuttgart/Ostfildern, Germany

"Effect of thin film nanoscale topography and chemical composition of thin films on their microfrictional behaviour"
Y. Gerbig, S.-I.U. Ahmed, D.G. Chetwynd, H. Haefke
Proc. of 1st Vienna International Conference Micro- and Nano-Technology, Vienna 2005, 305-311

"Lubrication of nano-engineered surfaces as a function of their topography"
Y. Gerbig, S.-I.U. Ahmed, D.G. Chetwynd, H. Haefke
Proc. of 1st Vienna International Conference Micro- and Nano-Technology, Vienna 2005, 293-298

Name of presenting author is underlined.

Other Presentations

"Morphogenesis of Cr-N thin films" (invited talk)
Y.B. Gerbig, H. Haefke
Research Institute for Technical Physics and Materials Science, Hungarian Academy of Sciences, 26 May 2004, Budapest, Hungary

"Structural evolution in Cr-N thin films"
Y.B. Gerbig, C. Nouveau, H. Haefke
German Physical Society (DPG), Spring Meeting of the Condensed Matter Division, 08-12 March 2004, Regensburg, Germany

Name of presenting author is underlined.